Department of Civil, Environmental & Construction Engineering

Structural Research

Repair Of Impact Damaged Utility Poles With Fiber Reinforced Polymers (FRP), Phase II

University of Central Florida

4000 Central Florida Blvd
Orlando, FL 32816-2450

Project Manager:
David Wagner

Principal Investigator:
Kevin R. Mackie, PhD PE

Research Assistants:
Cara I. Brown
Robert A. Slade
Zainab Mohsin

Funding Agency:
Florida Department of Transportation

Project No.
BDV24-977-04

FINAL REPORT

June 2015

Disclaimer

The opinions, findings, and conclusions expressed in this publication are those of the authors and not necessarily those of the State of Florida Department of Transportation.

Unit Conversion Table

SYMBOL	WHEN YOU KNOW	MULTIPLY BY	TO FIND	SYMBOL
LENGTH				
in	inches	25.4	millimeters	mm
ft	feet	0.305	meters	m
yd	yards	0.914	meters	m
mi	miles	1.61	kilometers	km

SYMBOL	WHEN YOU KNOW	MULTIPLY BY	TO FIND	SYMBOL
AREA				
in^2	square inches	645.2	square millimeters	mm^2
ft^2	square feet	0.093	square meters	m^2
yd^2	square yard	0.836	square meters	m^2
ac	acres	0.405	hectares	ha
mi^2	square miles	2.59	square kilometers	km^2

SYMBOL	WHEN YOU KNOW	MULTIPLY BY	TO FIND	SYMBOL
VOLUME				
fl oz	fluid ounces	29.57	milliliters	mL
gal	gallons	3.785	liters	L
ft^3	cubic feet	0.028	cubic meters	m^3
yd^3	cubic yards	0.765	cubic meters	m^3
NOTE: volumes greater than 1000 L shall be shown in m^3				

SYMBOL	WHEN YOU KNOW	MULTIPLY BY	TO FIND	SYMBOL
MASS				
oz	ounces	28.35	grams	g
lb	pounds	0.454	kilograms	kg
T	short tons (2000 lb)	0.907	megagrams (or "metric ton")	Mg (or "t")

SYMBOL	WHEN YOU KNOW	MULTIPLY BY	TO FIND	SYMBOL
TEMPERATURE (exact degrees)				
^oF	Fahrenheit	(F-32)/1.8	Celsius	^oC

SYMBOL	WHEN YOU KNOW	MULTIPLY BY	TO FIND	SYMBOL
FORCE and PRESSURE or STRESS				
lbf	pound force	4.45	newtons	N
kip	kilo pound force (1000 lb)	4.45	kilonewtons	kN
lbf/in^2	pound force per square inch	6.89	kilopascals	kPa

Technical Report Documentation

1. Report No.	2. Government Accession No.	3. Recipient's Catalog No.
4. Title and Subtitle Repair of Impact Damaged Utility Poles with Fiber Reinforced Polymers (FRP), Phase II		5. Report Date June 2015 6. Performing Organization Code
7. Author(s) Robert A. Slade, Cara I. Brown, Zainab Mohsin, Kevin R. Mackie		8. Performing Organization Report No.
9. Performing Organization Name and Address **University or Central Florida** 4000 Central Florida Blvd Orlando, FL 32816-2450		10. Work Unit No. (TRAIS) 11. Contract or Grant No. BDV24-977-04
12. Sponsoring Agency Name and Address **Florida Department of Transportation** 605 Suwannee Street, MS 30 Tallahassee, FL 32399		13. Type of Report and Period Covered Final Report 2/27/2014 – 6/30/2015 14. Sponsoring Agency Code
15. Supplementary Notes		

16. Abstract

Vehicle collisions with steel or aluminum utility poles are common occurrences that yield substantial but often repairable damage. This project investigates the use of a fiber-reinforced polymer (FRP) composite system for in situ repair that minimizes potential traffic interruptions. The FRP repair system consists of a filler material to restore a circular cross-section, a primer or adhesive layer, a pre-impregnated or field-impregnated FRP laminate, and a final coating for aesthetics and UV protection. The objective of this study is to develop a set of repair guidelines that can economically and effectively restore an impact-damaged utility pole to a safe working condition. The research plan was divided into three stages. The first stage is a material characterization of the constituents of several likely FRP repair systems, including characterization of the efficacy for installation on vertical poles. The second stage investigates the component-level responses of the repair systems. Mechanical testing to failure was performed for a variety of pole and dent geometries in a standard four-point flexural test setup. The final stage involves verifying the component-level tests using full-scale poles. The poles utilized for testing included both actual poles removed from service with vehicular impact damage as well as poles with mechanically-imparted dents. All full-scale tests were performed on poles with integral base plates oriented in a cantilever configuration and subjected the specimens to flexural monotonic loads to failure, cyclic fatigue loads to failure, and impact loads simulating vehicular impact using a pendulum. Geometric irregularities in the pole and access ports (hand holes) make design of the repair systems challenging. Laminates were oriented in the longitudinal direction on the tension and compression faces with transverse (circumferential) wraps located above and below any obstructions. Results show the repairs to be effective at restoring capacity, resisting cyclic/fatigue load demands, and not prone to instability when impacted with the equivalent of a light vehicle at low speed.

17. Key Word	18. Distribution Statement
glass fiber, basalt fiber, polyurethane, epoxy, debonding	No Restrictions

19. Security Classif. (of this report)	20. Security Classif. (of this page)	21. No. of Pages	22. Price
Unclassified	Unclassified	254	N/A

Acknowledgements

This report would not have been possible without the contributions of numerous members of the Structures Research Laboratory at the Florida Department of Transportation, specifically the project manager David Wagner. In addition, utility poles were donated to the project by several Florida Department of Transportation districts. The retrieval and transport of these poles was coordinated by Alberto Sardinas from District 4 and Debra Sjoberg from District 5. Professor Consolazio from the University of Florida provided technical information and the honeycomb materials for the impact block. Their contributions are acknowledged and greatly appreciated.

Executive Summary

Often when vehicles collide with steel or aluminum utility poles, the poles sustain substantial damage. However, this damage does not always induce the immediate failure of the pole or loss of stability of the mast arm or other supported structure. When this is the case, these structures must be replaced or repaired to maintain serviceability and prevent future structural failure. One potential option for the in situ repair of damaged utility poles is to use a fiber-reinforced polymer (FRP) composite repair system. The FRP repair system consists of a filler material to restore a circular cross-section, a primer or adhesive layer, a pre-impregnated or field-impregnated FRP laminate, and a final coating for aesthetics. The objective of this study is to develop a set of repair guidelines that can economically and effectively restore an impact-damaged utility pole to a safe working condition.

Background

The costs associated with replacement of damaged utility poles are substantial, mostly as they relate to interruption of service and site access/control. Similarly, traditional repair techniques can be just as costly, in the forms of time, money, and service-interruptions. Therefore, an *in situ* repair system that can be installed with minimal labor costs and does not require a service-interruption of the structure is preferable. Previous studies have found that fiber-reinforced polymer composites (FRP) can meet these installation requirements when applied to other infrastructure applications. This study investigates the use of such a system for repair of impact-damaged utility poles, with particular focus on the materials and geometry specific to utility poles that pose challenges for both installation of the repair system, but also on the mechanical performance under static and dynamic loads. Repair systems were selected specifically to minimize the number of layers of FRP laminates applied to the poles, thereby minimizing the material needed and improving the potential for quality control for the repair.

Objectives

There are two principal questions that will be answered in this report: (1) what FRP system or systems can be used to repair impact-damaged utility poles, and (2) how should these systems be installed? To address these questions, the research program was performed in three stages. The first stage is a material characterization of the constituents of several likely FRP repair systems, including characterization of the efficacy for installation on vertical poles. Standard tensile, bond, and compression tests were performed on candidate FRP laminates, dent filler materials, and steel/aluminum substrates. The second stage applies these FRP systems to pole segments and investigates the component-level responses of the repair systems. Mechanical testing to failure was performed for a variety of pole and dent geometries in a standard four-point flexural test setup. The role of dents on the mechanical performance of repaired and unrepaired specimens was investigated by mechanically imparting dents. Both steel and aluminum undamaged pole segments were selected from an inventory of poles removed from service. The final stage involves verifying the component-level tests using full-scale poles. The poles utilized for testing included both actual poles removed from service with vehicular impact damage as well as poles with mechanically-imparted dents. All tests were performed on poles with integral base plates oriented in a cantilever configuration. The full-scale investigation was performed using flexural

monotonic loads to failure, cyclic fatigue loads to failure, and impact loads simulating vehicular impact using a pendulum.

Findings

The material characterization tests showed that the high-density bidirectional glass and basalt fabrics were good candidates when paired with either polyurethane or epoxy resins. Bidirectional fabrics pre-impregnated with polyurethane and standard dry fabric for wet lay-up products are recommended from the component-level and full-scale tests. The dent filler was purposely high viscosity to prevent slump due to gravity and to promote bond between metal and laminate. The primer or adhesive materials were selected to be tacky with setting time conducive to the complicated geometry of longitudinal laminates and transverse circumferential laminates that surround access port (or commonly called hand hole) and dent regions. The pre-cured epoxy laminates, while potentially advantageous for storage, transport, and quality control, were difficult to install on tapered, multi-sided, and small diameter poles, and therefore are not recommended.

The component-level results indicated that even dents approaching 30-40% of the original diameter of the poles could be repaired with only a single layer of FRP (denoted as the single-ply tests). However, with the larger diameter specimens tested in four-point bending, there were some significant challenges in getting the flexural hinging to occur in the pole. Specimens were reinforced at the support points with steel plates to prevent local buckling of the cross-section, and where appropriate, at the load points as well. The repairs were purposely designed to provide the minimum number of layers necessary to restore capacity. Guidelines are provided for the number of layers and geometry of repair based on the dent depth (as a function of the pole diameter) and the target reinforcing ratio provided by the FRP.

The full-scale monotonic tests demonstrated the effectiveness of these proposed repairs on a variety of pole specimens retrieved from the field. Both mechanically-induced dents and field-induced (impact) dent damage were repaired with the proposed materials and composite design guidelines. A majority of specimens showed the repair system to have comparable strength to the original, undamaged, metallic poles, as evidenced by yielding of the base metal below the dented region and the formation of a plastic hinge near the pole base or in the dented region. The mobilizing of confining stress by the transverse circumferential wraps played an important role in the ultimate capacity of the repaired poles, but also, the compressive failure of the poles in the dent filler material and longitudinal compressive laminates appears to have limited the capacity in some cases. The location and geometry of the access ports, relative to the location and extents of the dent, also played an important role in the mechanical behavior of the repaired poles. Without sufficient development length for the transverse circumferential wrap because of the access port or because of the flexibility of the cross-section when the access port was not reinforced, the effectiveness of the repair system diminished substantially.

The cyclic/fatigue full-scale tests indicated that the composite repair system was not a fatigue-prone part. Specimens were subjected to more than 2 million cycles and a constant stress level, with minimal effect observed on the FRP. After 2 million cycles, the stress levels were increased gradually by 1000-cycle increments until failure occurred. The tube-to-transverse-plate welds were always the point of failure, not the repair system. Similarly, during the impact tests, no

substantial damage to the FRP repair system, nor loss of stability were observed. The repair system is therefore recommended for all the configurations of steel poles tested (circular or multi-sided) with or without access ports. However, denting and testing of the aluminum poles demonstrated that the base metal is prone to crack initiation and propagation due to the original impact, and therefore additional investigation of the impacted pole should be performed prior to application of the repair system.

Conclusions

The results of this study indicated that the FRP composite repair systems considered in this study were effective in restoring both field-damaged and laboratory-damaged utility poles to acceptable capacities, as well as restoring the visual geometry for aesthetic purposes. Unlike traditional applications of FRP strengthening for flexural members, walls, or columns, the impact-damaged regions in the utility poles considered in this study posed a significant challenge for both the design of the composite repair as well as actual installation of the repair. The design of the repair was complicated by the location and extents of the dent, potentially with the cross-sectional geometry of the pole being different than the original tapered geometry (at the center of the dent location usually). In addition, a majority of poles considered contained an integral access port (hand hole) or series of pedestrian buttons that prohibited a standard repair that may be employed for pipes, for example. The installation of the repair is challenging due to the need for a vertical layup of the laminates and application of the dent filler material. Materials were selected such that mechanical behavior was acceptable; however, emphasis was placed on ease with which the materials could be brought to the site and installed with good control over quality.

Table of Contents

DISCLAIMER ..... **II**
UNIT CONVERSION TABLE ..... **III**
TECHNICAL REPORT DOCUMENTATION ..... **IV**
ACKNOWLEDGEMENTS ..... **V**
EXECUTIVE SUMMARY ..... **VI**
Background vi
Objectives vi
Findings vii
Conclusions viii
LIST OF FIGURES ..... **XII**
LIST OF TABLES ..... **XVIII**
CHAPTER 1: INTRODUCTION **1**
1.1 Problem Statement 1
1.2 Research Objectives 1
1.3 Report Outline 2
CHAPTER 2: LITERATURE REVIEW **3**
2.1 Externally-Bonded FRP Composites 3
2.1.1 Epoxy-Matrix Composites 3
2.1.2 Polyurethane-Matrix Composites 3
2.1.3 Concrete Substrate 4
2.1.4 Metallic Substrate 4
2.1.4.1 Steel Substrate 4
2.1.4.2 Aluminum Substrate 6
2.2 Civil Infrastructure Applications of FRP 7
2.3 Modeling FRP Composites 7
2.3.1 FRP Material Properties 7
2.3.1.1 Material Properties of a Lamina 8
2.3.1.2 Strength Properties of a Lamina 9
2.3.2 FRP Bond Models 11
2.4 Modeling of Metallic Pole Structures 13
2.5 Overview of Current FRP Design Guidelines 14
2.5.1 United States 14
2.5.2 International 15
2.5.2.1 United Kingdom Standards 15
2.5.2.2 Japanese Standards 15
2.5.2.3 European Standards 16
2.5.2.4 Canadian Standards 16
CHAPTER 3: SMALL-SCALE MATERIAL CHARACTERIZATION **18**
3.1 FRP Repair Systems 18
3.1.1 Fiber Selection and Orientation 18
3.1.2 Matrix Selection 19
3.1.3 Epoxy Filler Selection 19
3.2 Composite Material Properties 21
3.2.1 Tensile Properties 21
3.2.2 Compressive Properties 22
3.2.3 Bond Properties 26
3.2.3.1 Peak Bond Strength 26
3.2.3.2 Bond-Slip Characterization 32
3.2.3.2.1 Experimental Configuration 32
3.2.3.2.2 Experimental Results 32
3.3 Epoxy Fill Material Properties 35
3.4 Pole Substrate Material Properties 37
CHAPTER 4: COMPONENT TESTING **38**
4.1 Damage Determination Tests 41
4.1.1 Damage Determination Test Matrix 42

4.1.2 Aluminum Substrate Tests ... 42
4.1.2.1 ALu-1.a ... 43
4.1.2.2 ALu-1.b ... 45
4.1.2.3 ALu-2.b ... 46
4.1.2.4 ALu-4.a ... 47
4.1.3 Steel Substrate Tests ... 48
4.1.3.1 STu-1.a ... 49
4.1.3.2 STu-1.b ... 50
4.1.3.3 STu-1.c ... 52
4.1.3.4 STu-1.d ... 53
4.1.3.5 STu-1.e ... 54
4.1.3.6 STu-1.f ... 56
4.1.3.7 STu-2.a ... 57
4.1.3.8 STu-2.b ... 59
4.1.4 Summary Damage Determination Test Results ... 59
4.2 Single-Ply Tests ... 61
4.2.1 Single-Ply Test Matrix ... 62
4.2.2 Aluminum Substrate Tests ... 62
4.2.2.1 ALw-4.b ... 63
4.2.2.2 ALw-5.b ... 66
4.2.2.3 ALw-6.a ... 67
4.2.2.4 ALw-7.a ... 69
4.2.2.5 ALw-8.a ... 70
4.2.3 Steel Substrate Tests ... 71
4.2.3.1 STw-3.a ... 72
4.2.3.2 STw-3.b ... 74
4.2.3.3 STw-4.c ... 75
4.2.4 Summary of Single-Ply Test Results ... 77
4.3 Wrap Configuration Tests ... 78
4.3.1 Test Configuration and Loading ... 79
4.3.2 Wrap Configuration Results ... 81
4.3.2.1 Compression Face Wraps ... 81
4.3.2.2 Tension Face Wraps ... 82
4.3.2.3 Neutral Axis Wraps ... 85
4.3.2.4 Transverse Strips Wraps ... 86
4.3.2.5 Compression and Transverse Strips Wraps ... 87
4.3.2.6 Tension and Transverse Strips Wraps ... 88
4.3.2.7 Neutral Axis and Transverse Strips Wraps ... 89
4.3.3 Summary of Wrap Configuration Results ... 90
CHAPTER 5: LARGE-SCALE MONOTONIC TESTING ... 92
5.1 Sample Poles ... 92
5.1.1 Monotonic Pole Tests ... 93
5.1.1.1 Field-Damaged Poles ... 95
5.1.1.2 Induced-Damage Poles ... 95
5.1.2 Cyclic Pole Tests ... 96
5.1.2.1 Induced-Damage Poles ... 96
5.1.3 Impact Pole Tests ... 96
5.1.3.1 Field-Damaged Poles ... 97
5.2 Large-Scale Test Results ... 97
5.2.1 Field-Damaged Poles ... 97
5.2.1.1 FD-1 ... 97
5.2.1.2 FD-2 ... 102
5.2.1.3 FD-3 ... 107
5.2.1.4 FD-5 ... 113
5.2.2 Steel Induced-Damage Poles ... 119
5.2.2.1 ST-5 ... 119
5.2.2.2 ST-6 ... 123
5.2.2.3 ST-8 ... 127
5.2.2.4 ST-12 ... 131
5.2.3 Aluminum Induced-Damage Poles ... 135

5.2.3.1 AL-1.c 135
5.2.3.2 AL-2.c 138
5.2.3.3 AL-3.c 143
5.3 Summary of Large-Scale Monotonic Test Results 147
CHAPTER 6: LARGE-SCALE FATIGUE AND IMPACT TESTING 148
6.1 Fatigue/Cyclic Testing 148
6.1.1 Fatigue/Cyclic Sample Poles 150
6.1.2 Fatigue Stresses by Using AASHTO Design Criteria 152
6.1.2.1 Nominal Stress-Based Design 152
6.1.2.2 Local Stress-Based Design 154
6.1.3 Fatigue Test For Poles in The Laboratory 158
6.1.3.1 ST-7 158
6.1.3.2 ST-10 165
6.1.3.3 ST-11 168
6.2 Impact Testing 176
6.2.1 Impact Sample Poles 178
6.2.2 Specimens Tested Using Impact Pendulum 182
6.2.2.1 IM-1 182
6.2.2.2 IM-2 188
CHAPTER 7: RECOMMENDATIONS 196
7.1 Material Recommendations 196
7.2 Wrap Geometry Recommendations 196
7.3 Repair Installation Recommendations 197
7.4 In-situ Installation on Impact-damaged Pole in Tallahassee 199
CHAPTER 8: CONCLUSIONS 204
8.1 Report Conclusions 204
8.2 Future Research 204
REFERENCES 206
APPENDIX A 209
APPENDIX B 226
APPENDIX C 229

List of Figures

Figure 1. Impact-damaged utility pole 1
Figure 2. Damaged steel mast arm, 3D scan 1
Figure 3. Schematic of FRP-steel bond failure modes (Zhao & Zhang, 2007) 5
Figure 4. Strain and stress distributions under various material conditions (Haedir et al., 2009) 5
Figure 5. CFRP reinforcement on steel monopole (Schnerch & Rizkalla, 2004) 6
Figure 6. Test of CFRP strengthened monopole (Schnerch & Rizkalla, 2004) 6
Figure 7. Stress-strain curve for an unidirectional composite under uniaxial tensile load along fibers (Kaw, 2006) ... 9
Figure 8. Common bond-slip relationship models (Lu et al., 2005) 12
Figure 9. Bond length models (Pantelides et al., 2003) 13
Figure 10. Pilgrim epoxy gel batch 1 20
Figure 11. Pilgrim epoxy gel batch 2 20
Figure 12. Sikadur 31 dent fill 1 21
Figure 13. Sikadur 31 dent fill 2 21
Figure 14. FRP compressive test diagram (ASTM D5467) 23
Figure 15. FRP compressive test variation setup 23
Figure 16. FRP compressive test, unloaded 24
Figure 17. FRP compressive test, under loading 24
Figure 18. QuakeBond™ J300SR composite compressive coupon data 24
Figure 19. NRi XT polyurethane composite compressive coupon data 25
Figure 20. GFRP filament folding failure 25
Figure 21. BFRP wrinkling failure 25
Figure 22. GFRP wrinkling failure 26
Figure 23. Substrate and FRP rupture 26
Figure 24. Circumferential bond test schematic 27
Figure 25. Picture of circumferential bond test 27
Figure 26. Load vs. longitudinal strains readings during circumferential bond test 27
Figure 27. Lap-shear bond test schematic (1) 28
Figure 28. Picture of lap-shear bond test (1) 28
Figure 29. Lap-shear bond test schematic (2) 29
Figure 30. Picture of lap-shear bond test (2) 29
Figure 31. PosiTest© manual adhesion tester schematic 30
Figure 32. Aluminum dolly schematic 30
Figure 33. Shear bond vs. normal bond strength of high-density BFRP systems 31
Figure 34. Shear bond vs. normal bond strength of high-density GFRP systems 31
Figure 35. Shear bond vs. normal bond strength of high-density CFRP systems 31
Figure 36. Bond-slip gauge configuration 32
Figure 37. Picture of bond-slip test specimen 32
Figure 38. QuakeBond™ J300SR-impregnated FRP bonded to steel substrate 33
Figure 39. NRi XT-impregnated FRP bonded to steel substrate 33
Figure 40. QuakeBond™ J300SR-impregnated FRP bonded to aluminum substrate 34
Figure 41. NRi XT-impregnated FRP bonded to aluminum substrate 34
Figure 42. Epoxy compression test samples 36
Figure 43. Epoxy compression instrumentation and sample stress-strain data 36
Figure 44. Pole specimens located in the yard prior to cutting for the component-level tests 38
Figure 45. Denting setup and actuator attachment 39
Figure 46. Dent application to pole ALw-5.b 40
Figure 47. ALw-5.b mesh created from 3D scan point cloud 40
Figure 48. STw-3.a mesh created from 3D scan point cloud 40
Figure 49. FD-3 mesh created from 3D scan point cloud 41
Figure 50. Cuts applied to aluminum component level test specimens 43
Figure 51. Aluminum damage determination test configuration 43
Figure 52. ALu-1.a laboratory-applied dent and test configuration 44
Figure 53. ALu-1.a test data 44

Figure 54. ALu-1.a plastic hinge failure at dent center 45
Figure 55. ALu-1.b laboratory-applied dent 45
Figure 56. ALu-1.b plastic hinging failure 46
Figure 57. ALu-1.b test data 46
Figure 58. ALu-2.b plastic hinging failure 47
Figure 59. ALu-2.b test data 47
Figure 60. ALu-4.a test configuration during loading 47
Figure 61. ALu-4.a local buckling at load applicator 48
Figure 62. ALu-4.a test data 48
Figure 63. Steel damage determination test configuration 49
Figure 64. STu-1.a pole with dented region shown in test setup 50
Figure 65. STu-1.a test data 50
Figure 66. STu-1.b dent before testing 51
Figure 67. STu-1.b test data 51
Figure 68. STu-1.b end weld failure 52
Figure 69. STu-1.c test setup 52
Figure 70. STu-1.c test data 53
Figure 71. STu-1.d test setup 53
Figure 72. STu-1.d test data 54
Figure 73. STu-1.d failed shape 54
Figure 74. STu-1.e test setup 55
Figure 75. STu-1.e test data 55
Figure 76. STu-1.e failed section 56
Figure 77. STu-1.f test setup 56
Figure 78. STu-1.f test data 57
Figure 79. STu-1.f failed pole section 57
Figure 80. STu-2.a test setup 58
Figure 81. STu-2.a test data 58
Figure 82. STu-2.a failure 58
Figure 83. STu-2.b testing and failure 59
Figure 84. STu-2.b test data 59
Figure 85. Aluminum damage determination normalized stress factor vs. dent depth 61
Figure 86. Steel damage determination normalized stress factor vs. dent depth 61
Figure 87. Aluminum single-ply test configuration 63
Figure 88. ALw-4.b initial loading 64
Figure 89. ALw-4.b failure modes 64
Figure 90. ALw-4.b test data 65
Figure 91. ALw-4.b combined test data 65
Figure 92. Progressive strain profiles at section CC' for pole ALw-4.b Test 2 66
Figure 93. ALw-5.b filled dent 66
Figure 94. ALw-5.b test data 67
Figure 95. ALw-5.b failure modes 67
Figure 96. ALw-6.a test data 68
Figure 97. ALw-6.a testing and failure 68
Figure 98. ALw-7.a test data 69
Figure 99. ALw-7.a failure modes 69
Figure 100. ALw-7.a displaced shape 70
Figure 101. ALw-8.a test data 71
Figure 102. ALw-8.a wrap and failure mode 71
Figure 103. Steel single-ply test configuration 72
Figure 104. Voids between composite wrap and steel substrate 73
Figure 105. STw-3.a test data 73
Figure 106. STw-3.a failure modes 74
Figure 107. STw-3.b repaired section in test setup 74
Figure 108. STw-3.b test data 75
Figure 109. STw-4.c dent and composite wrap 75

Figure 110. STw-4.c test data 76
Figure 111. STw-4.c failure modes 76
Figure 112. Aluminum single-ply normalized stress factor vs. dent depth 78
Figure 113. Steel single-ply normalized stress factor vs. dent depth 78
Figure 114. Wrap configuration test setup 80
Figure 115. Laminate layouts for single wrap configurations 80
Figure 116. Laminate layouts for combined wrap configurations 81
Figure 117. Compression wrap in test setup 81
Figure 118. Compression test data 83
Figure 119. Compression wrap failure modes 83
Figure 120. ST-17.a comparison of normalized compression strain slope 84
Figure 121. ST-17.a wrap and load configuration 84
Figure 122. Tension face wrap test data 84
Figure 123. Neutral axis wraps and loading geometry 85
Figure 124. Neutral axis example data 86
Figure 125. Transverse strips pole wraps and loading geometry 86
Figure 126. Transverse strips example data 87
Figure 127. Compression and transverse wrap configuration 88
Figure 128. Compression/transverse example data 88
Figure 129. Tension and transverse wrap configuration – failed section 89
Figure 130. Tension/transverse example data 89
Figure 131. Neutral axis/transverse wraps and loading geometry – pole ST-26.b 90
Figure 132. Neutral axis/transverse example data 90
Figure 133. Monotonic cantilever test setup 94
Figure 134. Field-damaged pole inventory before repair and testing 95
Figure 135. Original vehicular damage to access port region in FD-1 97
Figure 136. FD-1 exterior and interior views (taken after monotonic testing) 98
Figure 137. FD-1 test configuration 99
Figure 138. FD-1 load-displacement data 99
Figure 139. FD-1 load-strain data 100
Figure 140. FD-1 strain gauges 101
Figure 141. FD-1 failure modes 102
Figure 142. FD-2 dents and puncture prior to repair 102
Figure 143. FD-2 test configuration 103
Figure 144. FD-2 load-displacement data 103
Figure 145. FD-2 load-strain data 104
Figure 146. FD-2 strain gauges 105
Figure 147. FD-2 failure modes 106
Figure 148. FD-2 transverse wrap delamination 107
Figure 149. Vehicular dents present in FD-3 prior to repair 108
Figure 150. FD-3 test configuration 108
Figure 151. FD-3 Test 1 load-displacement data 108
Figure 152. FD-3 Test 1 load-strain data 109
Figure 153. FD-3 Test 2 load-displacement data 110
Figure 154. FD-3 Test 2 load-strain data 111
Figure 155. FD-3 strain gauges 112
Figure 156. FD-3 failure modes 112
Figure 157. Vehicular damage to FD-5 prior to repair 113
Figure 158. FD-5 test setup 113
Figure 159. FD-5 Test 1 load-displacement data 114
Figure 160. FD-5 Test 1 load-strain data 115
Figure 161. FD-5 Test 1 deformed shape and base plate failure 116
Figure 162. FD-5 Test 2 load-displacement data 116
Figure 163. FD-5 Test 2 load-strain data 117
Figure 164. FD-5 strain gauges 118
Figure 165. FD-5 failure modes 119

Figure 166. ST-5 test configuration 120
Figure 167. ST-5 load-displacement data 120
Figure 168. ST-5 load-strain data 121
Figure 169. ST-5 strain gauges 122
Figure 170. ST-5 after testing 123
Figure 171. ST-6 test configuration 123
Figure 172. ST-6 load-displacement data 124
Figure 173. ST-6 load-strain data 125
Figure 174. ST-6 strain gauges 126
Figure 175. ST-6 deflected shape at failure 126
Figure 176. ST-6 failure modes 127
Figure 177. ST-8 test configuration 128
Figure 178. ST-8 load-displacement data 128
Figure 179. ST-8 load-strain data 129
Figure 180. ST-8 strain gauges 130
Figure 181. ST-8 failure modes 131
Figure 182. ST-12 test configuration 132
Figure 183. ST-12 load-displacement data 132
Figure 184. ST-12 load-strain data 133
Figure 185. ST-12 strain gauges 134
Figure 186. ST-12 failure mode 134
Figure 187. AL-1.c test configuration 136
Figure 188. AL-1.c load-displacement data 136
Figure 189. AL-1.c load-strain data 137
Figure 190. AL-1.c strain gauges 138
Figure 191. AL-1.c failure modes 139
Figure 192. AL-2.c test configuration 139
Figure 193. AL-2.c load-displacement data 140
Figure 194. AL-2.c load-strain data 141
Figure 195. AL-2.c strain gauges 142
Figure 196. AL-2.c failure modes 142
Figure 197. AL-2.c after testing 143
Figure 198. AL-3.c test configuration 144
Figure 199. AL-3.c load-displacement data 144
Figure 200. AL-3.c test data 145
Figure 201. AL-3.c strain gauges 146
Figure 202. AL-3.c base plate failure 146
Figure 203. AL-3.c laminate surrounding access port cover 146
Figure 204. Typical light pole base 149
Figure 205. Fatigue cracking at the connection pole-base plate fillet weld toe (NCHRP-176, 2011) 149
Figure 206. Fatigue test actuator connection with stiffener at end section 151
Figure 207. Fatigue test connection to buttress with plate washers on top and bottom 151
Figure 208. Tube-to-transverse-plate connection, location of anticipated fatigue crack at the weld toe on the tube is shown in red (AASHTO, 2013) 153
Figure 209. Finite element model for finite life (ST-10) 154
Figure 210. Finite element model for finite life with supplemental FRP layer (ST-10) 155
Figure 211. FEM for infinite life 156
Figure 212. Enlarged mesh detail for notched area 156
Figure 213. FEM for finite fatigue life (ST-10) 157
Figure 214. FEM for infinite fatigue life (ST-10) 157
Figure 215. ST-7 test configuration 159
Figure 216. ST-7 test data during first 2 million cycles 160
Figure 217. ST-7 strain gauges 161
Figure 218. ST-7 load-displacement hysteresis during increasing fatigue category level 162
Figure 219. ST-7 steel strain data during higher stress level cycles 163
Figure 220. ST-7 FRP strain data during higher stress level cycles 164

Figure 221. ST-7 cracks after post-fatigue monotonic test 164
Figure 222. ST-7 failure modes after post-fatigue monotonic test 165
Figure 223. ST-10 test configuration 166
Figure 224. ST-10 load-displacement data during load ramps and all recorded cycles for the test 166
Figure 225. ST-10 load-strain data during load ramps and all recorded cycles for the test 167
Figure 226. ST-10 strain gauges 168
Figure 227. ST-10 wrap and crack at base weld 169
Figure 228. ST-11 test configuration 169
Figure 229. ST-11 displacement compliance during first 2 million cycles 170
Figure 230. ST-11 strain data during first 2 million cycles 171
Figure 231. ST-11 strain gauges 172
Figure 232. Load vs. displacement for ST-11 during increasing amplitude cycles 173
Figure 233. ST-11 steel strain data during higher stress level cycles 174
Figure 234. ST-11 FRP strain data during higher stress level cycles 175
Figure 235. ST-11 failure modes 176
Figure 236. Impact pendulum at Structures Research Center in Tallahassee (IM-2 on pedestal) 178
Figure 237. FEM for pendulum impact assembly (Consolazio et al., 2012) 179
Figure 238. Crushable nose for IM-1 after connecting to mass block 179
Figure 239. IM-1 connection to the pedestal foundation 180
Figure 240. IM-2 connection to the pedestal foundation 181
Figure 241. IM-1 test configuration 182
Figure 242. IM-1 test strain data 183
Figure 243. IM-1 strain gauges 184
Figure 244. IM-1 mass block acceleration data 185
Figure 245. IM-1 pole acceleration data 186
Figure 246. IM-1 accelerometers 186
Figure 247. IM-1 post-test state of the pole and crushable nose 187
Figure 248. IM-1 post-test state of repair material at impact location 188
Figure 249. IM-2 dent cavity volume requiring fill material 189
Figure 250. IM-2 test configuration 189
Figure 251. IM-2 strain data 190
Figure 252. IM-2 strain gauges 191
Figure 253. IM-2 mass block acceleration data 192
Figure 254. IM-2 pole acceleration data 193
Figure 255. IM-2 accelerometers 194
Figure 256. IM-2 post-test state of the pole and crushable nose 194
Figure 257. IM-2 forensic view of the repair material 195
Figure 258. In-situ damaged pole and site preparation 200
Figure 259. Pole surface preparation 201
Figure 260. Pole wrapping 202
Figure 261. Painting and final product 203
Figure 262. AL-1.c design drawing 210
Figure 263. AL-2.c design drawing 211
Figure 264. AL-3.c design drawing 212
Figure 265. ST-5 design drawing 213
Figure 266. ST-6 design drawing 214
Figure 267. ST-7 design drawing 215
Figure 268. ST-8 design drawing 216
Figure 269. ST-10 design drawing 217
Figure 270. ST-11 design drawing 218
Figure 271. ST-12 design drawing 219
Figure 272. FD-1 design drawing 220
Figure 273. FD-3 design drawing 221
Figure 274. FD-5 design drawing 222
Figure 275. IM-1 design drawing 223
Figure 276. Pole IM-2 design drawing 224

Figure 277. Caliark in-situ repair design drawing 225
Figure 278. FD-1 coupon stress-strain data 230
Figure 279. FD-2 coupon stress-strain data 230
Figure 280. FD-3 coupon stress-strain data 231
Figure 281. FD-5 coupon stress-strain data 231
Figure 282. ST-5 coupon stress-strain data 232
Figure 283. ST-6 coupon stress-strain data 232
Figure 284. ST-7 coupon stress-strain data 233
Figure 285. ST-8 coupon stress-strain data 233
Figure 286. ST-10 coupon stress-strain data 234
Figure 287. ST-11 coupon stress-strain data 234
Figure 288. ST-12 coupon stress-strain data 235
Figure 289. IM-1 coupon stress-strain data 235
Figure 290. IM-2 coupon stress-strain data 236

List of Tables

Table 1. Typical tensile properties of fibers used in FRP systems (Rizkalla & Busel, 2002) 18
Table 2. Fabric weave densities 19
Table 3. Manufacturer specifications for saturating resins and adhesives 19
Table 4. Manufacturer specifications for filler material 20
Table 5. Average tensile properties for each sample set 22
Table 6. Bilinear compressive properties for FRP impregnated with QuakeBond™ J300SR resin 24
Table 7. Bilinear compressive properties for FRP impregnated with NRi XT polyurethane resin 25
Table 8. Average ultimate bond stress achieved (psi) - Tyfo® 28
Table 9. Average ultimate bond stress achieved (psi) - CB, QB, and XT 29
Table 10. Bond-slip model properties for FRP systems adhered to steel substrate 35
Table 11. Bond-slip model properties for FRP systems adhered to aluminum substrate 35
Table 12. Epoxy compression test results 36
Table 13. Steel large-scale test specimen material properties 37
Table 14. Material properties obtained from previous pole study (Mackie et al., 2011) 37
Table 15. Damage determination test specimens 42
Table 16. Damage determination result summary 60
Table 17. Single-ply test specimens 62
Table 18. Single-ply result summary 77
Table 19. Wrap configuration test specimens 79
Table 20. Wrap configuration compression summary of results 83
Table 21. Wrap configuration tension summary of results 85
Table 22. Wrap configuration neutral axis summary of results 86
Table 23. Wrap configuration transverse strips summary of results 87
Table 24. Wrap configuration compression/transverse summary of results 88
Table 25. Wrap configuration tension/transverse summary of results 89
Table 26. Wrap configuration neutral axis/transverse summary of results 90
Table 27. Wrap configuration summary of results 91
Table 28. Large-scale testing matrix (contains specimens for Chapters 5 and 6) 92
Table 29. Large-scale pole specimen geometry (contains specimens for Chapters 5 and 6) 93
Table 30. Large-scale monotonic result summary 147
Table 31. Full –scale testing matrix for fatigue test 150
Table 32. Additional pole geometric parameters necessary for AASHTO equations 152
Table 33. Fatigue calculations for nominal stress 153
Table 34. Stress contour magnitudes in both U.S. and SI units from Figure 213 and Figure 214 (ST-10) 157
Table 35. Large-scale test matrix for impact test 181
Table 36. Guide for determining repair action 197

Chapter 1: Introduction

1.1 Problem Statement

Steel and aluminum utility poles, light poles, and mast arms are occasionally damaged by vehicle collision. In 2000, there were 1,103 fatalities and about 60,000 injuries related to utility pole crashes in the United States (Ivey & Scott, 2004). In many cases, the vehicular impact does not cause a global failure of the structure, but only induces localized damage, such as the damaged indicated in Figure 1. This damage may not cause immediate failure of the structure, but under extreme service loadings may result in a failure. Replacement of these poles is costly and often involves prolonged lane closures, service interruption, and temporary loss of functionality. Therefore, *in situ* repair of these damaged structures is preferable for effective asset management.

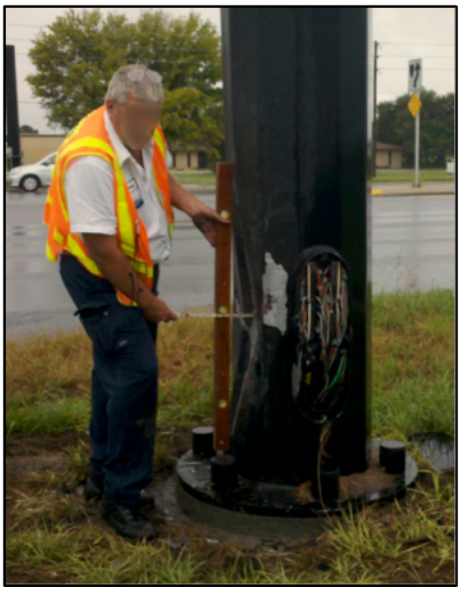

Figure 1. Impact-damaged utility pole

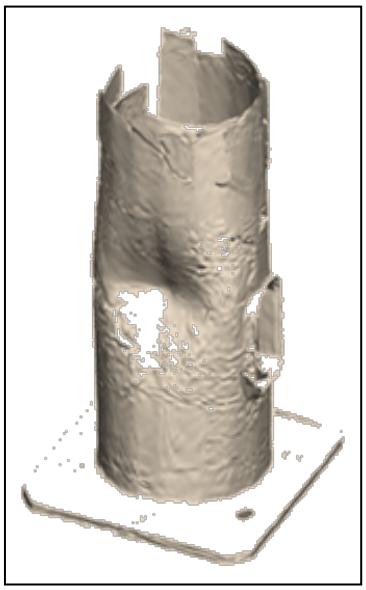

Figure 2. Damaged steel mast arm, 3D scan

Previous studies have shown that the capacity of impact-damaged poles can be adequately restored through the use of externally-bonded FRP composites (Mackie et al., 2011). The previous study considered simulated damage to 4 steel and 2 aluminum poles. A three-dimensional (3D) scan of the typical damage profile to a steel pole is shown in Figure 2. The proposed repair technique allows for relatively simple, inexpensive, and speedy restoration without the need for large equipment, service interruption, or lane closures. Therefore, this process will be examined and refined in this study, whereby guidelines will be developed for practical implementation.

1.2 Research Objectives

The principal objective of this study is to provide the Florida Department of Transportation with the following:

1) A detailed, theoretical background for the use of externally-bonded FRP composites to repair impact-damaged metallic utility poles.

2) A user-friendly design guide outlining the precise repair procedures required to restore a damaged utility pole to its original service capacity.

1.3 Report Outline

This research report is presented in the following format:

1) *Literature Review*: The literature presented is a comprehensive overview of the background, materials, and previous work integral to the motivation and understanding of the study being presented.

2) *Small-scale Material Characterization*: A comprehensive study of the material properties critical to the investigation and design of an externally-bonded FRP system capable of repairing damaged utility poles.

3) *Medium-scale Component Testing*: A set of tests to study the component properties and their interaction under loading so as to determine an optimum repair technique.

4) *Large-scale Utility Pole Testing:* A set of tests involving full-size cantilevered utility poles, in which the repairs derived in the component-level tests are verified for practical use. This includes monotonic static, fatigue, and impact testing.

5) *Conclusions*: Conclusions will be drawn from the experimental results, and potential areas of future research will be suggested.

6) *Repair Guidelines and Recommendations*: Based on the results of the tests conducted, recommendations concerning field applications will be made. Details are shown for application of the procedures to an in-situ repair.

Chapter 2: Literature Review

The following chapter includes the literature review that was conducted with this research project. This chapter initially covers the various components that make up externally-bonded fiber reinforced polymers (FRP), then surveys the applications of these composites as applied to civil infrastructure, discusses the standard approach used for modeling members reinforced with FRP, and finally overviews the current set of guidelines concerning structural FRP design. The literature and design guidelines specific to fatigue and dynamic impact to poles is contained in the fatigue and impact chapter.

2.1 Externally-Bonded FRP Composites

Fiber reinforced polymer (FRP) composites are advanced materials consisting of a fiber mesh impregnated with a polymer matrix. The fibers act as the primary strengthening element, while the matrix transfers stress to the fibers and maintains the fiber orientation. Externally-bonded FRP reinforcement is a structural repair technique in which these composites are adhered to the exterior surface of a structural member. This form of retrofit allows for simple and quick installation, while maintaining a low profile that can conform to the shape of the member. Additionally, by selecting different fibers or matrix materials, the properties of the FRP can be altered to produce composites tailored to each structure individually.

2.1.1 Epoxy-Matrix Composites

Epoxy resins are the most common matrix material used in FRP composites. Though epoxy resins are considered more expensive than many other matrix materials, they have several advantages that add to their popularity. Principal among these include high strength, low viscosity, good fiber wet out, low volatility, low shrinkage, and ease of availability (Kaw, 2006). When used as an externally-bonded repair, a wet layup application is typically selected. This involves combining the epoxy resin with a hardener that initiates a chemical reaction curing the mixture. The fiber mesh is then impregnated with the resin by saturation at room temperature. The FRP composite can then be affixed to the substrate directly, relying on the adhesive properties of the epoxy as it cures, or a separate adhesive primer layer can be used.

2.1.2 Polyurethane-Matrix Composites

Relatively new to the field of structural composites, polyurethanes are a group of resins that exhibit similar chemical and physical properties to each other. Generally, polyurethane resins display good fiber wet out and substrate adhesion, have a rapid cure time, are cost effective, and work well at low temperatures. However, research has shown that they also have limited thermal and hydraulic stability, are sensitive to bulk moisture, and are critically affected by curing conditions (Haber et al., 2009).

As opposed to epoxy resins, polyurethanes are activated by exposure to water. Therefore, a standard wet layup process is impractical. Instead, pre-impregnated (prepreg) woven fiber meshes are cut to length and hermetically sealed until installation, at which point they are exposed to water and set in place for curing. Typically this process involves the use of a separate adhesive primer layer to affix the polyurethanes prepreg to the substrate.

2.1.3 Concrete Substrate

Use of externally-bonded FRP composites to reinforce structural concrete members has become increasingly popular in the last few decades. Much research has been conducted to investigate the effectiveness of such a repair, and the mechanical response is well understood. Studies have shown that externally-bonded FRP composites can be used to improve the stiffness, static, cyclic, and fatigue load caring capacity, and environmental durability of a structural member (Buyukozturk et al., 2004).

However, a primary design consideration for FRP-strengthened concrete members is FRP debonding. Due to the unpredictable and brittle nature of a debonding failure, the FRP reinforcement may reduce the ductility of a member, thus decreasing the overall level of safety (Gunes et al., 2009). Another important design consideration is shear failure. Externally-bonded FRP tension reinforcement can cause a load to exceed the shear capacity of the RC member. Side bonding and U-jacketing of FRP can help to increase the shear capacity, but shear debonding and cover peel-off become critical failure modes (Pellegrino et al., 2008).

To overcome these design issues, several authors have suggested relatively simple semi-empirical models that avoid some of the complexities of fracture analyses for use in design calculations (Buyukozturk et al., 2004; Gunes et al., 2009; Kaw, 2006).

2.1.4 Metallic Substrate

Unlike concrete, externally bonded FRP has only recently been investigated for use on steel or aluminum structures. Due to the material characteristics of FRP and the ease with which it can be added to a structural element make it an ideal candidate for retrofit in many situations. However, one of the primary concerns associated with using FRP to reinforce metallic structures is the possible electro-chemical interaction. Specifically when dealing with carbon fiber composites, galvanic corrosion is a major concern. Due to the high degree of galvanic potential associated with carbon, if these composites come in contact with a metallic substrate that is low in the galvanic series, such as steel or aluminum, the potential for corrosion is large (Hollaway & Cadei, 2002). Therefore, precautions must be taken when dealing with CFRP reinforcement of steel or aluminum structures.

2.1.4.1 Steel Substrate

In 2007 a state of the art review was published in the journal of Engineering Structures that indicated the potential usefulness of FRP for retrofit of steel. This paper overviews standard bond test methodology, as well as suggests several steel HSS- and W-section retrofit schemes (Zhao & Zhang, 2007). A graphical description of the various failure modes associated with FRP Reinforced steel was taken from this study and is shown in Figure 3.

Studies involving FRP reinforcement of steel bridges began in 1990s and were shown to be a promising form or retrofit. These indicate that bonding FRP to the tension face of steel girder can increase the overall stiffness and strength of the structure (Miller et al., 2001). Furthermore, using FRP in conjunction with concrete grout to reinforce deficient steel column sections has also been examined (Karimi et al., 2010). Here, the FRP is primarily used as a confining formwork to house the concrete grout that encompasses the existing steel column member. This

composite repair technique was shown to increase the overall capacity of the member, but to the author's knowledge has not yet become commercially prevalent.

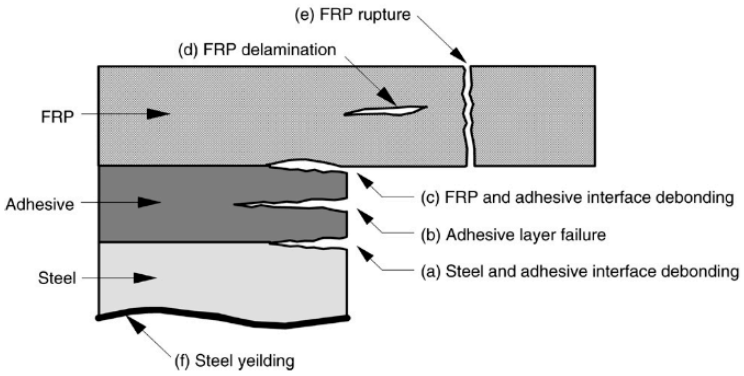

Figure 3. Schematic of FRP-steel bond failure modes (Zhao & Zhang, 2007)

A 2010 study out of Australia specifically examined FRP reinforcement of steel circular hollow sections (CHS). The focus was to derive an analytical method to determine the ultimate capacity of FRP reinforced CHS beams subjected to bending loads (Haedir et al., 2009). The moment capacities of the steel CHS and the FRP are derived for assumed elastic, elastic-perfectly-plastic, and plastic conditions, with the results compared against experimental data. The stress and strain distributions for these conditions are given in Figure 4. However, it should be noted that the method derived is only applicable for analysis of symmetrically round sections, and not damaged or dented cross-sections.

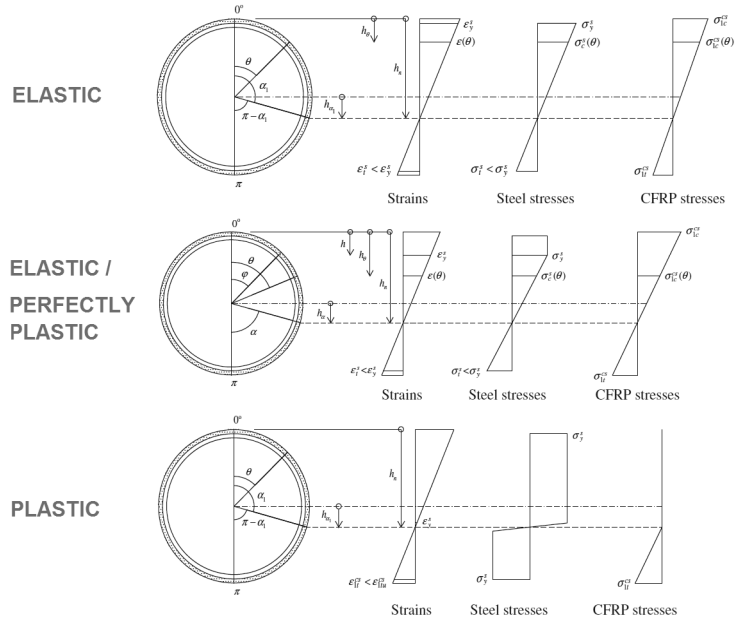

Figure 4. Strain and stress distributions under various material conditions (Haedir et al., 2009)

Additionally, a good deal of research has been conducted at North Carolina State University by Rizkalla, Dawood, and Schnerch on the topic of FRP reinforcement of steel poles. Paramount among these was a study involving polygonal monopoles strengthened with CFRP. These studies

involved pultruded CFRP plates or wet-layup CFRP sheets that were adhered at the base directly on the outside of large steel monopoles. Due the cross-sectional geometry of these poles, the FRP was applied in flat sheets as can be seen in Figure 5. These studies demonstrated that FRP is a viable option for increasing the strength and stiffness of poles subjected to a cantilever loading, as can be seen in Figure 6 (Schnerch & Rizkalla, 2004).

Figure 5. CFRP reinforcement on steel monopole (Schnerch & Rizkalla, 2004)

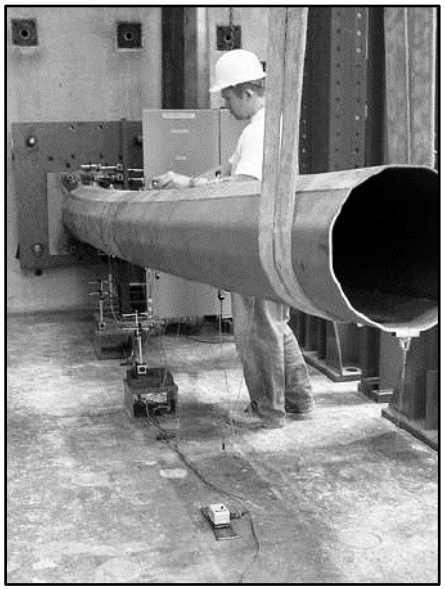

Figure 6. Test of CFRP strengthened monopole (Schnerch & Rizkalla, 2004)

One of the primary concerns associated with using FRP to reinforce metallic structures is a possible electro-chemical interaction. Specifically when dealing with carbon fiber composites, galvanic corrosion is a major concern. Due to the high degree of galvanic potential associated with carbon, if these composites come in contact with a metallic substrate that is low in the galvanic series, such as steel or aluminum, the potential for corrosion is large (Hollaway & Cadei, 2002). Therefore, precautions must be taken when dealing with CFRP reinforcement of steel or aluminum structures.

2.1.4.2 Aluminum Substrate

Investigation into the use of FRP reinforcement of aluminum sections is only in its infancy, with few comprehensive studies being completed. One study involving high-modulus carbon fibers and various commercial adhesives found that externally bonded FRP plates were effective in resisting web buckling of rectangular aluminum tube sections, though it was also found that little additional capacity was gained by extending the FRP beyond the load bearing region (Islam et al., 2011).

Other studies have been conducted within the past ten years to examine the use of FRP to repair fatigued joints on aluminum highway sign structures. Due to the previous design standards, this form of damage was resulting in failure of these structures. Therefore, several agencies such as the Delaware, Utah, and New York State departments of transportation funded studies which concluded that commercial FRP systems involving both glass and carbon fibers could be used to economically restore damaged aluminum joint connections (Bhattacharya & Seifried, 2005; Fam

et al., 2006; Pantelides et al., 2003). These studies focused on welded joint failure of a small-diameter section, and did not suggest a repair approach for the primary vertical component of sign structures. Few additional studies exist that have looked at the infrastructure applications of FRP reinforcement applied to aluminum structures.

2.2 Civil Infrastructure Applications of FRP

The use of externally-bonded FRP to reinforce civil infrastructure has been studied and developed for many years. Beginning with applications on concrete bridge girders and decks in the 1980s and extending to seismic retrofit of joint connections today. Studies have progressed to column and pile reinforcement (Sen et al., 2007), steel bridges (Schnerch et al., 2007), and pressurized pipe repair (Hauch & Bai, 1999; Schaumann et al., 2005). Several other studies have focused on reinforcing wood, concrete, and steel utility poles used to support power cables, cameras, lighting, signaling, and signage. Though, these studies primarily dealt with reinforcing the maximum carrying capacity of the structures, and not repairing damaged structures (Chahrour & Soudki, 2006; Lanier et al., 2009; Polyzois & Kell, 2007).

2.3 Modeling FRP Composites

Modeling of fiber reinforced polymers, as with any composite material, involves a more complicated design method then more traditional orthotropic, homogeneous materials. The benefits that can be obtained by combining multiple materials with different properties into a single composite material fundamentally require an advanced approach. The internal physical properties of an FRP act like an isotropic material and are modeled by the rule of mixtures, while the bond between FRP and substrate are typically described using fracture mechanics, and can often best be modeled with finite element method (FE) software.

2.3.1 FRP Material Properties

Externally-bonded FRP composites consist of a fiber mesh suspended within a polymer matrix. These composites have layers of fibers that produce a single dominant direction of stiffness and strength. By varying the orientation of these fiber layers, the overall properties of the element can be customized to fit the requirements of the design. Each individual layer, or lamina, can be analyzed separately, and then the macro-mechanical response of the laminate can be compiled from the component properties.

The mechanical properties of a lamina are described by the rule of mixtures, which states that the properties of the lamina are determined by the properties of the components within the composite, proportionately. For FRP composites, these proportions are volumetric. Total volume of fibers (in a single layer of FRP) divided by the total volume of fibers and matrix (in a single layer of FRP) is called the fiber volume fraction, and is typically abbreviated as V_f. The remaining volume of matrix divided by the total volume is called the matrix volume fraction, and is typically abbreviated as V_m. Therefore, the sum of V_f and V_m necessarily equals 1, assuming no voids are present within the lamina (Kaw, 2006).

2.3.1.1 Material Properties of a Lamina

Most FRP composites have a stress vs. strain relationship that behaves nearly linearly; therefore, Hooke's law can be used to accurately define these materials. That is, normal stress and strain are related through the elastic modulus (E), $\sigma = E\varepsilon$, and shear stress and strain are related through the shear modulus (G), $\tau = G\gamma$. In the longitudinal direction of the lamina (along fiber axis) a state of equilibrium exists where the force within the fibers (F_f) added to the force within the matrix (F_m) is equal to the total force within the lamina (F_c). The cross-sectional area of the fibers, matrix, and composite are defined as A_f, A_m, and A_c, respectively. The equilibrium equation can be rewritten as:

$$E_1\varepsilon_c A_c = \left(E_f\varepsilon_f A_f\right)_{\text{longitudinal}} + (E_m\varepsilon_m A_m)_{\text{longitudinal}} \tag{2-1}$$

or,

$$E_1\varepsilon_c = \left(E_f V_f\right)\varepsilon_f + (E_m V_m)\varepsilon_m \tag{2-2}$$

Assuming continuous composite action between the fibers and matrix, the displacement and strain across an axial section of the lamina are all equal, or in the longitudinal direction, $\varepsilon_c = \varepsilon_f = \varepsilon_m$. Therefore,

$$E_1 = \left(E_f V_f\right) + (E_m V_m) \tag{2-3}$$

In the transverse direction the fiber and matrix displacements compound sequentially. The relative thickness of the fibers, matrix, and composite are defined as t_f, t_m, and t_c, respectively. The equation of transverse displacement can be rewritten as:

$$\varepsilon_c t_c = \left(\varepsilon_f t_f\right)_{\text{transverse}} + (\varepsilon_m t_m)_{\text{transverse}} \tag{2-4}$$

or,

$$\frac{\sigma_c}{E_2} = \left(\frac{\sigma_f}{E_f}V_f\right) + \left(\frac{\sigma_m}{E_m}V_m\right) \tag{2-5}$$

In the transverse direction, the stress transfers between the matrix and fibers simultaneously, or the stresses are equal $\sigma_c = \sigma_f = \sigma_m$. Therefore,

$$\frac{\mathbf{1}}{\boldsymbol{E_2}} = \left(\frac{\boldsymbol{V_f}}{\boldsymbol{E_f}}\right) + \left(\frac{\boldsymbol{V_m}}{\boldsymbol{E_m}}\right) \tag{2-6}$$

Due to the poison's effect within the matrix (ν_m) and the fibers (ν_f), there is an overall relationship between the longitudinal and transverse strains in the lamina (ν_{12}). As previously established, the displacements in the longitudinal direction between the fibers, matrix, and total composite are equivalent, whereas in the transverse direction the displacements compound. Apply the Poisson relationship to the transverse displacement equation to form:

$$-\varepsilon_c(\nu_{12}t_c)_{\text{longitudinal}} = -\varepsilon_f\left(\nu_f t_f\right)_{\text{longitudinal}} - \varepsilon_m(\nu_m t_m)_{\text{longitudinal}} \tag{2-7}$$

or,

$$\nu_{12} = (\nu_f V_f) + (\nu_m V_m) \tag{2-8}$$

Similar to the transverse displacement, in shear, the fiber and matrix displacements compound sequentially:

$$\gamma_c t_c = (\gamma_f t_f)_{\text{shear}} + (\gamma_m t_m)_{\text{shear}} \tag{2-9}$$

To maintain system equilibrium, all shear forces must be equal, $\tau_c = \tau_f = \tau_m$. Therefore, applying Hooke's Law to the previous equation produces:

$$\frac{\tau_c}{G_{12}} t_c = \left(\frac{\tau_f}{G_f} t_f\right) + \left(\frac{\tau_m}{G_m} t_m\right) \tag{2-10}$$

or,

$$\frac{\mathbf{1}}{\boldsymbol{G_{12}}} = \left(\frac{\boldsymbol{V_f}}{\boldsymbol{G_f}}\right) + \left(\frac{\boldsymbol{V_m}}{\boldsymbol{G_m}}\right) \tag{2-11}$$

2.3.1.2 Strength Properties of a Lamina

While many theories describe the macroscopic failure criteria of a laminate, failure of a single layer lamina will occur in one of five distinct ways: (1) longitudinal tensile failure, (2) longitudinal compressive failure, (3) transverse tensile failure, (4) transverse compressive failure, or (5) in-plane shear failure.

Typically, the fibers within a lamina are substantially stiffer then the matrix material. Additionally, the strain at failure of the fibers is significantly less than that of the matrix. Once the composite reaches the ultimate strain of the fibers in the longitudinal direction, the fibers will fail. Neglecting the capacity of the unreinforced matrix, when the fibers fail the composite also fails, as is visible in Figure 7. Therefore, the critical value necessary for predicting longitudinal tensile failure is the ultimate strain of the fibers:

$$(\sigma_1^T)_{\text{ult}} = V_f(\sigma_f)_{\text{ult}} + V_m(\varepsilon_f)_{\text{ult}} E_m \tag{2-12}$$

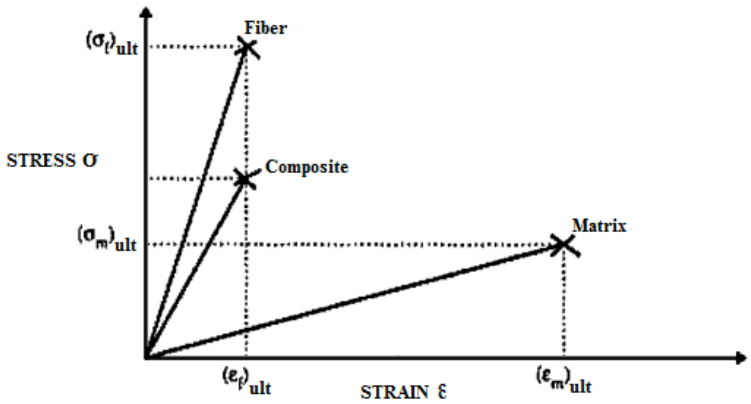

Figure 7. Stress-strain curve for an unidirectional composite under uniaxial tensile load along fibers (Kaw, 2006)

Longitudinal compressive failure typically occurs in one of three forms: matrix strain failure, fiber micro-buckling, or fiber shear failure. The dominant failure mode occurs for the state where $(\sigma_1^T)_{\text{ult}}$ is closest to zero. The derivations for the following failure criteria are not shown here, but can be found in (Kaw, 2006).

(1) Matrix strain failure mode:

$$(\sigma_1^T)_{\text{ult}} = \frac{E_1 (\epsilon_2^T)_{\text{ult}}}{\nu_{12}} \tag{2-13}$$

where $(\epsilon_2^T)_{\text{ult}}$ is empirically derived as,

$$(\epsilon_2^T)_{\text{ult}} = (\epsilon_m^T)_{\text{ult}}\left(1 - \sqrt[3]{V_f}\right) \tag{2-14}$$

(2) Fiber micro-buckling failure mode:

$$(\sigma_1^T)_{\text{ult}} = \min\left\{2\left[V_f + \left(1 - V_f\right)\frac{E_m}{E_f}\right]\sqrt{\frac{V_f E_m E_f}{3(1-V_f)}}, \frac{G_m}{(1-V_f)}\right\} \tag{2-15}$$

(3) Fiber shear failure mode:

$$(\sigma_1^T)_{\text{ult}} = 2(\tau_{12})_{\text{ult}} \tag{2-16}$$

When determining the transverse tensile or compressive failure stresses, several key assumptions are made: under transverse loading the stress in the fiber and matrix are equal, and in this mode the failure will initially occur in the matrix before the fibers. Knowing the fiber diameter (*d*) and effective spacing (*s*) of the lamina, it can be shown that the following two equations are true for both tension and compression loading:

$$(\varepsilon_2)_{\text{ult}} = \left[\frac{d}{s}\frac{E_m}{E_f} + \left(1 - \frac{d}{s}\right)\right](\varepsilon_m)_{\text{ult}} \tag{2-17}$$

and,

$$(\sigma_2)_{\text{ult}} = E_2(\varepsilon_2)_{\text{ult}} \tag{2-18}$$

Finally, to calculate the critical in-plane shear failure stress, the in-plane shear strain must be found based on the reasonable assumption that the shear strains in the fiber and matrix are equal and following the same procedure as in the previous failure mode, it can be shown that:

$$(\gamma_{12})_{\text{ult}} = \left[\frac{d}{s}\frac{G_{\text{m}}}{G_{\text{f}}} + \left(1 - \frac{d}{s}\right)\right](\gamma_{\text{m}})_{\text{ult}} \tag{2-19}$$

and,

$$(\tau_{12})_{\text{ult}} = G_{12}(\gamma_{12})_{\text{ult}} \tag{2-20}$$

2.3.2 FRP Bond Models

A complex state of stress can exists within the bond between an FRP and the substrate material. The relationship between the shear stress and slip of the FRP is typically used to describe the mechanics of the bond itself. The slip is the relative displacement of the FRP layer, with respect to the substrate. If sufficient bond length is present, the shear strain tapers to zero, so the total slip at the free end of the bond can be determined by integrating the strain along the length of the bonded area, parallel to the application of the shearing load. Similarly, the shear within the FRP can be found using the tensile modulus of the FRP and the ratio of axial strain to shear strain. The total slip and shear stress at the free end of a lap can be found by:

$$\tau = \sum \mathrm{E_f}\left(\frac{\mathrm{t_f}}{\mathrm{x_{i+1}}-\mathrm{x_i}}\right)(\varepsilon_{i+1}-\varepsilon_i) \tag{2-21}$$

and,

$$\mathrm{slip} = \int \varepsilon(x)dx = \sum\left(\frac{\varepsilon_{i+1}-\varepsilon_i}{\mathrm{x_{i+1}}-\mathrm{x_i}}\right)\left(\frac{x^2}{2}\right) + (\varepsilon_i \cdot x) \tag{2-22}$$

where ε_i is the axial strain reading at the point x_i, t_f is the thickness of the FRP plate, and E_f is the modulus of elasticity of the FRP (Mazzotti et al., 2005).

The American Concrete Institute has identified several specific failure modes for FRP reinforced concrete beams. These are (1) concrete crushing before reinforcing steel yielding, (2) steel yielding followed by FRP rupture, (3) steel yielding followed by concrete crushing, (4) cover delamination, and (5) FRP debonding.

For concrete beams in particular, debonding usually occurs within a thin layer of the concrete substrate directly below the bond line. This form of failure occurs when a large differential exists between the strains in the FRP and the concrete substrate (Gunes et al., 2009). To avoid this, ACI enforces the following strain limit state calculations:

$$\varepsilon_{fe} = \varepsilon_{cu}\left(\frac{h-c}{c}\right) - \varepsilon_{bi} \le \kappa_m \varepsilon_{fu} \tag{2-23}$$

where κ_m is given as (for SI units),

$$\kappa_m = \begin{Bmatrix} \frac{1}{60\varepsilon_{fu}}\left(1-\frac{\eta E_{FRP} t_{FRP}}{360000}\right) \le 0.9 \quad \text{for} \quad \eta E_f t_f \le 180000 \\ \frac{1}{60\varepsilon_{fu}}\left(1-\frac{90000}{3\eta E_{FRP} t_{FRP}}\right) \le 0.9 \quad \text{for} \quad \eta E_f t_f > 180000 \end{Bmatrix} \tag{2-24}$$

and ε_{fu} is the ultimate FRP strain, ε_{fu} is the maximum allowable strain in the FRP, ε_{cu} is the ultimate strain of the concrete, h is the beam height, c is the neutral axis depth, and ε_{bi} is the strain in the concrete substrate at time of installation. The limiting strain coefficient, κ_m is a function of the number of FRP layers (η), the thickness of each layer (t_{FRP}), and the modulus of elasticity of the FRP (E_{FRP}) (ACI, 2008).

Bond-slip relationships for FRP adhered to concrete have a shape that can accurately be described by several functional forms. The most common forms include linear, bilinear,

exponential, and linear-exponential relations. An example showing several of these curve shapes is presented in Figure 8.

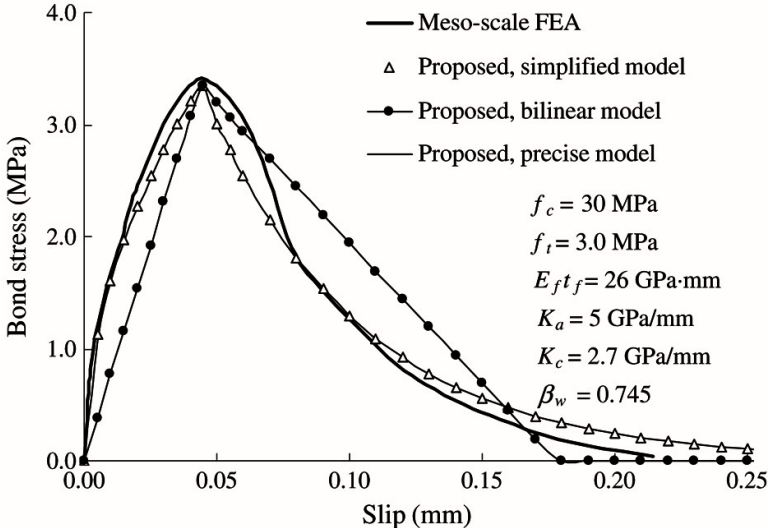

Figure 8. Common bond-slip relationship models (Lu et al., 2005)

Less research has been conducted to explore the behavior of FRP bonded to steel or aluminum substrates. The plane of debonding failure for metallic substrate usually differs from concrete, where failure occurs within the substrate. Metals tend to produce stronger bonds that induce failure within the adhesive layer, or between the adhesive and substrate interface. This form of debonding action also tends to occur more quickly, making experimental observations difficult (Akbar et al., 2010; Pantelides et al., 2003). Though it also has also been shown that, when modeled properly using calibrated contact or interface elements, prediction of the bond-slip behavior can be quite accurate (Su, 2008).

In a paper investigating bond of GFRP to aluminum joints subjected to fatigue loading, (Pantelides et al., 2003) suggested the following empirical model for determining the required FRP bond length to withstand both shear and tensile failures,

$$L_d = \frac{2P}{\pi D \tau_{avg}} \tag{2-25}$$

Where P = the design tensile load, D = the outside tube diameter, and τ_{avg} = the average shear stress developed between the aluminum surface and bonding layer of the GFRP composite. A triangular strain distribution was assumed, and a diagram outlining the derivation of this formula is given in Figure 9 (Pantelides et al., 2003).

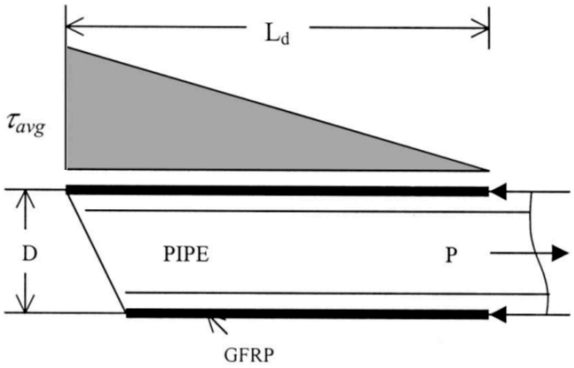

Figure 9. Bond length models (Pantelides et al., 2003)

2.4 Modeling of Metallic Pole Structures

Many studies have been performed in order to describe the behavior of damaged metallic tubular structures. The majority of these studies has been focused on applications to tubular members in offshore structures, and as such has focused on axial loading of the members (Hebor, 1994; Ostapenko & Padula, 1986; Pacheco & Durkin, 1988; Padula & Ostapenko, 1989). However, several researchers have also investigated the capacity of damaged or corroded members to resist lateral loadings (Duan et al., 1993; Durkin, 1987; Fatt et al., 1996; Zeinoddini et al., 1998, 1999).

In one such study, a finite element program was developed (Duan et al., 1993) to calculate the capacity of damaged tubular members. This program utilized a moment-thrust-curvature method developed previously. The assumptions for the analysis included small deflections, negligible shear and torsional deformations, and no strain reversal. Boundary conditions employed by this program are either pinned or pinned with small end restraints. The accuracy of this program was validated by comparison of predictions to test results and other analytical methods. This analysis demonstrated the versatility of the modeling method in application to numerous boundary conditions.

The most prevalent method in the literature for representing the deformed shape of damaged tubular members is the application of beam-on-elastic-foundation principles (Durkin, 1987). An analytical method is presented for predicting damage-induced strength reduction of tubular members subject to axial compression and end moments. An idealized dent shape was used, thus reducing the amount of detailed information on the dent geometry that is required for the analysis, which was based on beam-elastic-foundation relationships. As in the previous case, various end restraint conditions can be used with this method.

(Fatt et al., 1996) also used beam-on-elastic-foundation formulations to describe damage-deformed member shape for an investigation of response of a metallic tubular member to lateral dynamic loading. For this analysis, however, axial deformations were neglected, and the material of the member was assumed to be isotropic, time-independent, and rigid-plastic. The members were analyzed for a lateral impulsive load, and the results were compared to those of a computer program, DYNA 3D. The analytical deformations under-predicted those found by DYNA 3D by 25%. This difference was attributed to neglecting the bending mode of the shell.

2.5 Overview of Current FRP Design Guidelines

Multiple design guides and supporting documents have been created to codify a standard approach for designing externally-bonded FRP composite structures. Within the United States, ACI-440 has become the premier document on the subject. Internationally, multiple documents have been published including those by the Concrete Society of the UK, JSCE in Japan, and FIB in Europe. On the whole, these guidelines pertain to FRP reinforcement of reinforced concrete structures, with little guidance available for FRP reinforcement of steel or other metals.

2.5.1 United States

From 1991 onward, the American Concreter Institute (ACI) has sponsored the technical committee ACI-440 to examine FRP systems used to strengthen concrete structures. This committee has produced several documents attempting to set a standard for use of FRP in conjunction with concrete structures, including ACI-440.2R-08: Guide for the Design and Construction of Externally Bonded FRP Systems for Strengthening Concrete Structures. This document explicitly claims to offer:

- information on the history and use of FRP strengthening systems
- a description of the unique material properties of FRP
- recommendations on the engineering, construction, and inspection of FRP systems used to strengthen concrete structures (ACI, 2008)

The ACI-440.2R-08 document is based on over 20 years of research and investigation concerning FRP reinforcement of concrete structures. This research indicates that the primary area of uncertainty associated with any FRP/concrete systems is the bond interface, particularly for externally-bonded members. Additionally, as compared with more traditional systems FRP has not been thoroughly developed, and is unproven when applied to many design situations. For these reasons, the design guidelines in ACI-440 are intended to be highly conservative. Guidelines concerning degradation of the FRP capacity with time or due to cyclical loading are sparsely discussed in ACI-440. Instead, simple reduction factors are provided for various exposure and loading conditions of the structure.

Specific to flexural members, the document suggests that only five failure modes to be investigated for design purposes. These are (1) complete crushing of the compressive concrete, (2) yielding of the tension steel followed by FRP rupture, (3) yielding of the tension steel followed by concrete cruising, (4) shear delamination of the concrete cover layer, and (5) debonding of the FRP from the concrete. However, the documents and research presented in ACI-440 have not been adopted as a recognized building design code within the United States. Therefore, the design recommendations they make are merely suggestions, and not requirements. It should also be noted that the American Institute of Steel Construction (AISC) has likewise investigated the use of externally-bonded FRP to strengthen steel structures. AISC often includes research involving FRP applications on steel structures at sponsored conferences, such as the 2010 FHWA Bridge Engineering Conference. However, this research has not been developed into a single publication or formal design code at this time.

Additionally, the American Association of State Highway and Transportation Officials, AASHTO, published a design guide in 2009 titled “LRFD Bridge Design Guide Specifications

for GFRP-Reinforced Concrete Bridge Decks and Traffic Railings" in which several aspects of FRP reinforcement specific to bridge design were addressed. This guide offers a description of GFRP composite material properties, as well as provisions for the design and construction of concrete bridge decks and railings reinforced with GFRP reinforcing bars (AASHTO, 2009). As the title would indicate, this publication deals mostly with the use of FRP reinforcing bars and does not concentrate on externally-bonded reinforcement.

2.5.2 International

Outside of the United States, other governments and NGOs have explored the infrastructure applications of externally-bonded FRP. Notable among these are the provisions published by the Concrete Society of the UK (TR-55) (The concrete society, 2012), the Japan Society of Civil Engineers (JSCE No.41, 2001), the International Federation for Structural Concrete (FIB Bulletin 14, 2001), and the Canadian Standards Association (CAN/CSA-S806-02, 2007).

2.5.2.1 United Kingdom Standards

Beginning in the year 2000, the Concrete Society of the United Kingdom began publishing a document titled Technical Report No. 55 – Design Guidance for Strengthening Concrete Structures using Fiber Composite Materials. The original report was summarized in (Arya et al., 2002) and indicates that TR-55 is based on a limit state design philosophy and provides guidance on flexural strengthening of beams and slabs, shear strengthening of beams and columns, and flexural and compressive strengthening of columns. Additionally, TR-55 discusses the various FRP material types and their properties, acceptable field applications, workmanship and installation, as well as long-term monitoring of FRP reinforced structures (Arya et al., 2002). Similar to the ACI-440 document in the US, this report uses standard material properties that are then factored to account for uncertainty in the material, environmental exposure, and loading conditions. As with ACI-440, TR-55 only deals with FRP reinforced concrete structures, and does not discuss steel structures.

2.5.2.2 Japanese Standards

The Japan Society of Civil Engineers (JSCE) established a research committee in 1998 to compile a set of recommendations about the use of FRP sheets for retrofit and repair or strengthening of existing concrete structures. In 2001 JSCE published a document titled Recommendations for Upgrading of Concrete Structures with Use of Continuous Fiber Sheet. The primary areas examined in this publication are:

- The behavior of confined concrete structures
- Flexural debonding in FRP strengthened RC members
- Shear strengthening of columns and beams
- Retrofitting RC slabs with CFRP sheets
- Seismic retrofit of RC piers (Wu et al., 2007)

The final report put out by JSCE was a set of design guidelines similar to ACI-440 in the US and TR-55 in the UK. That is, a standard limit state design procedure is used to describe the ultimate behavior of FRP reinforced principal structural parts (JSCE No.41, 2001).

2.5.2.3 European Standards

The International Federation for Structural Concrete (FIB) is a not-for-profit association housed in Switzerland that produces European guidelines for concrete structures. Many of the guidelines set by FIB have been adopted in the Eurocode. FIB sponsors task group 9.3 to examine applications of FRP Reinforcement for Concrete Structures. The main objectives of TG9.3 are:

- The elaboration of design guidelines in accordance with the design format of Eurocode 2
- Link with other initiatives regarding material testing and characterization & development of standard test methods
- Participation in the international forum in the field of advanced composite reinforcement, stimulating the use of FRP for concrete structures
- Guidance on practical execution of concrete structures reinforced/prestressed/upgraded by FRP (FIB Bulletin 14, 2001)

Similar to the standard design approach described in other guidelines, the rule of mixtures is described in this document. However, another procedure is also accepted, where an FRP is designed based on the properties of the bare fiber alone. Here, the nominal width of the fiber mesh is used, along with the modulus and ultimate strength values of the fibers factored by a reduction value (r) to account for the matrix properties. This value is simply the empirically derived relation between the bare fiber properties and those of the composite, as shown in the equation $t_{fib}E_{fib}r = t_{frp}E_{frp}$, where t_{fib} and E_{fib} are the thickness and Young's modulus of the bare fibers, and t_{frp} and E_{frp} are the thickness and Young's modulus of the composite, respectively (FIB Bulletin 14, 2001).

2.5.2.4 Canadian Standards

In 2002 the Canadian Standards Association (CSA) published a document titled "Design and Construction of Building Components with Fibre-Reinforced Polymers." The scope of this document is described as providing requirements for:

- The design and evaluation of building components of fibre-reinforced polymers (FRP) in buildings and of building components reinforced with FRP materials. It is based on limit states design principles and is consistent with the National Building Code of Canada.
- The determination of engineering properties and design of self-supporting FRP components.
- The determination of engineering properties and design of FRP reinforced building components including bars, tendons, mats, grids, roving, sheets, and laminates.
- The designer to consider the possible effects of exposure to fire or elevated temperatures on the performance of FRP components and FRP reinforced components (CAN/CSA-S806-02, 2007).

Intelligent Sensing for Innovative Structures (ISIS) is a research network established in Canada in 1995 as a forum to develop and share innovative research on the topics of fiber reinforced polymers and fiber optic sensors. Previous to the release of CAN/CSA-S806-02, a state of the art report was sponsored by ISIS concerning strengthening of reinforced concrete structures with externally-bonded fiber reinforced polymers, and Theme-3 of ISIS has dealt with structural

strengthening and rehabilitation with FRP from 2002 onward; therefore, much information concerning Canadian standards of practice when designing FRP reinforcement is available from the ISIS research archives ((ISIS), 2006).

Chapter 3: Small-Scale Material Characterization

3.1 FRP Repair Systems

Many private companies, both nationally and regionally, produce FRP systems designed for use as externally-bonded reinforcement. However, few of these products are designed to adhere to metallic structures, and even fewer are specifically intended for repair of impact-damaged metallic utility poles, although the repair of metallic pipelines has similarities. Therefore, it was determined that an optimum FRP repair system could be produced by matching woven fiber sheets with available matrix material and structural adhesives. The properties of these systems would then be experimentally determined and compared. Finally, one (or more) of these systems would then be selected for additional testing.

3.1.1 Fiber Selection and Orientation

There are many different fiber types available to be used for infrastructure repair. Currently the most common types used for structural applications are carbon and E- or S-glass fibers. Aramid and basalt fibers have also been shown to have properties suitable for structural applications. Some typical values of the mechanical properties of these fiber types are shown in Table 1 below.

Table 1. Typical tensile properties of fibers used in FRP systems (Rizkalla & Busel, 2002)

Fiber Type	Elastic Modulus		Ultimate Strength		Rupture Strain (%)
	(10^3 ksi)	(GPa)	(ksi)	(MPa)	
General Purpose Carbon	32 to 34	220 to 240	300 to 500	2050 to 3790	1.2
E-Glass	10 to 10.5	69 to 72	270 to 390	1860 to 2680	4.5
S-Glass	12.5 to 13	86 to 90	500 to 700	3440 to 4140	5.4
General Purpose Aramid	10 to 12	69 to 83	500 to 600	3440 to 4140	2.5
General Purpose Basalt	-	90 to 95 [a]	-	2900 to 3200 [a]	-

[a] Indicates values taken from manufacturer specifications (Kamenny Vek)

Carbon fibers are generally considered the strongest fibers available on the market today; however, as previously stated, carbon has the potential to cause galvanic corrosion when placed in contact with other reactive materials such as steel or aluminum. Aramid fibers have a similar drawback. Aramid is known to be susceptible to degradation when exposed to ultraviolet light. This makes them less than ideal for placement on utility poles that will be continuously exposed to direct sunlight. For this reason, aramid fibers were not investigated within this study.

Previous studies on the use of externally bonded FRP applied to circular poles sections subjected to bending stresses found that fibers placed in both the axial (longitudinal) and circumferential (confining) orientation contributed to the restored capacity of the structure. It was also observed that achieving this by applying fibers in multiple separate layers, each comprised of unidirectional fibers was cumbersome. Therefore, a bi-directional weave has been selected for use in this study. To further simplify the installation process, a balanced weave (one with equal fiber reinforcement in two orthogonal directions) was also chose. Two weave densities were selected for each of the fibers, attempting to produce similar tensile capacities for each material. These fabric densities are shown in Table 2.

Table 2. Fabric weave densities

Fiber Type	High-Density Weave			Low-Density Weave		
	($^{oz}/_{yd^2}$)	style	code	($^{oz}/_{yd^2}$)	style	code
Carbon Fiber	12	Plain Weave	"CH"	6	Plain Weave	"CL"
Glass Fiber	24	Plain Weave	"GH"	11	Woven Tape	"GL"
Basalt Fiber	24	Plain Weave	"BH"	11	Plain Weave	"BL"

3.1.2 Matrix Selection

Three matrix options were chosen for investigation within this study. Two of these options are structural epoxy (EP) saturating resins that are intended for use as FRP matrices and are readily available. The first of these epoxy resins is QuakeBond™J300SR Saturating Resin produced by QuakeWrap Inc., an FRP retrofit company located in Tucson, AZ. The second epoxy resin option is CarbonBond™300, an epoxy produced by Carbon Wrap Solutions LLC, also located in Tucson. And the third matrix option is a pre-impregnated polyurethane (PU) resin called "XT" that is produced by Neptune Research Inc. located in Lake Park, Florida.

All three of these saturating systems come pared with structural adhesives used to bond the impregnated FRP sheets to the substrate. These adhesives are QuakeBond™J201TC, CarbonBond™200P, and Syntho-SubseaLV and are paired with resins from QuakeWrap Inc., Carbon Wrap Solutions LLC, and Neptune Research Inc., respectively. The manufacturer properties for all of these resins are provided in Table 3.

Table 3. Manufacturer specifications for saturating resins and adhesives

Resin Designation		Resin Type	Pot Life	Cure Time	Viscosity
QuakeBond™ J300SR	(QB)	2-part **EP** saturating resin	3-4 hrs	48 hrs [a]	1500-1600 cps
QuakeBond™ J201TC		2-part **EP** structural adhesive	90 mins	48 hrs [a]	"high tack"
CarbonBond™ 300	(CB)	2-part **EP** saturating resin	-	-	-
CarbonBond™ 200P		2-part **EP** structural adhesive	-	-	-
NRi " XT "	(XT)	H_2O-activated **PU** prepreg resin	30 mins	2 hrs [b]	-
Syntho-SubseaLV		2-part **EP** structural adhesive	20 mins	24 hrs [a]	"high tack"

[a] Cure time taken at 25ºC
[b] Cure time taken at 24ºC, after exposed to moisture

3.1.3 Epoxy Filler Selection

A required element of a successful repair of a dented utility pole is that it restores the pole to a generally round shape. For the FRP repair systems developed in this thesis, this is to be accomplished by the use of a dent filler material. The important characteristics of this filler material are that it be sufficiently viscous to apply to vertical poles in large quantities without significant sagging, and that it provide a surface to which the composite wrap can form an effective bond. Three commercially produced epoxies were evaluated for use in as filler materials in this study, and are summarized in Table 4. The evaluation of these materials consisted in trial applications to dented steel and aluminum utility poles. The workability, ease of

application to vertical poles, and resulting filler surface were observed and used to select the filler material to be used in the final repair systems.

Table 4. Manufacturer specifications for filler material

Filler Material	Compressive Strength	Compressive Modulus	Pot Life (at 25°C)	Price[a]
NRI Syntho-Poxy HC	8,000 psi	-	4-6 mins	$628.89/gal
Pilgrim EM 5-2 Gel	11,400 psi	1,459 ksi	20-30 mins	$40/gal
Sikadur 31, Hi Mod Gel	16,000 psi	795 ksi	60 mins	$52.98/gal

[a] The price is based on the cost at the time the materials were obtained

The Syntho-Poxy HC was evaluated first. Approximately one quart of the material was mixed by hand, according to manufacturer instructions, and was applied to a dented pole with small trowels. Initially, the epoxy was applied easily, without significant slumping. However, within approximately 10 minutes from mixing, the epoxy seized and became un-workable, and quickly gained a plastic consistency. Therefore, filling of the dent was not completed, as can be seen in Figure 10 and Figure 11.

Two dented poles were filled with the Pilgrim EM 5-2 Gel. The manufacturer specifies that up to 3 parts oven-dried aggregate to 1 part epoxy can be added. The first dent fill contained 1 part dry sand to 6 parts mixed epoxy, and the second 1 part dry sand to 3 parts mixed epoxy. The thixotropic gel was combined using a mixing drill. The first, lower sand content mix was applied to the dented pole easily, with minimal signs of slumping during application. However, when the fill was left to cure, the majority of the epoxy slid out of the dent, as shown in Figure 10. The second, higher sand content mix was applied to another dented pole, and was significantly stiffer than the first batch. To create a smooth, even surface on the fill, the pole was wrapped in wax paper during curing. The result, pictured in Figure 11, was an effective, even fill which blended well with the pole's surface.

Figure 10. Pilgrim epoxy gel batch 1

Figure 11. Pilgrim epoxy gel batch 2

Two poles were also filled with the Sikadur 31, Hi Mod Gel. The large size of the dent in one of these poles increased the difficulty of applying a complete fill without epoxy slumping. The fill was mixed with a drill mixer, according to manufacturer specifications. The workability of the mix was good, and there was no problem with slumping of the fill material. When the fill material had cured, the surfaces were sanded smooth. The resulting fills can be seen in Figure 12 and Figure 13.

The result of this filler evaluation was that the Pilgrim EM 5-2 Gel with a 1:3 sand additive and the Sikadur 31, Hi Mod Gel are acceptable options for inclusion in the FRP repair system. The workability Sikadur epoxy makes this material more favorable than then EM 5-2 Gel. Therefore, the Sikadur 31 Hi Mod Gel was chosen for inclusion in the repair system.

Figure 12. Sikadur 31 dent fill 1

Figure 13. Sikadur 31 dent fill 2

3.2 Composite Material Properties

All of the saturating resins listed in Table 3 were individually applied to each weave listed in Table 2, forming a single sample set; 12 sets in total. These sample sets were then tested to determine the tensile and bond properties of each. Additionally, two plates were formed for each set and exposed to ambient weather conditions for 365 days. One plate was left uncoated, and the other coated with Sherwin Williams Diamond-Clad Clear Coat B65-urethane per FDOT specifications for existing structural steel members.

3.2.1 Tensile Properties

Tensile tests were conducted at the University of Central Florida Structural Research Lab in Orlando, Florida. Coupons were produced from 12 × 12 in (304.8 × 304.8 mm) plates formed for each sample set consisting of two layers of bi-directional woven fibers impregnated by one of the saturating resins listed previously. These plates were allowed to cure for 48 hours and then trimmed to form approximately ten 12 × 1 in (304.8 × 25.4 mm) coupons for each set. The fibers were oriented in the 0º/90º directions with respect to the coupon geometry. These coupons were

then tested in an Instron/SATEC 200-kip universal testing machine (UTM) following ASTM D3039 testing standards.

Stress, strain, and load measurements were taken during testing. To measure strain, an Instron extensometer was used. To prevent damage to the equipment, the extensometer was removed from the specimen, and the strain readings were discontinued prior to failure of each specimen. After testing, the elastic modulus was calculated for each specimen from a linearization of the stress/strain readings taken up to removal of the extensometer. This value, along with the recorded stress at failure, was used to determine the linear strain at failure. Averages of these values for each sample set are presented in Table 5. It should be noted that the data exclude data values from any coupons that ruptured within the gripped region of the UTM.

Table 5. Average tensile properties for each sample set

Sample Set		Elastic Modulus	Stress at Failure	Strain at Failure
Resin	Fiber	(ksi)	(ksi)	(%)
CarbonBond™ 300	High-Density Basalt	2,063	31.6	1.53
QuakeBond™ J300SR		1,841	38.6	2.09
NRi XT Polyurethane		1,230	19.6	1.59
CarbonBond™ 300	Low-Density Basalt	2,111	31.9	1.51
QuakeBond™ J300SR		1,757	41.6	2.37
NRi XT Polyurethane		2,472	28.0	1.13
CarbonBond™ 300	High-Density Glass	1,041	34.6	3.32
QuakeBond™ J300SR		1,407	44.9	3.20
NRi XT Polyurethane		2,395	32.1	1.34
CarbonBond™ 300	Low-Density Glass	1,253	20.2	1.62
QuakeBond™ J300SR		1,318	20.2	1.53
NRi XT Polyurethane		1,920	23.2	1.21
CarbonBond™ 300	High-Density Carbon	2,600	62.9	2.42
QuakeBond™ J300SR		2,137	55.8	2.61
NRi XT Polyurethane		5,743	53.8	0.94
CarbonBond™ 300	Low-Density Carbon	4,680	56.8	1.21
QuakeBond™ J300SR		3,109	55.9	1.80
NRi XT Polyurethane		--	--	--

Several observations can be made from the FRP tensile data. As compared with the bi-directional fiber systems, the small scatter associated with the Fyfe Co. and Sika Corp. coupon data indicates that unidirectional FRP systems behave more consistently in tension then do bi-directional weaves. Additionally, the unidirectional glass and carbon systems had higher stiffness then the bi-directional systems tested. Specifically for the bi-directional EP systems, QB tended to outperform the equivalent glass and basalt CB systems; though the carbon fiber CB systems had the highest stiffness and ultimate rupture strength. Finally, the pre-impregnated polyurethane composites tended to behave more uniformly then the equivalent bi-directional EP systems.

3.2.2 Compressive Properties

To determine the response of the FRP systems under an axial compressive loading, a set of compressive tests was conducted for the QB and XT repair systems using high-density bi-directional basalt and glass fiber weaves (BH and GH). The testing procedure followed was a

variant of ASTM D5467 where an FRP plate is bonded to the top flange of a small aluminum beam and placed in four-point bending. A diagram of the testing configuration per the ASTM standard is given in Figure 14.

Due to the relatively low stiffness and expected high strength of the composites, the procedures were slightly modified for these systems. A 12 in long (305 mm) square aluminum tube section with 1 in (25 mm) outer width and 0.0625 in (1.58 mm) wall thickness was used as the core beam section. To prevent local buckling of the tube, the load points were reinforced by placing two small pieces of discontinuous #8 rebar within the tube.

The FRP was installed as a circumferential wrap around the aluminum tube section to help resist debonding and out-of-plane movement during testing. Finally, to induce sufficient strain within the FRP a 0.188 in (4.8 mm) thick aluminum plate was attached to the tension face of the pipe section with a single threaded bolt at the midpoint of the constant moment region. The width of this plate was cut to 5 in (127 mm) and 7 in (178 mm) for the XT and QB systems, respectively. A schematic of this setup is given in Figure 15.

Testing took place at the University of Central Florida Structural Research Lab in Orlando Florida using an Instron/SATEC 200 kip UTM. The load was applied at 0.1 in/min (0.04 mm/s) in a four-point bending configuration as shown in Figure 16 and Figure 17. The top point loads were spaced at 2 in (51 mm) on center, and the clear span was set to 10 in (254 mm). A single 6 mm 120 Ω foil strain gauge was adhered in the axial direction to the top of the FRP within the constant moment region. The load and strain reading were recorded for each test.

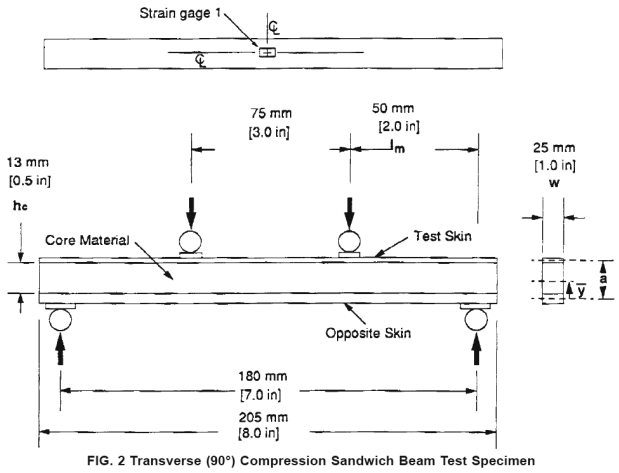

Figure 14. FRP compressive test diagram (ASTM D5467)

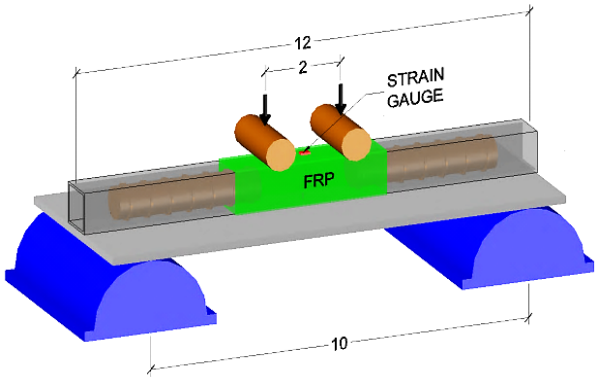

Figure 15. FRP compressive test variation setup

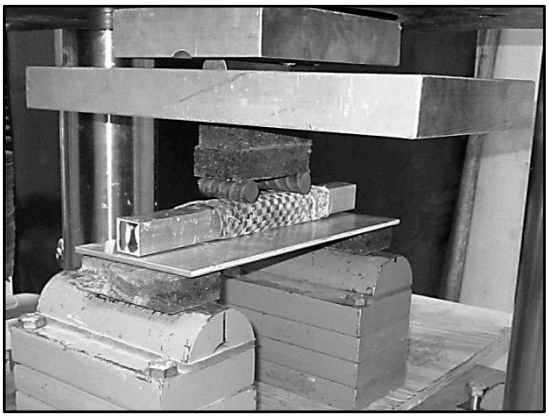

Figure 16. FRP compressive test, unloaded

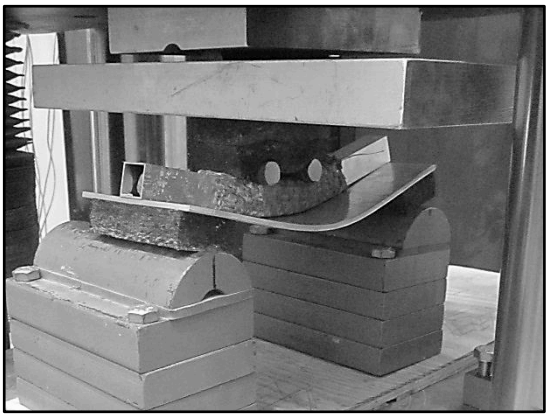

Figure 17. FRP compressive test, under loading

The compressive stress acting on the FRP was calculated per ASTM specifications and is plotted for each test in Figure 18 and Figure 19 with respect to the strain readings. The compressive modulus can then be determined from a linear fit of this data. ASTM permits the use of both linear and bilinear compressive moduli; therefore, a two part bilinear fit was found for each FRP system tested. These bilinear fits are also shown in each figure.

The compressive modulus is defined as the slope of the first segment of the bilinear relationship. These values were derived and are presented in Table 6 and Table 7 for the QB and XT systems, respectively. The stress and strain values at the transition point and at ultimate failure are also given in the tables.

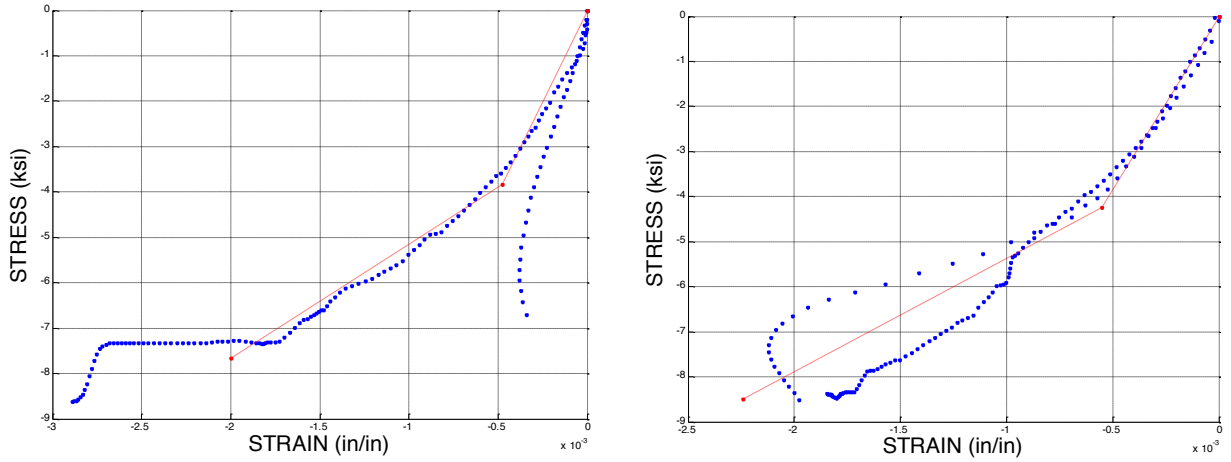

(a) High Density Basalt Fiber

(b) High Density Glass Fiber

Figure 18. QuakeBond™ J300SR composite compressive coupon data

Table 6. Bilinear compressive properties for FRP impregnated with QuakeBond™ J300SR resin

Fiber Type	Compressive Modulus (ksi)	Transition Stress (ksi)	Transition Strain (%)	Failure Stress (ksi)	Failure Strain (%)
High-Density Bi-Directional Basalt	8,050	3.828	0.05	7.657	0.20
High-Density Bi-Directional Glass	7,694	4.247	0.06	8.494	0.22

Table 7. Bilinear compressive properties for FRP impregnated with NRi XT polyurethane resin

Fiber Type	Compressive Modulus (ksi)	Transition Stress (ksi)	Transition Strain (%)	Failure Stress (ksi)	Failure Strain (%)
High-Density Bi-Directional Basalt	4,295	5.235	0.12	10.471	0.93
High-Density Bi-Directional Glass	8,789	6.167	0.07	12.333	0.64

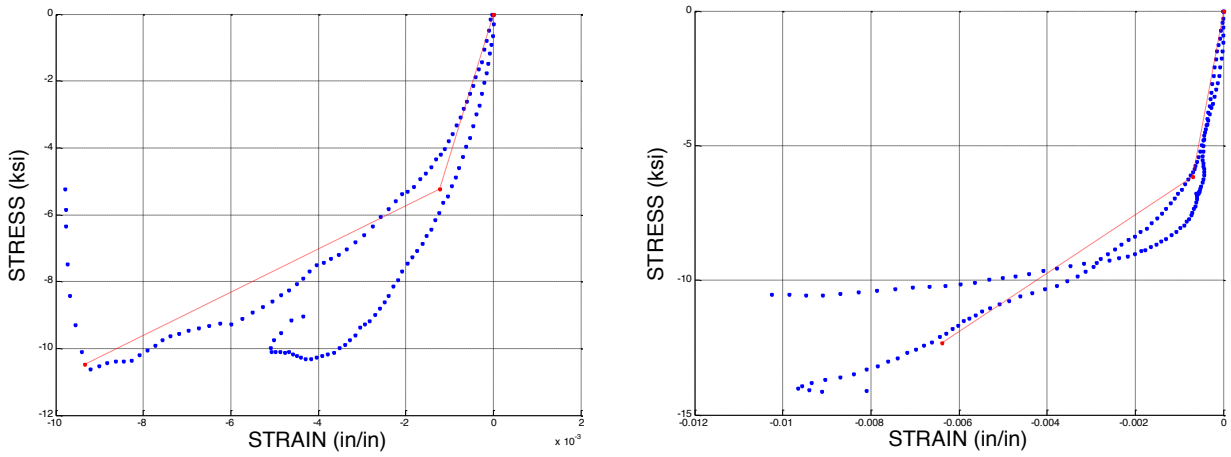

(a) High Density Basalt Fiber **(b) High Density Glass Fiber**

Figure 19. NRi XT polyurethane composite compressive coupon data

Inducing true compressive failure proved to be difficult. Often the failure occurred when the aluminum substrate hinged beneath the FRP, inducing debonding, and ultimately, folding of the compressive fibers. This form of failure can be seen in Figure 20, Figure 21 and Figure 22. Additionally, both high-density BFRP tests involving XT polyurethane resin failed when the aluminum substrate ruptured beneath the tension FRP, causing the tensile FRP to also rupture (see Figure 23). For this reason, the ultimate failure values shown should be taken as a lower limit, and not necessarily as the compressive failure capacity.

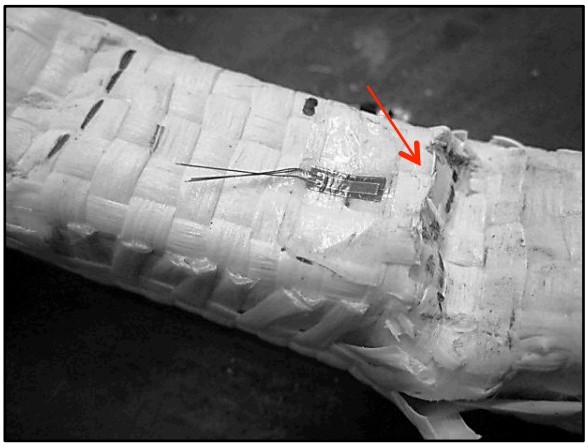

Figure 20. GFRP filament folding failure

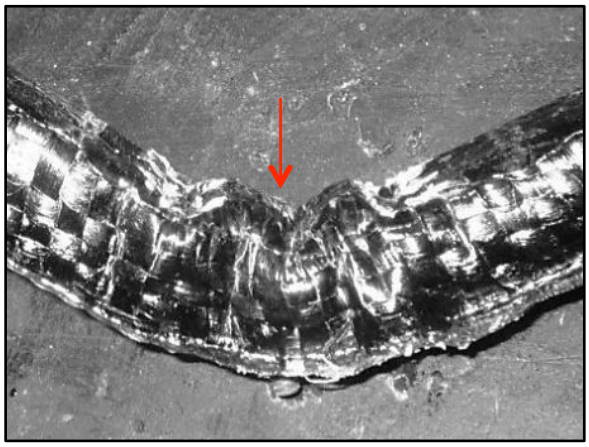

Figure 21. BFRP wrinkling failure

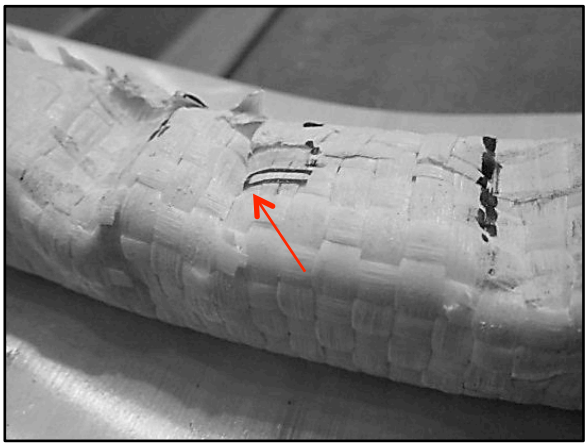

Figure 22. GFRP wrinkling failure

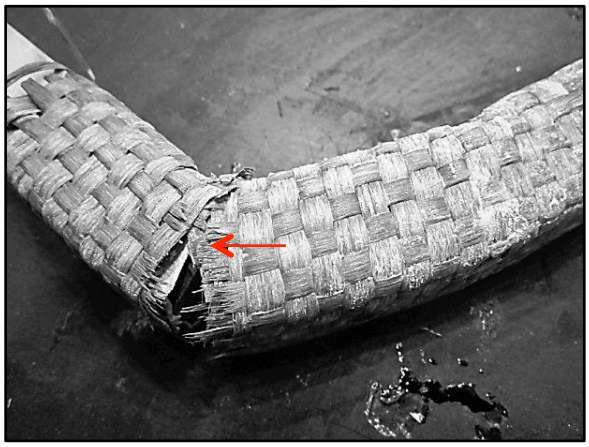

Figure 23. Substrate and FRP rupture

3.2.3 Bond Properties

The interface between a bonded FRP composite and the substrate can involve a complex state of stress. Shear and normal stresses, as well as peeling effects, can all play a role in determining how a bond failure might occur. For this reason, few simple models accurately describe composite debonding. However, average peak bond stresses acting over a relatively small area will be used to make an initial comparison of the various systems. A more detailed understanding of the debonding phenomena can then be found through more extensive experimental bond-slip modeling.

3.2.3.1 Peak Bond Strength

Three small-scale tests were performed to examine the bond strength of the various FRP systems. The first of these tests involved circumferentially laminated steel pole sections placed in tension to investigate the effects of curvature on shear bond strength. The second set of tests used a single-lap setup to find average peak shear stress values for each FRP system. The third test used an adhesion tester to find the peak normal bond stress.

The first of the small-scale bond strength tests involved the use of a small pole section taken from one of the tested steel poles in a previous study (Mackie et al., 2011), approximately 18 in long. The section tapered 8.437 in to 8.625 in (214 mm to 219 mm) in diameter. This section was split through their circumferences and then the two pieces were stacked and laminated together with a single layer of the Tyfo® SEH-51 GFRP composite lapped around the exterior as shown in Figure 24.

The GFRP was then cut a distance away from one side of the split in the pole sections to restrict the GFRP bond length. The bond length on the opposite side ranged from three to four times the restricted length to ensure that debonding would occur on the intended side. An 8 x 8 x ¾ in (203 x 203 x 19 mm) steel plate was attached to both ends of the pole sections with ½-in fillet welds around the perimeter. High strength threaded rods were bolted through these plates and anchored to the UTM as shown in Figure 25.

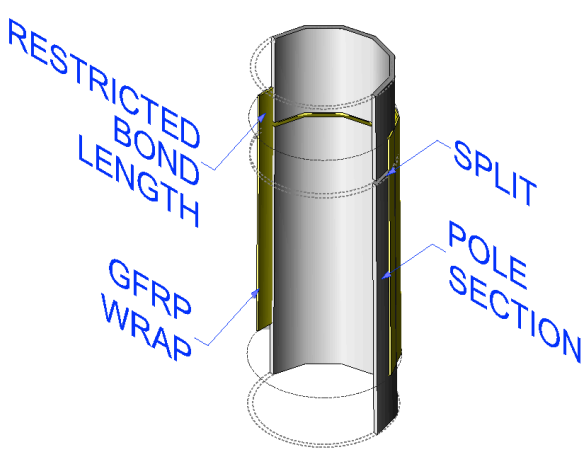

Figure 24. Circumferential bond test schematic

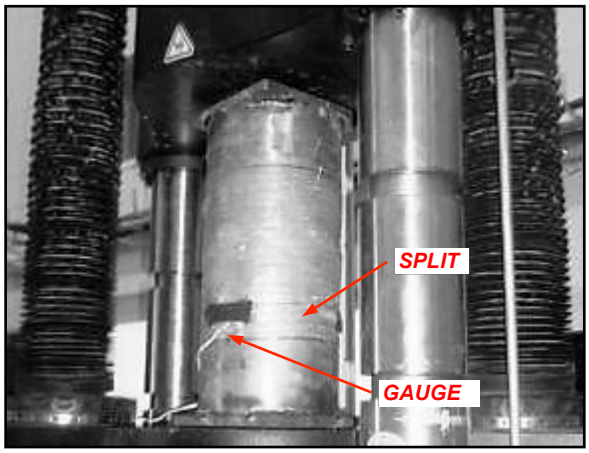

Figure 25. Picture of circumferential bond test

A tension force was applied to these specimens until the GFRP debonded from the steel and caused the two pieces of the pole to separate. The specimen was tested three times with minimal bond lengths of 2.25 in, 1.75 in, and 1.25 in (57 mm, 44.5 mm, and 32 mm) resulting in ultimate loads of 34.5 kips, 29.0 kips, and 25.4 kips (153 kN, 129 kN, and 113 kN), respectively. Strain data was collected from three axial 6 mm 120 Ω strain gauges spaced evenly around the circumference of the pole at the midpoint of the restricted bond area for the third test (shown in Figure 26).

It was observed during these tests that debonding did not occur uniformly around the circumference of the specimens. Instead, the debonded region spread in the axial direction locally before spreading circumferentially. This observation is confirmed in Figure 26, as the strain gauges show large increases in local strain (due to local debonding of the GFRP from the substrate) at different points during the loading. Additionally, the rate at which the debonding occurred was not uniform for each test, happening most rapidly for the 1.75 in (44.5 mm) length and most gradually for the 2.25 in (57 mm) bond length.

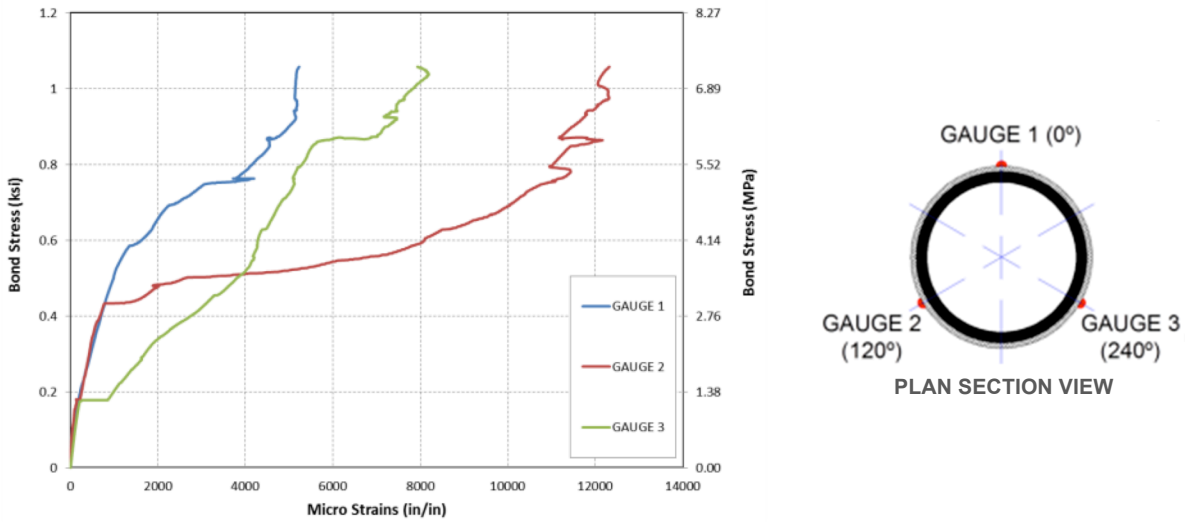

Figure 26. Load vs. longitudinal strains readings during circumferential bond test

The second of the small-scale bond strength tests involved single-lap tension testing of several metal coupons. The dog-bone coupons were obtained from pole segments from a previous study (Mackie et al., 2011). These were first cut across the 1.5 in (38 mm) portion and then laminated back together with a single layer of Tyfo® SEH-51 GFRP on the side which corresponded to the exterior surface of the pole, as shown in Figure 27 and Figure 28. The bonds were limited along one side of the cut and then tested, resulting in debonding failure on the side with shorter bond length (steel limiting bond lengths were 0.5 in to 3.5 in). Aluminum coupons were also tested in this configuration (limiting bond lengths were 1.5 in to 3 in). The maximum load achieved before failure averaged over the bonded area is taken as the average ultimate bond stress.

The results of each of these tests are presented in Table 8. The data shows that as the bond length increases, the stress becomes more evenly distributed along this length, causing the average bond strength to approach a constant value. The trend formed by the single-lap coupon tests is consistent with the circumferentially laminated pole section. The relationship between these sets of data indicates that single-lap bond testing reasonably describes the average bond strength around the circular geometry of a pole section, or there was no substantial effect of the cross section curvature on the normal and shear stresses at failure in tests performed.

Table 8. Average ultimate bond stress achieved (psi) - Tyfo®

Substrate Material	Restricted Bond Length (in)									
	0.5	1.0	1.25	1.5	1.75	2.0	2.25	2.5	3.0	3.5
Steel	1260	820	- -	703	- -	600	- -	751	459	517
Steel (pole section)	- -	- -	761	- -	621	- -	574	- -	- -	- -
Aluminum	- -	- -	- -	1430	- -	1180	- -	467	365	- -

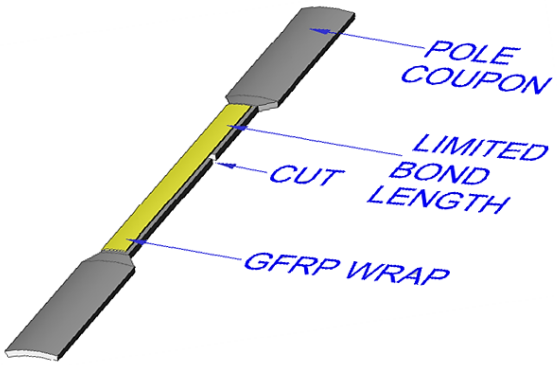

Figure 27. Lap-shear bond test schematic (1)

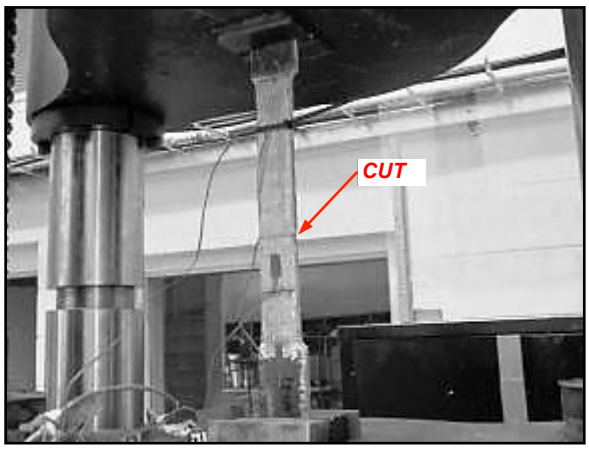

Figure 28. Picture of lap-shear bond test (1)

Further single lap-shear tests were conducted using the CB, QB, and XT reinforcement systems and each of the high-density bi-directional fibers listed in Table 2. These tests used flat rectangular aluminum or galvanized steel sections that were all approximately 12 in (305 mm) long and 1.5 in (38 mm) wide. The steel and aluminum plates were 0.25 in (6 mm) and 0.188 in (5 mm) thick, respectively, and the same grade as poles taken from the field to be used for the component-level testing.

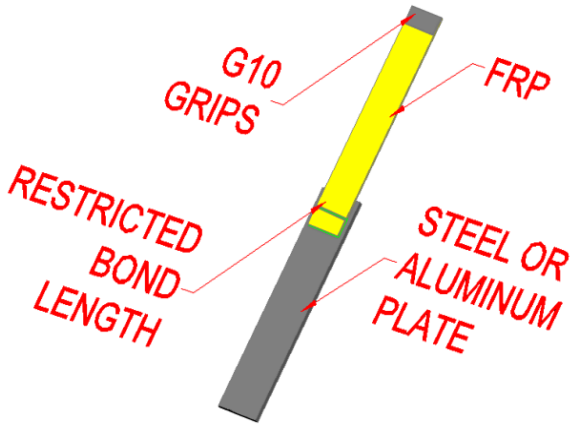

Figure 29. Lap-shear bond test schematic (2)

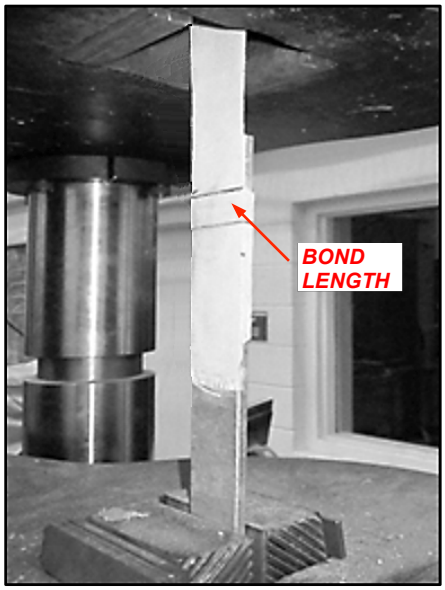

Figure 30. Picture of lap-shear bond test (2)

Table 9. Average ultimate bond stress achieved (psi) - CB, QB, and XT

Adhesive	Matrix Material	Substrate Material	Average Lap-Shear Bond Stress		
			High-Density Basalt Fiber	High-Density Carbon Fiber	High-Density Glass Fiber
QuakeBond™ J201TC	QuakeBond™ J300SR	Aluminum	911.78	654.29	711.36
		Steel	777.08	636.36	466.16
CarbonBond™ 200P	CarbonBond™ 300	Aluminum	451.52	1,194.13	1,079.80
		Steel	383.75	784.51	616.52
Syntho-SubseaLV	NRi XT Polyurethane	Aluminum	515.66	663.30	308.33
		Steel	440.45	349.24 psi	266.41

The FRP was bonded to the plates with approximately 0.5 in (13 mm) of overlap and 4 in to 8 in (102 mm to 204 mm) of FRP overhanging the plate (see Figure 29). G10 fiberglass grips were adhered to the ends of the FRP to prevent crushing. The metal plate and FRP were loaded directly into the UTM for testing as shown in Figure 30. The results of these lap shear bond tests are given in Table 9.

Along with the shear stress tests described previously, a series of tests to determine the maximum normal bond stresses were conducted for each system. These tests were conducted using 20mm aluminum dollies and a PosiTest© Manual Adhesion Tester sold by DeFelsko following ASTM D4541, the Standard Test Method for Pull-Off Strength of Coatings Using Portable Adhesion Testers (Type A5). This document states that this test method maximizes tensile stress as compared to the shear stress applied by other methods; therefore, the results may not be directly comparable.

Each high-density FRP system described previously was bonded to steel and aluminum plates using the paired adhesives listed in Table 9. Multiple 20-mm aluminum dollies were then adhered to the top of the FRP layer. A circular groove was etched around the base of these dollies through the FRP, but leaving the substrate intact (see Figure 32). Finally, the Manual Adhesion Tester was used to apply a normal uplift force to the aluminum dollies until debonding occurred, and the peak debonding stress was electronically recorded. The testing configuration is shown in Figure 31.

Due to the variability of the results, many repetitions were necessary to produce data that reasonably describes the normal bond stress. Often, the dollies would debond from the FRP before the FRP would debond from the substrate. When this occurred a normal bond stress data point was not collected.

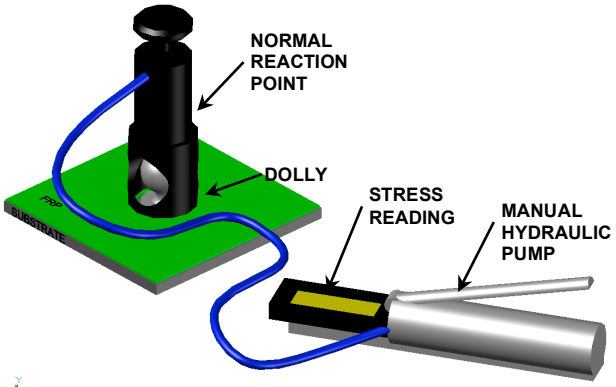

Figure 31. PosiTest© manual adhesion tester schematic

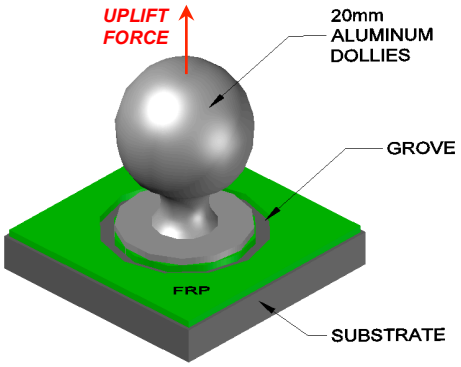

Figure 32. Aluminum dolly schematic

The results of the normal pull-off tests are plotted against the results of the single-lap bond tests for each system tested. These are given in Figure 33 through Figure 35. It can be seen from this data that the highest variability occurred with the high density carbon fiber systems. Additionally, the QuakeBond™ (QB) system tended to outperform the CarbonBond™ (CB) and NRI polyurethane (XT) systems when dealing with high density Glass and Basalt fibers. For these two fiber types, the NRI system was the most consistent, but also demonstrated the lowest peak bond stresses.

Both the normal and shear bonds of each FRP system were higher for aluminum than steel substrates. Additionally, the FRP systems with the largest strains at failure (QB for BH, CB for GH, and QB for CH) seemd to also have higher average bond stresses at failure. This indicates that softer materials can more evenly distribute the bond stresses, thus achieving higher average bond strengths. Conversely, the polyurethane composites consistently produced the lowest strains at failure, as well as the lowest average shear and normal bond strengths.

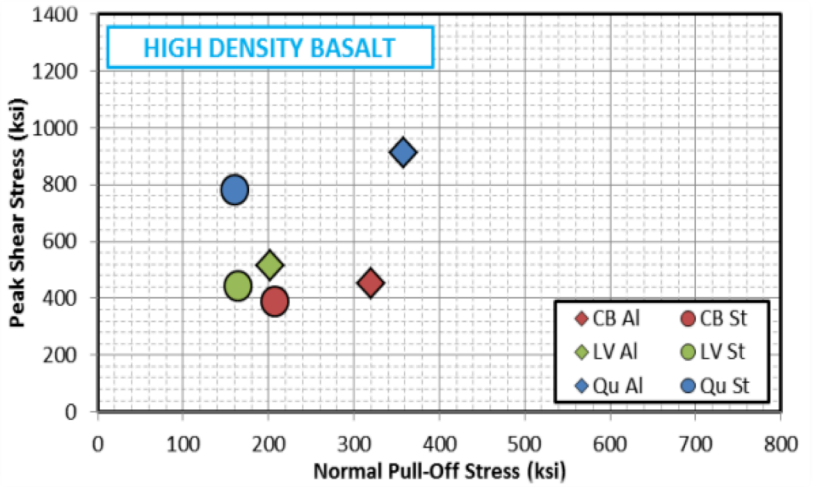

Figure 33. Shear bond vs. normal bond strength of high-density BFRP systems

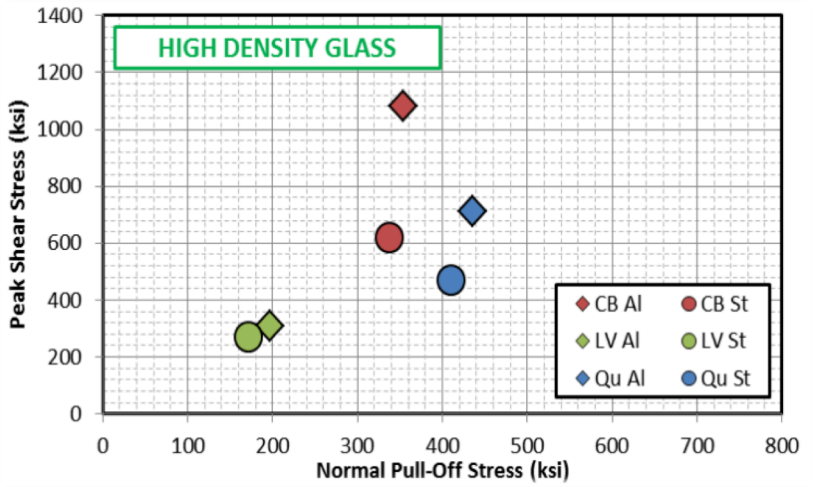

Figure 34. Shear bond vs. normal bond strength of high-density GFRP systems

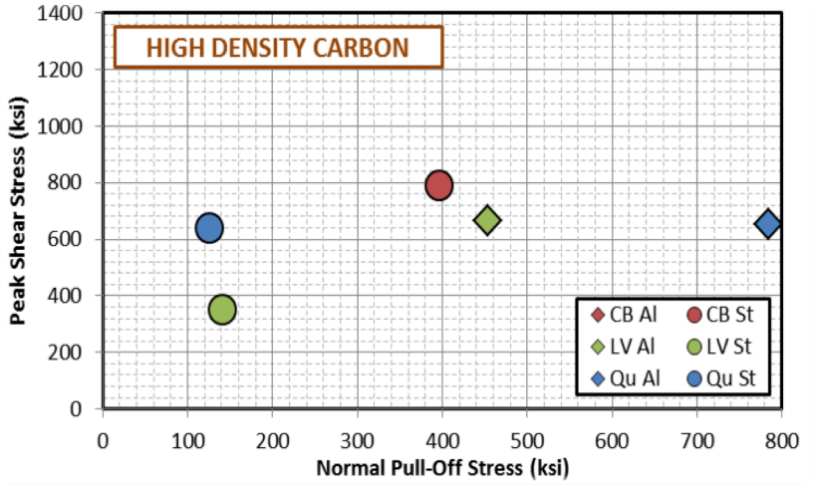

Figure 35. Shear bond vs. normal bond strength of high-density CFRP systems

3.2.3.2 Bond-Slip Characterization

An initial comparison of the average peak bond stresses described previously indicates that among the epoxy systems tested, the QB system outperformed the CB systems for bond between basalt or glass fiber composites to both steel and aluminum. Therefore, the QB repair system was selected for additional investigation. For comparison purposes, bond-slip modeling was also performed for the basalt and glass fiber polyurethane systems. The testing procedures and results of these tests are presented in the following subsections.

3.2.3.2.1 Experimental Configuration

The specimens used for these tests involved 1.5 in (38 mm) wide aluminum or galvanized steel plates with a single 1.0 in (25 mm) wide double-layer plate of FRP lap-bonded to one side. The plates were made from 0.25 in (6.35 mm) thick galvanized A572 steel and 0.188 in (4.78 mm) thick AA6063 aluminum, similar to that used in FDOT standard utility poles and mast-arms. The bond areas were 1 in (25 mm) wide and initially 2.0 in (51 mm) in length for each specimen, and then extended to 3.0 in (76 mm) in length for the aluminum tests so as to better observe the entire bond development length. QuakeBond™ J201TC EP adhesive was used to bond the FRP to the substrate for each test.

Four 3-mm 120 Ω strain gauges were adhered to the outer layer of FRP along the 2.0 in (51 mm) bond lengths, and five gauges were used along the 3.0 in (76 mm) bond length to map the strain gradient. The 2 in and 3 in gauge layouts are schematically shown in Figure 36. These specimens were then tested in a tension-loading configuration with a displacement controlled loading rate of 0.03 in/min (0.0125 mm/s). The grips of the UTM were adjusted to achieve vertical alignment of both the FRP coupon and metal plate with minimal induced moment. The testing configuration can be seen in Figure 37. To prevent damage occurring to the fibers from the UTM during loading, G10 fiberglass plates were adhered to the gripped portion of the polyurethane FRP coupons.

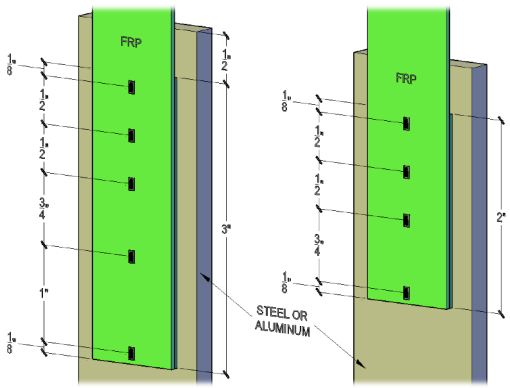

Figure 36. Bond-slip gauge configuration

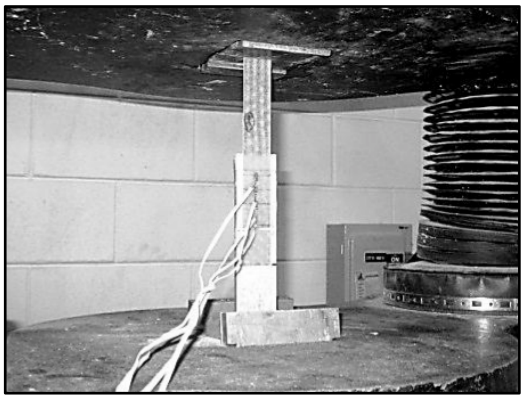

Figure 37. Picture of bond-slip test specimen

3.2.3.2.2 Experimental Results

The results of the bond-slip experimental modeling are given in this section. Four specimens were prepared and tested for each permutation of BH and GH fibers (see Table 2 for fiber

information) impregnated with QB and XT repair systems and adhered to aluminum and galvanized steel substrate. The total shear and total slip at the free end of the bond were found at multiple load steps for each specimen using Equations 21 and 22 presented in Chapter 2.

The strain gauges were carefully adhered in the direction of loading, with an attempt being made to place the gauges completely on fibers oriented in the axial direction. However, on several occasions one or more of the gauges appeared to be recording inaccurate values, most likely due to the strain gauge length relative to the transfer length, particularly for steel. When this occurred, the results were considered erroneous and were discarded. Therefore, only two sets of data are presented for each set of specimens tested. This data is given in Figure 38 through Figure 41 for each fiber type, FRP system, and substrate.

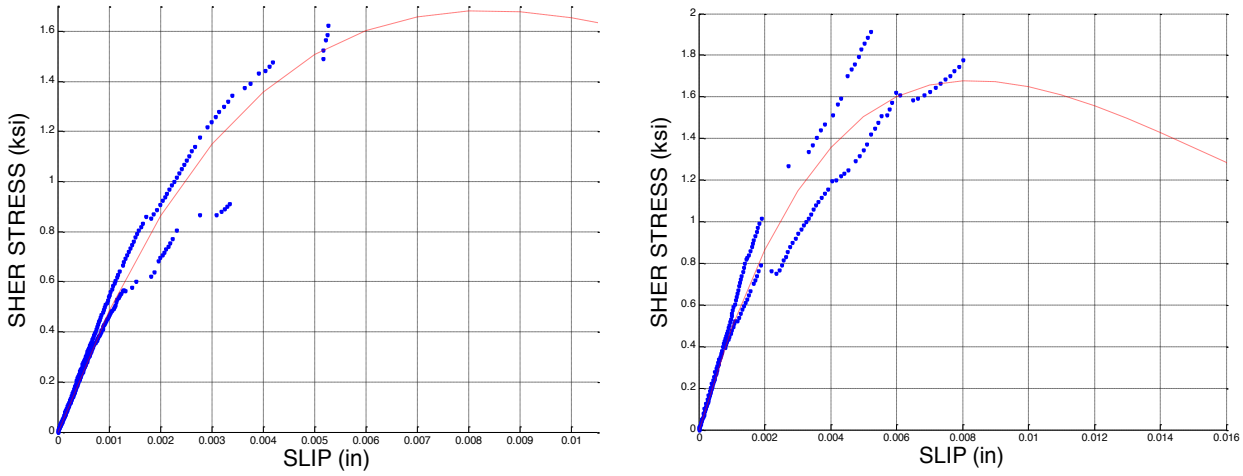

(a) High Density Basalt Fiber **(b) High Density Glass Fiber**

Figure 38. QuakeBond™ J300SR-impregnated FRP bonded to steel substrate

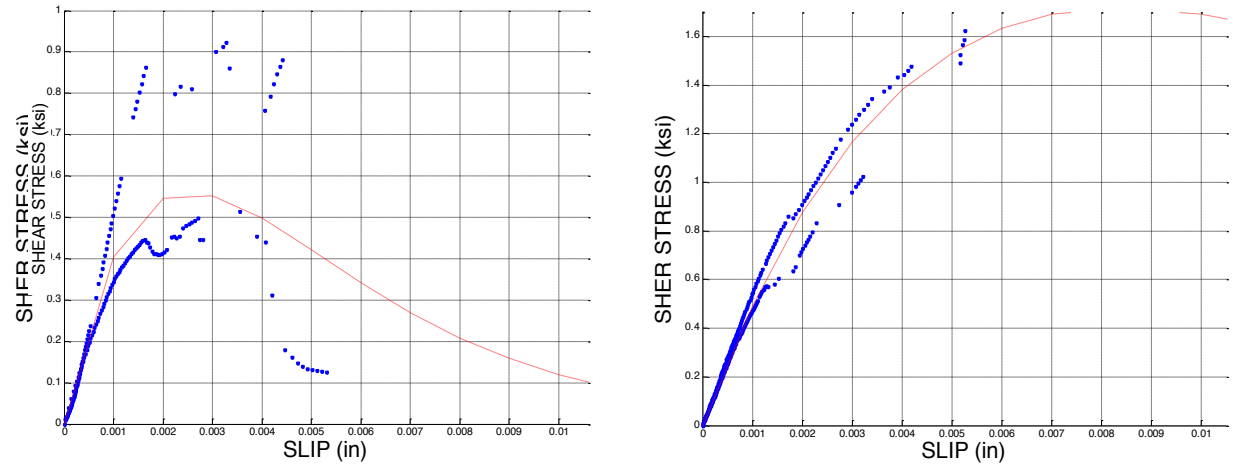

(a) High Density Basalt Fiber **(b) High Density Glass Fiber**

Figure 39. NRi XT-impregnated FRP bonded to steel substrate

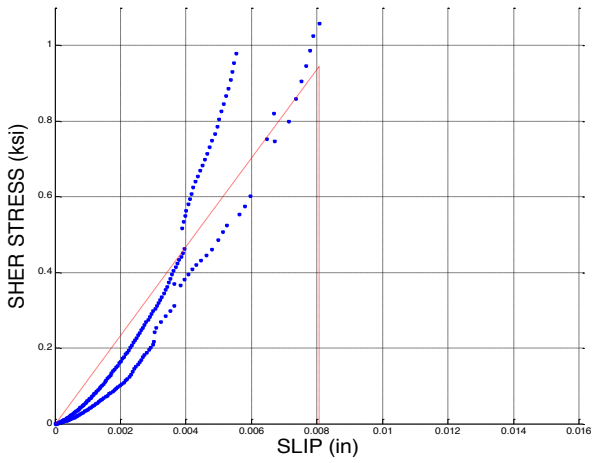

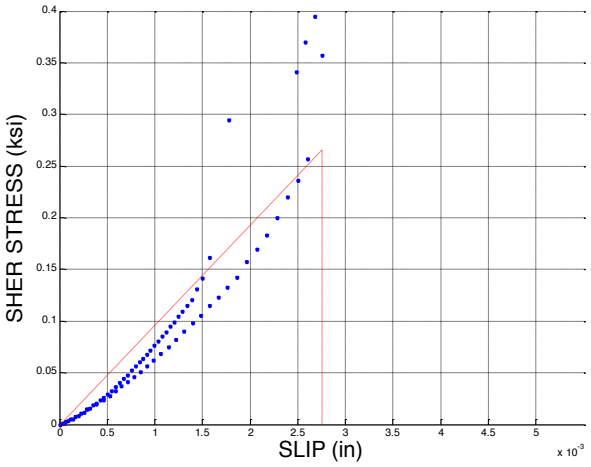

(a) High Density Basalt Fiber **(b) High Density Glass Fiber**

Figure 40. QuakeBond™ J300SR-impregnated FRP bonded to aluminum substrate

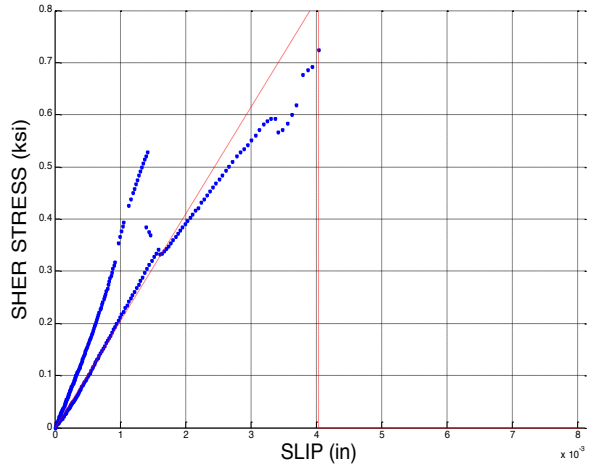

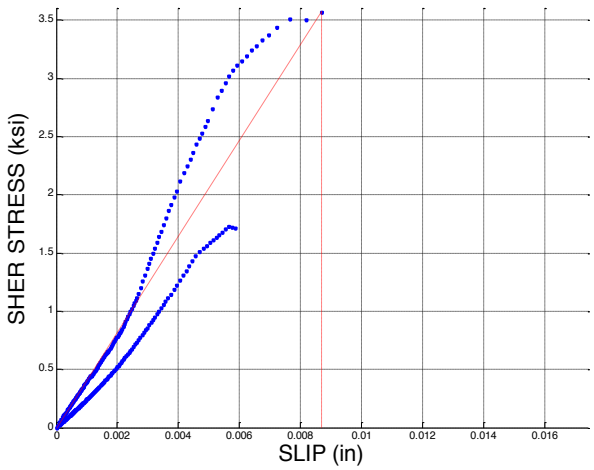

(a) High Density Basalt Fiber **(b) High Density Glass Fiber**

Figure 41. NRi XT-impregnated FRP bonded to aluminum substrate

As mentioned in chapter two, several functional forms are commonly used to describe the bond-slip relationship of FRP. Two of these forms were fitted to each set of data using a standard nonlinear regression tool within the Matlab software program (implementing the Levenberg-Marquardt algorithm of nonlinear least squares). Exponential and bilinear models were selected due to the ease with which they can be incorporated into the MSC.Marc nonlinear finite element program. These bond-slip models are defined by the functions:

$$\tau(s)_{\text{exponential}} = G_C \left(\frac{S}{V_C{}^2}\right) e^{-S/V_C} \tag{3-1}$$

and,

$$\tau(s)_{\text{bilinear}} = 2\left(\frac{G_C}{V_C}\right)\left(\frac{S}{V_C}\right) \tag{3-2}$$

where $\tau(s)$ is the total shear defined as a function of slip, S is the total slip, and V_C and G_C are parametric constants that relate to the slip at peek shear and overall scale of the function,

respectively. By defining the V_C and G_C values that best fit the experimental data, an expected shear stress can be found for any given slip increment.

Additionally, the mean squared error (mse) for both of these fitted functions was calculated for each set of tests. The accuracy of each fit is defined as $(1 - mse)(100\%)$. These parameters, as well as the fit accuracy value for both functions are presented in Table 10 and Table 11. The model with the best-fit value for each test is also shown with the test data in Figure 38 through Figure 41.

Table 10. Bond-slip model properties for FRP systems adhered to steel substrate

Matrix Material	Fiber Type	Exponential Model			Bilinear Model		
		G_C	V_C	fit	G_C	V_C	fit
QuakeBond™ J300SR	High Density Basalt	**0.0380**	**0.0083**	**98.57%**	0.0008	0.0024	94.49%
	High Density Glass	**0.0381**	**0.0083**	**99.50%**	0.0010	0.0023	98.49%
NRi XT Polyurethane	High Density Basalt	**0.0392**	**0.0084**	**99.69%**	0.9892	0.0023	98.66%
	High Density Glass	**0.0039**	**0.0026**	**98.12%**	0.5905	0.0027	94.15%

Best fit model parameters are shown in **bold**

Table 11. Bond-slip model properties for FRP systems adhered to aluminum substrate

Matrix Material	Fiber Type	Exponential Model			Bilinear Model		
		G_C	V_C	fit	G_C	V_C	fit
QuakeBond™ J300SR	High Density Basalt	604.47	2.5017	99.86%	**0.0004**	**0.0030**	**99.86%**
	High Density Glass	0.0025	4.5838	99.03%	**0.0005**	**0.0029**	**99.03%**
NRi XT Polyurethane	High Density Basalt	0.0052	3.5714	93.22%	**0.0010**	**0.0022**	**93.23%**
	High Density Glass	0.0101	0.0056	99.74%	**0.0007**	**0.0026**	**99.48%**

Best fit model parameters are shown in **bold**

3.3 Epoxy Fill Material Properties

Compression tests were performed on the Sikadur 31 Hi Mod Gel dent filler material. These tests were performed in accordance with ASTM D695. Cylindrical molds were used to form the compressive samples that were 4 in high and 2 in diameter, as shown in Figure 42. The epoxy was allowed to cure for 48 hours before being removed from the molds.

Testing was performed in the UTM at a load rate of 0.05 in/min. Strain gauges (6 mm, 120 Ω) were used to measure the axial strain at quarter and half points along the gauge length, as shown in Figure 43 (a). An additional gauge was used to measure the transverse strain in the middle of the gauge length. An example of the axial stress-strain behavior is displayed in Figure 43 (b) for Sample 5. The individual and average capacities of the epoxy measured in all cylinder tests are shown in Table 12. The strain data reported in the table are for the axial strain gauge direction.

(a) Cylinder mold

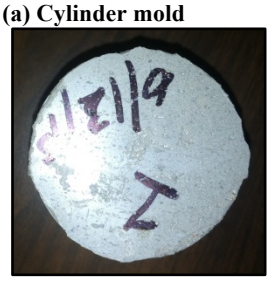

(b) Molded epoxy sample

(c) Cylinder mold

(d) Molded epoxy sample

Figure 42. Epoxy compression test samples

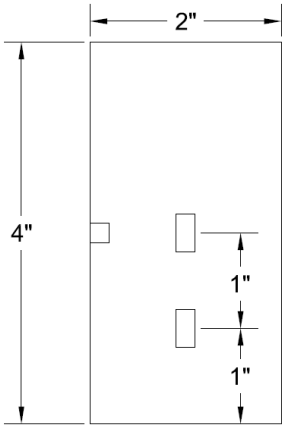

(a) Cylinder strain gauge placement

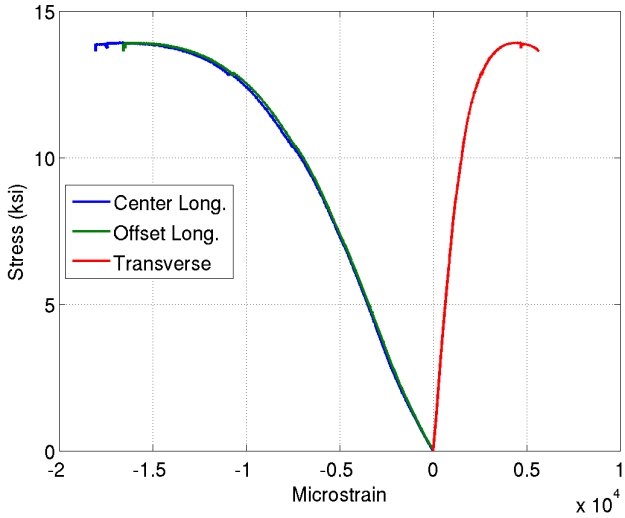

(b) Sample 5 stress-strain data

Figure 43. Epoxy compression instrumentation and sample stress-strain data

Table 12. Epoxy compression test results

Sample	Strength (ksi)	Maximum Strain (με)	Elastic Modulus (ksi)
1	13.15	-14845	1809
2	13.51	-11031	1847
3	13.05	-10360	1575
4	13.52	-13648	1149
5	13.93	-18060	1515
6	14.27	-18475	1238
7	13.38	-16735	1323
8	13.45	-16404	1411
9	13.15	-6658	1602
Average	**13.59**	**-14944**	**1497**

3.4 Pole Substrate Material Properties

To better characterize the range of alloys and material properties present in the inventory of poles retrieved for testing during this project, several dogbone coupons were cut from the large-scale test specimens. A representative sample was chosen from amongst the monotonic, cyclic, and impact specimens. The dogbones were removed from the upper portion of the pole (not from the region where the wraps and dents were present). Due to the destructive nature of removing the coupons, the results presented herein are therefore potentially affected by any mechanical loading experienced by the poles not only prior to acquisition for this project, but also due the loading received in the laboratory tests.

The pole substrate materials were tested for their tensile properties at the UCF Structures Lab. Dogbone samples were cut from 13 steel poles, with 3-5 samples per pole. An Instron extensometer was used to measure strain and was removed prior to rupture of the coupons; therefore, the strain at ultimate stress is not reflected except for those tests conducted in tandem with a strain gauge mounted to the coupon. The yield stress and elastic modulus results are summarized in Table 13. Details from each individual test, presented in the form of stress-strain curves, are shown in Appendix C. The strain and moduli readings were obtained for a majority of specimens from an extensometer; however, slip of the clips resulted in erroneous readings, so the moduli from Table 14 were used to compute theoretical load capacities.

Table 13. Steel large-scale test specimen material properties

Specimen	Coupons tested	Average Yield Stress (ksi)	Average Elastic Modulus (ksi)
FD-1	3	54.8	17840
FD-2	4	49.2	29240
FD-3	4	46.6	15250
FD-5	3	51.1	17267
ST-5	4	55.9	29190
ST-6	4	70.7	28020
ST-7	4	55.9	26180
ST-8	3	59.7	22080
ST-10	4	54.8	20420
ST-11	3	54.8	18033
ST-12	4	54.9	23220
IM-1	4	53.6	16254
IM-2	3	66.8	26220

In addition to the dogbone coupons obtained from the large-scale pole specimens in this project, additional material data was obtained from previous work (Mackie et al., 2011). This set of data had a more consistent extensometer modulus reading, and is the only set that contained aluminum substrate material tests. The results are summarized here in Table 14.

Table 14. Material properties obtained from previous pole study (Mackie et al., 2011)

Specimen	Coupons tested	Average Yield Stress (ksi)	Average Elastic Modulus (ksi)
Steel	3	53.8	29600
Aluminum	3	33.0	8250

Chapter 4: Component Testing

As a major portion of this research, an extensive testing program was performed in order to investigate the performance of externally-bonded FRP repairs of damaged utility poles. As an initial investigation of repair system performance, a series of three sets of tests using pole segments in a four-point bending configuration was performed. The pole segments were obtained by cutting an inventory of complete or partial pole specimens down to size. The original inventory of poles used for the component-level testing did not have base plates, as illustrated in Figure 44. The results of these tests informed the design of repairs implemented in full-scale tests performed on poles with base plates in a cantilever configuration designed to simulate the wind loading experienced by utility poles in the field. This chapter discusses the implementation of the initial component-level investigation tests and a summary of their results.

Figure 44. Pole specimens located in the yard prior to cutting for the component-level tests

The series of initial investigation tests included three sets of tests in order to investigate different facets of the repair system. The first of these was a set of damage determination tests, which were performed on poles with varying degrees of damage in order to determine the effect of this damage on the stiffness and strength of the pole. A set of tests following the damage determination was called the single-ply test set. This set of tests consisted of several poles, again damaged to various degrees, repaired with a single, uniform layer of FRP composite. Finally, a set of tests investigating different configurations of FRP wrap repairs was performed on

undamaged poles. These tests, along with a summary of their results, are discussed in this chapter.

Damage determination and single-ply specimens were damaged in the laboratory by rapid application of a point loading using an MTS with steel spherical attachment. An example of the denting setup and attachment used to strike the poles is shown in Figure 45. Loading and deformation data were taken during the denting process, which created a round, localized mechanically-imparted dent that was largely repeatable between different pole segments. The rate of dent application was between 2 and 3 in/sec. An example of the denting data is shown in Figure 46. It was often noted that, when applying larger dents, significant global bending of the pole occurred. The poles with more global damage were not tested, as the induced dent was not representative of the field impact-damage that commonly occurs, and was too severe to be repaired by an FRP wrap. Poles with bends this extreme would always be replaced in the field. The exaggeration of extents of the dent seen in the poles without base plates was of course mitigated when denting the full-scale poles with integral base plates.

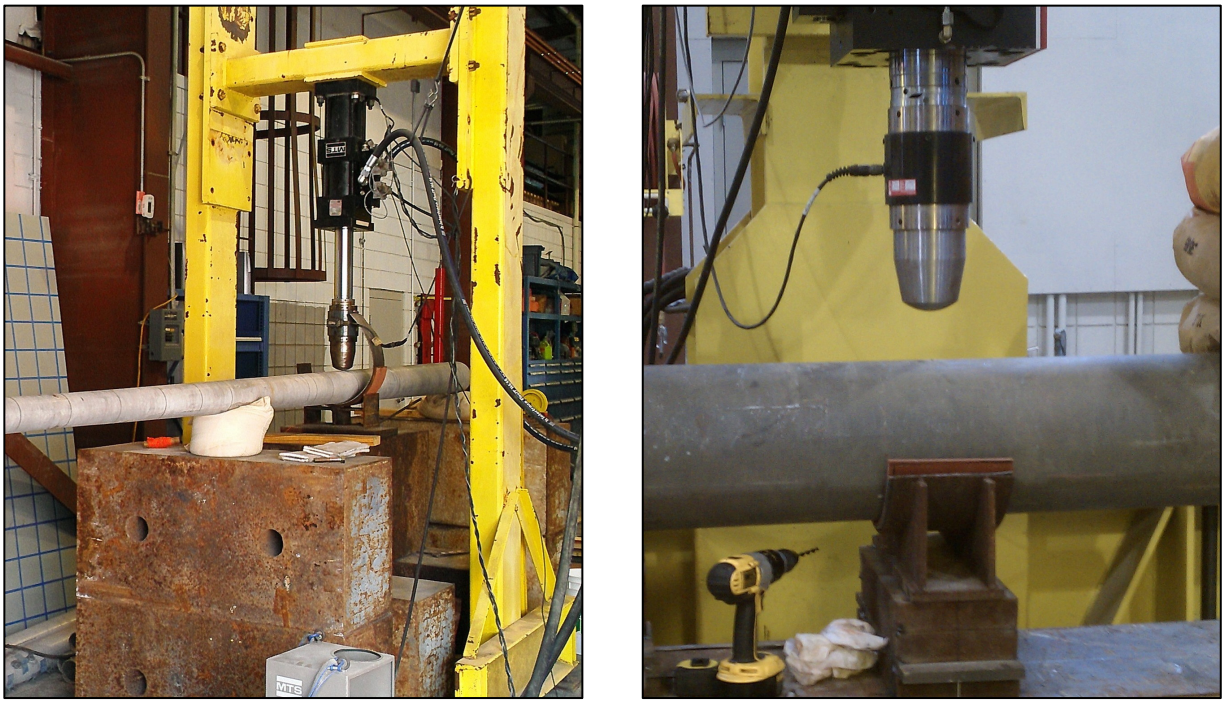

(a) Denting of aluminum component-level specimen **(b) Denting head attached to actuator**

Figure 45. Denting setup and actuator attachment

Once poles were dented in the laboratory, the damaged sections of several poles were scanned with a 3D laser scanner in order to create point clouds that were subsequently used to generate a finite element model of the damaged surface. Examples of the scanned point clouds are shown in Figure 47 for pole ALw-5.b and Figure 48 for pole STw-3.a, respectively. A full point cloud scan of a field-damaged pole with the base plate still attached (FD-3) is shown in Figure 49. The base plate, pedestrian buttons, and several impact regions are discernable from the image.

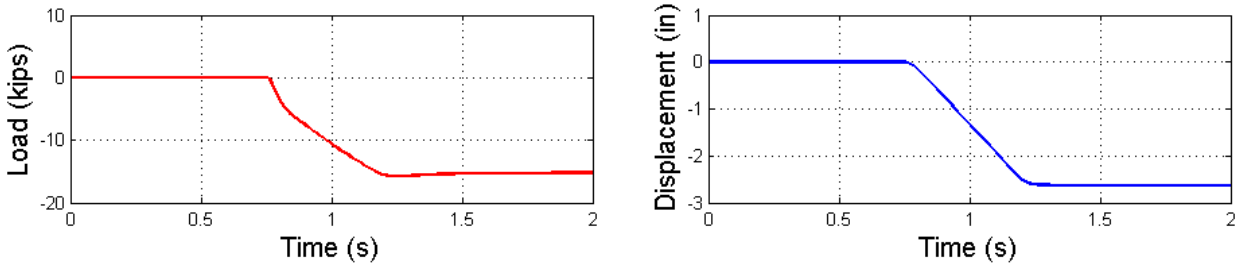

(a) Denting load vs. time **(b) Denting displacement vs. time**

Figure 46. Dent application to pole ALw-5.b

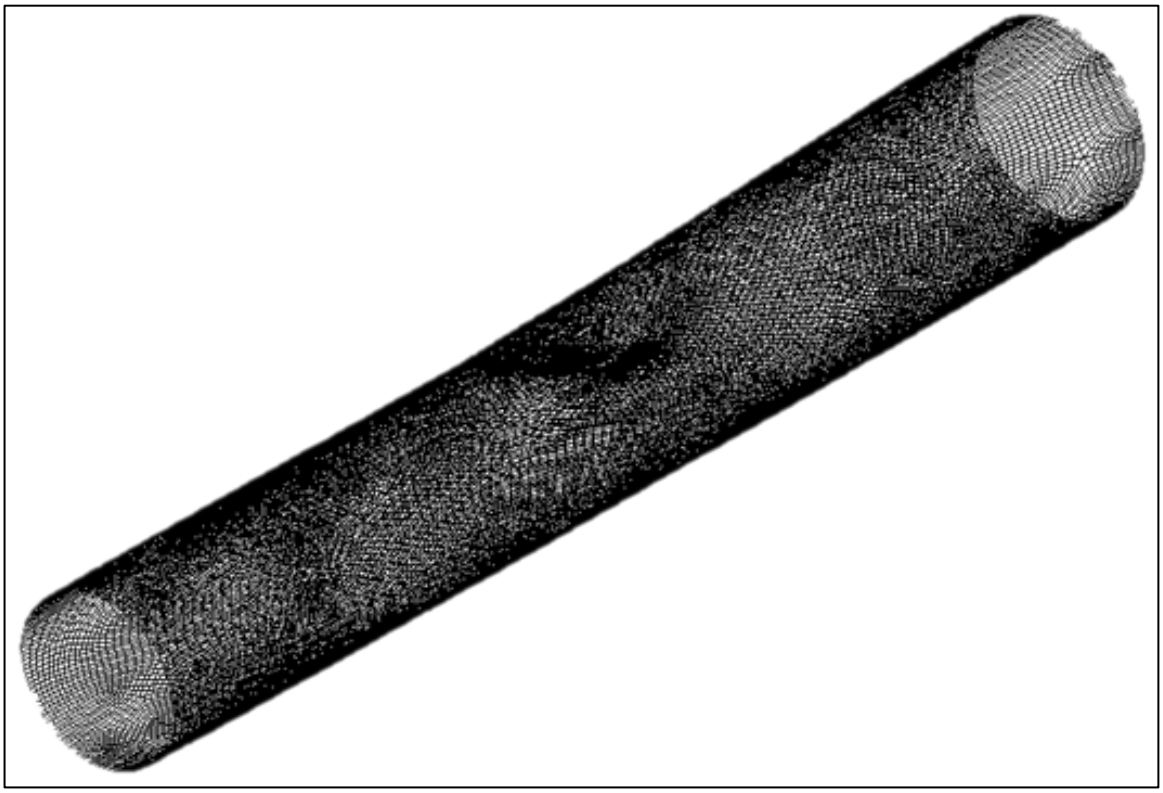

Figure 47. ALw-5.b mesh created from 3D scan point cloud

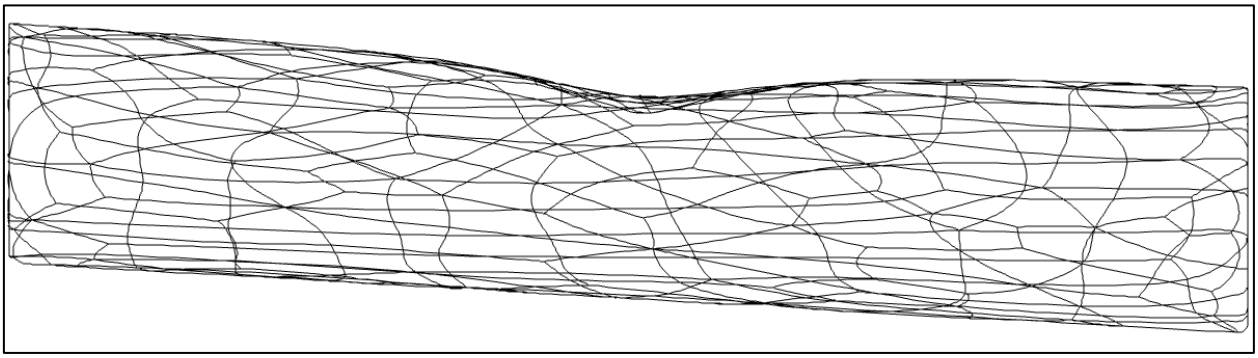

Figure 48. STw-3.a mesh created from 3D scan point cloud

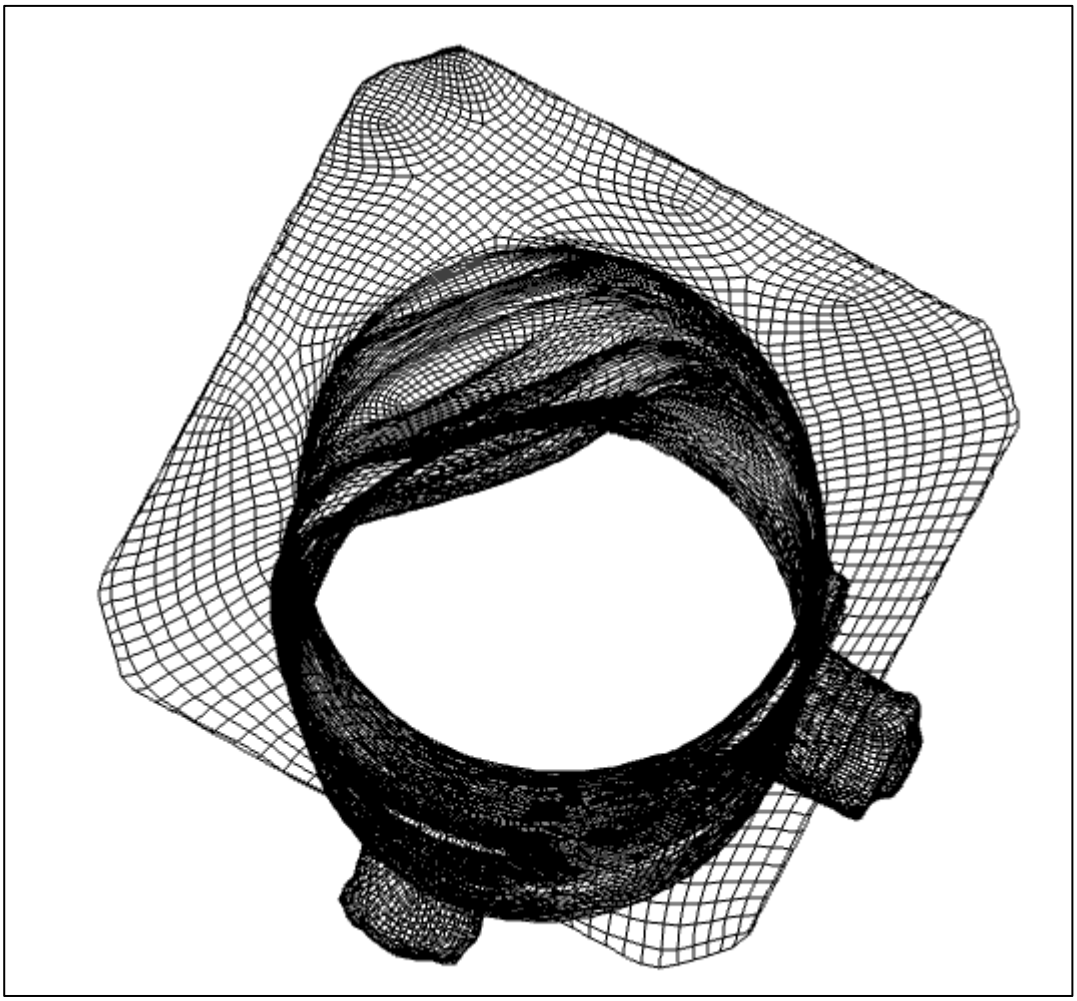

Figure 49. FD-3 mesh created from 3D scan point cloud

4.1 Damage Determination Tests

The Damage Determination tests were performed at the Marcus H. Ansley Structural Research Center in Tallahassee, FL. The four-point bending test configuration is shown in Figure 51 and Figure 63. These loading configurations were designed to emulate wind loading on a utility pole in the region of the dent. Wind loading is typically assumed to have a parabolic distribution along the length of the pole, thus creating a cubic shear force distribution, and a fourth degree bending moment distribution. Since this is difficult to replicate in a laboratory test, the loading configuration was chosen in order to create the ratio of bending moment and shear force at the dent location as is created by wind loading. The asymmetric loading creates constant shear and linear non-constant moment within the loading zone.

Curved supports and load applicators were fabricated for these tests, and were lined with neoprene or rubber pads. The locations of strain and displacement measurements are shown in Figure 51 and Figure 63. The strain gauges were all 6 mm 120 Ω foil-backed resistance gauges. The displacement transducers (labeled as D2, D3, D5, and D6) were laser Balluff BOD 66-M type sensors. The center displacement gauge was a UniMeasure string potentiometer. The

support measurements (D1 and D7) were TML SDP-200D shaft type sensors. The displacement-controlled loading rate for these tests was approximately 0.1 in/min using an 800 kip servo-hydraulic Enerpac actuator. The load, strain, and displacement data obtained from these tests were used to determine the effect of pole denting, as is discussed in the following section.

The challenge during both the damage determination and single-ply tests was the poles with small aspect ratios (flexural span relative to the diameter). Due to the thin-walled circular hollow sections (mostly the steel specimens due to the range of diameters tested), local deformation of the pole cross-sections occurred at both the support and load points. The result was localized failure at locations of stress concentrations that led to premature estimates of the failure load capacity. In extreme cases (small aspect ratios), the cross-section would deform elastically along the entire length of the pole rather than allowing flexure. Therefore, several of the poles were stiffened at the ends (or load points) using vertical stiffener plates inside the cross-section or transverse plates (end caps) externally at both ends.

4.1.1 Damage Determination Test Matrix

As mentioned above, the Damage Determination (DD) tests were performed in order to ascertain the effect of dents of various depths on the strength and stiffness of highway poles. The details of this program are shown in Table 15. The length is the center-to-center distance between the two supports. The large-diameter and small-diameter values are specified at the centerline of the left (north) and right (south) supports, respectively. Seven (7) aluminum and five (5) steel poles were tested with dent depths ranging from 5 to 26%. One undamaged aluminum pole and two undamaged steel (one round and one 18-sided) poles were also tested as a control set. All diameters shown in this chapter are the outer diameter unless otherwise noted.

Table 15. Damage determination test specimens

Pole ID	Section Geometry	Length (ft)	Large Diameter (in)	Small Diameter (in)	Diameter at Dent (in)	Dent Depth (in)	Dent Depth (%)
ALu-1.a	Round	9	5.73	4.56	5.00	0.25	5.0
ALu-1.b	Round	9	6.51	5.34	5.86	0.75	13
ALu-2.b	Round	9	6.51	5.34	5.86	1.50	26
ALu-4.a	Round	9	5.73	4.56	5.00	-	-
STu-1.a	Round	11	13.375	11.75	12.40	3.00	24
STu-1.b	Round	11	15.25	13.5	14.20	3.125	22
STu-1.c	Round	11	13.5	11.75	12.44	2.75	22
STu-1.d	Round	11	10.625	8.9375	9.62	1.375	14
STu-1.e	12-sided	11	10.25	8.75	9.36	1.75	19
STu-1.f	18-sided	11	11.875	10.25	10.94	2.375	22
STu-2.a	Round	11	11.6875	10.0625	10.83	-	-
STu-2.b	18-sided	11	9.75	8.25	8.71	-	-

4.1.2 Aluminum Substrate Tests

The aluminum alloy AA 6036-T6 pole sections tested in this program were cut from one of two utility pole geometries. Poles ALu-1 through ALw-6 were cut from poles 27 feet in length, and poles ALw-7 and 8 were cut from 36-foot-long poles. The first step in the testing process, cutting

the pole specimens, was carried out using a band saw according to Figure 50. These resulting pole sections were dented as discussed above. Three (3) aluminum poles were tested with dent depths ranging from 5 to 26%. One undamaged aluminum pole was also tested as a control. The testing configuration for the aluminum component level tests is also shown, in Figure 51.

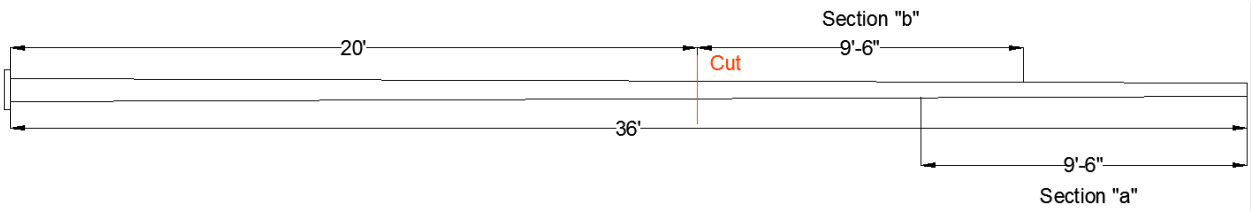

(a) Poles AL-1 through 6

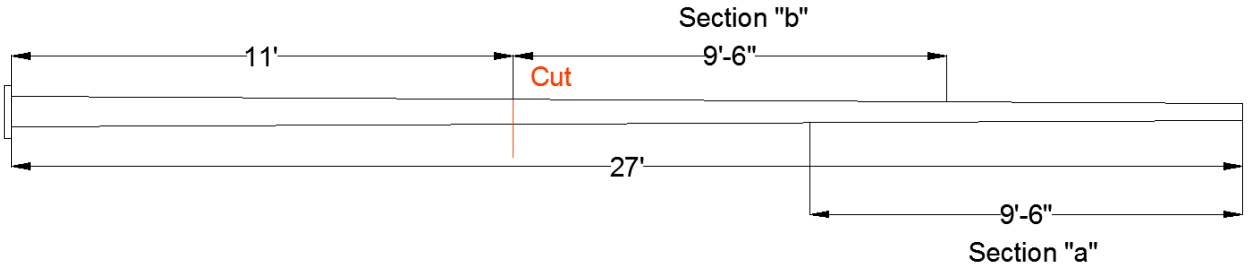

(b) Poles AL-7 and 8

Figure 50. Cuts applied to aluminum component level test specimens

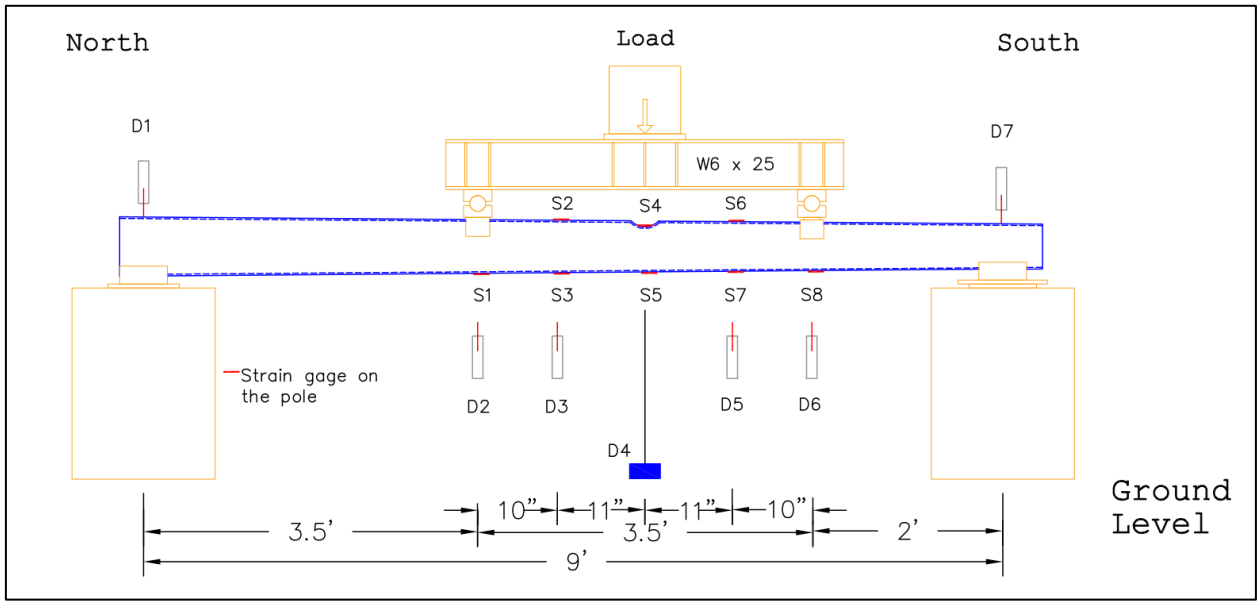

Figure 51. Aluminum damage determination test configuration

4.1.2.1 ALu-1.a

The first dented poles to be tested were cut from pole ALu-1. The narrower end of this pole, ALu-1.a, received a dent with a depth of approximately 5% of the outer diameter at the dent location, or 0.25 in (see Figure 52). The pole section tapers from an outer diameter of approximately 5.75 in to 4.5 in on the support span. At the dent location, the outer diameter is approximately 5.0 in. The test setup is shown in Figure 52, and was prepared in accordance with

the configuration in Figure 51. Displacement gauges D1 and D7 are intended to measure the settlement at the supports as well as crushing of the cross-section. However, significant rotation at the supports prevents these measurements from cleanly capturing the settlement behavior, and makes the determination of the displacement profile difficult.

Figure 52. ALu-1.a laboratory-applied dent and test configuration

When tested, pole ALu-1.a carried a maximum load of approximately 7.62 kips. Measured strain and displacement data are shown in Figure 53. Plastic hinging occurred at the center of the applied dent as can be seen in Figure 54. The maximum moment at the location of the hinge was calculated from the maximum load as 10.0 kip·ft. From the strain curves, it can be seen that gauges S4 and S5, which are located on the top and bottom of the dented section, respectively, show fast-growing strains after the peak load has been achieved. This indicates that the section at the dent is deforming plastically. The tensile and compressive strains experienced at the dent center at the time of maximum loading were measured as 6080 με and -3972 με, respectively.

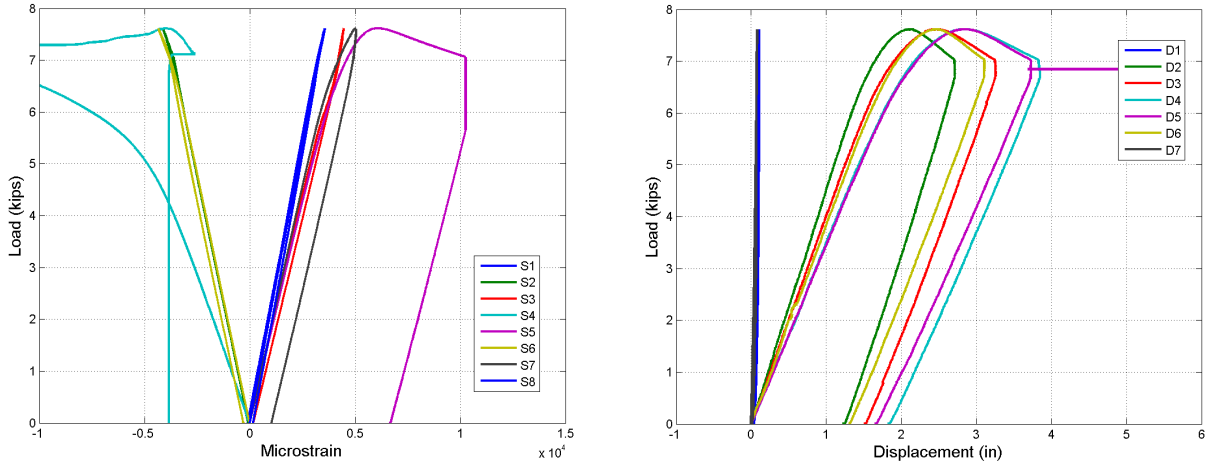

(a) Load vs. strain **(b) Load vs. displacement**

Figure 53. ALu-1.a test data

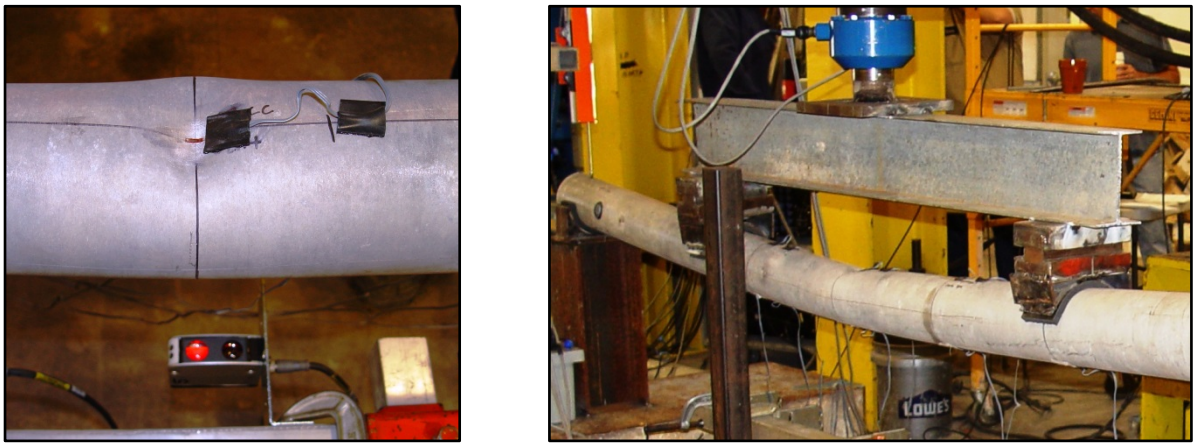

Figure 54. ALu-1.a plastic hinge failure at dent center

4.1.2.2 ALu-1.b

The ALu-1.b pole section was taken from the middle section of pole ALu-1. This section, and all other aluminum *b* pole sections, has an outer diameter ranging from 6.6 in to 5.4 in across the support span. The outer diameter at the location of the applied dent is approximately 5.77 in, and the dent depth is 0.75 in, or about 13% of the outer diameter (Figure 55). The load, support, strain gauge, and displacement gauge configuration is the same as that of the previous tests.

Figure 55. ALu-1.b laboratory-applied dent

The data collected from pole ALu-1.b is shown in Figure 57. The maximum load experienced by this pole was about 12.34 kips, at which point a plastic hinge formed at the dent location, as shown in Figure 56. This failure corresponds to a maximum moment of 16.2 kip-ft at the location of failure. The maximum load induced a tensile strain at the dent section of 5414 με, and a compressive strain of -9928 με at this location.

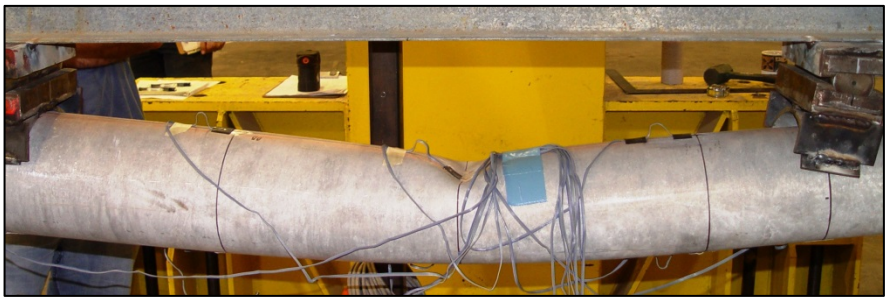

Figure 56. ALu-1.b plastic hinging failure

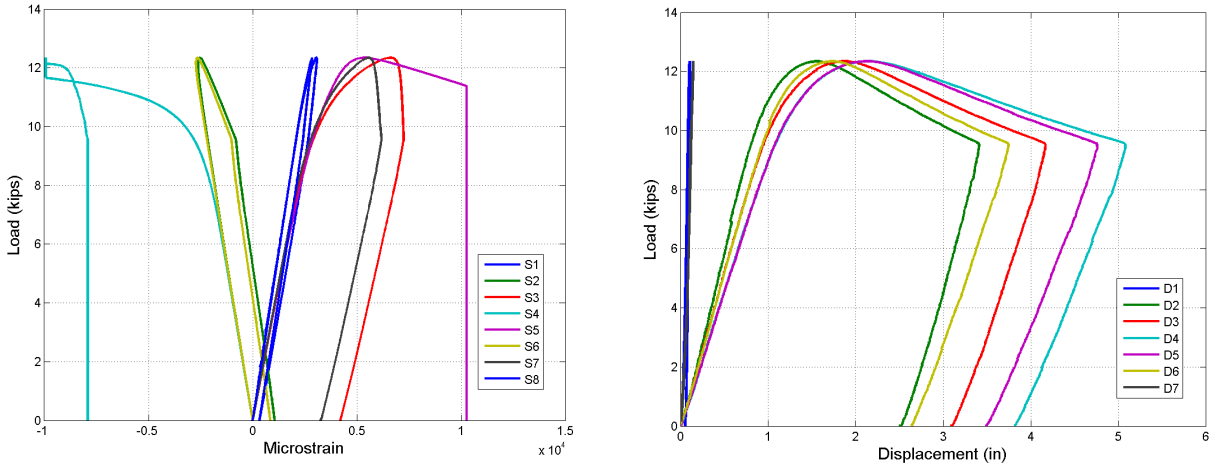

(a) Load vs. strain **(b) Load vs. displacement**

Figure 57. ALu-1.b test data

4.1.2.3 ALu-2.b

Section ALu-2.b has the same geometry as section ALu-1.b, but was dented to approximately twice the depth. The 1.5 in dent has a depth of about 26% of the pole's undented diameter at that location. The maximum load carried by this pole was approximately 8.12 kip, which created a moment of 10.7 kip-ft at the dent center. The corresponding strains at the dent section were 4222 με in tension, and -10458 με in compression. This large compressive strain indicates that the dented area deformed significantly during loading, and that the behavior of the section was greatly affected by the presence of the dent. This is confirmed by the moment capacity measured for this pole, which is significantly reduced from the control capacity, indicating that the strength of the section is largely reduced by denting. The final plastic hinging mechanism that formed in the pole is shown in Figure 58. The load, displacement, and strain data obtained during this test are shown in Figure 59.

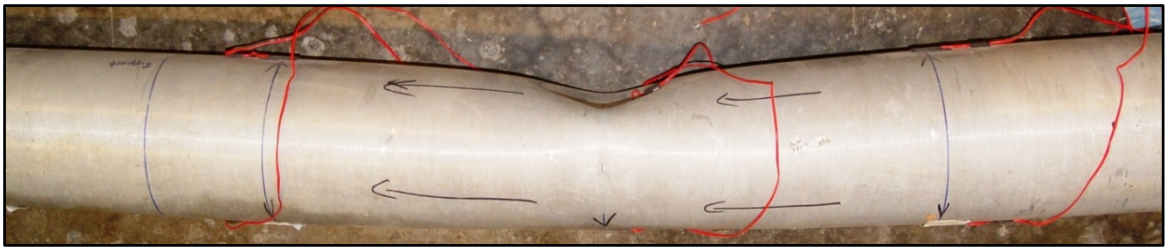

Figure 58. ALu-2.b plastic hinging failure

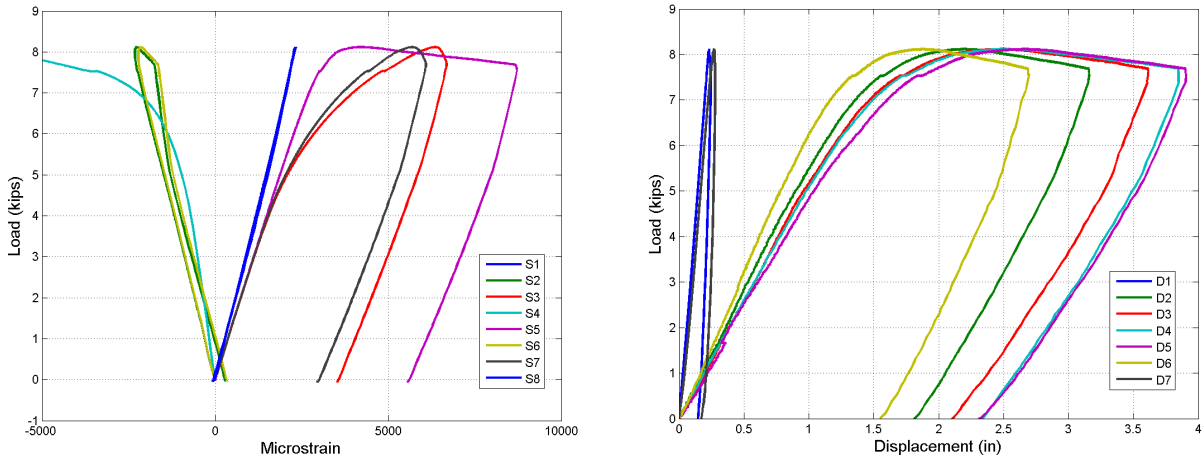

(a) Load vs. strain **(b) Load vs. displacement**

Figure 59. ALu-2.b test data

4.1.2.4 ALu-4.a

Pole ALu-4.a was tested as a control, that is, without being dented. The pole section was cut from the narrowest (or *a*) end of a 27-foot aluminum pole, and has the same geometry as section ALu-1.a. The test setup is shown in Figure 60. Load was applied to the pole section, and the strains and displacements are shown in Figure 62. The pole achieved a maximum load of approximately 8.43 kips before undergoing local buckling of the section at the outside edge of the south load applicator, as shown in Figure 61.

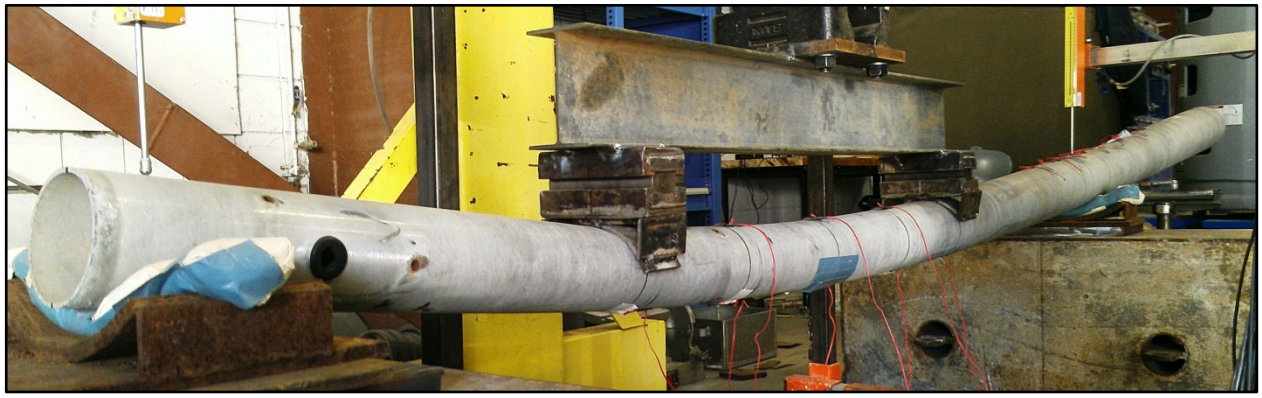

Figure 60. ALu-4.a test configuration during loading

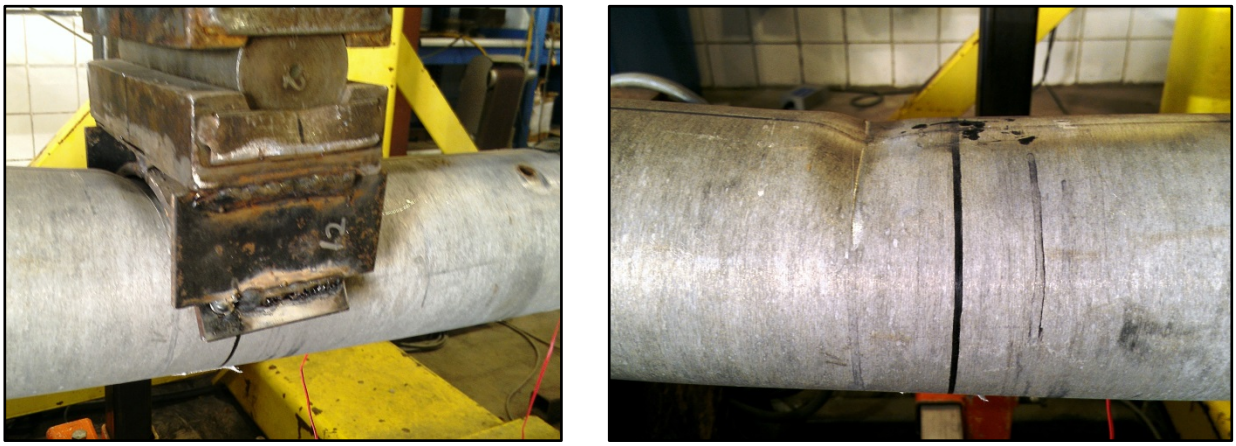

Figure 61. ALu-4.a local buckling at load applicator

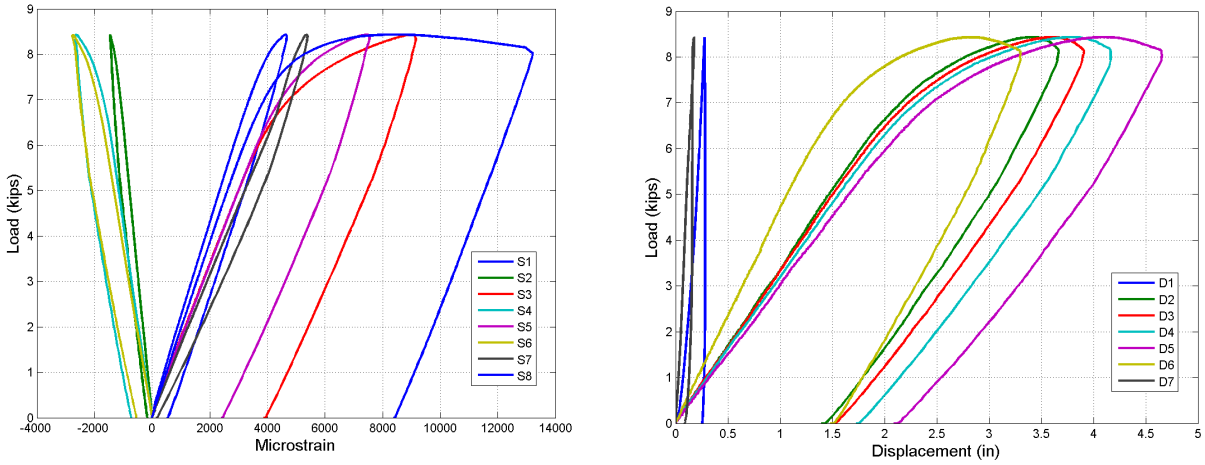

(a) Load vs. strain **(b) Load vs. displacement**

Figure 62. ALu-4.a test data

It is likely that the load applicator initiated failure by creating a small dip in the pole surface. The maximum moment at the location of the hinge were 12.3 kip-ft. The maximum strain and deflection on the bottom of the section at the center of loading were measured as 7539 με and 4.17 in, respectively, both measured on the underside of the section at the center of loading. The tensile and compressive strain values when maximum load was achieved were 7395 με and -2627 με, respectively. If the local buckling had not occurred under the load applicator, it is likely that the section at the center of loading would have withstood its theoretical maximum capacity, which is calculated from the theoretical plastic moment. This theoretical capacity has a value of 10.12 kips, and is approximately 1.2 times the load actually held by the pole.

4.1.3 Steel Substrate Tests

The steel Damage Determination tests were carried out much in the same way as the aluminum tests, except with a slightly different loading configuration. The steel test setup is illustrated in Figure 63. For these tests, a manually controlled displacement rate of 0.5 in/min was used as nearly as possible. Eight (8) steel poles were tested, five (5) round and three (3) multi-sided. Two poles, one round and one multi-sided, were tested as undented controls. The remaining six (6) poles were dented to depths ranging from 14 to 25% of the pole diameters. The size of the poles

ranges from 9.6 in to 14.2 in in diameter at the locations of the applied dents. Each of the poles had a wall thickness of 0.1875 in. In order to arrest local section deformations at the locations of the supports, various reinforcement methods were used. The results of each steel Damage Determination pole test are presented and discussed in the following section.

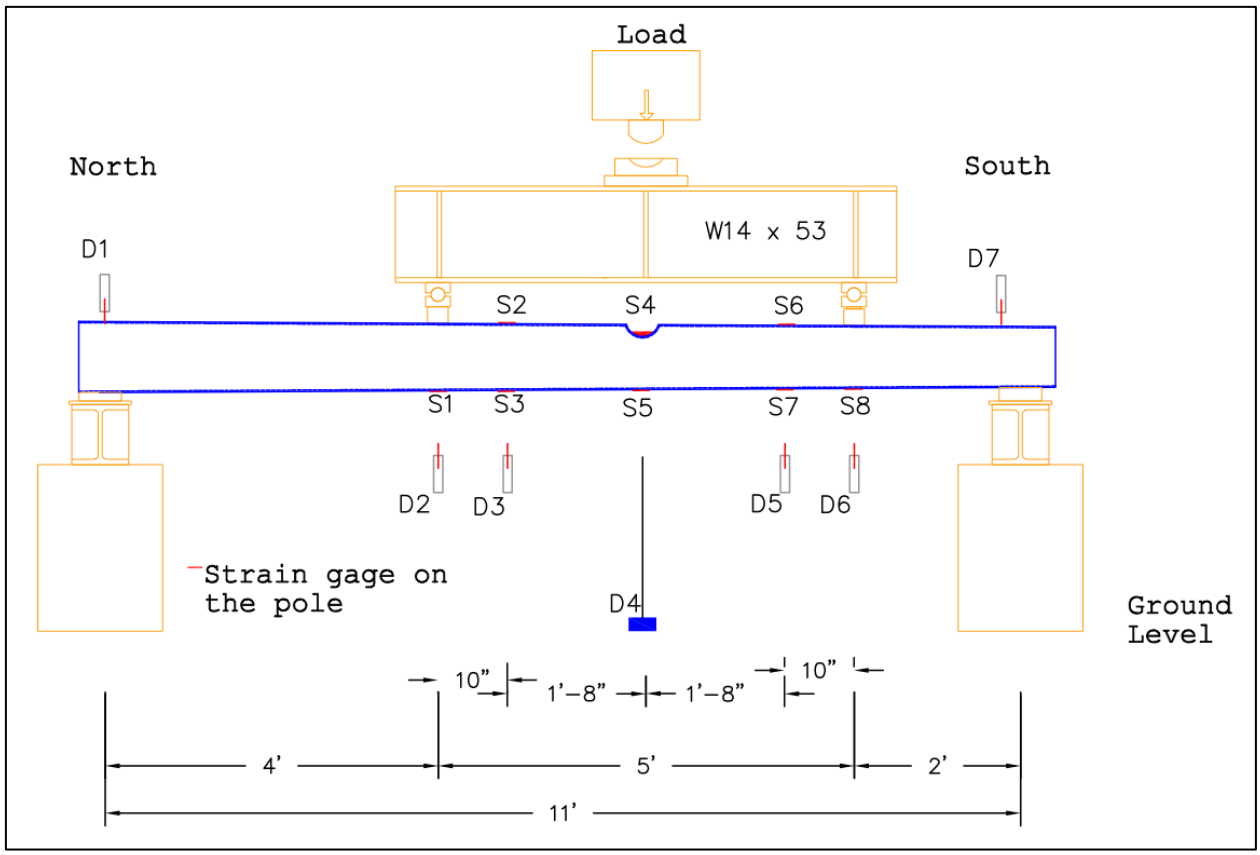

Figure 63. Steel damage determination test configuration

4.1.3.1 STu-1.a

The first of the steel Damage Determination specimens, STu-1.a, was a round pole ranging in diameter from 13.375 in to 11.75 in. The 3 in dent was 24.2% of the 12.4 in diameter at that location, as shown in Figure 64. The test setup was prepared in accordance with the diagram in Figure 63. Circular steel plates were welded to the ends of the pole section in order to limit local deformations at the supports.

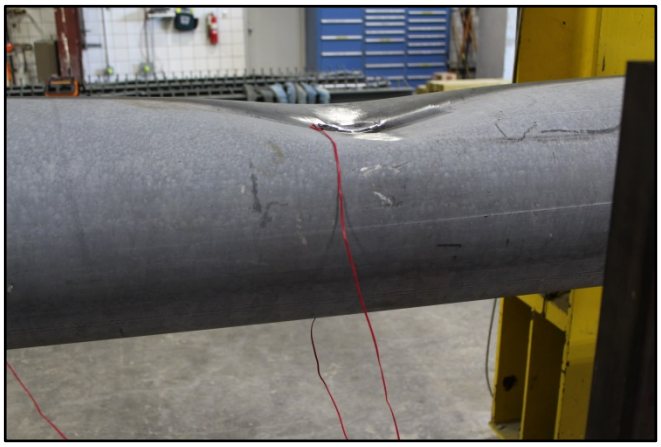

Figure 64. STu-1.a pole with dented region shown in test setup

The load-displacement and load-strain data are plotted in Figure 65. The displacement profile indicates that the largest displacement (1.43 in) was measured at D4, which is located at the dent center. Additionally the greatest strains on the compression and tension faces occurred at the dent center in gauges S4 and S5, respectively. The extreme strain values in compression and tension were -3133 με and 3433 με, respectively. The difference in these values may indicate the magnitude of the residual strain in the dented region. The maximum load carried by this pole was 50.3 kips, which corresponds to a maximum moment of 70.9 kip-ft at the dent location. The ratio of this value to the theoretical yield strength of the undented section is 1.30. When this is normalized by the theoretical maximum value for an undented section (2.53), the result is 0.51. This indicates that the dent has decreased the capacity of the pole by roughly 50%.

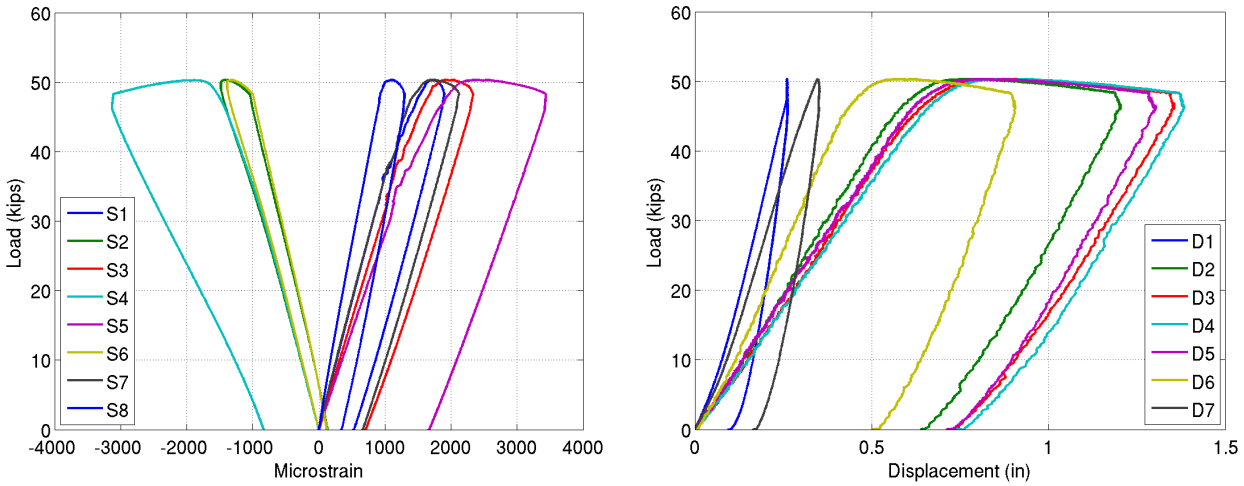

(a) Load vs. strain **(b) Load vs. displacement**

Figure 65. STu-1.a test data

4.1.3.2 STu-1.b

STu-1.b had a dent of 3.125 in. The diameter of the pole is 13.5 in at the smaller end and 15.25 in at the larger end. The diameter at the location of the dent was 14.2 in, making the dent depth 22% of the outer diameter. During the denting of this pole, a crack formed in the dented region, as shown in Figure 66. As with pole STu-1.a, circular end caps were welded to the section ends.

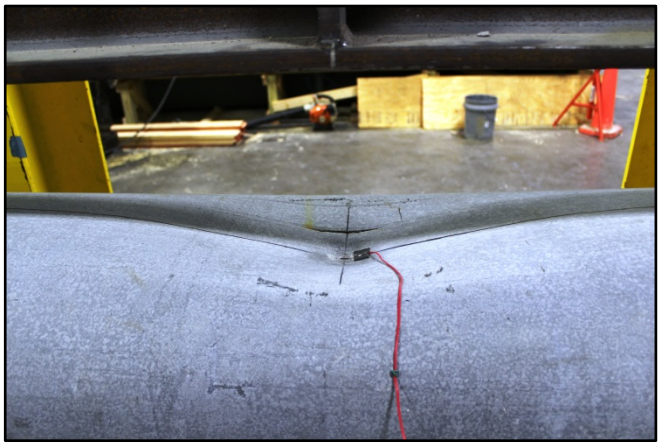

Figure 66. STu-1.b dent before testing

The maximum load carried by STu-1.b was 61.0 kips, which corresponds to a moment at the dent center of 86.0 kip-ft. This load is approximately 47% of the theoretical undented capacity. However, at this load the welds connecting the southern end cap to the pole failed, and the pole section at the south support collapsed (see Figure 68). Loading was stopped before full yielding had occurred at the dent location. However, based on the test data shown in Figure 67, the strain values at S4 and S5 indicate that the dent section was close to yield. The maximum tensile and compressive strains were measured as 1497 με at S5 and -1420 με at S6, respectively. The maximum displacement was measured with D7 at the south support to be 1.098 in.

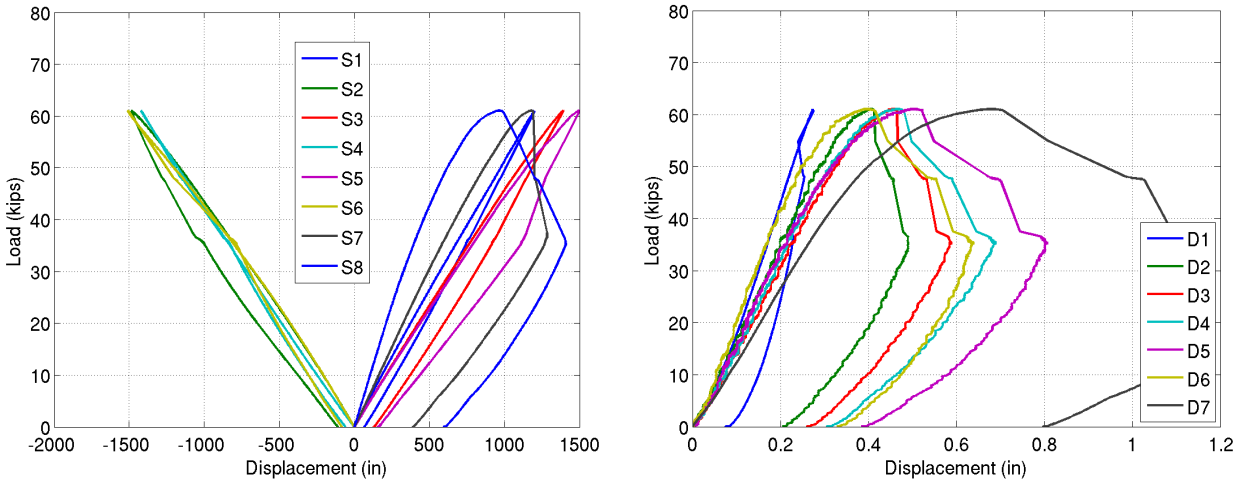

(a) Load vs. strain **(b) Load vs. displacement**

Figure 67. STu-1.b test data

Figure 68. STu-1.b end weld failure

4.1.3.3 STu-1.c

Similar in size to STu-1.a, pole STu-1.c ranged in diameter from 11.75 in to 13.5 in, the diameter at the dent location being 12.44 in. The dent depth was 2.75 in, or 22.1% of the outer diameter. The test setup, showing the circular welded end caps, is pictured in Figure 69.

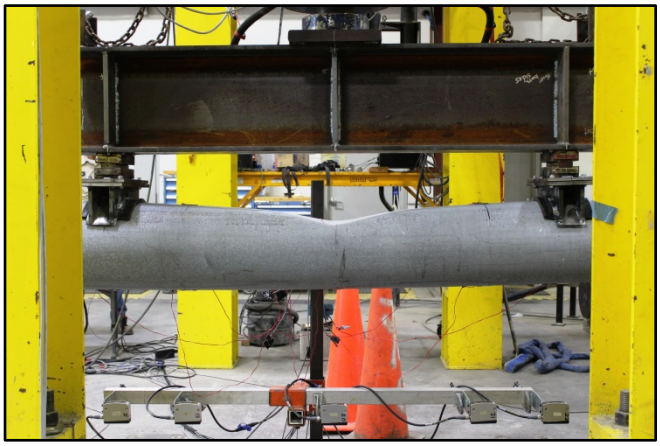

(a) Loading configuration

(b) End bracing

Figure 69. STu-1.c test setup

Pole STu-1.c formed a plastic hinge in the section of the dent at a load of 53.6 kips, or a bending moment of 75.5 kip-ft. The strain and displacement data are displayed in Figure 70. The extreme tensile and compressive strains experienced at the yielded section were 3216 με and -4348 με, respectively. The maximum displacement of the pole was 1.25 in.

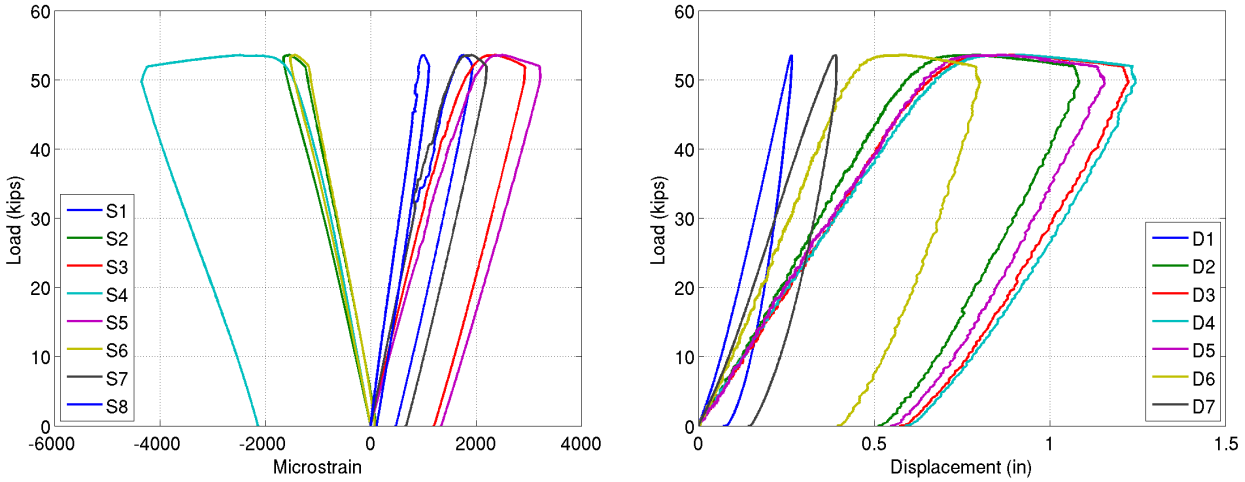

(a) Load vs. strain **(b) Load vs. displacement**

Figure 70. STu-1.c test data

4.1.3.4 STu-1.d

Pole STu-1.d was given a 14.3% dent. This dent had a depth of 1.375 in at the point where the pole's diameter was 9.62 in. The large diameter end of the pole was 10.62 in wide, and the small diameter end was 8.93 in. Two plates were welded inside the ends of the pole section as bracing in order to prevent excessive deformation at the supports. This pole was tested in the configuration shown in Figure 71.

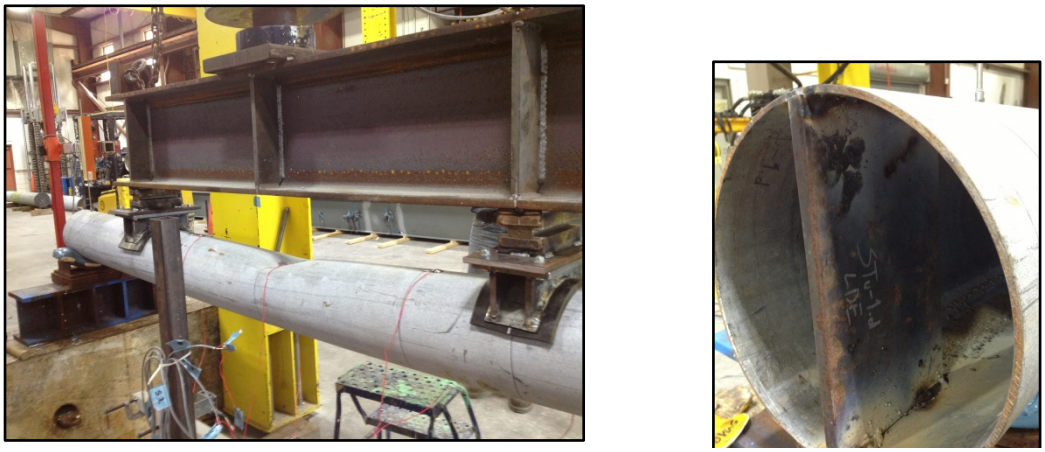

(a) Loading configuration **(b) End bracing**

Figure 71. STu-1.d test setup

The greatest load carried by this pole before failure was 43.5 kips, or 61.3 kip-ft at the dent location. The predominant failure mode was plastic hinging of the steel pole at the dented section. This is illustrated by the strain data plotted in Figure 72. The gauges at the dented section, S4 and S5, give the extreme strains of -11079 με and 14796 με, respectively. The maximum displacement of 2.18 in was measured at gauge D4, also positioned at the dent center. The failed section is shown in Figure 73. The measured capacity of this dented pole was approximately 75% of the theoretical capacity of the undented pole.

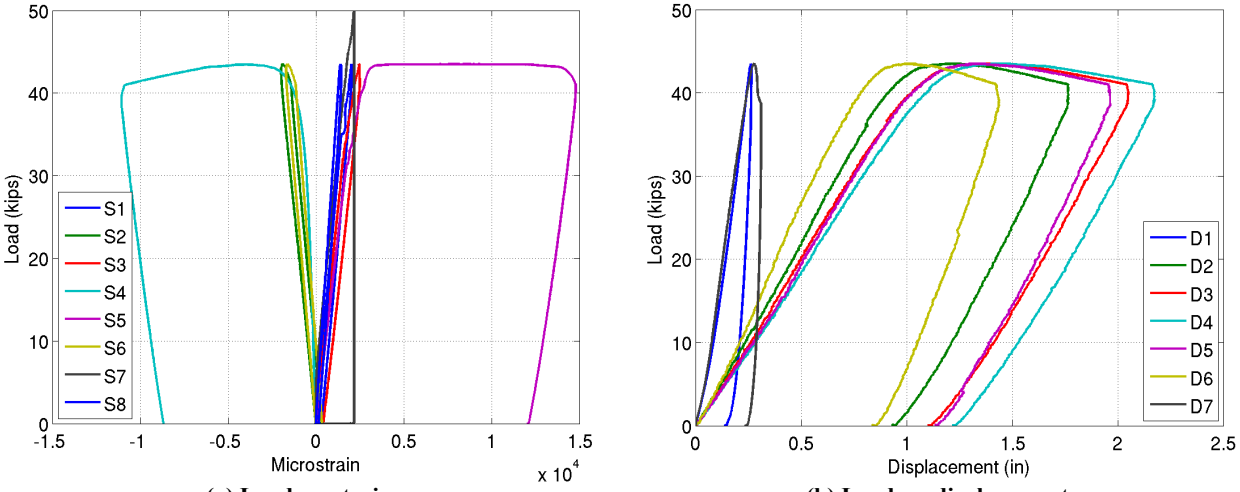

(a) Load vs. strain **(b) Load vs. displacement**

Figure 72. STu-1.d test data

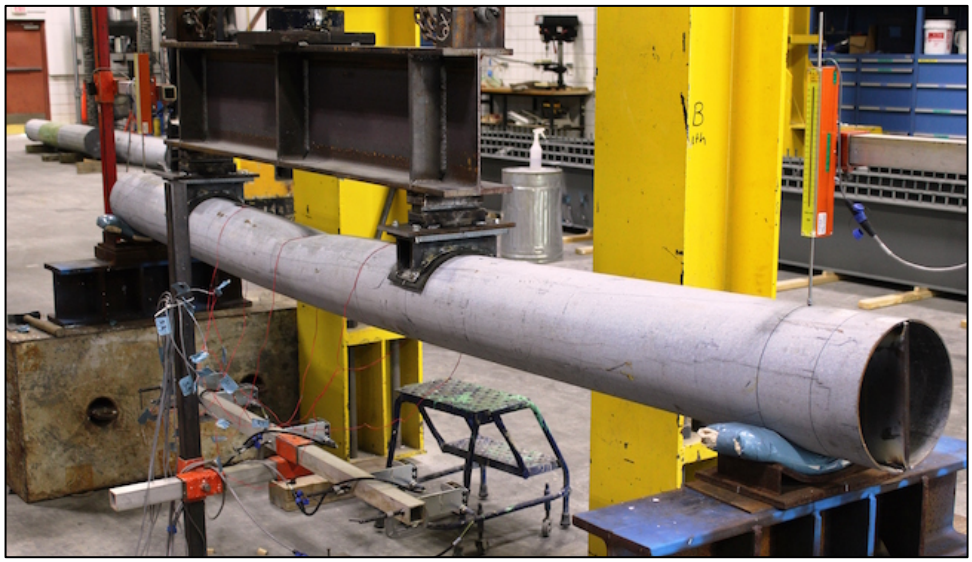

Figure 73. STu-1.d failed shape

4.1.3.5 STu-1.e

Pole STu-1.e is a 12-sided monopole with a diameter ranging from 8.75 in to 11.88 in. The pole was dented to a depth of 1.75 in, or 18.7% of the outer diameter. The pole is shown in the test setup before loading in Figure 74. The pole was loaded to 45.7 kips before failing. This value is approximately 46% of the theoretical undented pole capacity. The maximum moment experienced by the pole at the section of the dent center was 64.4 kip-ft. The load-strain and load-displacement data is plotted in Figure 75.

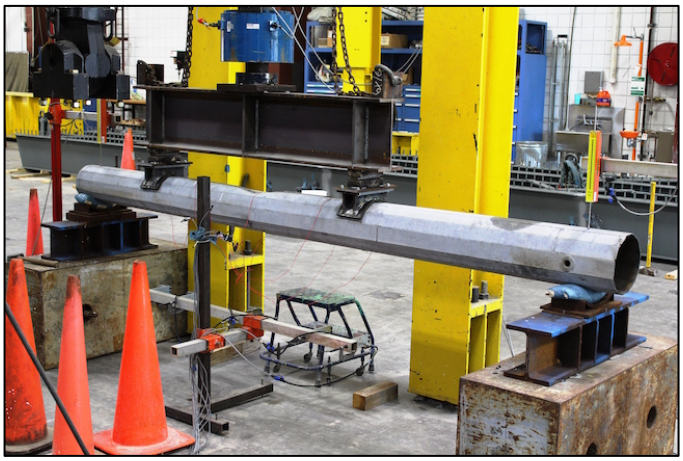

Figure 74. STu-1.e test setup

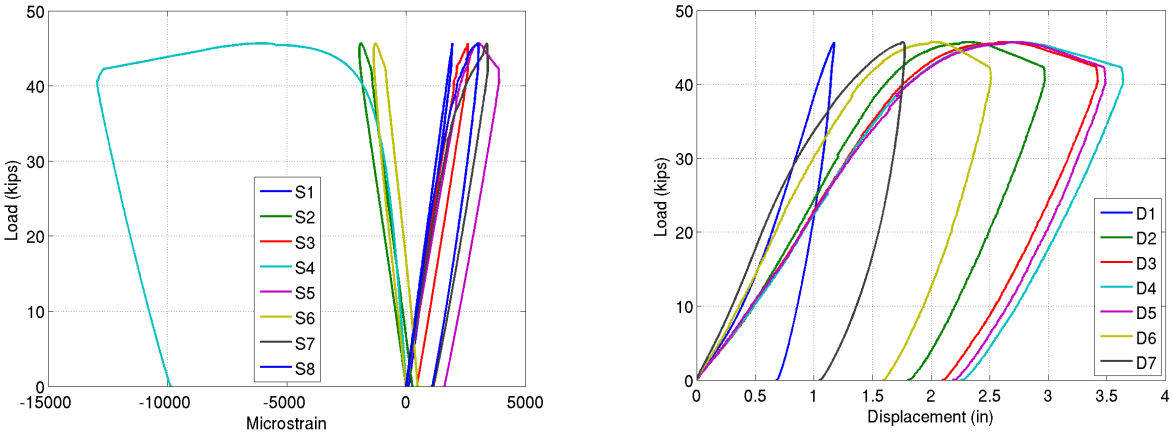

(a) Load vs. strain **(b) Load vs. displacement**

Figure 75. STu-1.e test data

The maximum displacement of this pole was 3.64 in, and occurred at the dent section. The extreme strain data, as can be seen in Figure 75 (a), were -12954 με in compression, and 3885 με in tension. The compression strain was more than three times greater in magnitude than the tensile strain. This indicates that the dented region underwent large local deformations before the tension face yielded. The final failure mode is shown in Figure 76.

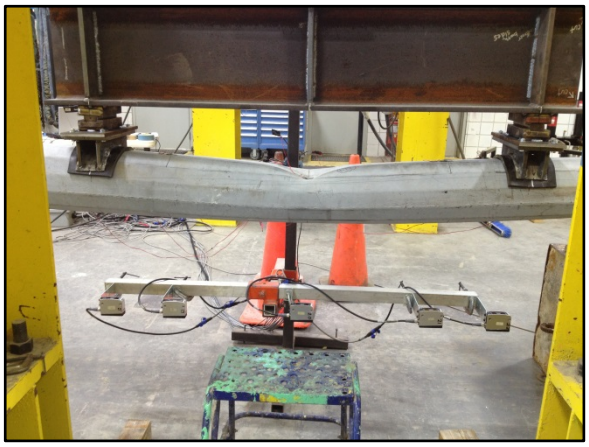

Figure 76. STu-1.e failed section

4.1.3.6 STu-1.f

Another monopole, STu-1.f has 18 sides and a diameter ranging from 10.25 in to 15 in. The applied dent had a depth of 2.375 in, or 21.7% of the outer diameter. The test setup is shown in Figure 77. The new capacity of the dented pole was measured as 60.1 kips, or 84.7 kip-ft. This load is about 42% of the undented pole capacity. The measured test data are plotted in Figure 78.

Figure 77. STu-1.f test setup

The maximum displacement induced in this pole was measured at D4 to be 1.91 in. The extreme compressive strain of -7278 με occurred at gauge S4, within the dent. The gauge S5 failed and produced no data for this test. The failure mode of this pole was plastic hinging at the section of the deepest dent depth, as is shown in Figure 79.

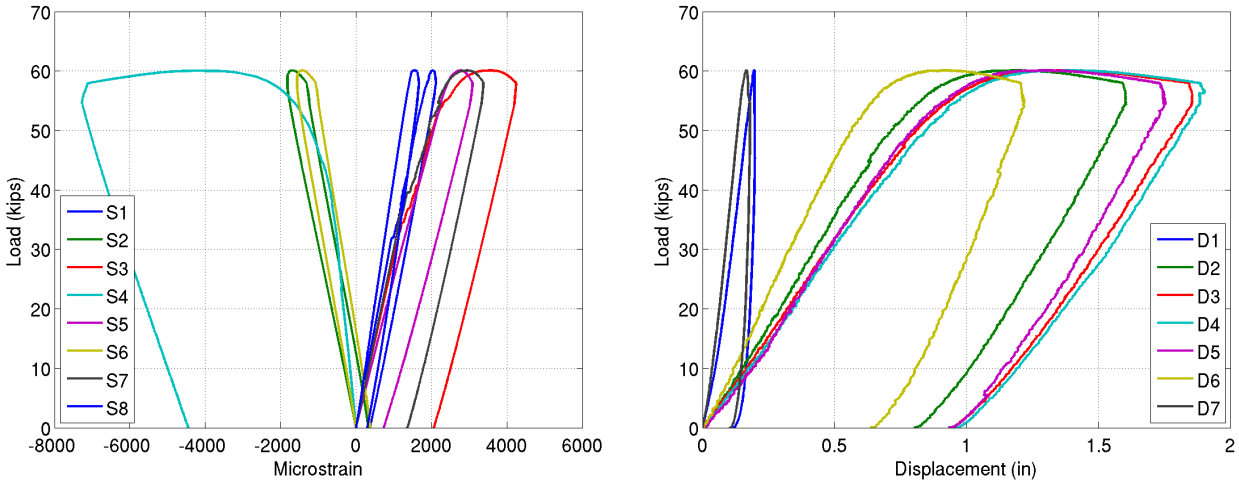

(a) Load vs. strain **(b) Load vs. displacement**

Figure 78. STu-1.f test data

Figure 79. STu-1.f failed pole section

4.1.3.7 STu-2.a

Two undented control pole sections, STu-2.a and STu-2.b were tested in addition to the dented poles discussed above. Pole STu-2.a is a round pole with a diameter of 10.83 in at the center of loading, or the location that a dent would have been applied. The test setup is shown in Figure 80. The pole held a peak load of 56.2 kips. The carried load is approximately 75% of the theoretical bending capacity. The reason for the lower capacity is that the pole failed in local buckling at the northern load application point, as is shown in Figure 82. The loading data is shown in Figure 81. The maximum displacement in this pole was measured as 1.31 in at gauge D4. The extreme strains were 4596 με in tension at the gauge S5 at the center of loading, and -2062 με in compression at gauge S2 located just south of the northern load point. The data taken from gauge S5 shows a sudden increase in strain at approximately 45 kips. This indicates a localized yielding of the steel at tension face center of loading.

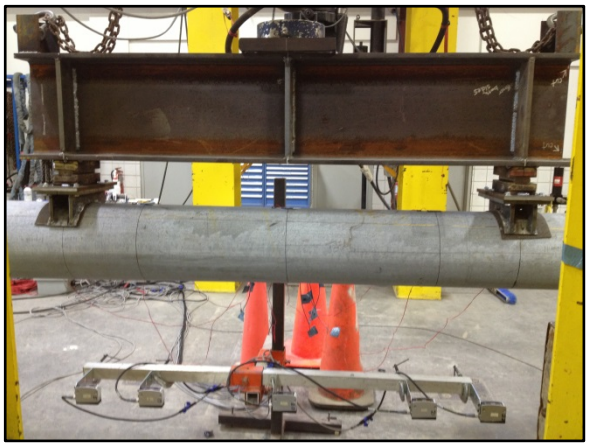

Figure 80. STu-2.a test setup

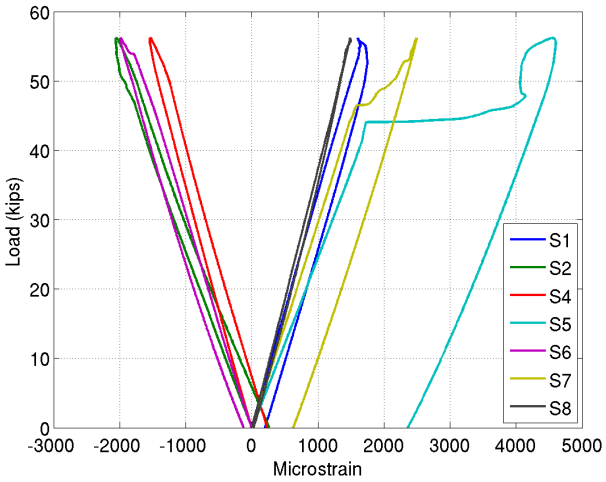

(a) Load vs. strain

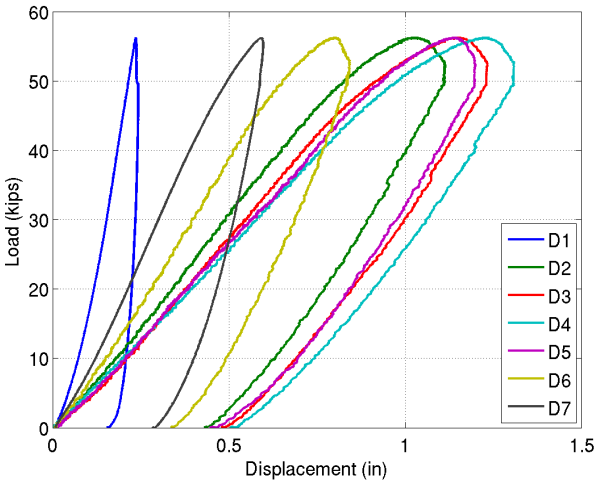

(b) Load vs. displacement

Figure 81. STu-2.a test data

(a)

(b)

Figure 82. STu-2.a failure

4.1.3.8 STu-2.b

The second undented pole to be tested was an 18-sided pole with a diameter of 8.71 in at the center of loading. The load carried by this pole was measured as 56.2 kips, or 79.2 kip-ft at the failure location. The test data for this test are shown in Figure 83. Again, this specimen failed in local buckling at the northern load application point at about 60% of the theoretical capacity. The failed specimen is shown in Figure 84. The extreme strains and displacement occurred at the section just south of the northern load point. These measurements, from gauges S2, S3, and D3, are -2345 με, 4283 με, and 2.06 in, respectively.

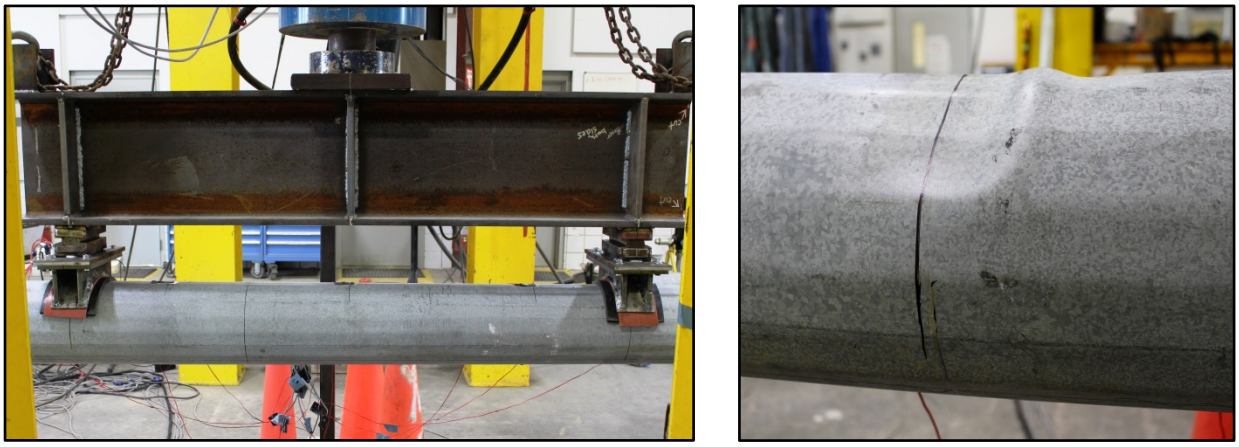

(a) Test setup **(b) Local buckling failure**

Figure 83. STu-2.b testing and failure

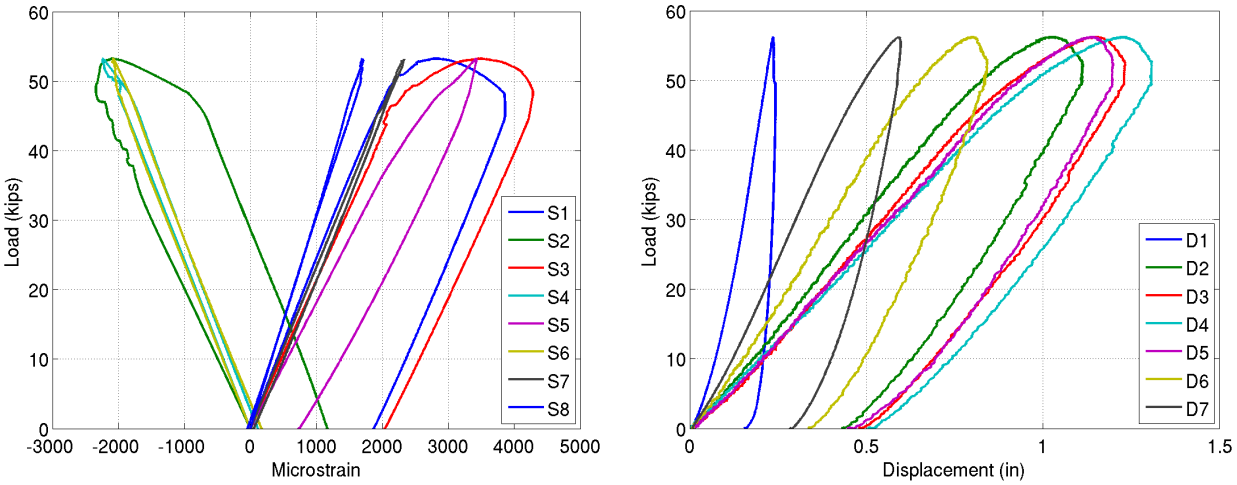

(a) Load vs. strain **(b) Load vs. displacement**

Figure 84. STu-2.b test data

4.1.4 Summary Damage Determination Test Results

Because of the various geometries of the pole sections tested for damage quantification, the test results can be synthesized through the non-dimensional quantity of the stress factor, F_σ. This

factor is calculated from the peak experimental moment experienced and the undamaged section modulus at the location of denting, or at the location of pole failure if different from the dent location, and the yield stress of the pole material. This factor minimizes the effects of varying geometry between the different pole specimens. However, such a stress factor analysis is not independent of the diameter of the pole (theoretically, it is analogous to the plastic moment over the yield moment). Therefore, the stress factors were then normalized by the theoretical maximum value for an undented pole. The resulting normalized factor is shown in the equation below.

$$F_\sigma = \frac{M_u}{Z\sigma_y} \tag{4-1}$$

Table 16. Damage determination result summary

Pole ID	Section Geometry	Dent Depth (%)	Normalized Stress Factor	Failure Mode
ALu-1.a	Round	5.0	0.83	Hinging
ALu-1.b	Round	13	1.00	Hinging
ALu-2.b	Round	26	0.66	Hinging
ALu-4.a	Round	-	1.02	Local Steel Buckling
STu-1.a	Round	24	0.51	Hinging
STu-1.b	Round	22	0.47	Hinging
STu-1.c	Round	22	0.54	Hinging
STu-1.d	Round	14	0.75	Hinging
STu-1.e	12-sided	19	0.46	Hinging
STu-1.f	18-sided	22	0.42	Hinging
STu-2.a	Round	-	0.75	Local Steel Buckling
STu-2.b	18-sided	-	0.60	Local Steel Buckling

This stress factor has been calculated for each of the Damage Determination specimens, and is shown plotted for each of the aluminum specimens in Figure 85 against the dent depth as a percentage of the outer diameter. It is important to note when considering this data that the failure of pole ALu-4.a was likely accelerated by the effect of the steel load applicator creating a localized failure at the contact point with the pole. Considering the behavior of the dented poles illustrated by Figure 85, it was seen that a gradual decrease in the normalized capacity occurred in poles as the dent depth increased.

Similarly, the normalized stress factors for the steel poles tested are shown in Figure 86. Here, the various section geometries have been differentiated. As in the case of the aluminum poles, the steel control poles, ST-2.a and b, failed through localized buckling of the steel. This accounts for the low capacity values measured in these poles. It is apparent from this plot that denting had a more detrimental effect on the capacity of multi-sided poles than round steel poles. It is also evident that the capacity of damaged steel poles decreased as the depth of damage increased.

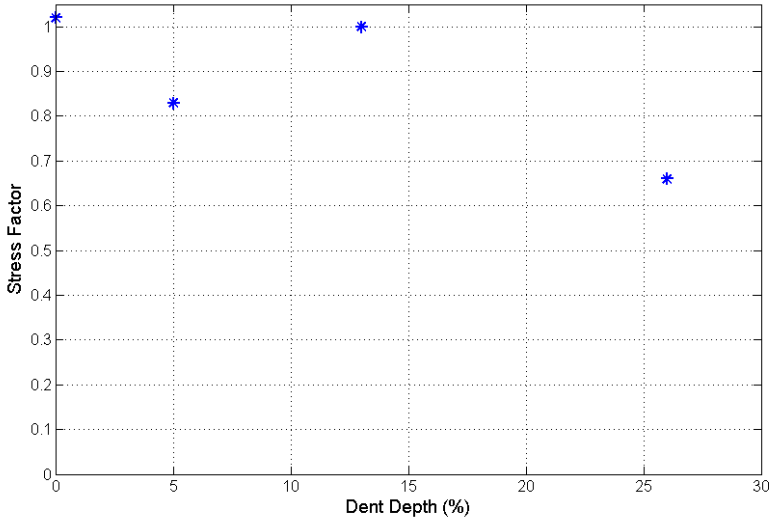

Figure 85. Aluminum damage determination normalized stress factor vs. dent depth

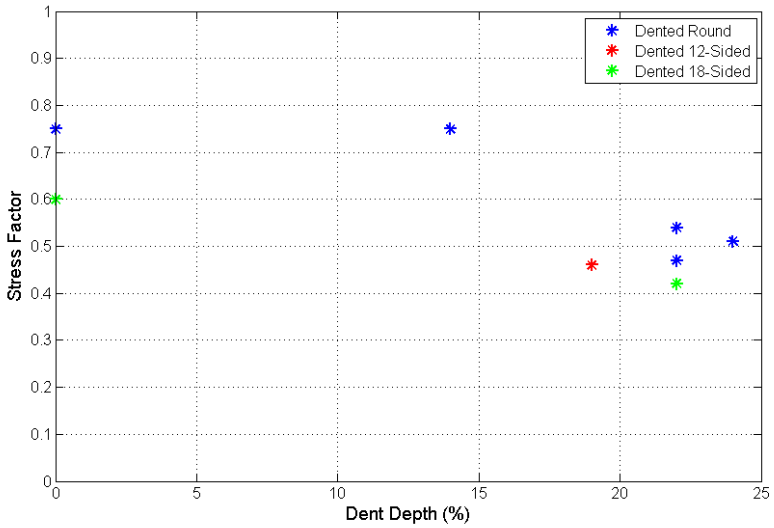

Figure 86. Steel damage determination normalized stress factor vs. dent depth

4.2 Single-Ply Tests

The Single-Ply tests were performed at the Marcus H. Ansley Structural Research Center in Tallahassee, FL using a similar test setup to the Damage Determination tests. The four-point bending test configuration is shown in Figure 51 and Figure 63 for aluminum and steel, respectively. The test setups are the same as the Damage Determination tests, only the location and numbering of strain gauges is different due to the presence of the FRP wraps.

4.2.1 Single-Ply Test Matrix

The Single-Ply wrap test specimens were repaired with a one layer wrap of three different FRP systems. The FRP systems selected were: (1) high density bi-directional glass fibers pre-impregnated with NRi polyurethane resin, (2) high density bi-directional basalt fibers pre-impregnated NRi polyurethane resin, and (3) pre-cured sheets of high density bi-directional glass fibers in QuakeBond epoxy resin. The objective of this set of tests was to determine the effectiveness of a uniform single layer of FRP repair. This information was then to be used in the design of repair wrap systems. The details of the Single-Ply test matrix are shown in Table 17. The span is the center-to-center distance between the supports. The large diameter and small diameter values are measured at the left (north) and right (south) supports, respectively.

Table 17. Single-ply test specimens

Pole ID	Section Geometry	Span (ft)	Large Diameter (in)	Small Diameter (in)	Diameter at Dent (in)	Dent Depth (in)	Dent Depth (%)	Repair System
ALw-4.b	Round	9	6.51	5.34	5.86	1.06	21	Glass/PU
ALw-5.b	Round	9	6.51	5.34	5.86	1.875	33	Fill Only
ALw-6.a	Round	9	5.73	4.56	5.00	1.50	30	Glass/EP
ALw-7.a	Round	9	5.73	4.56	5.00	1.25	25	Basalt/PU
ALw-8.a	Round	9	5.73	4.56	5.00	1.31	26	Glass/EP
STw-3.a	18-sided	11	15	13.75	14.63	3.25	22	Glass/EP
STw-3.b	Round	10.29	16	14.5	15.10	3.625	24	Basalt/PU
STw-4.c	Round	10.5	9.0625	7.5	8.49	2.50	29	Basalt/PU

4.2.2 Aluminum Substrate Tests

The aluminum Single-Ply specimens were prepared and tested at the Marcus H. Ansley Structural Research Center, and the test configuration, similar to that of the Damage Determination tests, is shown in Figure 87. Again, steel fabricated supports and load applicators were used, with neoprene or rubber linings. The locations of the displacement gauges and the 6-mm, 120-Ω strain gauges are indicated in the figure. The FRP wrap extends between the loading points for these tests. Although field repairs of damaged poles would not extend over such a long section, extending the wrap allows elimination of possible bond development length concerns and concentration on other failure methods. Five (5) aluminum Single-Ply tests were performed on fully or partially repaired pole sections. The results of these tests are presented in the following section.

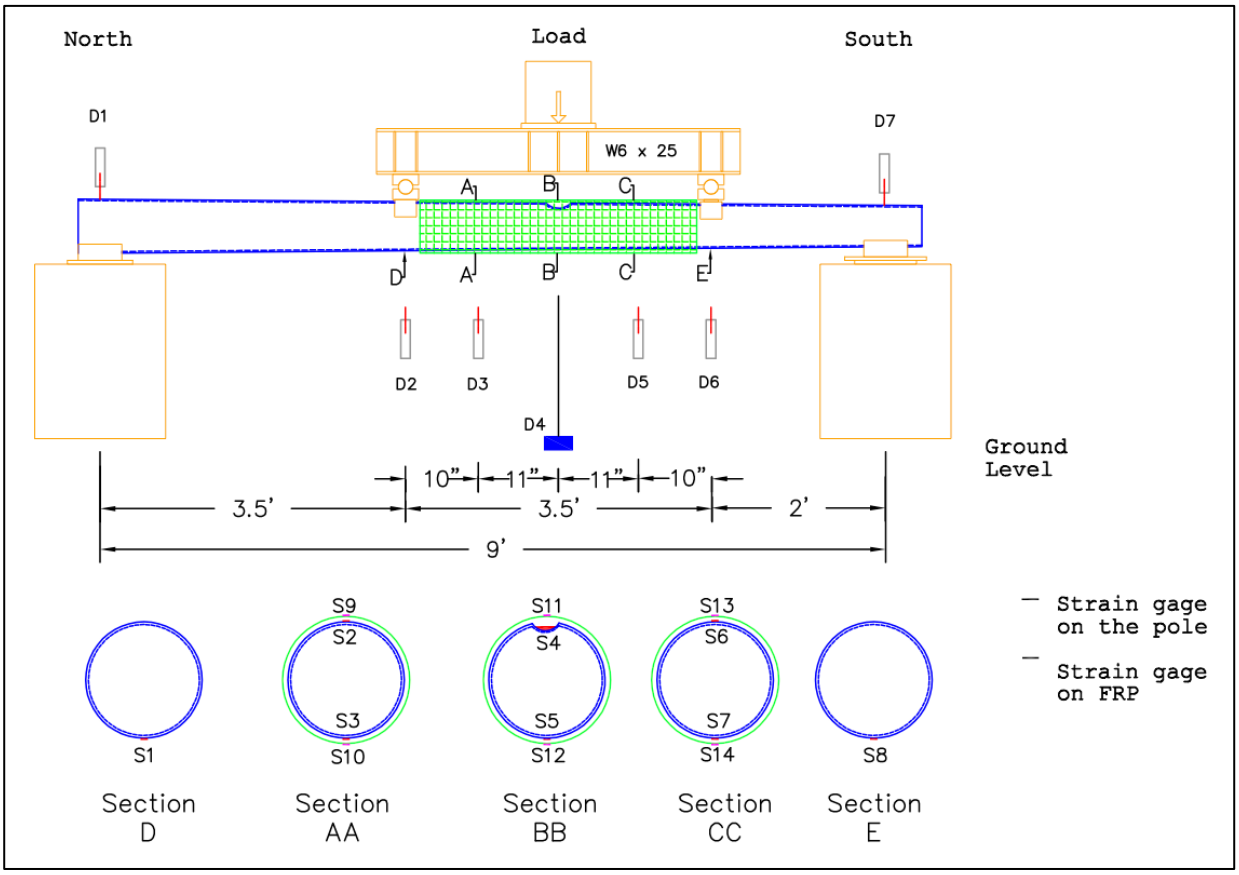

Figure 87. Aluminum single-ply test configuration

4.2.2.1 ALw-4.b

Pole ALw-4.b was dented to a depth of 25% of the outer diameter, or 1.25 in. This dent was filled with the viscous epoxy gel and was reinforced with a single layer of the glass fiber/polyurethane matrix composite according to the procedure outlined previously. The composite wrap extended to the edge of the load applicators.

The first attempt to test pole section ALw-4.b had to be aborted because the I-beam used to distribute the load from the MTS actuator to the two loading points experienced flange buckling under the applied load (see Figure 88). The pole was unloaded from a load of 15.1 kips, leaving a residual mid-span deflection of approximately 0.8 in. A new spreader beam was used to continue loading the pole to 17.7 kips (Figure 90). This load is approximately 188% of the theoretical capacity of an undented, unwrapped pole of the same geometry. This increase in capacity is quite extreme. It is possible that the thickness of the pole walls is inhomogeneous, and that the yielded section of the pole has a greater thickness than that measured at the ends of the pole segment. Variations in pole thickness have been noted in other poles, and this could account for the large measured capacity of this pole. As is shown in Figure 91, the residual strain and displacement from test 1 were added to the displacements measured in test 2. The strain values are taken from the gauges on the aluminum (S5) and composite (S12) surfaces on the bottom of the section at the midpoint of loading.

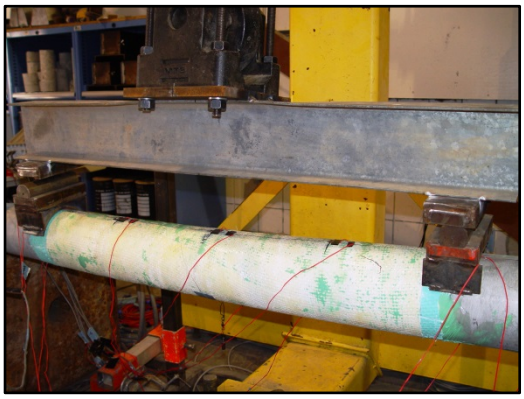

(a) Glass/polyurethane composite wrapped pole test

(b) Flange buckling of load spreader beam

Figure 88. ALw-4.b initial loading

(a) FRP buckling failure

(b) FRP buckling failure

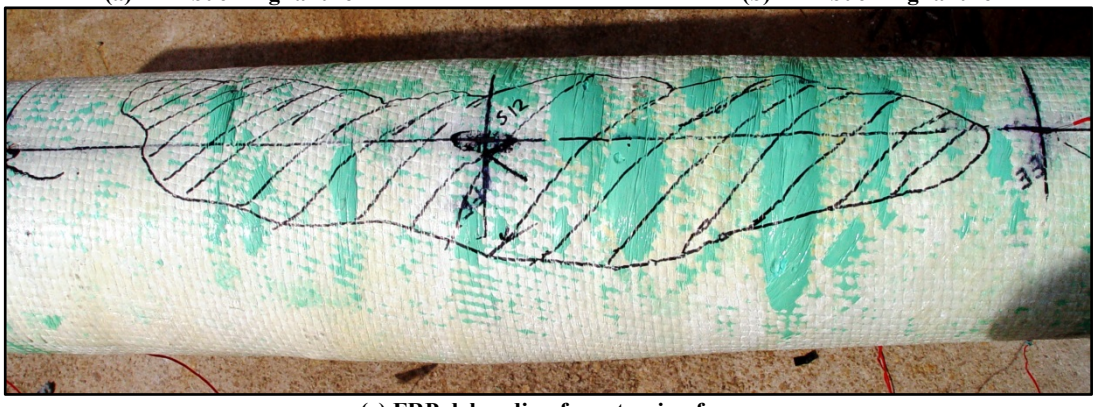

(c) FRP debonding from tension face

Figure 89. ALw-4.b failure modes

This yields maximum mid-span deflection, strain in aluminum, and strain in composite values of 4.4 in, 7361 με, and 4756 με, respectively. Fiber buckling was seen to have occurred on the compressive face of the pole at 1 in and 3 in from the dent center toward the small diameter end (Figure 89). Debonding of the fibers was noted on the tension side of the pole. The debonded area is shown in Figure 89. The strain profile plotted in Figure 92 during test 2, with gauges S6, S7, S13, and S14, shows that debonding of the tension face laminate occurs between 16 and 17 kips of applied load. It appears from this plot that the compressive wrap does not have a good bond from the beginning of the test, which is also the case from the beginning of test 1. However, the likely cause of the apparent lack of bond is the placement of gauge S13 directly

over gauge S6, which would cause a very localized bond weakness. The final failure of the pole occurred through plastic hinging at the dent location.

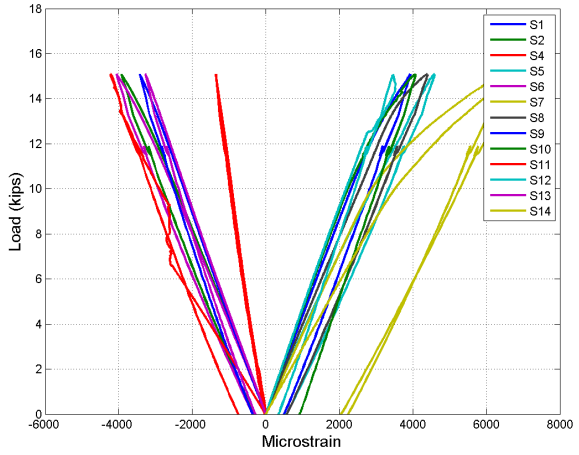

(a) Load vs. strain, Test 1

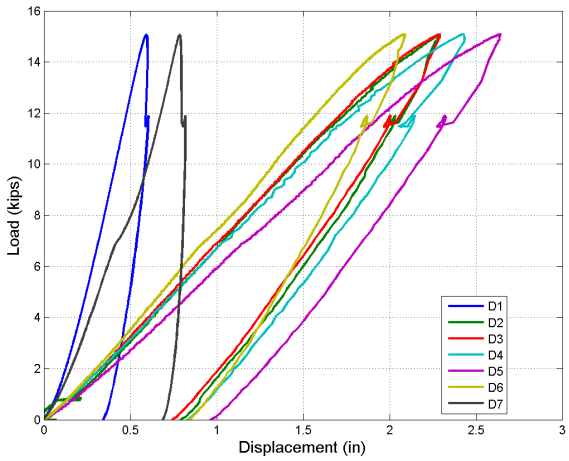

(b) Load vs. displacement, Test 1

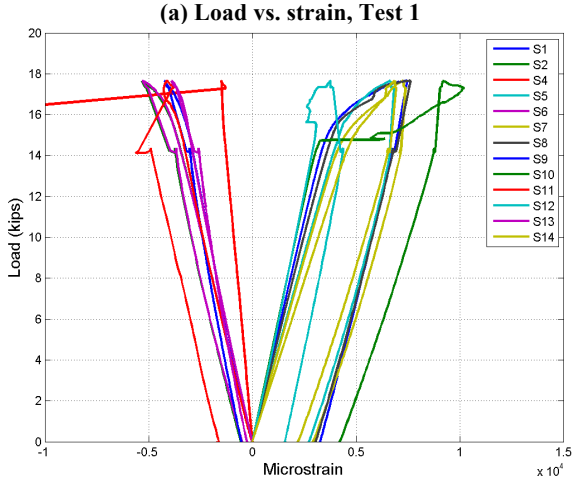

(c) Load vs. strain, Test 2

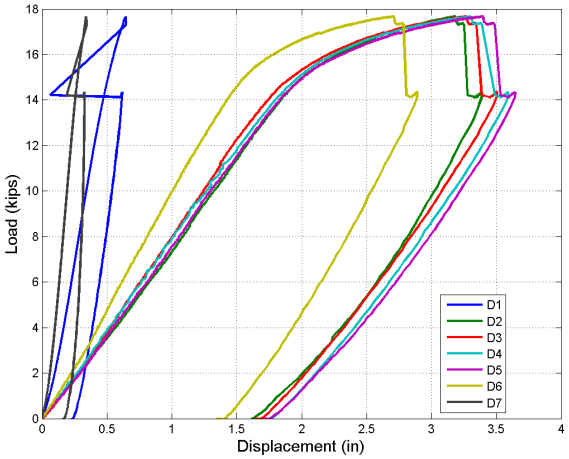

(d) Load vs. displacement, Test 2

Figure 90. ALw-4.b test data

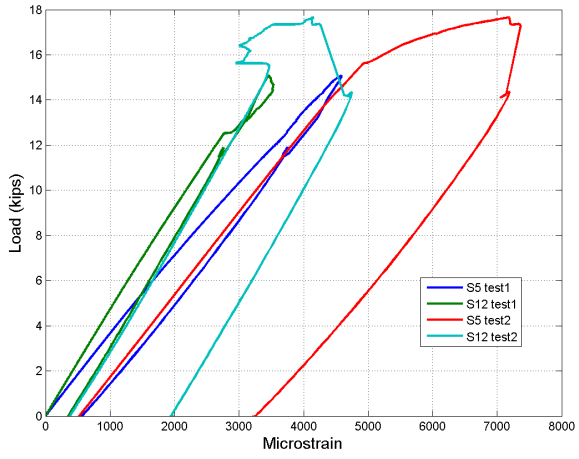

(a) Load vs. combined strain

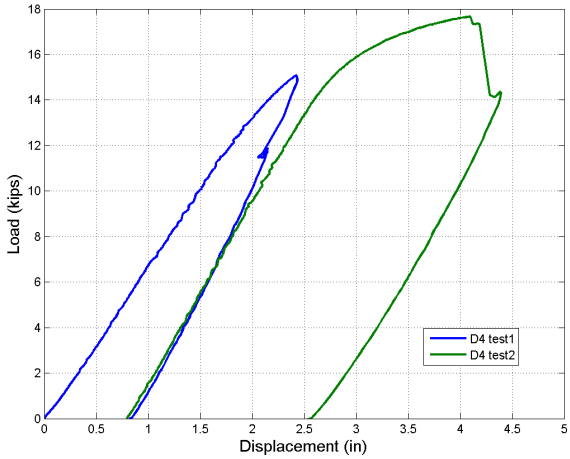

(b) Load vs. combined displacement

Figure 91. ALw-4.b combined test data

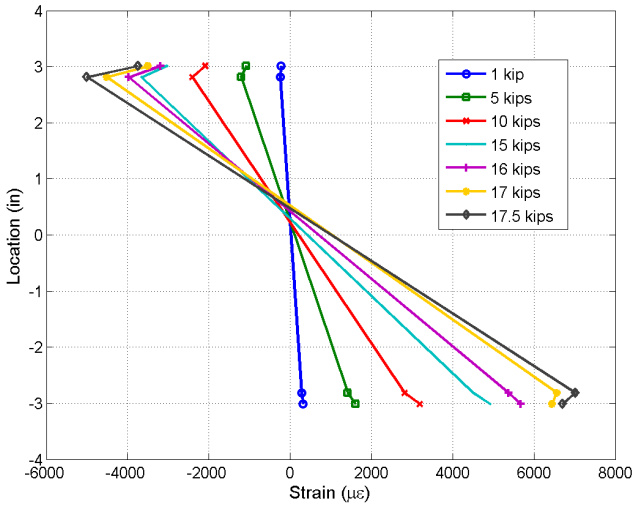

Figure 92. Progressive strain profiles at section CC' for pole ALw-4.b Test 2

4.2.2.2 ALw-5.b

The first of the Single-Ply tests to be performed, ALw-5.b, investigates the effect of the epoxy dent filler in restoring pole capacity, and therefore a composite wrap was not applied to this pole. The pole was tested with only the gel dent filler portion of the repair, as shown in Figure 93. The epoxy gel filler was wrapped in wax paper during curing in order to maintain a smooth, round fill surface. The depth of the dent for this pole was approximately 1.875 in, or 33% of the outer diameter.

Figure 93. ALw-5.b filled dent

The strain and displacement data from this test are plotted below. As can be seen from these plots in Figure 94, the maximum load sustained by this pole was approximately 11.6 kips. This load induces a moment of 15.2 kip-ft at the dent center. The point at which the fill material begins compressive failure can also be seen in Figure 95 (a). After this point, the mode of pole failure is plastic hinging at the dent, as can be seen in Figure 95 (b).

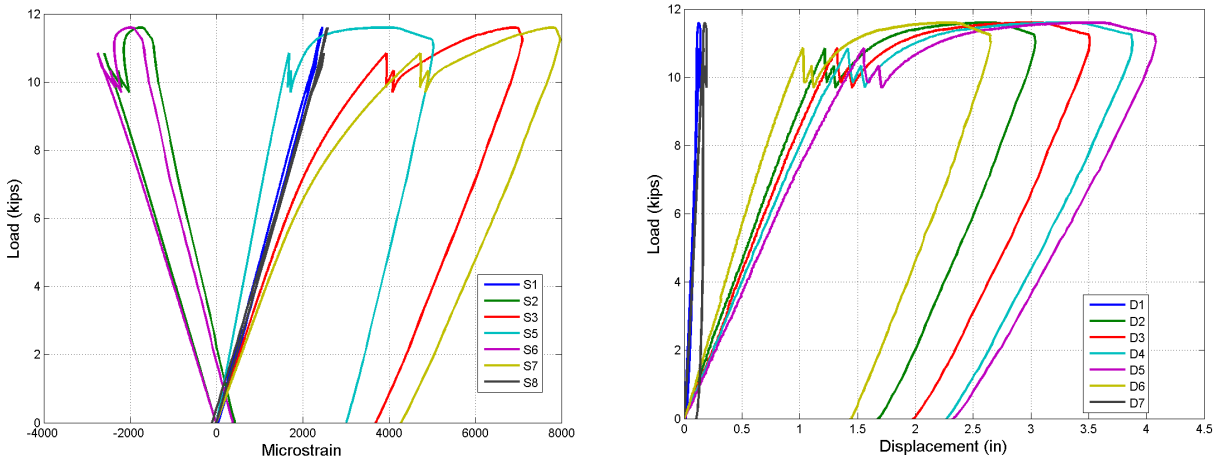

(a) Load vs. strain **(b) Load vs. displacement**

Figure 94. ALw-5.b test data

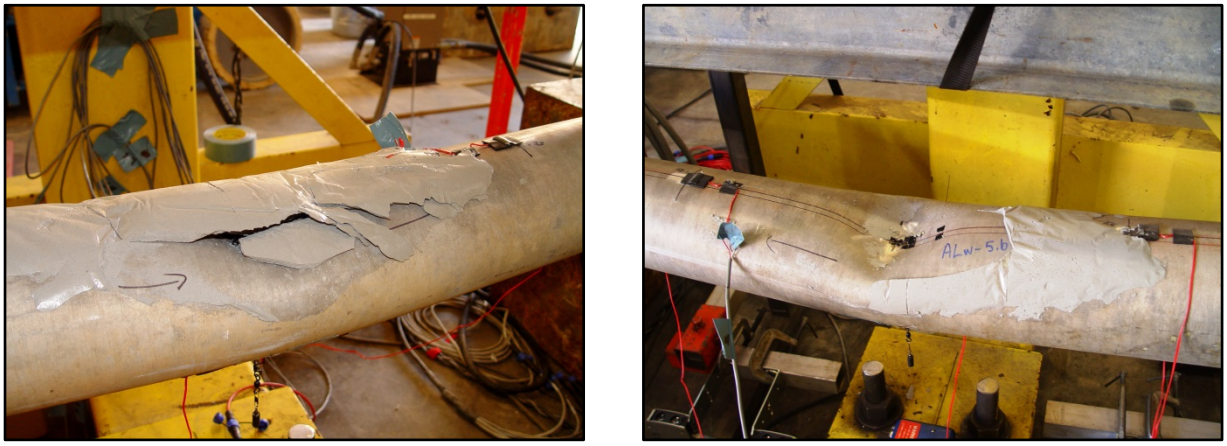

(a) Compressively-failed epoxy fill **(b) Aluminum plastic hinging failure**

Figure 95. ALw-5.b failure modes

4.2.2.3 ALw-6.a

This pole was wrapped with two layers of the glass/epoxy composite. The 1.5-in (30%) dent on this pole, however, was only partially filled with the QuakeBond Tack Coat epoxy, rather than the Sikadur gel. Several of the strain gauges underneath the FRP wrap were inoperable during testing. The data from the remaining strain and displacement gauges are plotted in Figure 96. The pole failed in a sudden rupture of the aluminum at the narrower end of the composite wrap. This location corresponds to the lowest bending moment within the loading region.

The maximum load sustained by the pole was 7.98 kip. This load created a bending moment at the dent location and at the rupture point of 10.5 and 9.64 kip-ft, respectively. The reason for the failure at this location can be seen in Figure 97. In parts (d) and (e) of this figure, the ruptured cross-section is shown, and it can be seen that two bolt holes have been drilled into this pole just under the composite wrap. These holes weakened the pole section at this location, causing the premature substrate failure. The ruptured section, pictured in Figure 97 (d), has an uneven wall thickness, which is thicker in many locations than the thickness of the pole that was measured before testing. This fact necessitates increasing the theoretical capacity of this pole. At a load of

approximately 7.25 kip, a small drop in load was detected, presumably due to the failure of the QuakeBond fill. Because of the incompleteness of the fill, the effect is not as great as that seen when the Pilgrim fill is used. However, the fill does contribute slightly to the structural stiffness. Although this test does not allow for quantification of the increase in pole capacity due to the FRP wrap because the failure occurred outside of the wrapped region, this data can be used to obtain a lower limit for the capacity of the dented region.

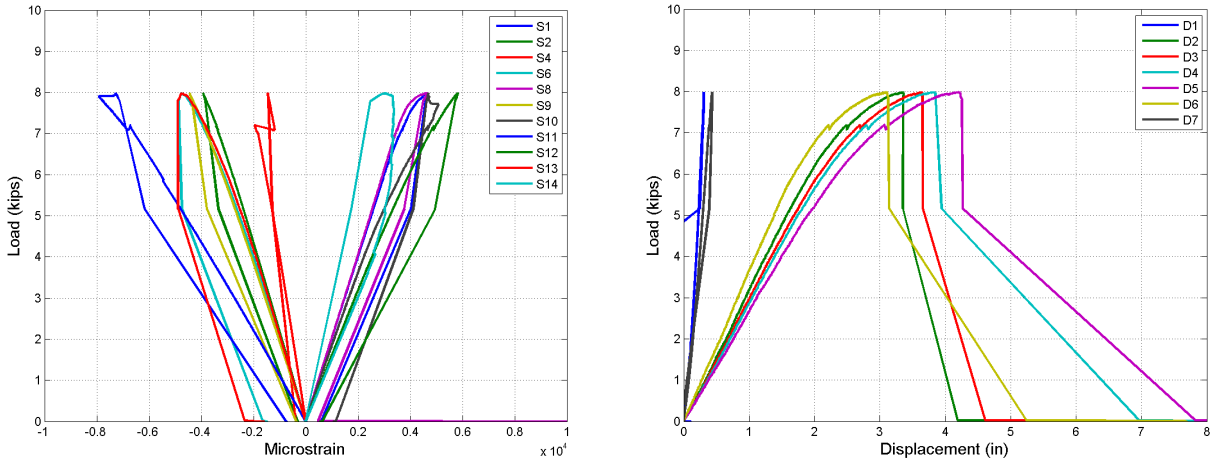

(a) Load vs. strain **(b) Load vs. displacement**

Figure 96. ALw-6.a test data

(a) Wrap and test configuration

(c) Rupture joint

(d) Ruptured section

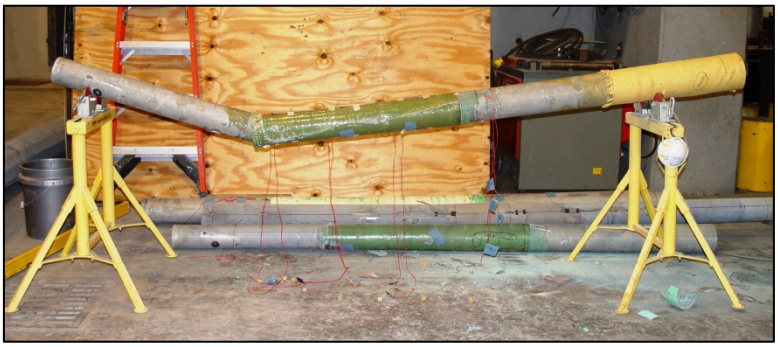

(b) Aluminum rupture failure

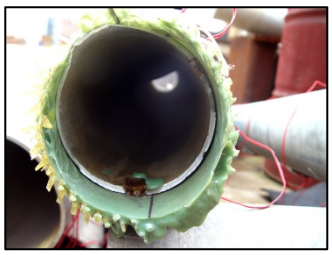

(e) Ruptured section

Figure 97. ALw-6.a testing and failure

4.2.2.4 ALw-7.a

Pole ALw-7.a was dented to a depth of 1.25 in, or 25% of the pole's outer diameter at the dent location. The dent was then filled, and the pole wrapped with a layer of basalt fiber/PU composite. Several strain gauges on this pole were not functional at the time of testing. The strain and displacement data that were gathered are shown in Figure 98. The fibers on the top of the pole buckled at several points, as is shown in Figure 100. Buckling was observed at the center of the dent, and 6-8 inches from the dent along the pole in both directions. Debonding of the fibers also occurred on the tension face.

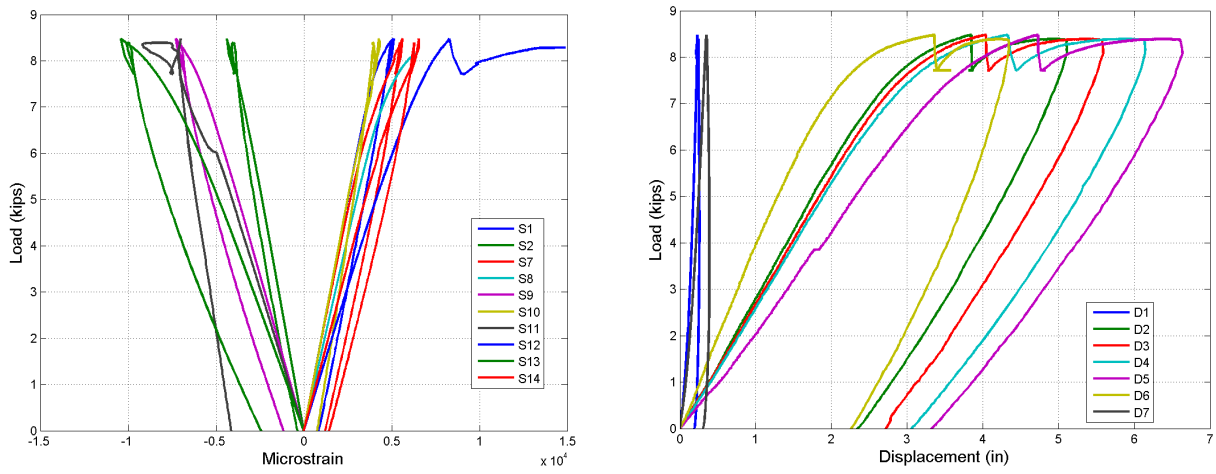

(a) Load vs. strain **(b) Load vs. displacement**

Figure 98. ALw-7.a test data

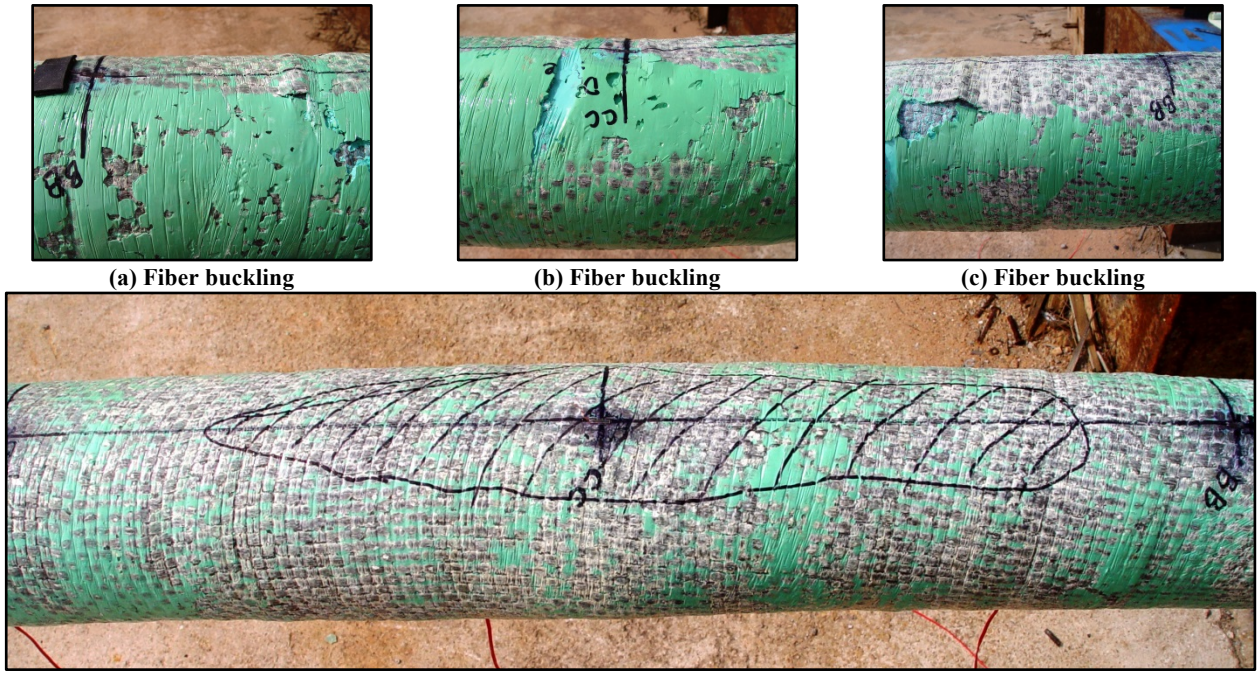

(a) Fiber buckling **(b) Fiber buckling** **(c) Fiber buckling**

(d) Debonded composite

Figure 99. ALw-7.a failure modes

The final pole failure was plastic hinging in the dented region. The capacity of the pole was measured as 8.48 kips. The maximum sustained moment was 11.1 kip-ft. A drop in the load occurred just after yielding of the pole section, as can be seen in Figure 98. A corresponding jump in the strain data at gauge S12, placed on the laminate surface over the center of the dent. This drop likely corresponds to the failure of the epoxy filler material, indicating that the fill material itself does not improve the strength of a composite wrapped section, except in its contribution to out-of-plane buckling resistance in the compressive reinforcing fibers. The compressive failure of the FRP laminate was first detected by strain gauge S11 at a strain value of approximately 9205 με, which is near to the compressive failure strain of -9300 με determined for this composite from material testing, as discussed in Chapter 3. Debonding behavior is detected by strain gauge S12, located at the dent center on the tension side of the pole. The final displaced shape of the pole after testing is shown in Figure 100.

Figure 100. ALw-7.a displaced shape

4.2.2.5 ALw-8.a

This single-ply specimen was wrapped with one layer of Glass/EP composite after being dented to a depth of 1.3125 in, or 26% of the outer pole diameter. When the wrap was applied to this pole, the wrap extended beyond the load application points for the pole. Therefore, the composite was cut with a rotary tool, and removed from the area under the load applicators. However, when the laminate was cut, the rotary disk penetrated deeper than intended, and etched a grove in the aluminum pole material at the south end of the wrap. Additionally, examination of the failed revealed that a bolt hole had been drilled into the substrate at this same location. When the pole was loaded, the reduced cross-section at this point caused the aluminum to rupture at a maximum load of 7.51 kips.

Strain and displacement data are shown in Figure 101. This failure load corresponds to a maximum moment at the dent location of 9.86 kip-ft. However, as the failure mode was aluminum rupture outside of the composite wrap, these values provide a minimum capacity of the repaired dent area. The strain measurements at the dent location at the time of aluminum rupture are 4513 με on the tension face and -1165 με on the compression face. When compared with the strain data for the other poles tested, these values are much lower than of the expected failure strains. This implies that, had ALw-8.a experienced a plastic failure at the dent, the capacity would have been much greater. The wrap and failure of pole ALw-8.a are shown in Figure 102.

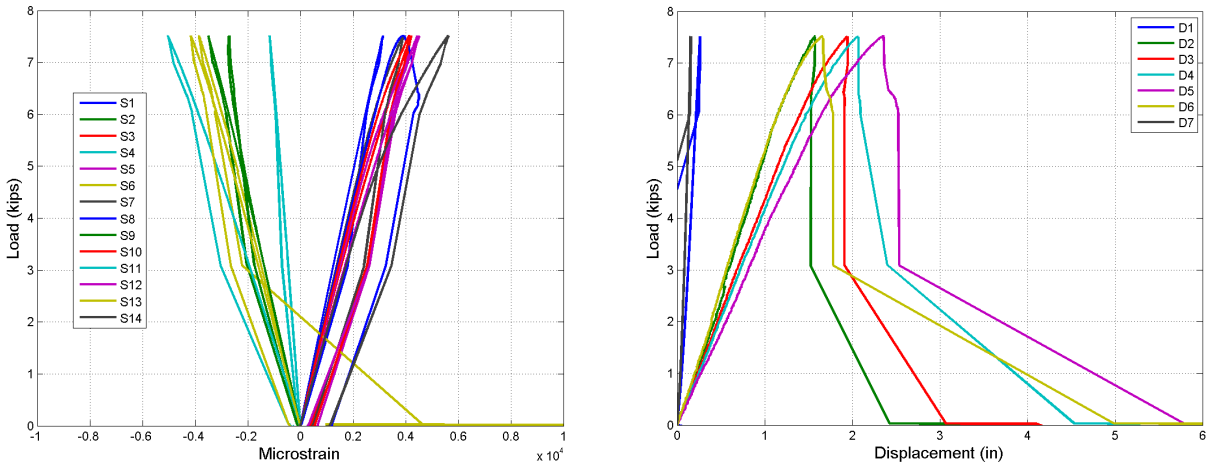

(a) Load vs. strain **(b) Load vs. displacement**

Figure 101. ALw-8.a test data

(a) Glass/QuakeBond epoxy composite wrap **(b) ALw-8.a failure**

(c) Aluminum rupture **(d) Ruptured surface**

Figure 102. ALw-8.a wrap and failure mode

4.2.3 Steel Substrate Tests

The steel Single-Ply tests were carried out in a similar manner to the previously discussed tests. Three pole sections were tested, one repaired with each of the three repair systems. The test configuration used for these tests is shown in Figure 103. Additional gauges were used in these tests to measure the strain behavior of the composite repair systems.

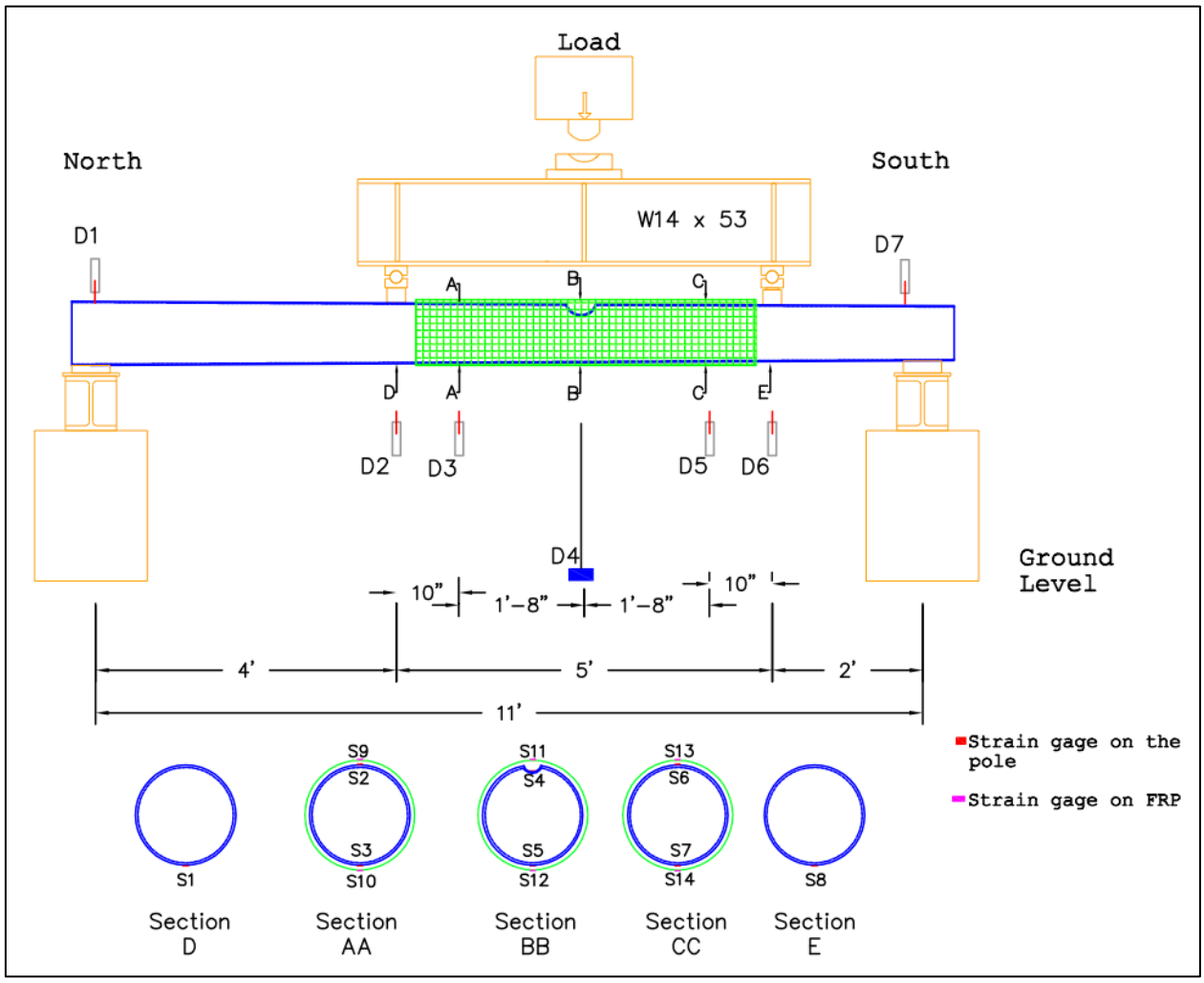

Figure 103. Steel single-ply test configuration

4.2.3.1 STw-3.a

The first of the steel Single-Ply poles to be tested, STw-3.a, is a monopole with 18 sides. The diameter increases from 13.75 in at the small end to 15 in at the large end. Circular end caps were used to reinforce the section. The applied dent has a depth of 3.625 in, which is 24% of the pole's outer diameter at the point of application. The pole section was repaired with a glass fiber/QuakeBond epoxy resin composite. The composite wrap extended beyond the dent to the load applicators, as with the aluminum Single-Ply tests. Before the wrap was applied, the dent was filled with the Sikadur 31 Hi Mod Gel epoxy. Because of the multi-sided shape of this pole, the pre-cured epoxy composite did not form perfectly to its surface. Voids between the pole surface and the composite existed at several points between the pole corners, as shown in Figure 104.

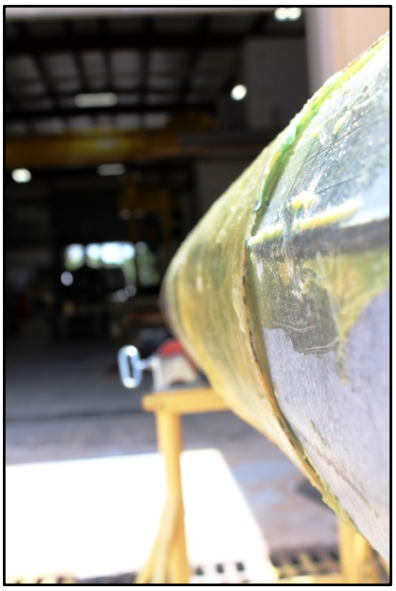

Figure 104. Voids between composite wrap and steel substrate

The data taken during testing is plotted in Figure 105. Most of the strain gauges that were intended to be applied to the steel substrate were not applied before the composite wrap. Therefore, only gauges S1 and S8 measured the strain in the steel. Gauges S2 through S7 were placed on top of the GFRP repair in the locations that they would have held on the steel pole, which are also the locations intended for gauges S9 through S14. Because some of these gauges were placed in areas where voids existed between the composite and the pole, additional gauges were placed near these gauges on portions of the wrap that appeared to have a good bond. Gauges S9 and 11 were placed just east of gauges S2 and S4, respectively, gauge S10 was placed just south of gauge S4, and S12 was placed just west of S6.

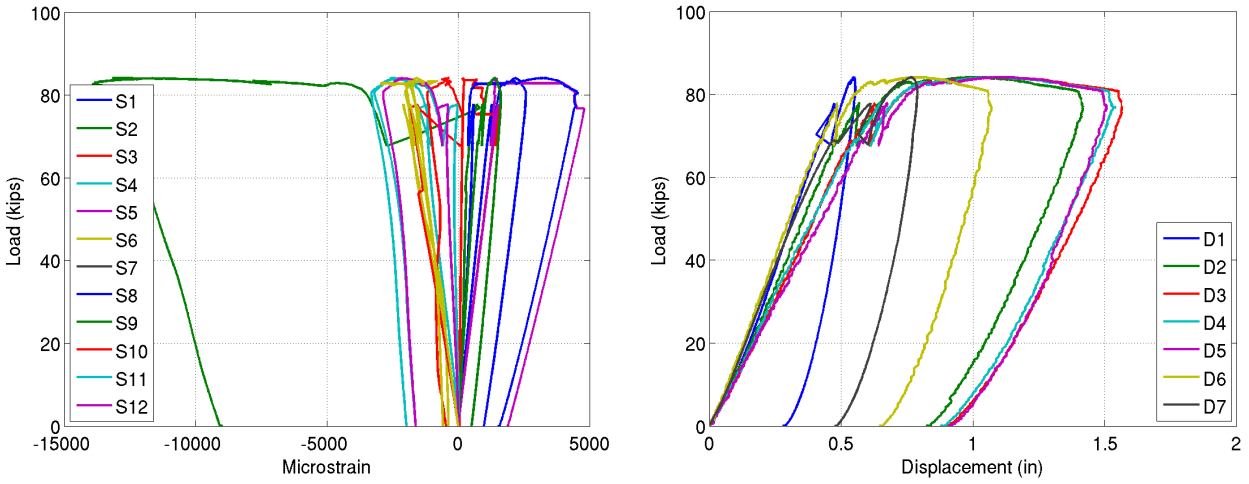

(a) Load vs. strain **(b) Load vs. displacement**

Figure 105. STw-3.a test data

The maximum load carried by this pole was 84.1 kips, or 118.5 kip-ft at the location of failure, or the location of the dent. Portions of the repair debonded from the tension side of the pole along the centerline, and major buckling of the fibers occurred 7 in to 18 in north of the dent center, as

can be seen in Figure 106. The final pole failure mode was plastic hinging near the center of the dent. The maximum deformation measured during this test was 1.57 in. This pole underwent extended deformation at or near the peak load before the load began to decrease, as compared to the unrepaired poles. This was likely aided by the confinement provided by the FRP repair.

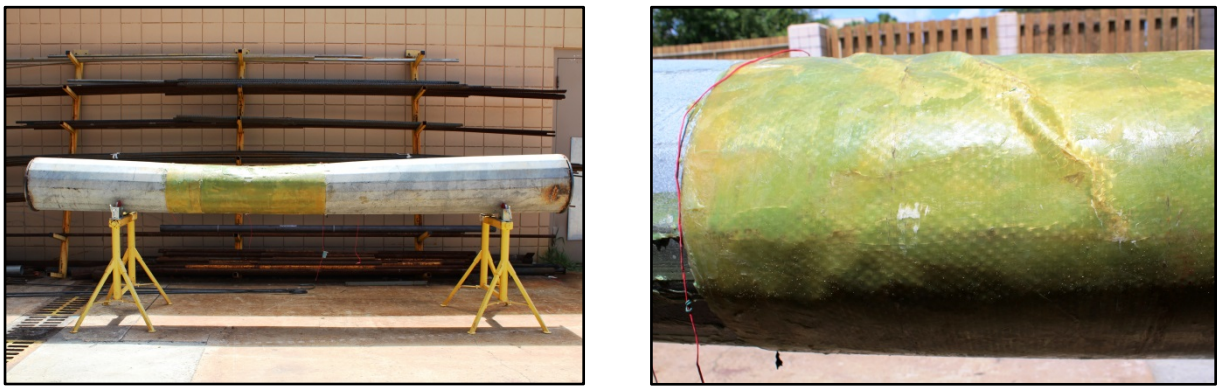

(a) Plastic hinging at dent **(b) Compressive fiber buckling**

Figure 106. STw-3.a failure modes

4.2.3.2 STw-3.b

Pole STw-3.b was larger in diameter than STw-3.a and had a round cross-section. The diameter at the center of the dent was 15.10 in, and circular steel plates were welded to the section ends to reinforce pole against local failure at the supports. A 3.625 in, or 24% dent was induced in this pole, and it was repaired with a basalt/polyurethane composite wrap, as can be seen in Figure 107. The pole was slightly shorter than the other steel single-ply specimens, and therefore the test setup was modified slightly by decreasing the total span. The data taken during loading is plotted in Figure 108.

Figure 107. STw-3.b repaired section in test setup

The maximum load sustained by this specimen was 66.7 kips, which corresponds to a maximum bending moment of 94.1 kip-ft at the dent. The pole collapsed locally at the south support before yielding occurred in the wrapped region. The maximum strains occurred in the FRP repair near the edges of the wrap in gauges S9 (-8381 με) and S14 (4643 με). The maximum displacement was measured with gauge D7, located above the south support as 1.46 in. At about 45 kips, the

strain in the FRP began to increase more rapidly as the repair resisted the collapse of the pole's cross-section.

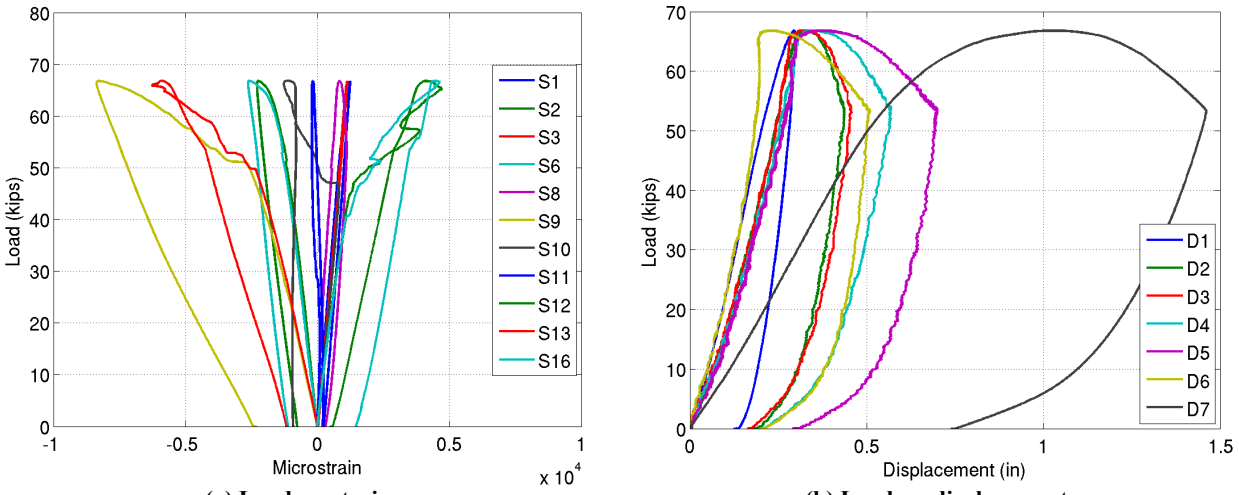

(a) Load vs. strain **(b) Load vs. displacement**

Figure 108. STw-3.b test data

4.2.3.3 STw-4.c

The final pole to be tested, STw-4.c, was dented to 29% of its outer diameter. The dent was applied at a point in the pole where a hole had been cut to allow for a crosswalk button to be placed, as shown in Figure 109. A barrier was placed over this opening when the dent was filled in order to prevent the fill epoxy from flowing into the pole. The diameter of the pole at the dent center was approximately 8.50 in. The filled dent area was wrapped with a basalt/polyurethane composite repair as shown in Figure 109. When the pre-preg wrap materials were opened, it was found that portions of the resin had partially cured in the packaging. The wrap was shaped to the pole as closely as possible, but the cured portions of the wrap did not allow a clean application.

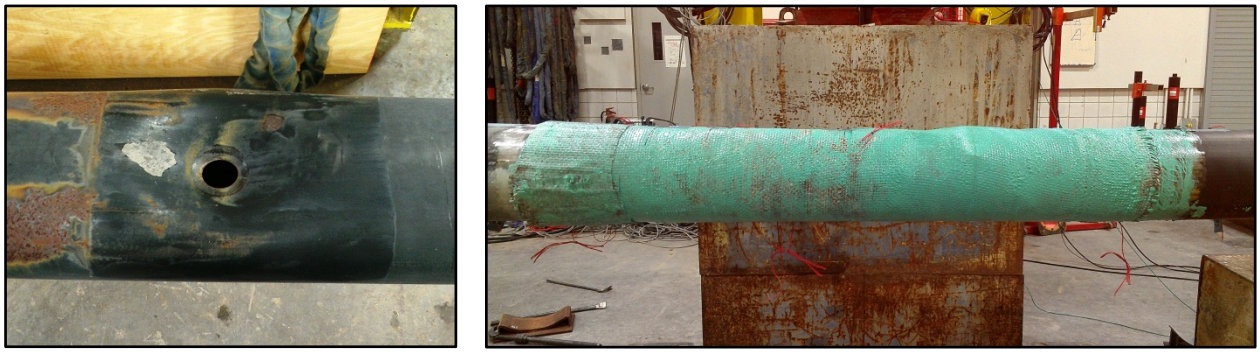

(a) STw-4.c dent over button opening **(b) STw-4.c composite wrap**

Figure 109. STw-4.c dent and composite wrap

Pole STw-4.c was loaded in the same manner as the previous steel Single-Ply tests, and the data taken during loading is shown in Figure 110. The capacity of the dented and repaired pole was measured as 32.2 kips, or 45.4 kip-ft at the center of loading. The maximum displacement in the pole was measured at D4, or the center of loading, to be 3.43 in. The extreme strains in the steel were measured at sections AA and CC. Gauges S2 and S6 measured maximum compressive

strains of approximately -1575 με. Similarly, the maximum tensile steel strains were measured with gauges S3 and S7 to be approximately 3700 με. The compressive steel gauge at the dent, gauge S4, failed to produce data for this test. In the FRP, the extreme strains were measured at gauges S12 and S13 as 8190 με and -4900 με, respectively.

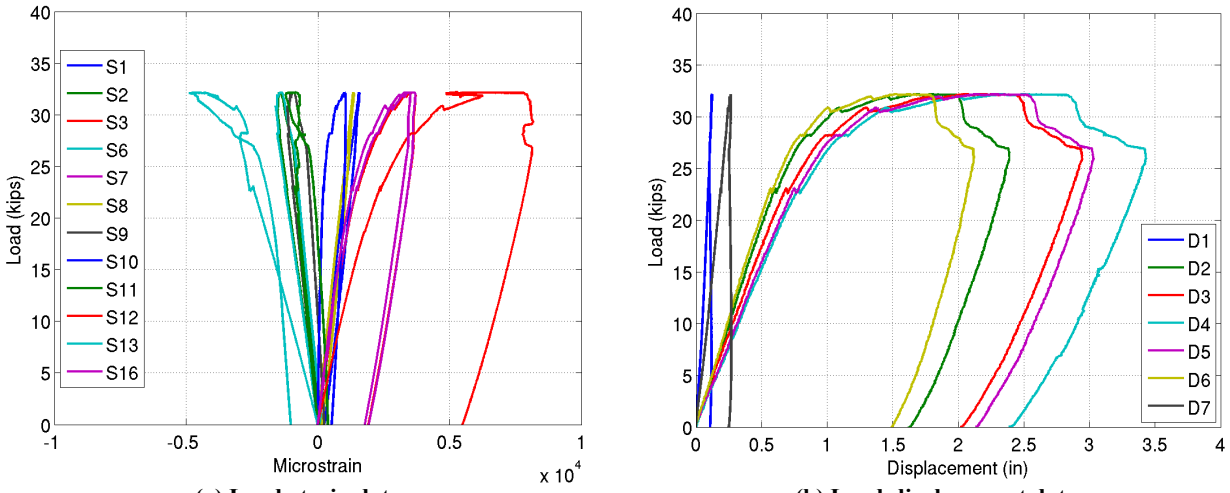

(a) Load-strain data **(b) Load-displacement data**

Figure 110. STw-4.c test data

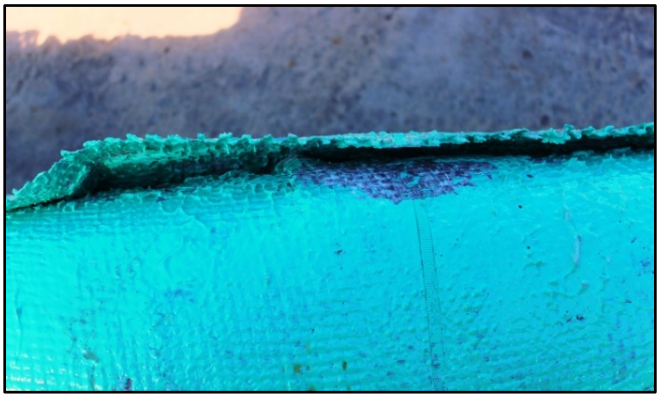

(a) Broken seam of FRP wrap

(b) Torn FRP wrap under load applicator

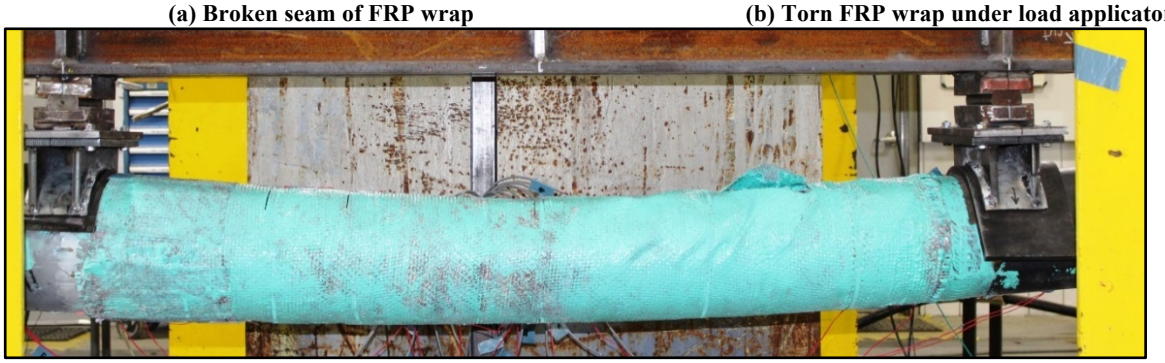

(c) Hinged pole section

Figure 111. STw-4.c failure modes

Several factors contributed to the ultimate failure of this pole section. The partially pre-cured composite wrap did not form perfectly to the pole's surface, and the as the pole deformed the

seam of the wrap pulled apart, as is shown in Figure 111. Also, the brittle wrap tore underneath the load applicator. Finally, the epoxy fill material buckled, and the pole hinged at the dent.

4.2.4 Summary of Single-Ply Test Results

The results of the Single-Ply tests are processed and presented in a similar manner to that of the Damage Determination tests. The normalized stress factors, computed using Equation 4-1, are shown in Table 18 for each of the Single-Ply test specimens. The failure mode of each pole is also listed. While most poles finally failed through plastic hinging of the substrate, various failure behaviors of the composite wrap and other repair materials are noted. It is important to note the failure modes of each specimen when considering the numerical results. For example, poles ALw-6.a and 8.a failed through rupture of the aluminum substrate outside of the wrapped region. Therefore, these results provide the lower-limit capacity of the repaired sections, rather than giving the increase in strength provided by the wraps.

The additional failure modes listed, debonding and compressive buckling of the FRP, both occur more suddenly than hinging failure in the substrate. This should be considered in the design of full-scale repair systems. Analysis of pole ALw-4.b produced a stress factor of 1.88. However, this is likely due to variations in the thickness of this pole from the measured thickness, rather than reflecting an actual capacity increase of 88%. Based on this result, it is estimated that the actual thickness of the pole section was approximately 0.3125 in, rather than 0.1875 in. If this is the case, then the actual stress factor would be approximately 1.18, which is more consistent with the results from the other Single-Ply tests.

Table 18. Single-ply result summary

Pole ID	Section Geometry	Dent Depth (%)	Repair System	Normalized Stress Factor	Failure Mode
ALw-4.b	Round	21	Glass/PU	1.88	Debonding/Hinging
ALw-5.b	Round	33	Fill Only	0.97	Hinging
ALw-6.a	Round	30	Glass/EP	0.87	Aluminum Rupture
ALw-7.a	Round	25	Basalt/PU	0.92	Fiber Buckling/Hinging
ALw-8.a	Round	26	Glass/EP	0.81	Aluminum Rupture
STw-3.a	18-Sided	22	Glass/EP	1.10	Fiber Buckling/Debonding/Hinging
STw-3.b	Round	24	Basalt/PU	0.81	Steel Local Buckling
STw-4.c	Round	29	Basalt/PU	1.27	Debonding/Hinging

The wrapped steel pole stress factors are also shown in Table 18. The 18-sided pole, STw-3.a, has a normalized stress factor of 1.10, which indicates that the glass/pre-cured epoxy wrap effectively restored the capacity of the damaged pole. The round steel poles repaired with the basalt/polyurethane composite, STw-3.b and STw-4.c, give stress factor measurements of 0.81 and 1.27, respectively. The lower-capacity pole, STw-3.b, failed in local buckling of the steel at the support, which accounts for the relatively low increase in capacity.

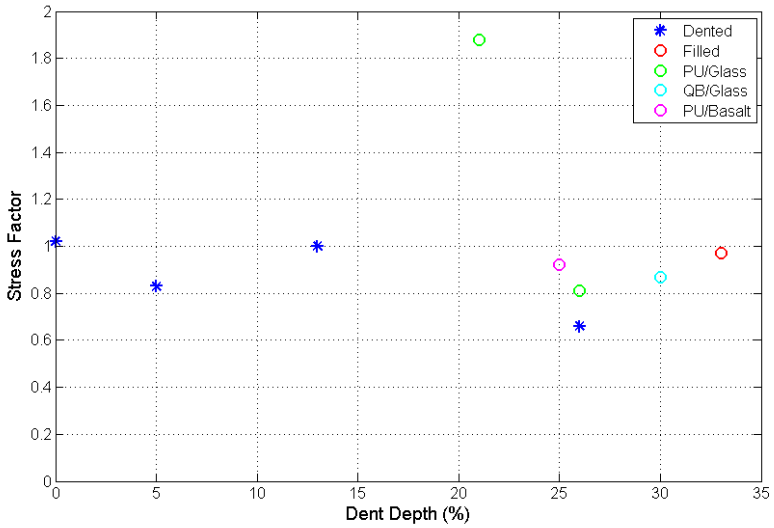

Figure 112. Aluminum single-ply normalized stress factor vs. dent depth

The normalized stress factors have been plotted for the aluminum and steel poles in Figure 112 and Figure 113, respectively. The data points from the Damage Determination tests have also been included for reference. It is apparent from each of these plots that the single-layer FRP composite wraps are able to effectively improve the capacity of damaged metallic pole sections. From these results, it is determined that the majority of dented utility poles can be restored to their full capacity with a single- or double-layer composite repair.

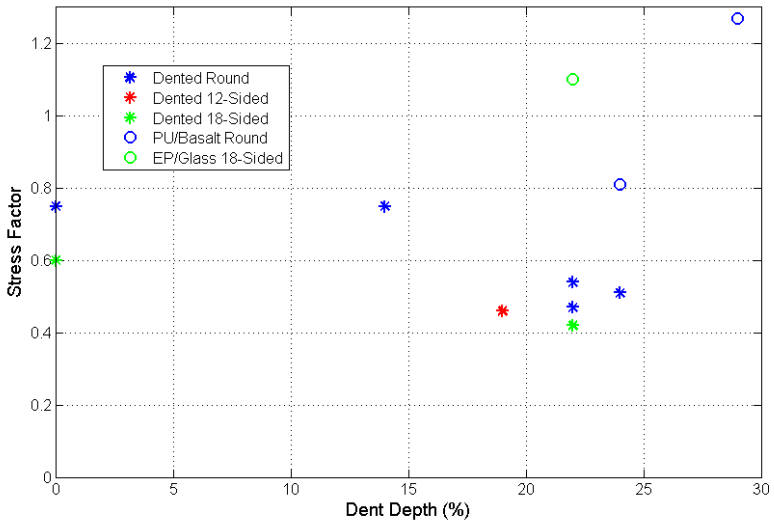

Figure 113. Steel single-ply normalized stress factor vs. dent depth

4.3 Wrap Configuration Tests

The final set of component-level tests performed in this project was the wrap configuration test. This set of test involved testing 14 tapered, undented steel utility pole sections in a four-point

loading configuration. Seven different wrap configurations were included in the test matrix, shown in Table 19. The objective of these tests was to make a more detailed investigation into the mechanics of FRP repairs of metallic pole structures. Each of the wrap configurations listed in Table 19 was designed to isolate, as closely as possible, one element of a composite repair in order to investigate its contribution to the overall repair effectiveness. The purpose was not to obtain an increased pole capacity, but rather to monitor and understand the FRP load transfer and failure. An understanding of these mechanics will allow the development of more efficient, cost-effective composite repairs.

Table 19. Wrap configuration test specimens

Pole ID	Repair System	Diameter (in)		Wrap Configuration
		North Support	South Support	
ST-13	Basalt/PU	6.25	7	Transverse Strips
ST-17.a	Basalt/PU	7.1875	8.5	Tension Face
ST-17.b	Basalt/PU	7.8	8.625	Compression Face
ST-19.a	Basalt/PU	6.375	7.625	Compression/Transverse
ST-19.b	Basalt/PU	6	7.25	Compression/Transverse
ST-20.a	Basalt/PU	6.5	7.75	Tension Face
ST-20.b	Basalt/PU	7.1	8	Neutral Axis
ST-21.b	Basalt/PU	8.22	9.06	Neutral Axis
ST-25	Basalt/PU	6.75	7.75	Compression Face
ST-26.a	Basalt/PU	4.75	6.0	Transverse Strips
ST-26.b	Basalt/PU	9.845	10.7	Neutral Axis/Transverse
ST-27.a	Basalt/PU	10.6	11.4	Neutral Axis/Transverse
ST-27.b	Basalt/PU	7.875	9	Tension/Transverse
ST-27.c	Basalt/PU	9.12	9.96	Tension/Transverse

The poles employed for the wrap configuration tests had smaller diameters than some of those in the damage determination and single-ply tests, thus minimizing the effects of cross-section deformations at the point of strain monitoring. However, due to the non-symmetric load points (especially at the north side) and close spacing of the load points, it is expected that the transverse strains will be substantially higher than theoretical values at some locations in the cross-section.

4.3.1 Test Configuration and Loading

The wrapping of these poles used the same procedure as the Single-Ply tests described in the previous section. The loading configuration was chosen to simulate, between the load application points, the state of stress of a pole under a linear wind loading. The ratio between the extreme fiber moment and shear stresses at the center of loading caused by the offset four-point bending is the same as the ratio of extreme fiber stresses in the section 2.5 ft above the base of a utility pole under wind loading. The loading configuration is shown in Figure 114.

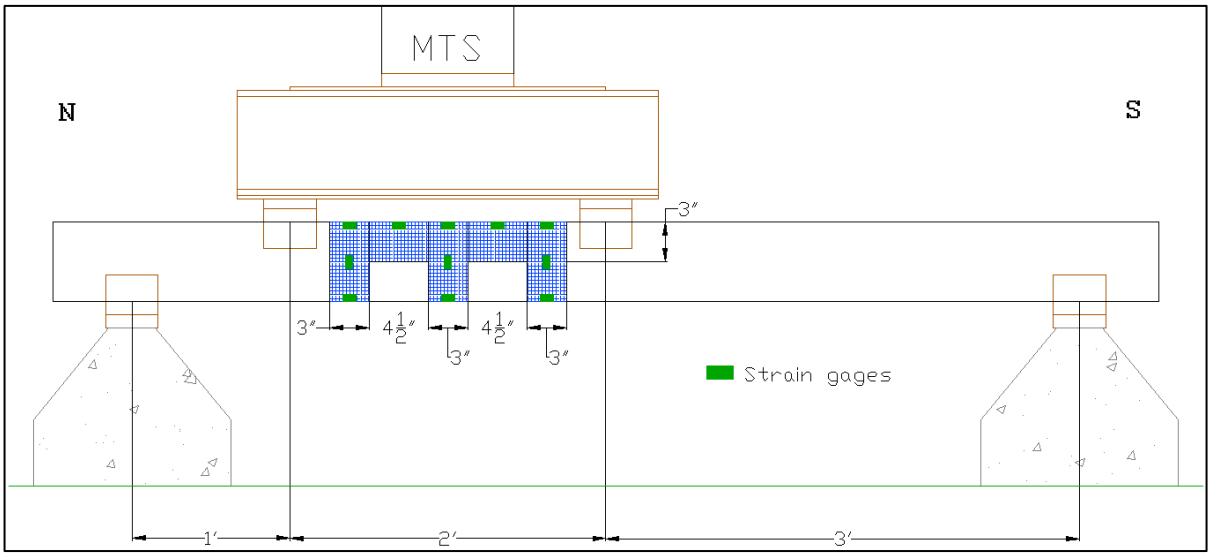

Figure 114. Wrap configuration test setup

Schematics of the different wrap configurations, including strain gauge locations, are shown in Figure 115 for the individual configurations and Figure 116 for the combined configurations. The compression and tension face wraps are designed to investigate the load-carrying action of a composite wrap on these portions of the section without the effects of confinement. The transverse, or circumferential, wrap was chosen to determine the shear load action of a repair. Finally, the neutral axis wrap is intended to provide information on the shear resistance provided by the composites. The tension/transverse, compression/transverse, and neutral axis/transverse wraps are intended to determine whether the confinement provided by the transverse wraps is able to improve the performance of the other wrap designs.

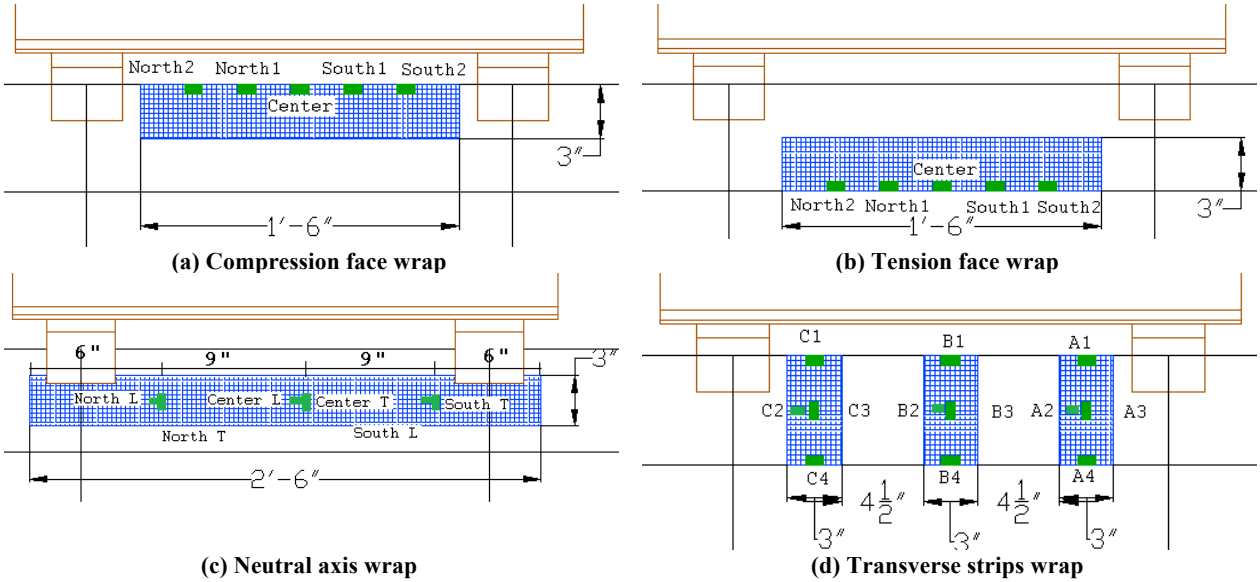

(a) Compression face wrap

(b) Tension face wrap

(c) Neutral axis wrap

(d) Transverse strips wrap

Figure 115. Laminate layouts for single wrap configurations

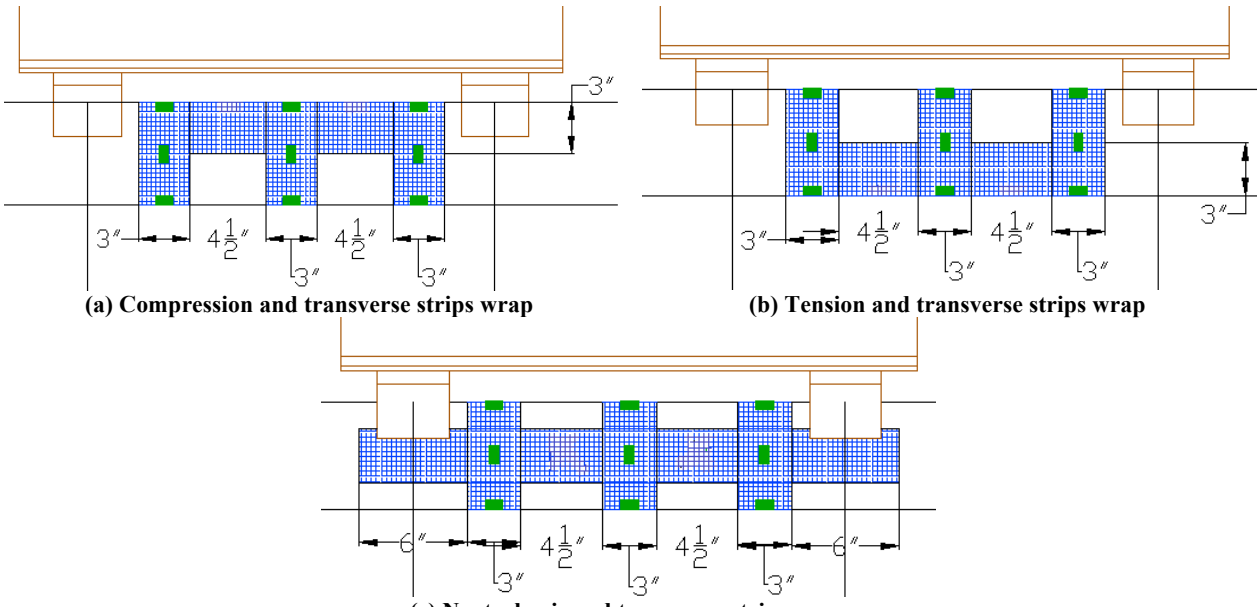

Figure 116. Laminate layouts for combined wrap configurations

4.3.2 Wrap Configuration Results

4.3.2.1 Compression Face Wraps

Two poles were wrapped with a compression face wrap, as shown in Figure 115 (a). These two poles, ST-17.b and ST-25, had average diameters of 8.07 in and 6.90 in, respectively, and were each loaded as shown in Figure 114 and Figure 117. Both poles failed through yielding of the steel section under the southern load point. This is due to the imbalance of the moment due to the offset of the load from the center of the support span. The two poles behaved in a similar manner, and the load-displacement and load-strain data for pole ST-25 are shown in Figure 118.

Figure 117. Compression wrap in test setup

As can be seen in Figure 118, the capacity of the poles was reached, and loading was continued beyond the peak. As the test progressed, the steel pole formed a plastic hinge failure underneath the southernmost load point. This is the location of the greatest moment carried by the pole. The hinging occurred before any failure of the FRP wrap was detected. As the test was continued

beyond the peak loads, debonding of the wraps began, initiating at the southern end, and progressing northward. It can be seen in Figure 118 that debonding of the composite occurred under each of the southern gauges. The other gauges remain at a constant strain level after steel failure. As the debonding occurs after yielding of the steel, it is probable that the debonding action was mainly due to interfacial shear between the laminate and the steel. The debonded laminates and poles after testing are shown for both compression wrap specimens in Figure 119.

The results of the compression Wrap Configuration tests are summarized in Table 20. In this table, the slope of the bending strain plotted against the applied moment, as measured at the center of loading in the FRP, normalized by the theoretical bending strain in the steel at that location is listed for each pole. The theoretical bending strain was calculated using the relationship below.

$$\varepsilon_{theory} = \frac{1}{E}\left(\frac{My}{I}\right) \tag{4-2}$$

An example plot showing these normalized slopes is shown in Figure 120 (note it is for a tension face wrap specimen). These normalized strain slopes indicate the effectiveness of the FRP in transferring load in the wrapped section, while removing the effects of variations in diameter and cross-section geometry of the poles. A normalized slope greater than one is an indication that the FRP wrap is able to transfer load effectively in the section, and to improve the strength of the section. The slopes shown for poles ST-17.b and ST-25 are less than unity. This indicates that the compression face wraps do not improve the load transfer capabilities of the pole section.

4.3.2.2 Tension Face Wraps

The tension face poles, ST-17.a and ST-20.a, were tested in the same manner as the compression poles, except that the wrap and gauges were placed as shown in Figure 115 (b) and Figure 121. The average diameters of the poles were 7.66 and 7 in, respectively. As with the compression poles, both of the tension face wrap poles failed through steel section yielding at the southern load point. Loading continued after steel yielding in order to gather data on the wrap behavior. As with the previous tests, debonding occurred in the tension face wraps progressively in the south two thirds of the FRP. Representative displacement and strain data are shown in Figure 122.

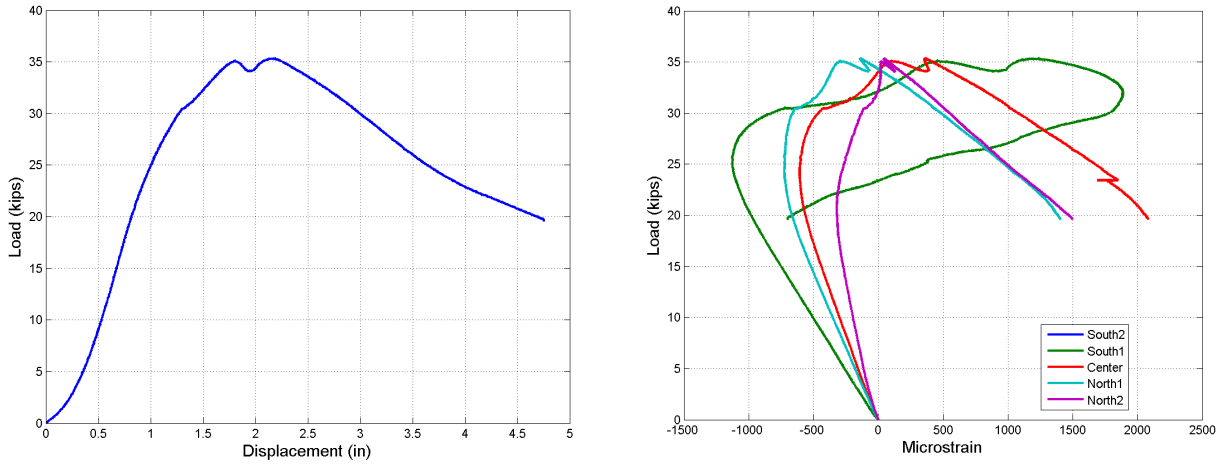

(a) ST-25 load-displacement (b) ST-25 load-strain

Figure 118. Compression test data

(a) ST-25 after loading

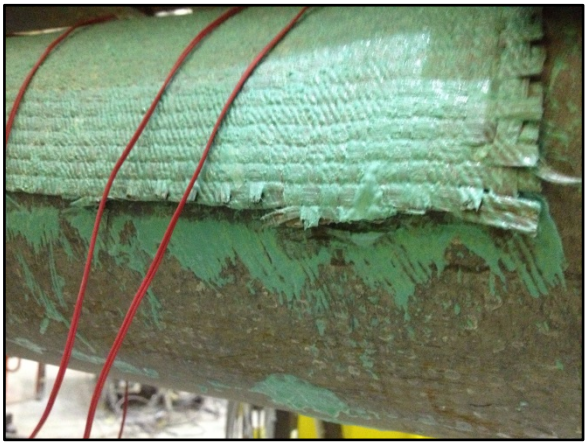

(b) ST-17.b debonded laminate

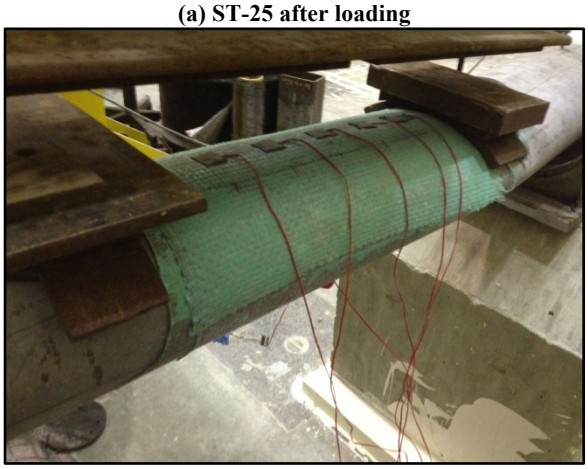

(c) ST-17.b after loading

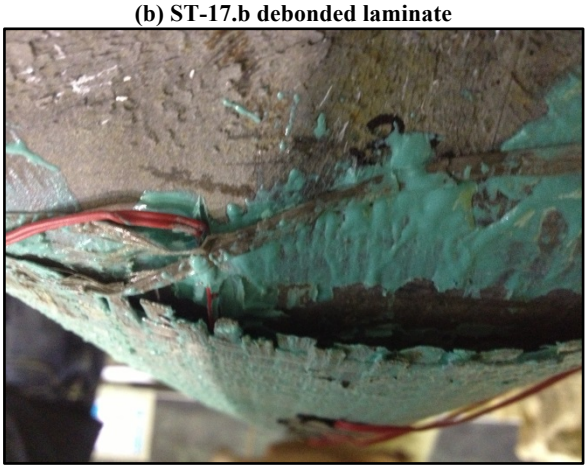

(d) ST-17.b debonded laminate

Figure 119. Compression wrap failure modes

Table 20. Wrap configuration compression summary of results

Pole ID	Normalized Bending Strain Slope
ST-17.b	0.67
ST-25	0.57
Average	**0.62**

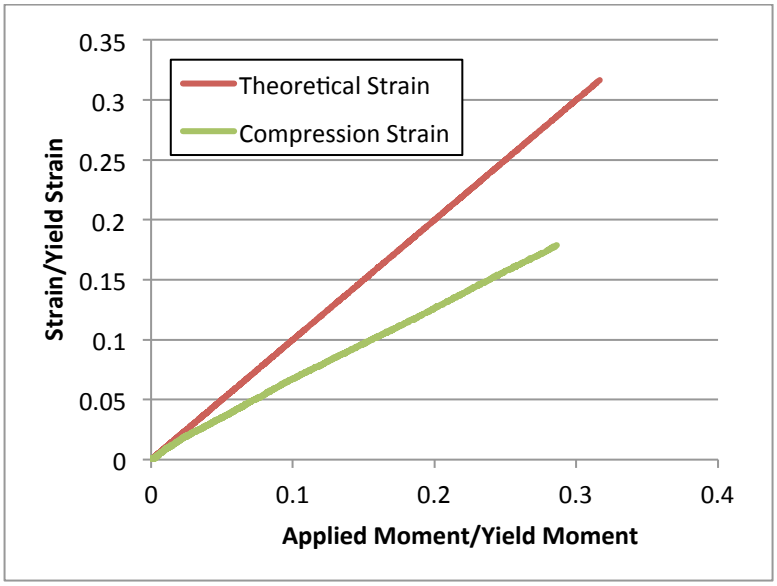

Figure 120. ST-17.a comparison of normalized compression strain slope

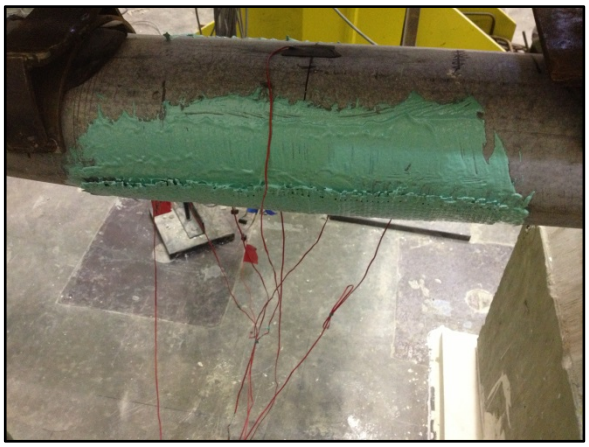

Figure 121. ST-17.a wrap and load configuration

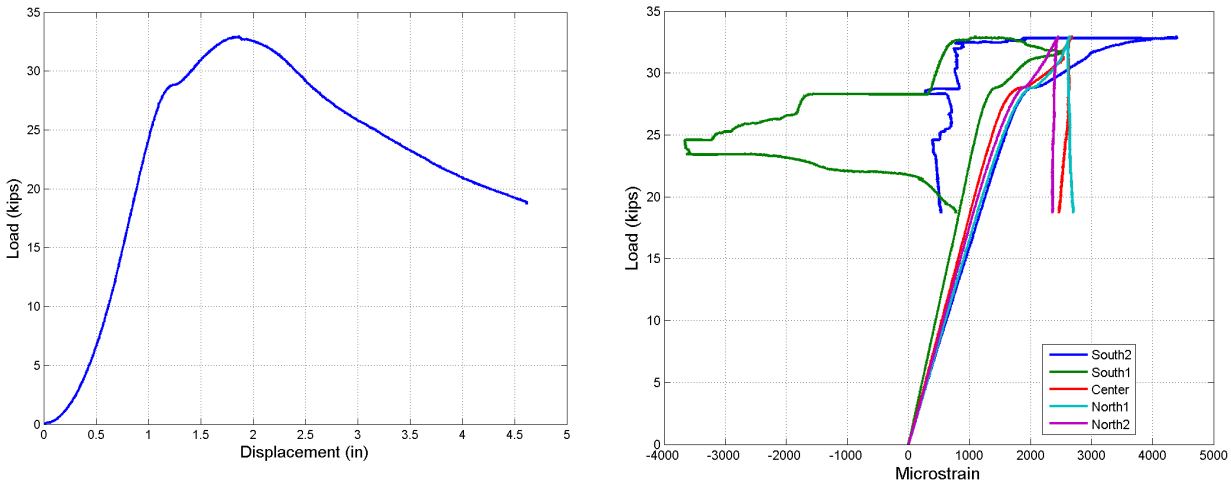

(a) ST-20.a load-displacement data **(b) ST-20.a load-strain data**

Figure 122. Tension face wrap test data

Normalized strain slopes at the center of loading are presented in Table 21 for the tension wrap poles, as was done with the compression wrap poles. The theoretical tensile strains were calculated in the same way as the compressive strains calculated above. The slopes listed are greater than unity, indicating that the tension face wrap is very effective in increasing the load-carrying capacity of the steel sections. The behavior of these wraps is significantly higher than that of the compression face wraps.

Table 21. Wrap configuration tension summary of results

Pole ID	Normalized Bending Strain Slope
ST-17.a	1.89
ST-20.a	1.13
Average	**1.51**

4.3.2.3 Neutral Axis Wraps

The neutral axis wrap configuration is shown in Figure 115 (c). Two poles were tested with this wrap type with basalt/polyurethane composites (ST-20.b and ST-21.b). These tests were performed in order to measure the effectiveness of an FRP repair at the bending neutral axis. The strain measurements were all taken in the transverse and longitudinal directions. The wraps are shown in Figure 123, and the load-displacement and load-strain data for pole ST-20.b are shown in Figure 124. The values listed in Table 22 illustrate that the neutral axis FRP strips were fully engaged in load transfer in the section, with strain slopes of roughly three times the theoretical value of the transverse strain in the steel at the center of loading.

(a) Pole ST-20.b **(b) Pole ST-21.b**

Figure 123. Neutral axis wraps and loading geometry

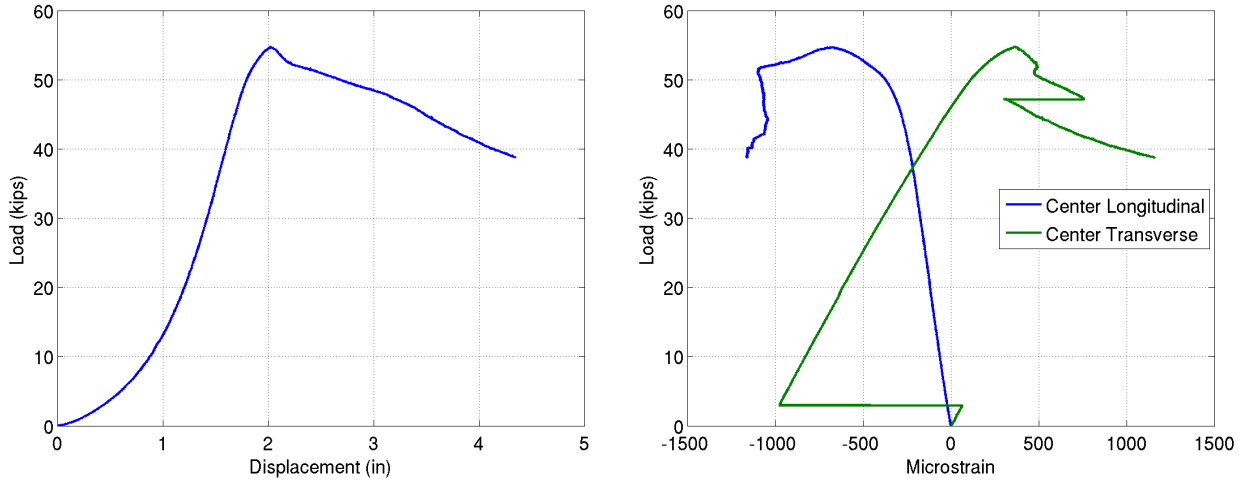

(a) ST-20.b load-displacement data **(b) ST-20.b load-strain data**

Figure 124. Neutral axis example data

Table 22. Wrap configuration neutral axis summary of results

Pole ID	Normalized Transverse Strain Slope
ST-20.b	2.60
ST-21.b	3.05
Average	**2.82**

4.3.2.4 Transverse Strips Wraps

Two poles were tested after being wrapped with three transverse FRP strips; both received basalt/polyurethane repairs (ST-13 and ST-26.a). For this wrap configuration, measurements were taken of both bending and transverse strains, as is indicated in Figure 115 (d). The wrapped pole sections are shown in Figure 125. An example of the load-displacement and load-strain data is shown in Figure 126. Again, the pole failed underneath the southern load point. Debonding of the transverse wraps occurred after steel yielding, beginning on the tension side of the southernmost strip, and continuing up to the compression side and north to the other strips.

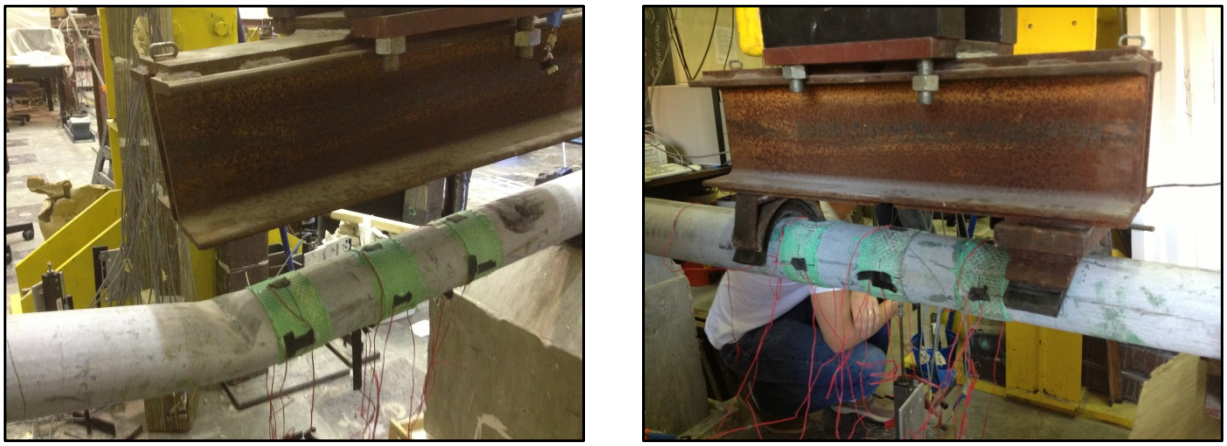

(a) Pole ST-13 **(b) Pole ST-26.a**

Figure 125. Transverse strips pole wraps and loading geometry

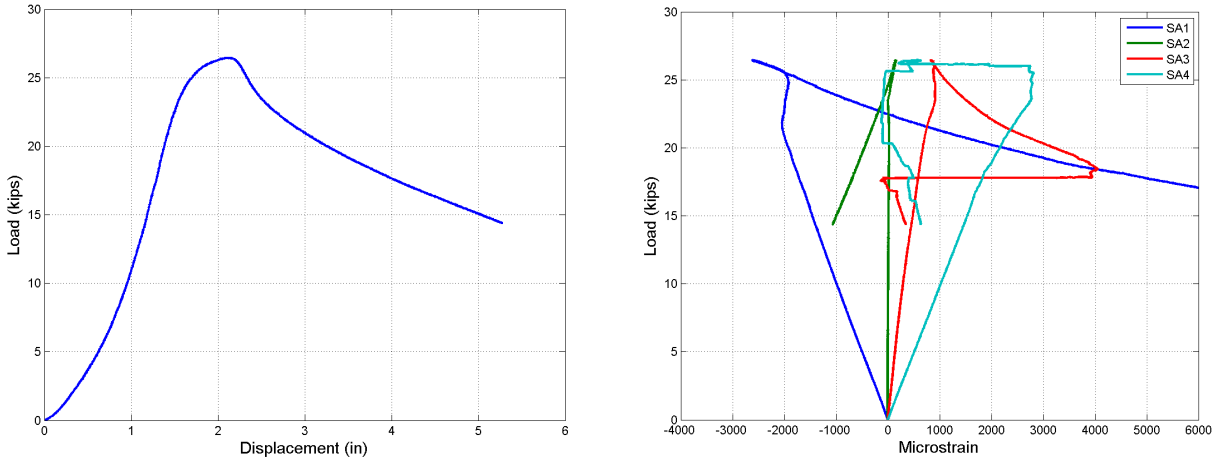

(a) ST-26.a load-displacement data **(b) ST-26.a load-strain data**

Figure 126. Transverse strips example data

As a summary of the test results, normalized strain slopes as measured in the center transverse strip are shown in Table 23. As can be seen from the normalized strain slopes, the transverse strips are fully engaged in transferring both bending and transverse loading. The transverse strains in the FRP are particularly notable, having values of more than twice of the theoretical value of steel transverse strain.

Table 23. Wrap configuration transverse strips summary of results

Pole ID	Normalized Bending Strain Slope		Normalized Transverse Strain Slope
	Compression	Tension	
ST-13	1.60	2.28	2.44
ST-26.a	0.93	1.18	2.24
Average	**1.26**	**1.73**	**2.34**

4.3.2.5 Compression and Transverse Strips Wraps

Two poles were tested for each of the combination wraps, all of which utilized the basalt/polyurethane FRP material. The two poles that were wrapped on the compression faces with transverse strips were ST-19.a and ST-19.b. The average diameters of these poles were 6.74 in and 6.44 in, respectively. The wrap geometry is shown in Figure 116 (a), and the wraps are pictured in Figure 127. The placement of the strain gauges is the same as that used in the transverse wrap configuration. Representative loading data is shown in Figure 128. The strain behavior of this wrap geometry is summarized in Table 24. The bending strains listed here indicate that this wrap configuration improves the load-transfer mechanisms on the tension face within the transverse strips, the compression face wrap does not improve the performance of the section. Additionally, it does not appear that the effectiveness of the compression face wrap is significantly improved by the addition of transverse strips.

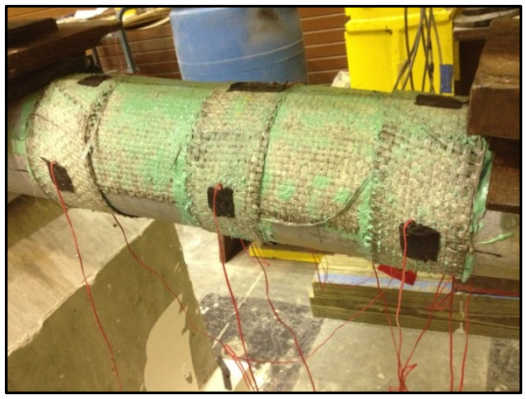

Figure 127. Compression and transverse wrap configuration

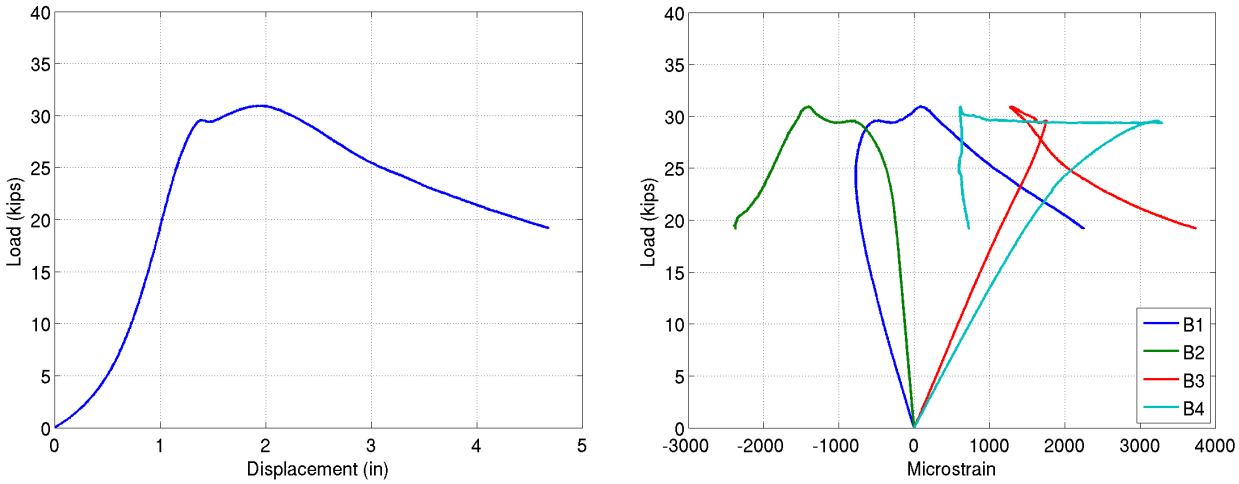

(a) ST-19.b load-displacement **(b) ST-19.b load-strain**

Figure 128. Compression/transverse example data

Table 24. Wrap configuration compression/transverse summary of results

Pole ID	Normalized Bending Strain Slope		Normalized Transverse Strain Slope
	Compression	Tension	
ST-19.a	0.77	1.44	7.33
ST-19.b	0.61	1.08	6.97
Average	**0.69**	**1.26**	**7.15**

4.3.2.6 Tension and Transverse Strips Wraps

The tension/transverse wrap poles, ST-27.b and ST-27.c, possessed average diameters of 8.20 in and 9.40 in, respectively. The wrap geometry is pictured in Figure 129. The wrap and gauges were prepared in accordance with Figure 116 (b). The measured load, displacement, and strain behavior for pole ST-27.b are illustrated in Figure 130. The strain data gathered from Pole ST-27.a indicated that the entire section within the loading region was in tension, rather than bending. This is due to the offset of the load from the center of the span. The ST-27.c pole experienced extreme local buckling – almost folding - of the steel at the southern load point. This caused the pole to behave almost as a catenary member, completely in tension. The normalized strain behavior is summarized in Table 25.

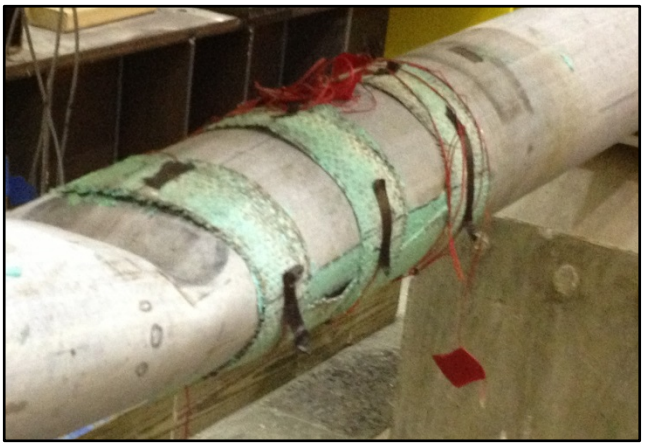

Figure 129. Tension and transverse wrap configuration – failed section

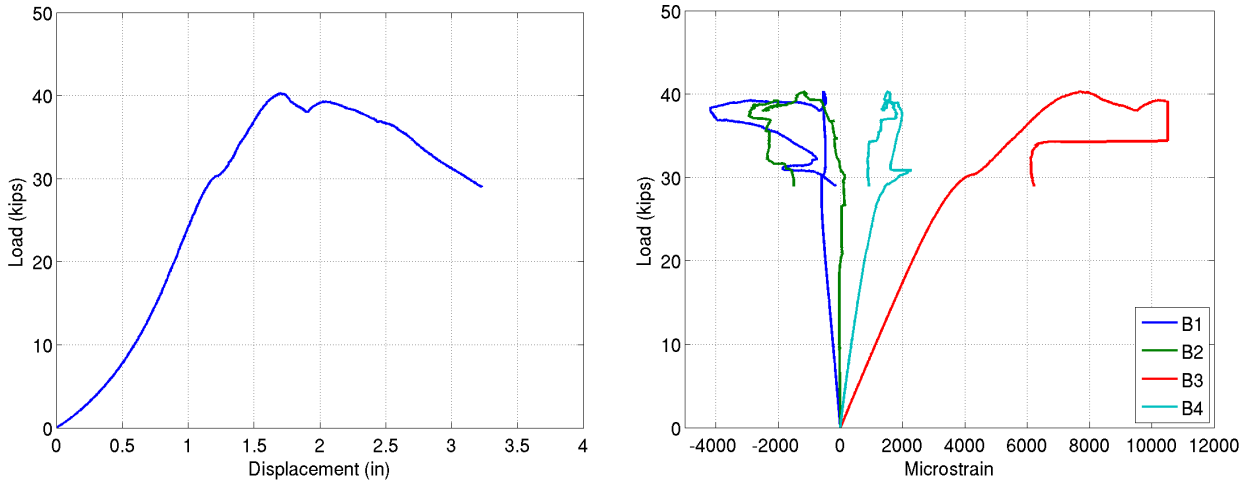

(a) ST-27.b load-displacement **(b) ST-27.b load-strain**

Figure 130. Tension/transverse example data

Table 25. Wrap configuration tension/transverse summary of results

Pole ID	Normalized Bending Strain Slope Compression	Tension	Normalized Transverse Strain Slope
ST-27.b	0.69	1.08	8.19
ST-27.c	N/A	N/A	N/A
Average	**0.69**	**1.08**	**8.19**

4.3.2.7 Neutral Axis and Transverse Strips Wraps

The neutral axis and transverse strips wrap configuration is shown in Figure 116 (c). The two poles tested with this wrap type, ST-26.b and ST-27.a, have average diameters of 10.125 in and 10.875 in, respectively. The wraps are shown in Figure 131. Representative test data is shown in Figure 132. The normalized strain slopes listed in Table 26 are approximately three times the slopes measured in the neutral axis wraps, but are comparable in value to the strain measurements from the transverse strip wraps. The reason for this disparity is the confinement provided by the transverse wraps.

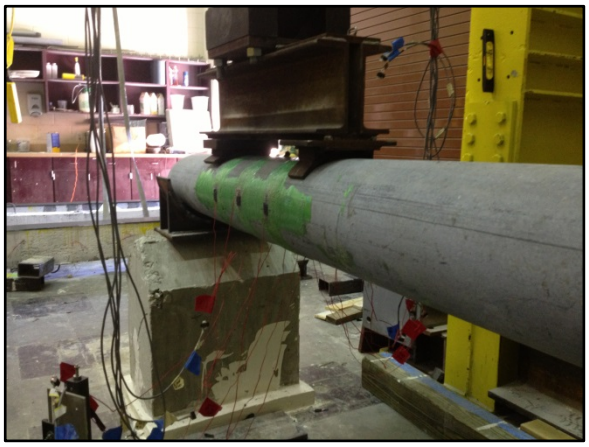

Figure 131. Neutral axis/transverse wraps and loading geometry – pole ST-26.b

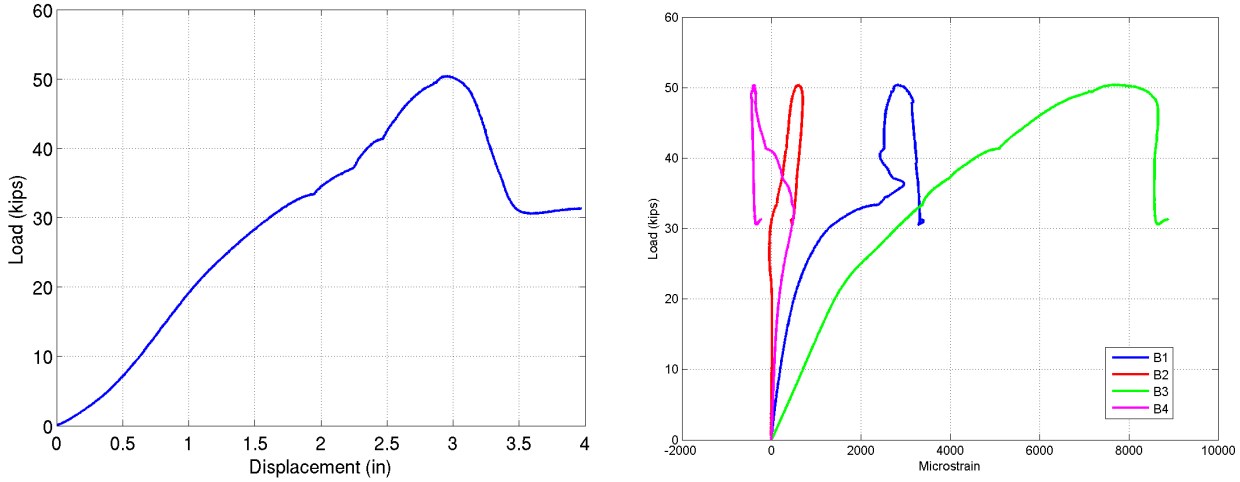

(a) ST-27.a load-displacement data **(b) ST-27.a load-strain data**

Figure 132. Neutral axis/transverse example data

Table 26. Wrap configuration neutral axis/transverse summary of results

Pole ID	Normalized Transverse Strain Slope
ST-26.b	6.02
ST-27.a	6.93
Average	**6.56**

4.3.3 Summary of Wrap Configuration Results

The Wrap Configuration tests were performed in order to determine which wrap geometries are most effective in aiding load transfer in a repaired metallic pole section. Average normalized slopes of strain-moment plots have been determined for each wrap type, representing its ability to improve the mechanical capacity of a section. These values are reported in Table 27. The results of the Wrap Configuration tests are limited to the PU/basalt repair system.

As with traditional FRP repair strategies, providing tension wraps led to a moderate improvement in the behavior of the repaired poles. Based on these results it can be determined

that compression face wraps are not, in themselves, effective in improving the mechanics of a repaired section. However, the confinement of a complete transverse wrap allows the compression FRP to engage in load transfer. The measured transverse strains, including those in the neutral axis wraps, all indicate that the FRP wrap is active in the transverse direction. The elastic distortions of the thin-walled sections at the load points and peak moment location are resisted by the transverse wraps. This beneficial confining stress is well established in axial-flexural members; however, appears to provide additional stiffness and strength in the flexure-only pole specimens as well.

From this data, it is concluded that, whenever possible, FRP wraps should completely encircle the repaired pole section. When this is not possible due to features in the pole geometry, the wrap should extend at least half of a circumference around the pole, unless the damage is minor. The extension beyond the dented and filled region should be sufficient to fully develop the transverse wrap.

Table 27. Wrap configuration summary of results

Wrap Configuration	Normalized Bending Strain Slope		Normalized Transverse Strain Slope
	Compression	Tension	
Compression	0.62	-	-
Tension	-	1.51	-
Neutral Axis	-	-	2.82
Transverse	1.26	1.73	2.34
Compression/Transverse	0.69	1.26	7.15
Tension/Transverse	0.69	1.08	8.19
Neutral Axis/Transverse	-	-	6.56

Chapter 5: Large-Scale Monotonic Testing

Several full-scale tests were performed on damaged and repaired steel and aluminum poles. The repair systems were designed using the experience and data gained in the component-level testing stage. This chapter details the full-scale tests of poles to determine strength and behavior of the repair poles under a monotonically increasing displacement applied to the tip of the pole. The same two FRP repair systems employed in the component-level tests were employed in the full-scale tests. However, difficulties encountered in wrapping smaller-diameter and multi-sided poles with the pre-cured QB sheets led to only a single larger-diameter pole (ST-5) to be targeted with this repair system. During wrapping of ST-5, similar issues were encountered; therefore, the remaining large-scale poles with epoxy utilized the same materials but with traditional on-site wet lay-up, labeled as QB Wet here.

No mechanical anchorage for the laminates to the pole base was provided for either the wraps extending in the pole longitudinal direction, nor those in the circumferential direction. Therefore all results are based on the repair laminates being properly developed using only the adhesive layer and any debonding resistance provided by circumferential layer(s) providing confinement to the longitudinal layer(s), where possible based on the geometry of the dents and any ports or buttons.

5.1 Sample Poles

Table 28 shows the testing matrix for the full-scale tests, and includes information on the loading method, repair type and wrap dimensions, and damage level of each pole specimen. Each pole specimen consists of the first 11 ft of pole length above the base, and has an intact base plate by which it will be anchored for loading. The poles are also tapered and the diameter and dent geometry are provided in Table 29.

Table 28. Large-scale testing matrix (contains specimens for Chapters 5 and 6)

Pole ID	Fiber Type	Matrix Type	Loading Type	Wrap Dimensions (in)				No. of Layers
AL-1.c	G	QB Wet	Monotonic	22×30				1
AL-2.c	G	PU	Monotonic	22×30				1
AL-3.c	B	PU	Monotonic	5×28	8×28	15×28	26×28	1
ST-5	G	QB Wet	Monotonic	57×49	8×58	6×60		1
ST-6	G	PU	Monotonic	6×68	12×68	32×53		1
ST-7	B	PU	Cyclic	45×54				1
ST-8	B	QB Wet	Monotonic	4×60	21×60	51×49		1
ST-10	G	PU	Cyclic	4×58	12×58	44×49		1
ST-11	G	QB Wet	Cyclic	9×58	12×58	6×58	48×26	1
ST-12	B	PU	Monotonic	14×54	50×54			2
FD-1	G	PU	Monotonic	6×54	10×54	24×42		1
FD-2	B	QB Wet	Monotonic	11×48	6×48	40×14		1
FD-3	G	PU	Monotonic	6×44 x2	9×44 x2	20×60		1
FD-5	B	PU	Monotonic	6×44 x2	9×44	12×44	20×67	1
IM-1	B	PU	Impact	6×44	9×44	26×31		1
IM-2	G	QB Wet	Impact	9×78 x3	70×45			1

Table 29. Large-scale pole specimen geometry (contains specimens for Chapters 5 and 6)

Pole ID	Loading Type	Dent Depth		Dent Height Above Base	Angle Between Port and Dent	Outer Diameter (in)	
		(in)	(%)			Large	Small
AL-1.c	Monotonic	1.5	18	16″	-	8.3125	7.0525
AL-2.c	Monotonic	1.875	23	16″	-	8.3125	7.0525
AL-3.c	Monotonic	2.375	30	22″	180°	8	6.75
ST-5	Monotonic	3.563	18	16″	180°	20.5	19.25
ST-6	Monotonic	3.75	19	16″	150°	20.25	19
ST-7	Cyclic	2.563	16	22″	-	16.5625	15.3
ST-8	Monotonic	4.25	24	22″	90°	17.625	16.375
ST-10	Cyclic	3.625	21	16″	90°	17.625	16.375
ST-11	Cyclic	3.25	19	16″	90°	17	15.75
ST-12	Monotonic	4	25	22″	-	16.5625	15.3
FD-1	Monotonic	3.06	24	19.75″	0°	16.125	14.865
FD-2	Monotonic	1	7	16.5″	90°	14.25	13
FD-3	Monotonic	2.563	21	48″	145°	13	11.75
FD-5	Monotonic	2.563	24	44.5″	125°	11	9.75
IM-1	Impact	1.375	13	32″	135°	11	9.75
IM-2	Impact	5.75	28	33″	130°	21.5	19.75

All loading methods and pole specimens are summarized briefly in this section. Results and details for those specimens identified in Table 28 for monotonic testing are provided in this chapter. Results and more detailed information about loading and test setup for those specimens identified for cyclic and impact testing are provided in Chapter 6.

All large-scale pole specimens were retrieved from the field, regardless of whether they were damaged from vehicular impact or not. The specimens that suffered vehicular impact damage while in service are labeled as field-damaged in the following sections. The specimens that were not damaged in-situ were dented in the laboratory as described in the component-level tests and are labeled as induced-damage poles in the following sections. The state of the materials (base metal, welds, etc.) was largely unknown due to the environmental and mechanical conditioning the pole specimens may have received during the service life prior to being decommissioned. Some information was obtained from individual base metal coupon tests (Section 3.4); however, the degradation of localized areas within the tube and base flange, welds, etc. remain unknown in this study.

5.1.1 Monotonic Pole Tests

The monotonic loading test configuration cantilevers the pole horizontally from a precast concrete block tower to which its base plate is bolted, as shown in Figure 133. The 11 ft poles are loaded vertically 9 ft from the base monotonically until failure. In this setup, the poles are aligned so that the center of the dented area is on the opposite side of the applied load (the dented area is on the compression face). The load was applied using an Enerpac servo-controlled hydraulic actuator with capacity of 800 kip. The load was applied using load control at a rate of 0.1 kip/sec. A 50 kip load cell was mounted in series with the existing 600 kip Enerpac load cell to measure the applied force during the tests (higher resolution on the load levels expected for

the poles). The tests were stopped when the actuator stroke was exhausted or when noticeable damage developed after the peak load was achieved.

The test setup was made modular to accommodate the range of different steel pole (ST- and FD-specimens) anchor bolt patterns. This was accomplished by attaching the 2 in thick steel plate to the buttress using four (4) 1.5 in diameter threaded rods. An additional 1/2 in thick plate with a common bolt pattern at the four corners was then welded to the existing pole base plates for each specimen. The ½ in thick plate was secured to the 2 in plate with 3/4 in diameter bolts by way of spacer plates (the bolts were placed prior to installation of 2 in plate and the spacer plates enabled wrench access for securing the bolt heads) placed between the buttress and 2 in thick plate. The spacer configuration was consistent with both the 2 in and ½ in bolt patterns.

After testing of FD-5, it was discovered that the ½ in plates were too flexible; therefore, an additional pair of bolts was added on the top and bottom to prevent prying of the plates. All subsequent monotonic tests used this six (6) bolt setup, with 1 in bolts replacing the original ¾ in ones. The aluminum poles (AL- specimens) all shared a common anchor bolt pattern and were bolted directly to the 2 in plate using a matching pattern fabricated during the pilot project (Mackie et al., 2011). Details of the plate weld and bolt patterns for the monotonic specimens are shown in Appendix B.

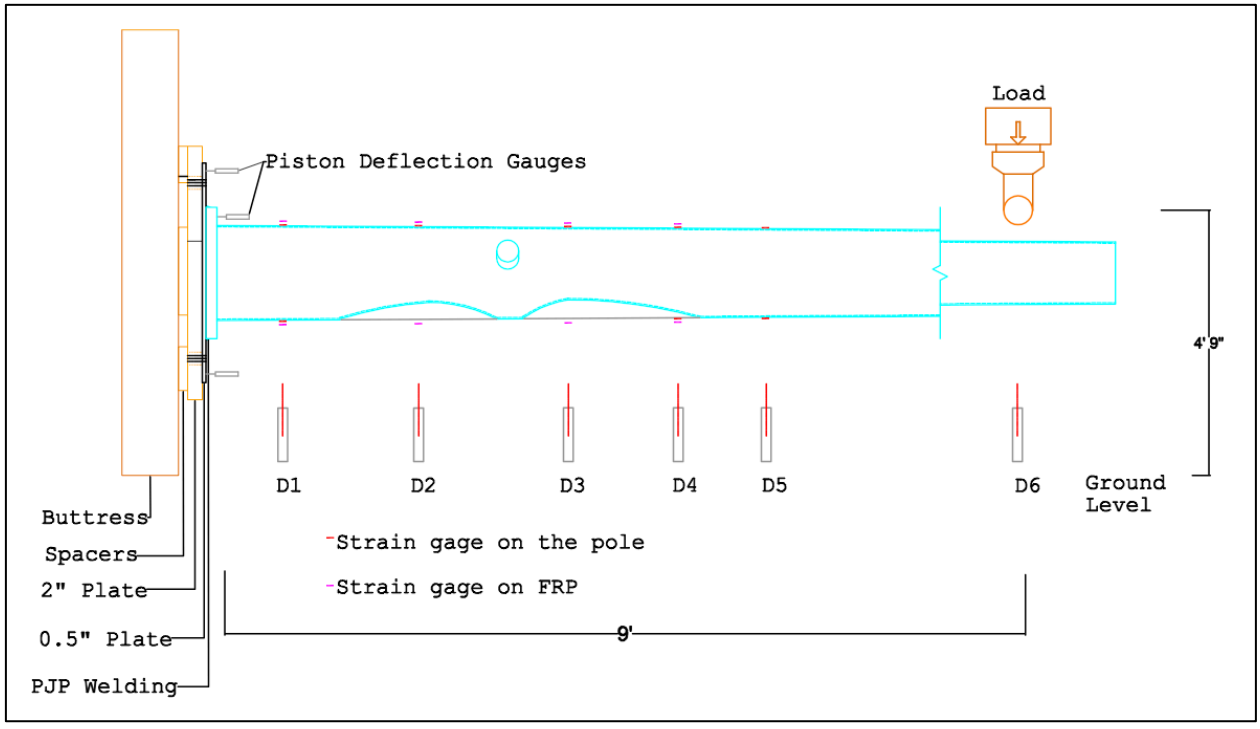

Figure 133. Monotonic cantilever test setup

Each monotonic pole specimen was instrumented with both displacement and strain gauges during testing. A common set of 6 (Balluff BOD 66M) laser displacement gauges were used at distances of 9, 27, 45, 63, 95, and 129.625 in from the face of the buttress. These gauges are labeled consistently as D1 (closest to buttress) through D6 (under the load application point) in all full-scale monotonic tests, as shown in Figure 133. The actual distance above the top of the

pole base plate varies from test to test due to the thickness of the individual pole bases and the ½ in spacer plate that was not used in the case of the aluminum poles. The strain gauge plan used for each pole was specific to the locations of damage and the FRP repairs; therefore, the strain gauge numbering and location is presented separately for each pole with the results. Standard 6 mm 120 Ω foil-backed resistive strain gauges were used throughout.

5.1.1.1 Field-Damaged Poles

Four (4) steel utility poles that had been impact-damaged in the field were used for monotonic testing of the FRP repair systems. Repairs were designed for the poles based on the extent of the damage according to the protocol developed in the component-level testing phase. Because the damage was applied to these poles by accidental vehicle impacts, the damage is irregular, and often there are multiple dent locations on a single pole. These pole specimens (FD-1, FD-2, FD-3 and FD-5) have dents ranging from 7% to 24% of their outer diameters. The walls of the poles are 3/16 in, and the base diameter range from 11 to 16 in. The details of each poles geometry and damage will be discussed further in the results section. Several field-damaged poles as they were retrieved from the field are shown in Figure 134.

Figure 134. Field-damaged pole inventory before repair and testing

5.1.1.2 Induced-Damage Poles

The laboratory-damaged poles were dented by the method used for the component level tests as described in Section 4.1. The four (4) steel pole specimens (ST-5, ST-6, ST-8 and ST-12) were dented to depths ranging from 2.56 to 4.00 in, or 16% to 25% of the undented diameter. Three (3) aluminum poles were also dented and tested under monotonic loading in the laboratory (AL-

1, AL-2 and AL-3). These poles had damage ranging from 1.50 to 2.38 in 18% to 30% of the original diameter at the dent location. These specimens will be discussed in further detail in the results portion of this section. During mechanical denting of the aluminum poles, several specimens developed brittle cracks and ruptured during denting. This observation is consistent with the cracking that was observed in the aluminum specimens tested in Slade and Mackie (2011). Therefore, it is recommended that prior to any field repairs to aluminum impact-damaged poles that a more extensive forensic investigation of cracks is performed. Cracks have been observed initiating at the stiffened edges of the access port, longitudinal seam, and in the base plates at the location of the anchor bolts.

5.1.2 Cyclic Pole Tests

The same horizontal cantilever configuration was used from the monotonic pole testing. However, positive attachment was required at the connection of the pole tip to the actuator. Therefore, a vertical stiffener was welded to the inside of the pole at the location of the tip, and a connection was fabricated. A series of steel plates and stiffeners was fabricated to allow positive attachment between the actuator and pole tip for each specimen. A 55 kip MTS actuator was used to replace the 800 kip Enerpac used during the monotonic tests. The cyclic load protocol was based on applying a target of 2 million cycles in an endurance test under load control with the same positive and negative load excursions during each cycle. The target load level for each pole during the 2 million cycles was computed based on AASHTO, the details of this calculation are presented in Chapter 6. For the two pole specimens that survived the 2 million cycle endurance test, the load level was subsequently increased and an additional 1000 cycles was performed at each increasing load level until failure was achieved.

5.1.2.1 Induced-Damage Poles

The laboratory-damaged poles were dented by the method used for the component level tests as described in Section 4.1. The three (3) steel pole specimens (ST-7, ST-10, and ST-11) were dented to depths ranging from 2.56 to 3.25 in, or 16% to 21% of the undented diameter. These specimens will be discussed in further detail in the results portion of Chapter 6.

5.1.3 Impact Pole Tests

The component and full-scale monotonic and cyclic tests demonstrated that the FRP-repaired poles have substantial capacity and are not susceptible to damage under repeated loading. Given the proximity of many poles to traffic, the potential for a second impact within the previously damaged and repair area has a high probability. Therefore, a set of two impact tests were performed with the impact pendulum facility at the Marcus H. Ansley Structures Research Center. The pedestal foundation location of the pendulum was used, and the poles were mounted in a vertical cantilever configuration. The direction of impact was toward the dented region, causing damaged to the previously dented and repaired region, to assess stability and efficacy of the wrapping procedure. A 12-ft drop height was utilized for the impact tests and the details of the mass, instrumentation, and results are presented in Chapter 6.

5.1.3.1 Field-Damaged Poles

Two (2) steel utility poles that had been impact-damaged in the field was used for impact testing of the FRP repair systems. The repair was designed for the poles based on the extent of the damage according to the protocol developed in the component-level testing phase. Because the damage was applied to these poles by accidental vehicle impacts, the damage is irregular, and often there are multiple dent locations on a single pole or the extent of the dent is larger than some of the mechanically-dented poles mentioned previously. The two poles had dents ranging from 1.375 to 5.75 in, or 11% to 27% of the undented diameter. The detailed geometry and damage are discussed further in the results of Chapter 6.

5.2 Large-Scale Test Results

The results are presented in three subsections. The first subsection is for the steel field-damaged poles (with the FD prefix). The second subsection is for the laboratory-damaged steel poles (with the ST prefix). Finally, the third subsection is for the laboratory-damaged aluminum poles (with the AL prefix). All diameters shown in this chapter are the outer diameter unless otherwise noted.

5.2.1 Field-Damaged Poles

5.2.1.1 FD-1

The first field-damaged pole specimen is a multi-sided steel pole that was severely dented by a vehicle collision. The pole's access port is within the dented area, which extends approximately from 3.5 in to 3 ft above the base plate, as shown in Figure 135. The diameter of the pole is approximately 16.125 in at the base, and the wall thickness transitioned from a value of 3/16 in at the pole tip to 5/16 in at the pole base. The dent was repaired with a single-layer FRP wrap over an epoxy fill. The access port was capped in order to allow the dent to be filled. For cases such as this in the field, it would be possible to cut a new access port on the undented face and design the wrap accordingly; however, this was not performed due to time limitations.

Figure 135. Original vehicular damage to access port region in FD-1

The FRP system consisted of glass fibers and a polyurethane resin. The geometry of the FD-1 pole and repair are shown in Appendix A. A main wrap laminate was used which extended approximately halfway around the pole's circumference, and 46 in from the base plate. Three transverse circumferential wraps were placed on top of the main wrap that encompassed the entire circumference of the pole and were 10 in, 6 in, and 6 in wide, from the bottom, respectively. The FRP reinforcing ratio at the base was approximately 25% (area of FRP was not adjusted for fiber volume fraction). The transverse wraps on the opposite face to the dented region are shown in Figure 136 (a). An interior view of the pole indicating the extent of damage in the existing access port region is shown in Figure 136 (b). The hole in the base metal in the photos was due to removal of metal for thickness testing after monotonic testing.

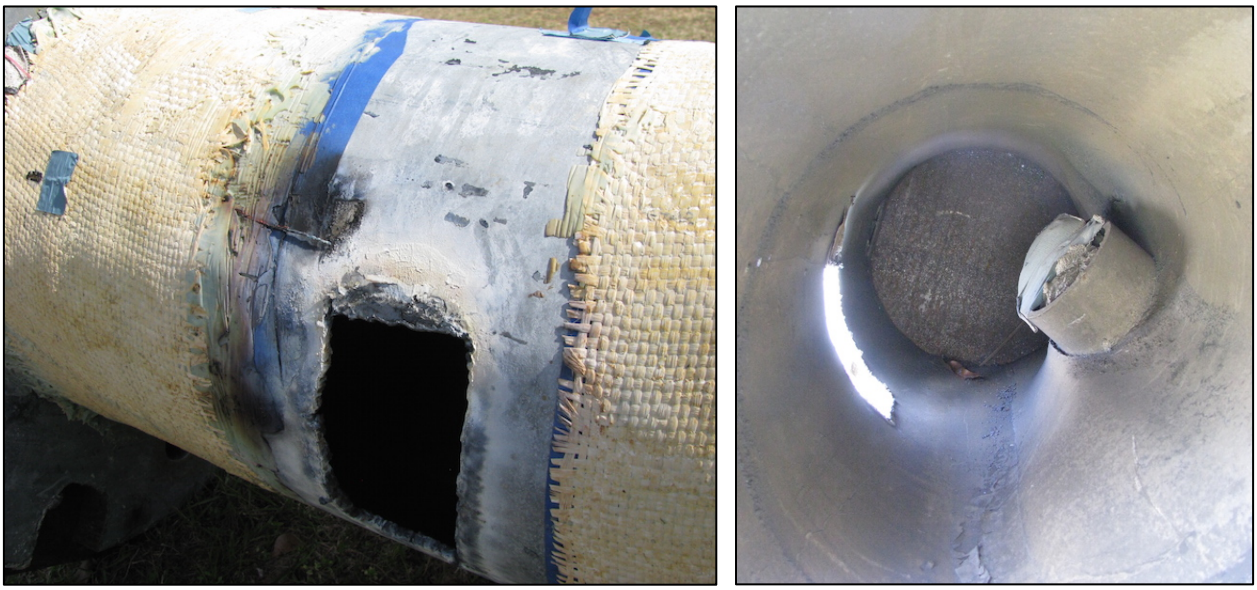

(a) Side opposite damaged region (the metal portion was removed after testing for measuring thickness) **(b) Interior view with base plate attached**

Figure 136. FD-1 exterior and interior views (taken after monotonic testing)

The pole was tested to a load of 30 kip in a cantilever configuration, as shown in Figure 137. The load-displacement and load-strain data are shown in Figure 138 and Figure 139, respectively. The locations of the various strain gauges are shown in Figure 140. For clarity, the strain data are divided into six different plots. The first two plots show the compression strain measurements taken from longitudinal gauges located on the top side of the pole and the FRP wrap, respectively, in its test configuration. The third and fourth plots show the tensile strain measured from longitudinal gauges on the lower side of the pole on the steel and FRP surfaces. Finally, the last two plots show the measurements taken from the transverse gauges, which were placed transversely along the pole's neutral axis. Such a layout is adopted for all the steel pole specimens presented.

Figure 137. FD-1 test configuration

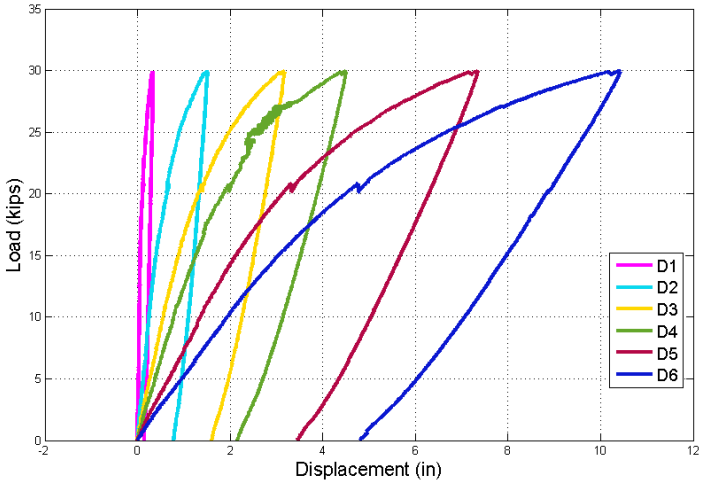

Figure 138. FD-1 load-displacement data

There was a slight drop in the load at approximately 21 kip and again at 30 kip before the test was stopped prior to failure of the pole. The welds near the neutral axis of the pole on the west side had ruptured, as seen in Figure 141 (a), and the setup had not been designed for loads higher than this. Based on cross-sectional measurements taken from the top of the pole when retrieved from the field, the theoretical yield load was estimated as only 31.8 kip. However, a section of the pole removed from the base after the test indicated the wall thickness was substantially larger, leading to a revised estimate of the yield load of 41.8 kip.

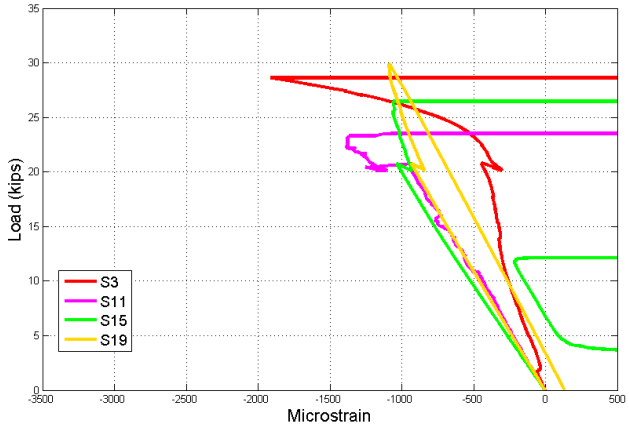

(a) FD-1 load-steel compressive strain data

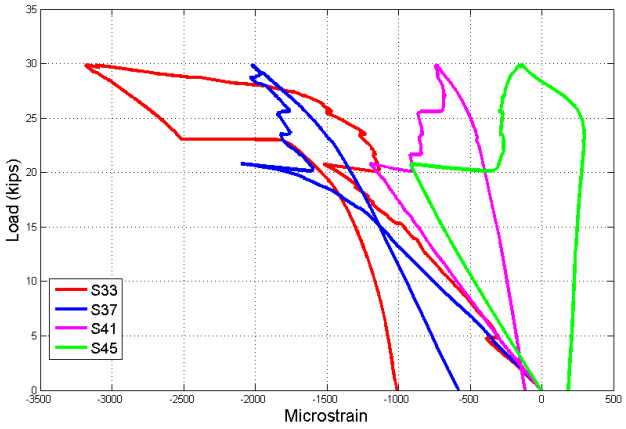

(b) FD-1 load-FRP compressive strain data

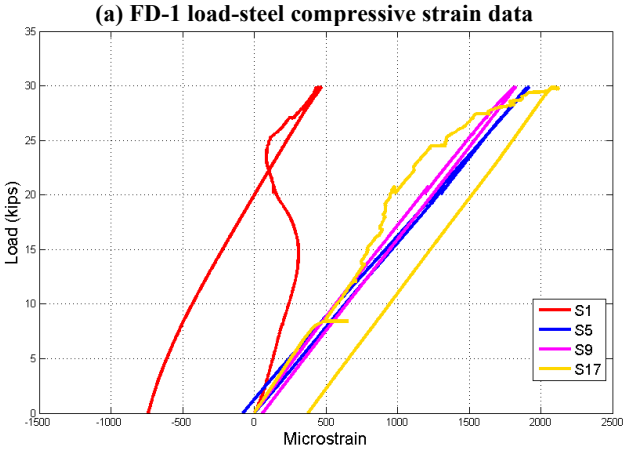

(c) FD-1 load-steel tensile strain data

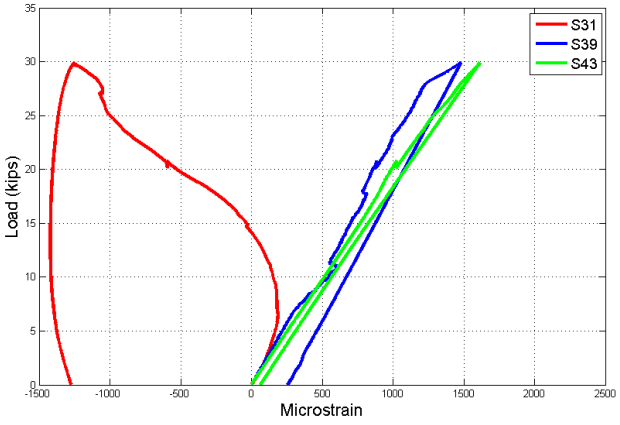

(d) FD-1 load-FRP tensile strain data

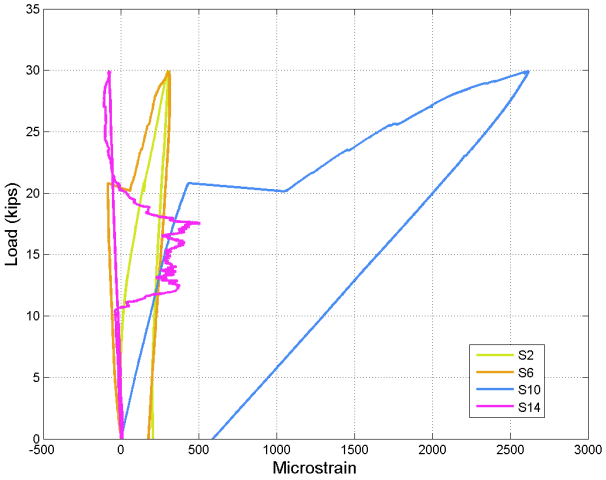

(e) FD-1 load-steel transverse strain data

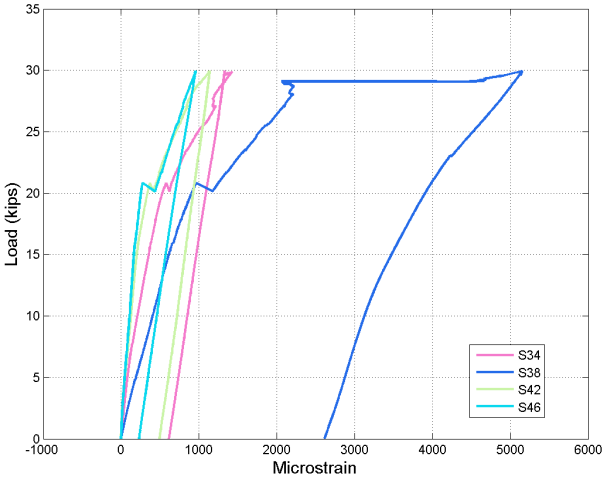

(f) FD-1 load-FRP transverse strain data

Figure 139. FD-1 load-strain data

The compressive steel gauge at the base (S3) indicates that the steel near the pole base was close to yielding. Although, interestingly, both the steel and FRP tension gauge at the same cross-sections began to unload rather than developing a similar tensile strain. There were potentially voids in the wrap as there is no compatibility between the steel and FRP strains even at low loads at this location. Alternatively, the prying of the base plate due to the weld failure may have resulted in different strain localizations near the base. Yielding strains were also measured in

tension in gauge S17 at section 5 and transversely in gauge 10 at section 3. The regions indicated as debonded from sounding the pole after the test are shown as the hatched areas in Figure 141 (b).

The relatively small steel transverse strains at all locations except section 3 show that the complex dented shape did not behave like a standard circular hollow section. However, the fill material appears to have provided substantial ability for stress to redistribute within the cross-section as the FRP transverse strains exceeded 1000 με at sections 1 and 2. In addition, the pole appeared to have yielded both above and below the dented region (sections 1 and 5), implying that the capacity of the repaired region was larger than the demand after the repair engaged, possibly shifting the critical section above the repaired region. As the test was terminated at 30 kip of load, it is not known what the failure load would have been prior to hinge formation at sections 1 and 5 (or in the repaired region); therefore, the achieved ratio of experimental to theoretical load of 72% is a lower bound datum.

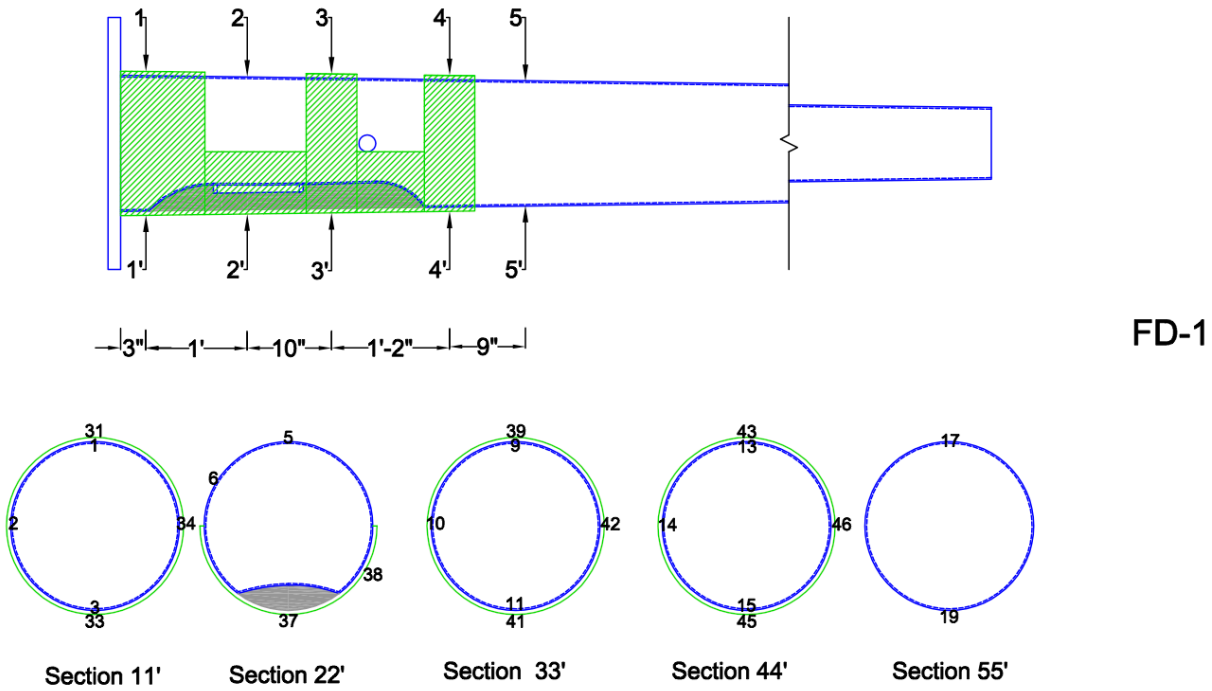

Figure 140. FD-1 strain gauges

(a) Ruptured pole base plate welds near bolt on west side of pole

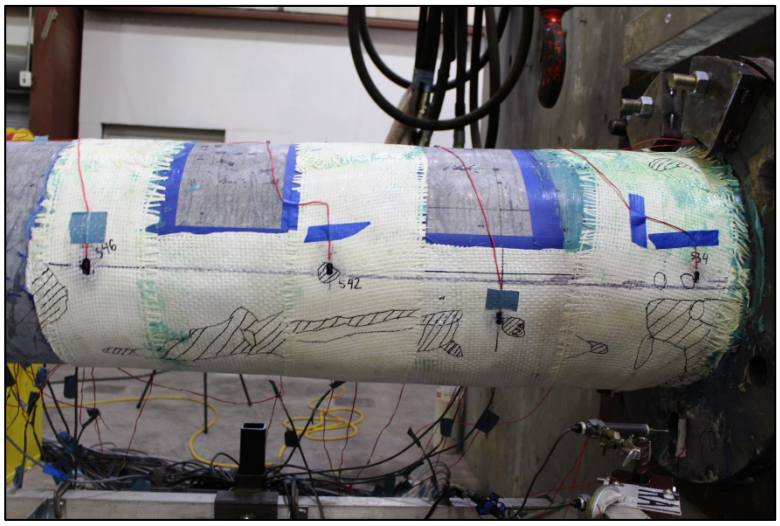

(b) Debonded areas of FRP wrap

Figure 141. FD-1 failure modes

5.2.1.2 FD-2

FD-2 is a 12-sided utility pole that has been damaged by an impact in the field. There are two small dents located approximately 90° from the pole's access port, 15 in and 17.5 in above the base plate. These dents are 0.625 in and 1 in deep, respectively. The 1 in dent is about 7% of the pole's outer diameter in depth. In addition to these dents, there is a puncture hole in the steel pole 5 in above the base. This puncture hole is approximately 3.0 in wide by 3.5 in high, and has sharp edges. Details of the damage are shown in Figure 142. The access port on this pole is large, both in perimeter geometry as well as the height and thickness of the side wall (that reinforces the access port) extending outwards from the surface of the pole. The reinforcing side wall is approximately 5 in from the pole surface as the curvature of the pole increases away from the center of the access port.

(a) Interior view showing puncture

(b) Dented area and puncture

Figure 142. FD-2 dents and puncture prior to repair

This pole was repaired with a wet epoxy/basalt fiber FRP wrap. The dents and the puncture hole were filled with epoxy before the wrap was applied. The main body of the wrap was a 14 in wide laminate centered horizontally over the dent. The width of the wrap was chosen so that the wrap did not cover the access port and was symmetrical over the damaged areas. The wrap extended vertically from the base plate approximately 3'-6 1/8". This height was selected to allow a 6 in high transverse wrap to be applied to the top of the repair system above the access port. The lower transverse wrap was 11 in high, covering the pole surface between the base plate and the bottom of the access port. The pole and repair geometry, including placement of displacement and strain gauges, are shown in Appendix A. The FRP reinforcing ratio at the base was approximately 34% (area of FRP was not adjusted for fiber volume fraction).

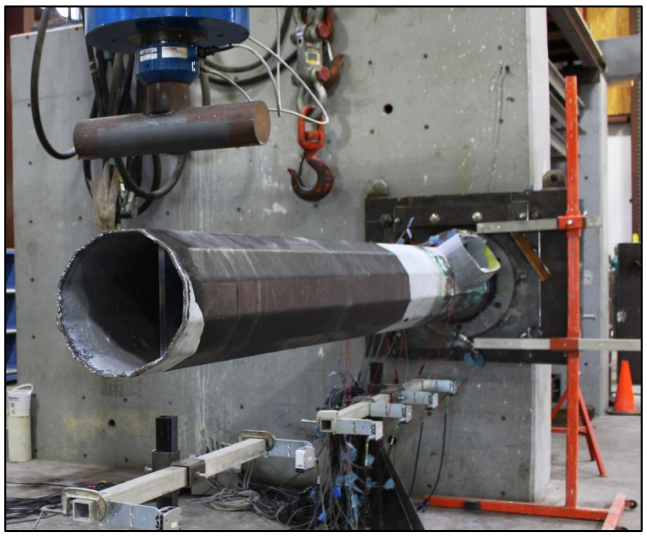

Figure 143. FD-2 test configuration

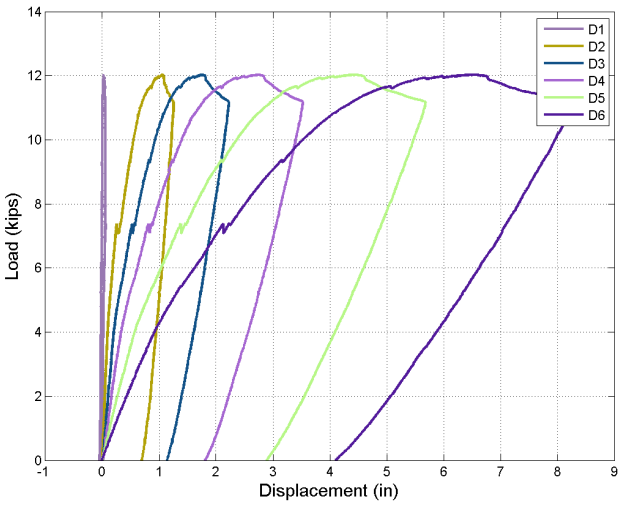

Figure 144. FD-2 load-displacement data

The pole was tested to failure in a cantilever configuration, as shown in Figure 143. The reinforced access port (with substantial side wall) is clearly visible in the figure. The load-

displacement and load-strain data are shown in Figure 144 and Figure 145, respectively. The locations of the various strain gauges are shown in Figure 146.

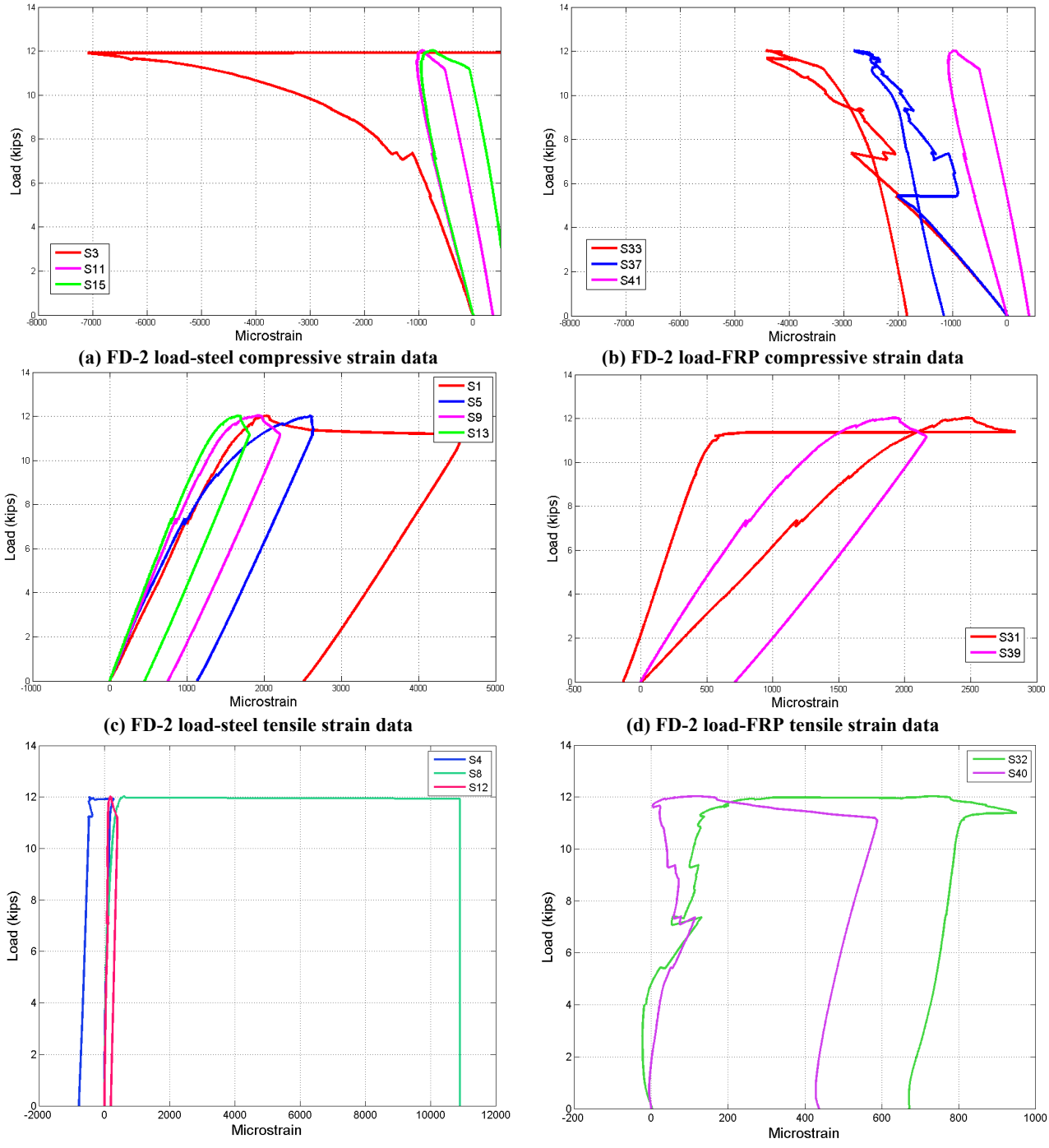

(a) FD-2 load-steel compressive strain data

(b) FD-2 load-FRP compressive strain data

(c) FD-2 load-steel tensile strain data

(d) FD-2 load-FRP tensile strain data

(e) FD-2 load-steel transverse strain data

(f) FD-2 load-FRP transverse strain data

Figure 145. FD-2 load-strain data

The peak load achieved was approximately 12 kip. The theoretical yield load of the pole is 13 kip; therefore, the repair was largely successful in returning the pole to the estimated capacity. The undamaged capacity was computed without the presence of the access port, puncture holes,

etc., and therefore, the wrap appears to have added substantial capacity to the specimen. The peak steel strains at section 1 were 5000 με and -7000 με in tension and compression, respectively, indicating substantial yielding of the substrate. The steel strains closer to the base would have been larger, and the formation of the plastic hinge at the base is evident from the transverse strains mobilized in the FRP at section 1 near the peak load.

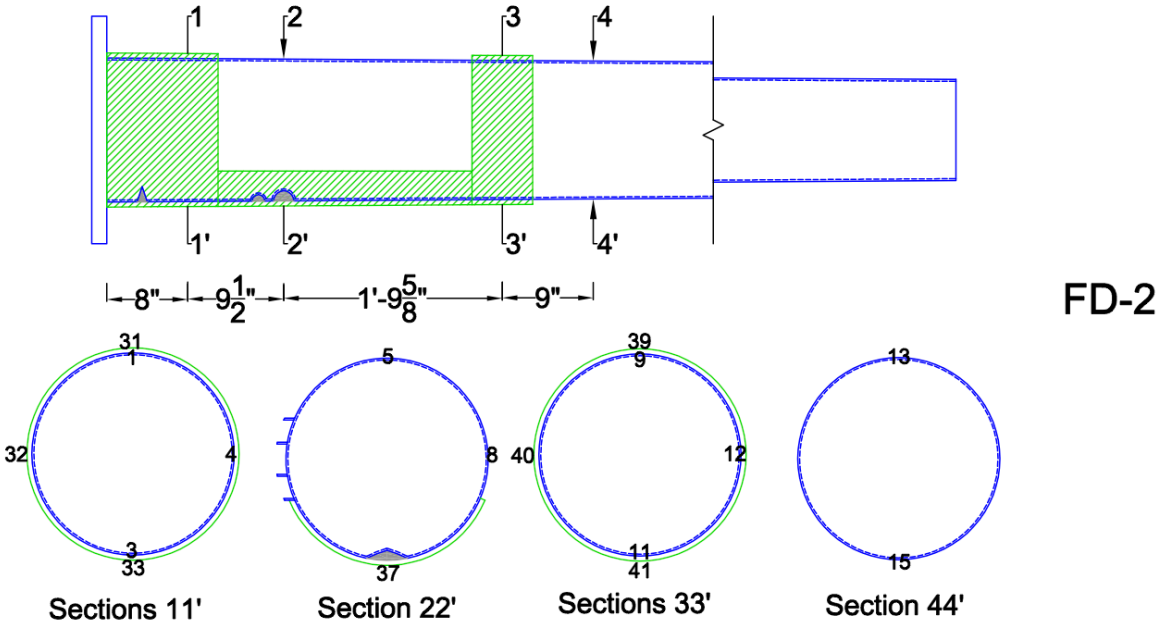

Figure 146. FD-2 strain gauges

The strain data shows clear debonding at section 1 on both the tension and compression sides. It appears the compression face debonding occurred around 7 kip and may be related to failure of the dent filler. There is a jump in the load-displacement at this load. The tension debonding did not happen until just after the peak load and slight softening had occurred. This is confirmed with the failure pictures shown in Figure 147 (b)-(d). The transverse strains on this pole are small, indicating perhaps the wrap was not engaged or not developed as it should have been (or the location of the transverse gauges were not in the right place). The reason for failure may be due to compressive steel failure at the location of the puncture. Review of the original pole photos prior to repair indicates that the gash is substantial. This may have caused the steel to fold inwards rather than dilate the cross-section outwards.

Interestingly, this doesn't explain why the estimated yield load wasn't reached, although the effect of the dented region on the capacity was also observed to be lower for non-round steel poles in the component-level tests. The compression steel gauges show extremely high strain (well in excess of yield). It appears the tensile steel gauge reaches yield at the peak load, which may be significant. The strain gauge (tensile steel S5) just in front of the access port shows higher strain than even S1, indicating the extremely large access port side wall may have been causing torsion and stress concentrations within the section, even though it may have increased the initial elastic stiffness of the pole. The effect of torsion on the cross-section appears to have played a role in the debonding and buckling pattern visible in Figure 147 (b).

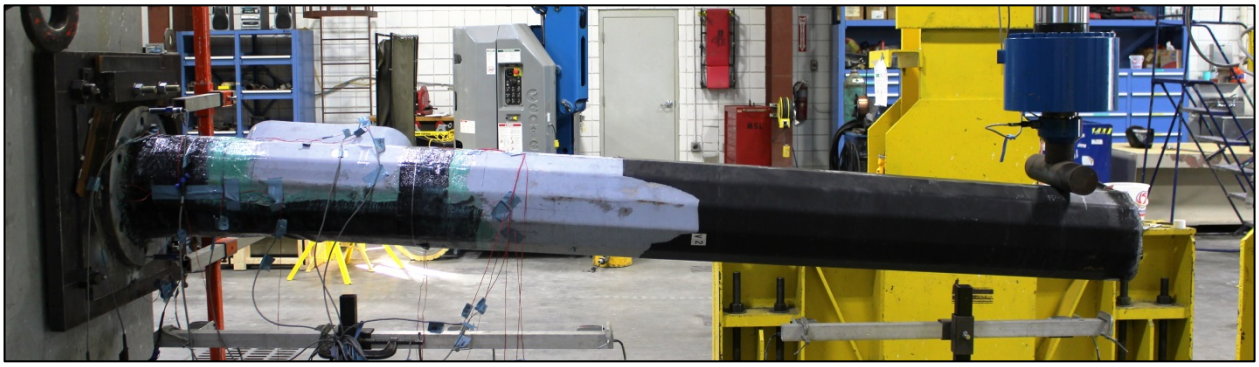

(a) Deflected shape of pole during loading

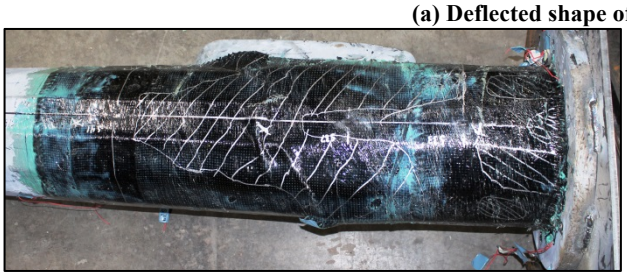

(b) Compression face – debonded FRP

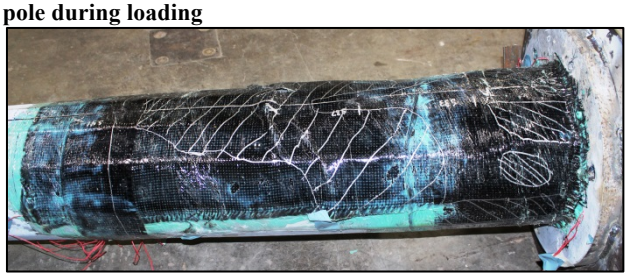

(c) East face – debonded and ruptured FRP

(d) West face – debonded and ruptured FRP

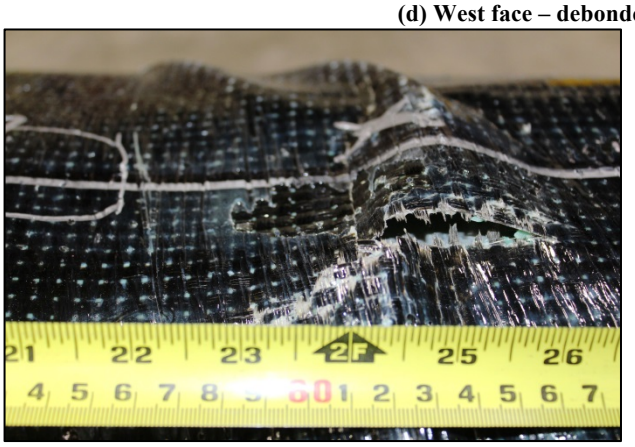

(e) Ruptured and buckled FRP

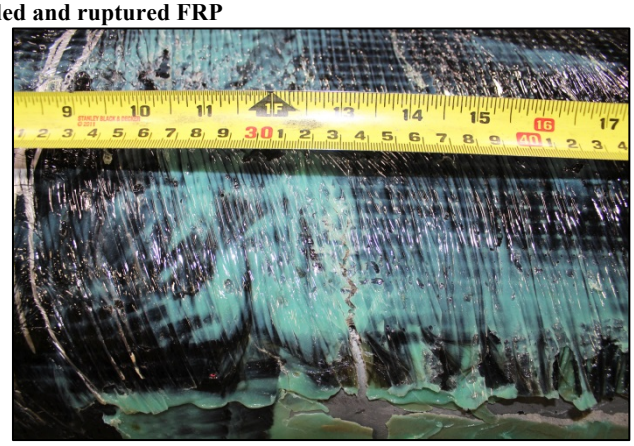

(f) Ruptured FRP

Figure 147. FD-2 failure modes

While the amount of FRP in the longitudinal direction appears to have been sufficient on this pole, the transverse layer does not appear to have been extended far enough up the cross-section. This is particularly evident in Figure 147 (a) and partially explains the relatively small transverse strains mobilized during the tests. The longitudinal wrap appears to have completely debonded from the pole both at the location of the access port, as well as the location on the opposite face of the pole, as shown in Figure 148. Either the size of the longitudinal wrap provided was not sufficient to develop the circumferential strains, or the debonding evident in Figure 148 occurred because of voids and imperfections during wrapping because of the 12-sided geometry of the pole.

(a) Delamination and separation of the transverse wrap near the access port

(b) Delamination and separation of the transverse wrap on the face opposite to the access port

Figure 148. FD-2 transverse wrap delamination

5.2.1.3 FD-3

Pole FD-3 is circular and has two pedestrian crosswalk signal buttons and an access port (see Appendix A). This pole has two major dents, as shown in Figure 149, in addition to some minor damage closer to the base. The deepest dent is located approximately 4 ft above the base plate and is 2.56 in deep (21% of the undented diameter). The dent center is approximately 145° from the access port centerline. The pole was repaired with a single-layer of glass fibers saturated with a polyurethane matrix. The wrap geometry consists of a main 20 in wide 5 ft long laminate beginning at the base of the pole and four circumferential wraps located 0′, 2′ 3.5″, 4′ 2.5″, and 5′ 5.5″ above the base plate. The bottom three transverse circumferential wraps were 9 in wide and the last one 6 in wide. These full-perimeter wraps protect against premature delamination of the main wrap. The FRP reinforcing ratio at the base was approximately 40% (area of FRP was not adjusted for fiber volume fraction). The pole is shown in the cantilever test configuration in Figure 150.

Figure 149. Vehicular dents present in FD-3 prior to repair

Figure 150. FD-3 test configuration

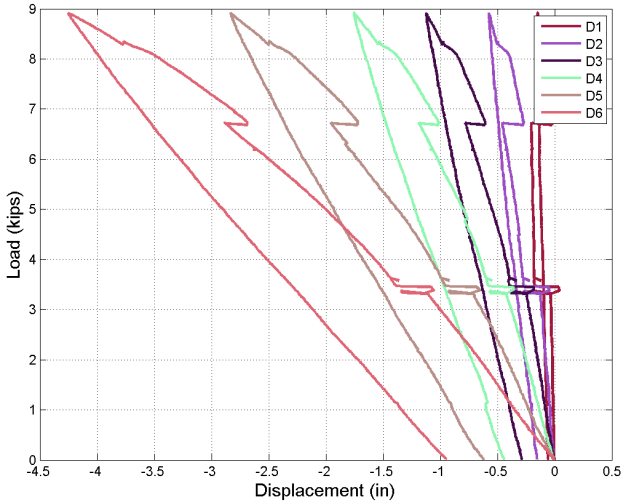

Figure 151. FD-3 Test 1 load-displacement data

Pole FD-3 was tested twice, hence the test data is identified here as originating from Test 1 and Test 2, respectively. The loading was stopped the first time (Test 1), because the wrong load cell was connected to the data acquisition system. The specimen was unloaded and the 50 kip load cell connected before commencing with Test 2. The load-displacement and load-strain data for

Test 1 are shown in Figure 151 and Figure 152, respectively. The locations of the various strain gauges are shown in Figure 155.

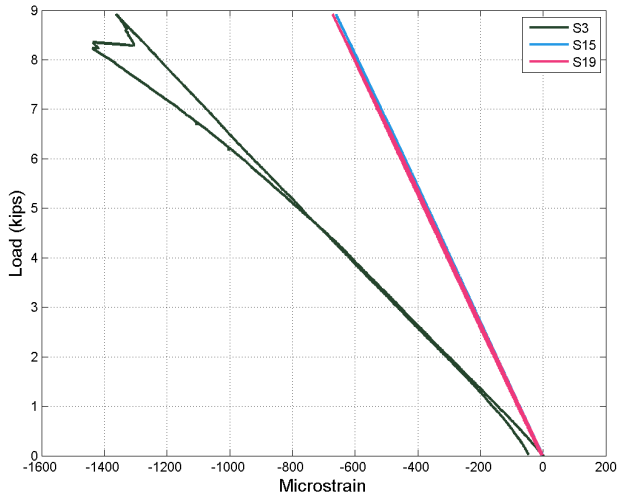

(a) FD-3 Test 1 load-steel compressive strain data

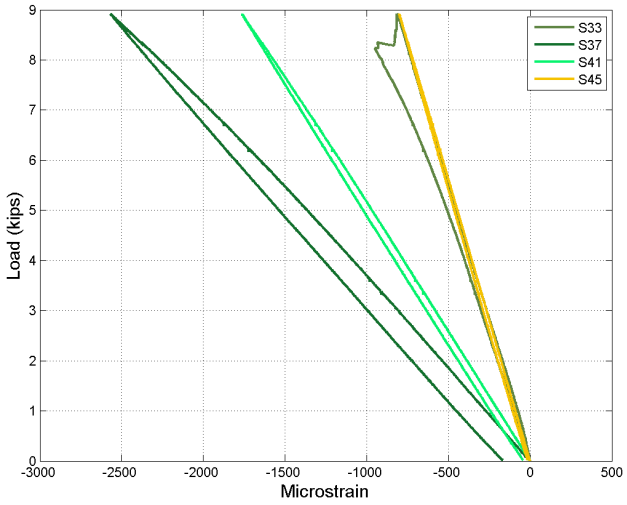

(b) FD-3 Test 1 load-FRP compressive strain data

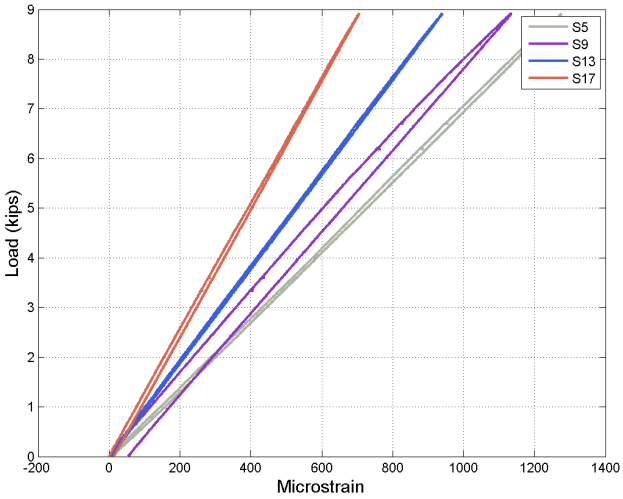

(c) FD-3 Test 1 load-steel tensile strain data

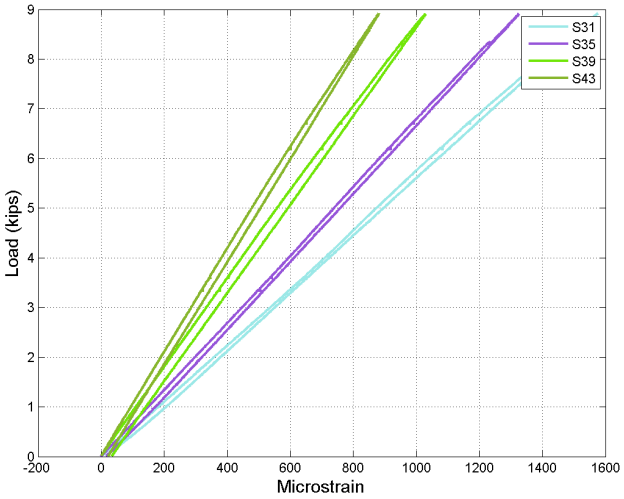

(d) FD-3 Test 1 load-FRP tensile strain data

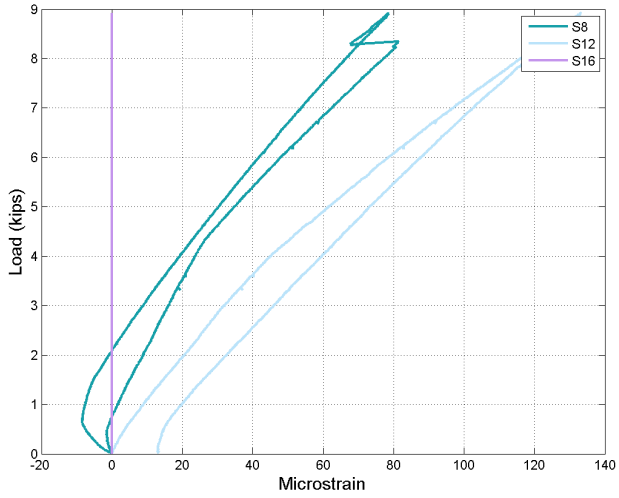

(e) FD-3 Test 1 load-steel transverse strain data

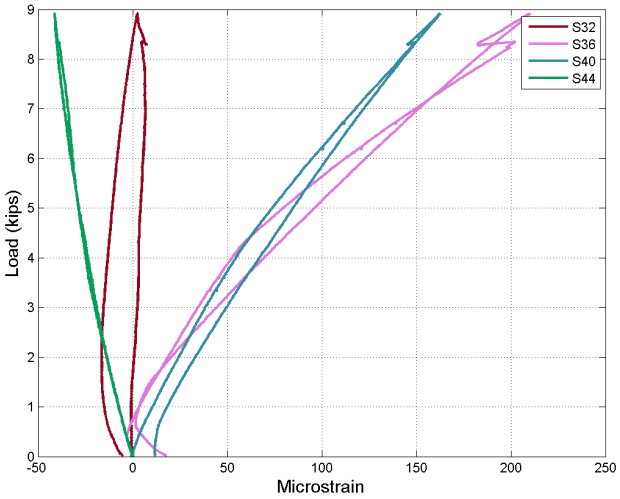

(f) FD-3 Test 1 load-FRP transverse strain data

Figure 152. FD-3 Test 1 load-strain data

The peak load achieved during Test 1 was approximately 9 kip. At this load level, a majority of the responses from the longitudinal strain gauges were linear. Although clearly the softening of the elastic stiffness had occurred, especially after the slight jump in load at 8.3 kip. The sudden drop in the compressive steel and FRP strain at section 1 indicates the dent fill near section 2 was crushed or there was debonding on the compression face (potentially in the locations of the dent fill material). A residual displacement of approximately 0.9 in was present after unloading. No debonding was evident during the first test. However, gauge S1 was not recording data and there appears to have been no initial strain compatibility between the compressive metal and FRP gauges at section 1.

The load-displacement and load-strain data for Test 2 are shown in Figure 153 and Figure 154, respectively. The locations of the various strain gauges are the same as used for Test 1 and shown in Figure 155. Test 2 was halted at approximately 11.5 kip of applied load due to the actuator stroke limit being reached. The residual displacement from Test 1 was removed from the displacement readings shown in Figure 153. The load was still gradually increasing, although the specimen was clearly near the peak load. The displaced shape of the pole at the peak load is shown in Figure 156 (a).

The theoretical yield load of the pole was 10.2 kip; therefore, the repair was likely successful in returning the pole (with extensive impact damage) to the original capacity. As with FD-5, the dented regions were higher up the pole and subjected to a lower moment demand than the base of the pole. Therefore, the ultimate failure would likely have been governed by yielding at the base. However, it also indicates that the FRP repair was sufficient to prevent premature hinging at either section 2 or 3. The Test 1 peak load was almost the same as the load at the marked change in stiffness observed in Test 2; however, there is little indication from the strain data of a correspondence.

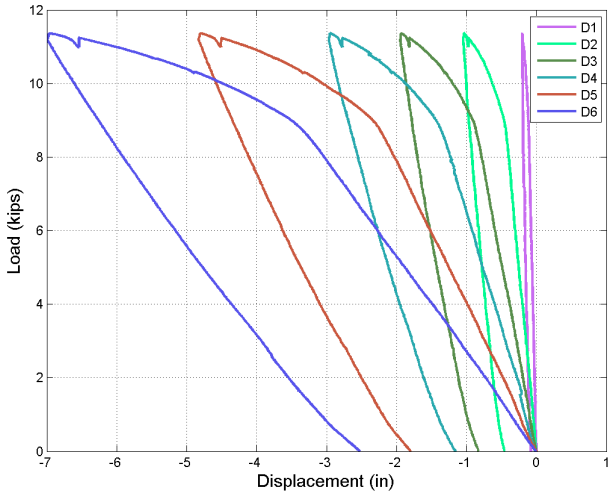

Figure 153. FD-3 Test 2 load-displacement data

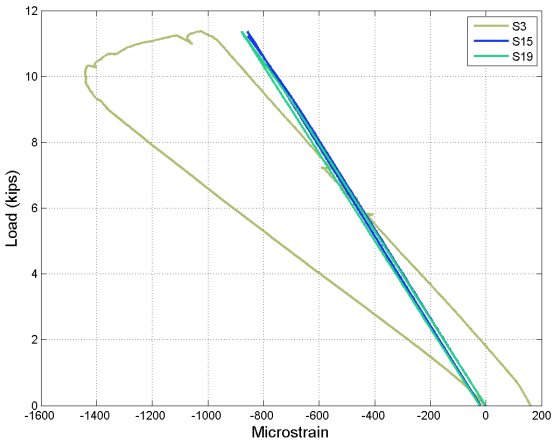

(a) FD-3 Test 2 load-steel compressive strain data

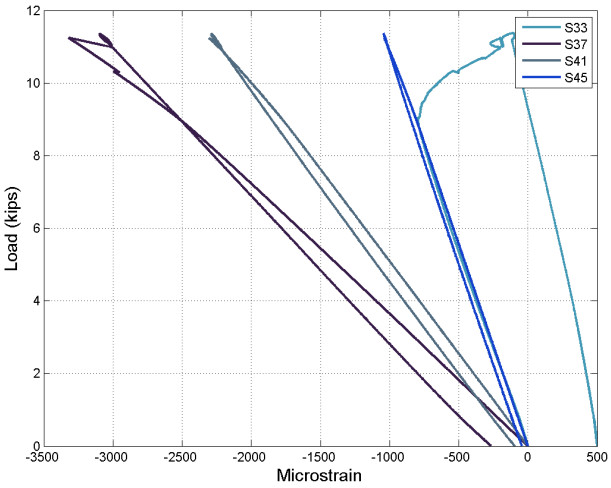

(b) FD-3 Test 2 load-FRP compressive strain data

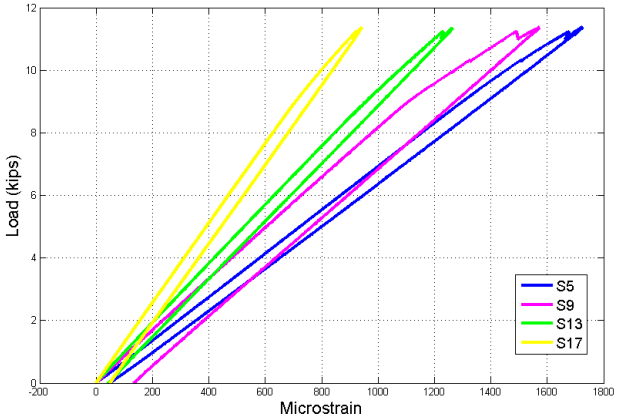

(c) FD-3 Test 2 load-steel tensile strain data

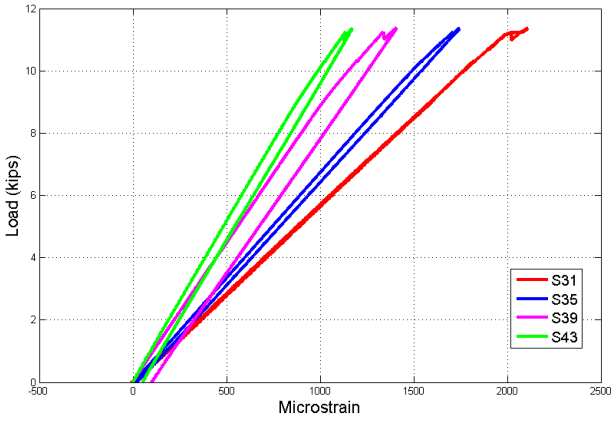

(d) FD-3 Test 2 load-FRP tensile strain data

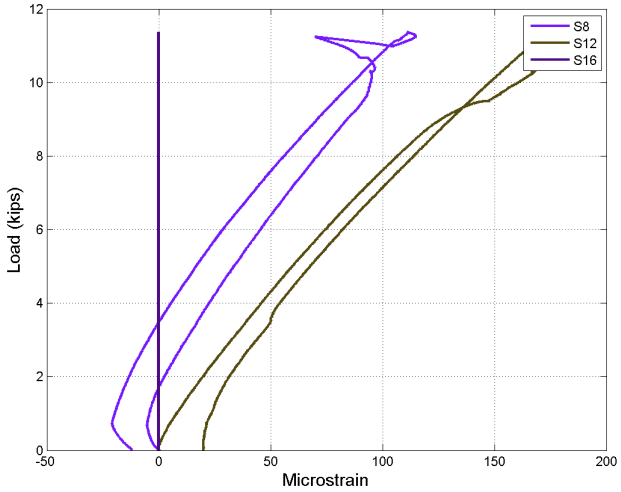

(e) FD-3 Test 2 load-steel transverse strain data

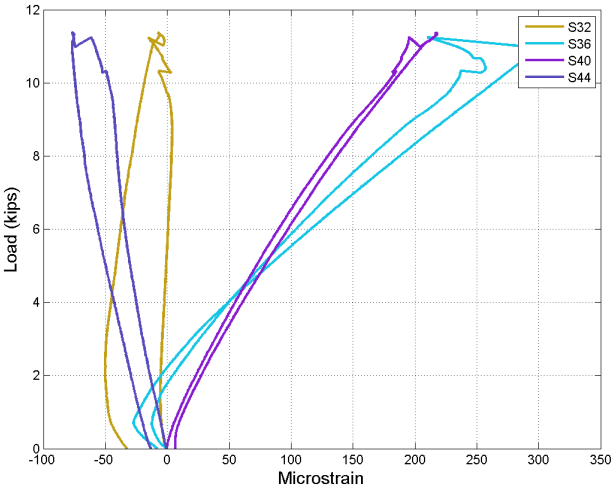

(f) FD-3 Test 2 load-FRP transverse strain data

Figure 154. FD-3 Test 2 load-strain data

The strain stiffnesses appear similar to Test 1, except S3 and S33, which exhibited the drop in strain at 8.3 kip in Test 1. No significant transverse strains were registered during Test 1 or Test 2. The gauge S1 was missing (base tension steel gauge), so it was difficult to confirm if yielding occurred at or near the base. Tension steel gauge S5 is located just in front of the access port, so

stress concentration at this location may be limiting the capacity of the pole. Inspection of the pole indicates some bulging of the wrap at the base; however, no debonding is evident, except from the potential area on the compression face shown in Figure 156 (b). The bulging may be due to the compressive failure, or may be due to accumulation of primer during the original repair in the presence of the minor damage at the base. Compression damage is corroborated by the FRP compression strain readings at gauge S37.

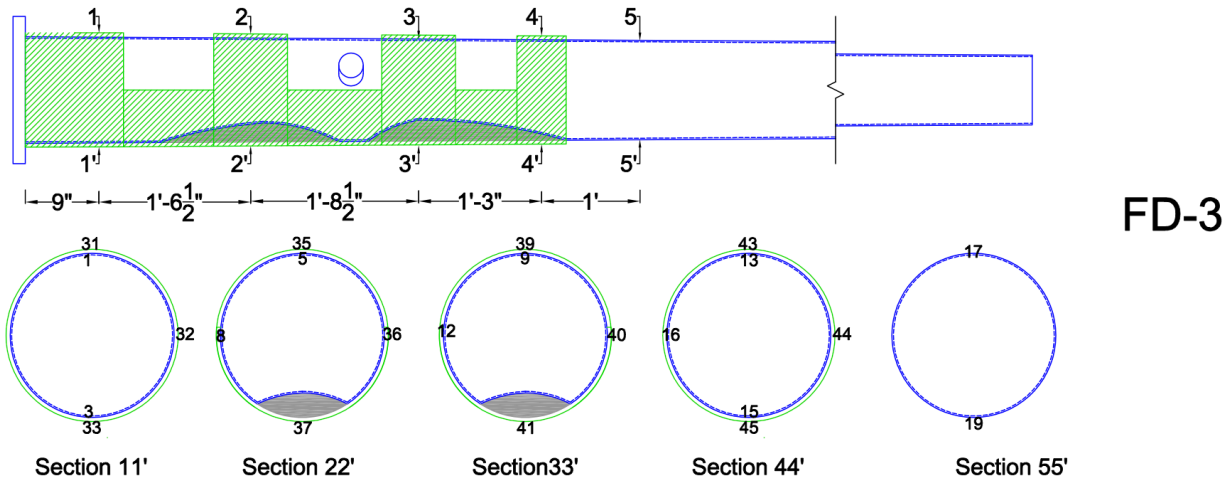

Figure 155. FD-3 strain gauges

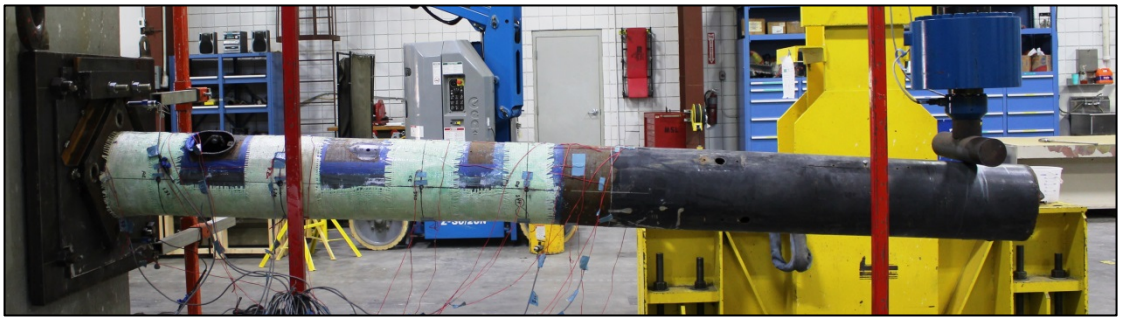

(a) Failed shape

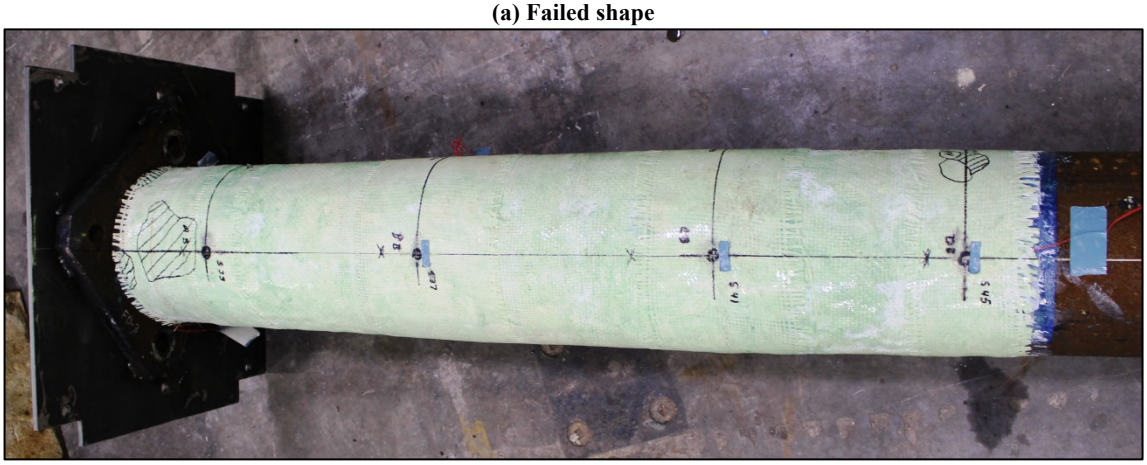

(b) Compression face of FRP

Figure 156. FD-3 failure modes

5.2.1.4 FD-5

Pole FD-5 was dented quite severely in the field to a depth of approximately 2.56 in, or 24% of its outer diameter. The dent is centered 3'-8.5" above the base plate, and approximately 125° from the centerline of the access port (see Appendix A). The pole has both a small access port and a pedestrian button. The extents of the damaged region are large, as shown in Figure 157. The dent was repaired with a single-layer of basalt/polyurethane FRP wrap over an epoxy fill. A main wrap laminate was used which extended 20 in around the pole's circumference, beginning 6 in above the base plate and extending 5'-7". Four transverse circumferential wraps were placed on top of the main wrap and were 6 in, 12 in, 9 in, and 6 in wide, from the bottom, respectively. The FRP reinforcing ratio at commencement of reinforcement (~6 in above the base) was approximately 40% (area of FRP was not adjusted for fiber volume fraction).

Figure 157. Vehicular damage to FD-5 prior to repair

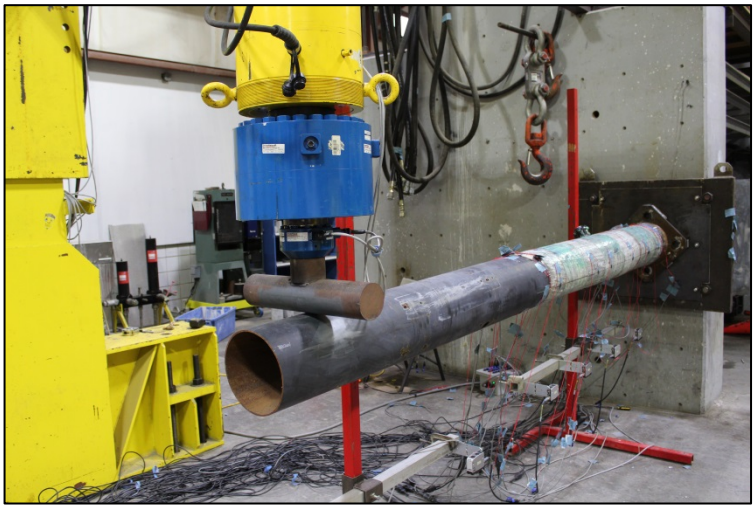

Figure 158. FD-5 test setup

The pole was tested as shown in Figure 158. Although the pole was dented substantially, the location of the primary dent (above the base) ensured a reduction in the peak moment demand experienced at the dented cross-section. However, loading was stopped before failure of the pole during Test 1 due to excessive bending/prying of the base plate connection to the concrete buttress (the ½ in plate). As mentioned in Section 5.1.1, this prompted the addition of 2 bolts to

prevent future deformation of the pole base connection. The deformation of the plate (as seen in Figure 161) caused the side welds to fail and there may have been some yielding in the base flange. Loading was applied until failure in Test 2 after the changes to the pole base connection were made. The load-displacement and load-strain data for Test 1 are shown in Figure 159 and Figure 160, respectively. The locations of the various strain gauges are shown in Figure 164.

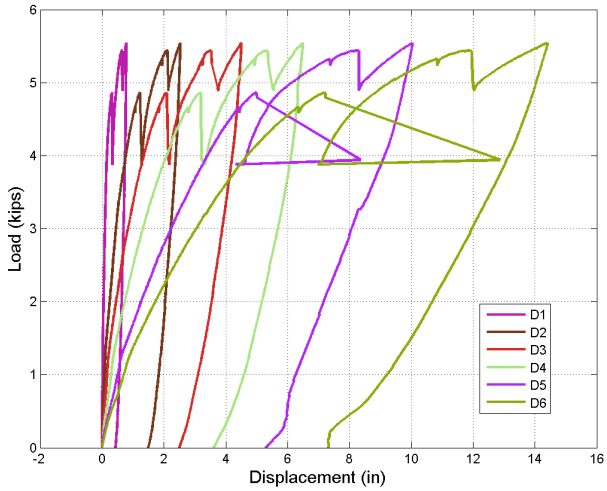

Figure 159. FD-5 Test 1 load-displacement data

The peak load achieved during Test 1 was approximately 5.5 kip. However, based on the load-displacement curves in Figure 160 (a), it is evident there were two occasions where yielding of the connection plate, rupture of welds, and/or slip of the bolts resulted in ratcheting (sudden jumps in displacement, or due to displacement-controlled loading, a sudden drop in load at the same displacement). This occurred first at 4.8 kip and then again at 5.5 kip. Unloading of the sections can be discerned in a majority of the strain measurements in Figure 160. The excessive deformation of the pole due to rotation near the connection is evident from the displaced shape in Figure 161 (a). The prying of the ½ in plate from the 2 in plate at the end of Test 1 is shown in Figure 161 (b).

Substantial yielding of the cross-section below the access port had initiated during Test 1. The compressive strain in S3 reached -6000 με and tensile strain in S5 and S9 were near yield. In addition, the transverse strains at section 3 were rapidly increasing (section 3 is in the region of minor damage below where the main dented profile begins), indicating hinge formation in the vicinity of the pole base. The expansion of the fill material or engagement of the transverse wrap at section 3 resulted in an increase in the strain stiffness after the first load jump. It is also likely that FRP buckling had initiated in the center of the dent (sections 4 and 5), given the sudden increase in compressive strain at the first load jump.

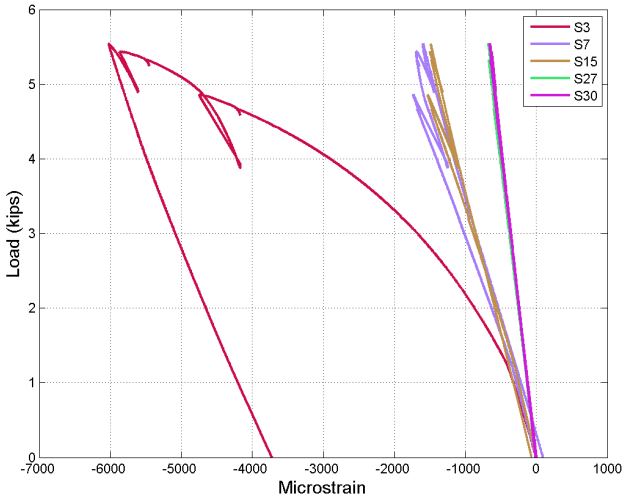

(a) FD-5 Test 1 load-steel compressive strain data

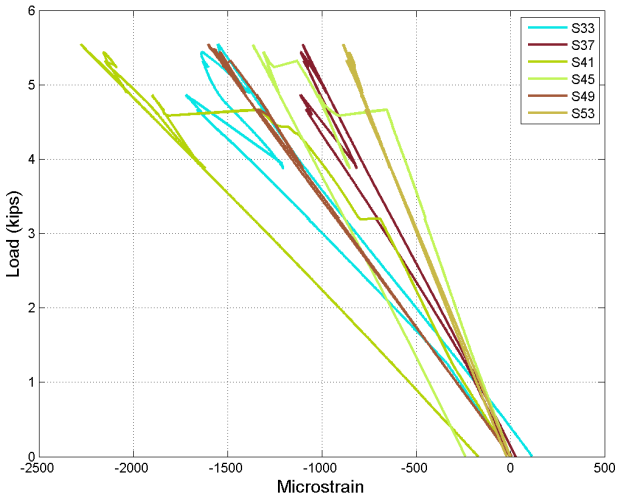

(b) FD-5 Test 1 load-FRP compressive strain data

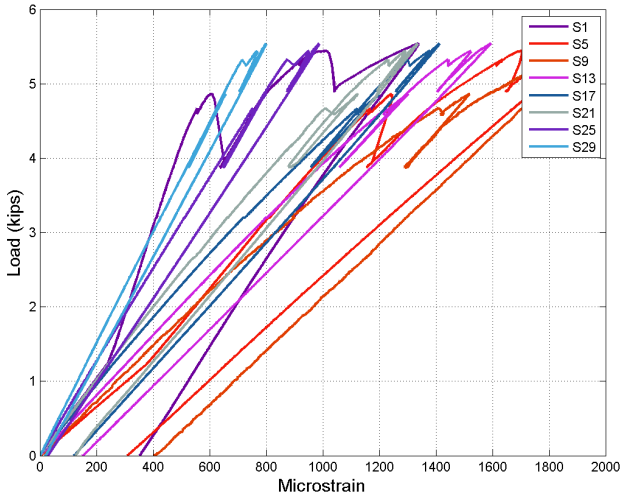

(c) FD-5 Test 1 load-steel tensile strain data

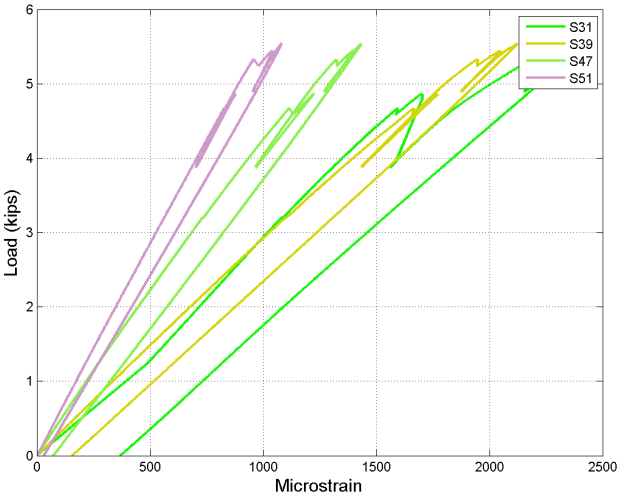

(d) FD-5 Test 1 load-FRP tensile strain data

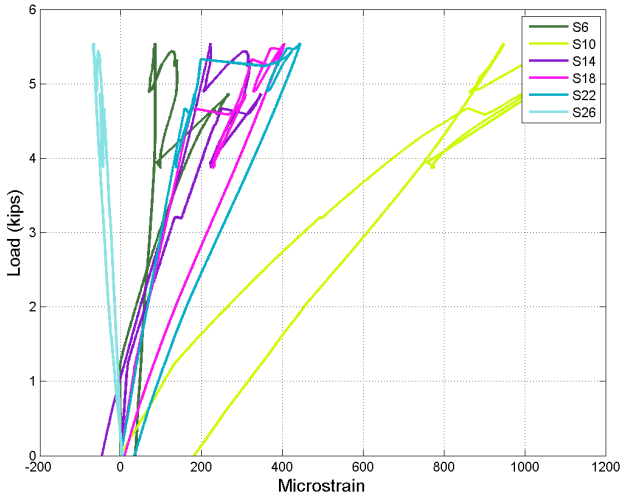

(e) FD-5 Test 1 load-steel transverse strain data

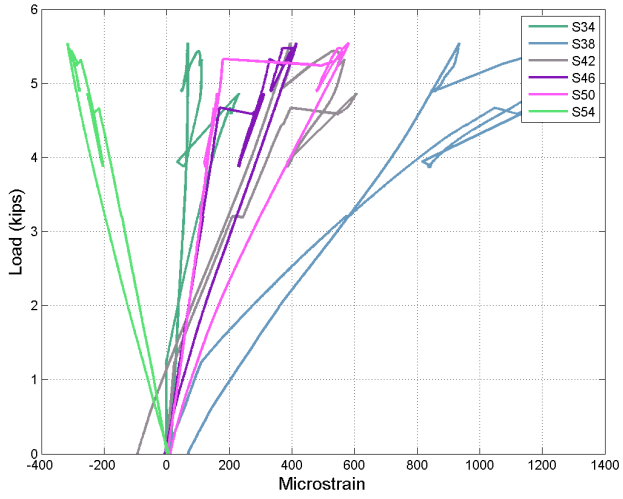

(f) FD-5 Test 1 load-FRP transverse strain data

Figure 160. FD-5 Test 1 load-strain data

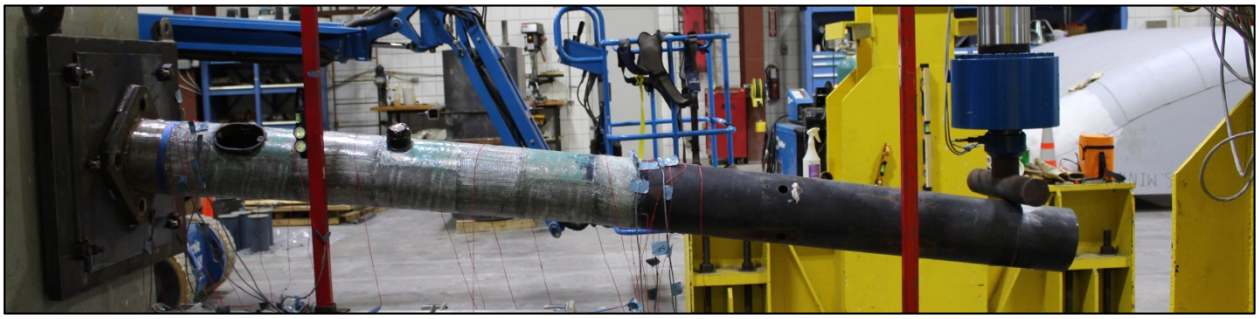

(a) Displaced shape

(b) Compression face of FRP

Figure 161. FD-5 Test 1 deformed shape and base plate failure

The load-displacement and load-strain data for Test 2 are shown in Figure 162 and Figure 163, respectively. The locations of the various strain gauges are the same as Test 1 and shown in Figure 164. During Test 2, the peak load achieved was approximately 8.3 kip. The estimated yield load for the undamaged pole was 8 kip; therefore, it appears the repair was successfully in returning the pole to the original capacity. Similar to FD-3, the location of the major damage was at a location of lower moment demand; however, the repair was successful in preventing the hinge from forming in these locations.

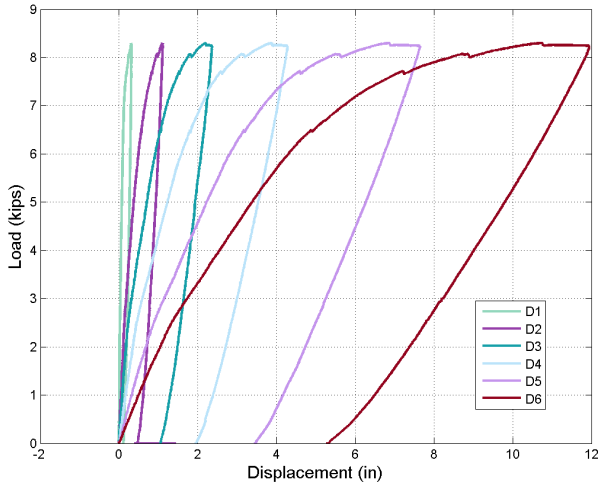

Figure 162. FD-5 Test 2 load-displacement data

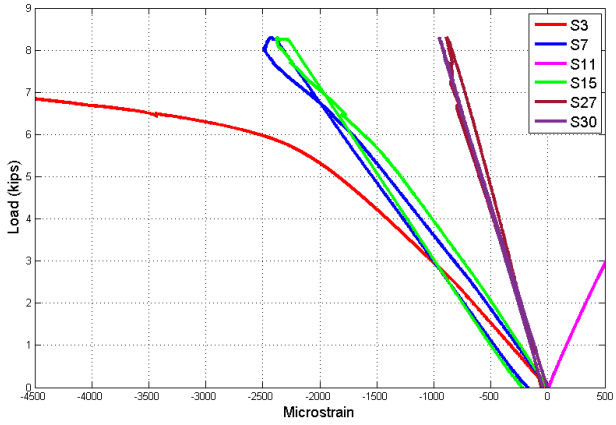

(a) FD-5 Test 2 load-steel compressive strain data

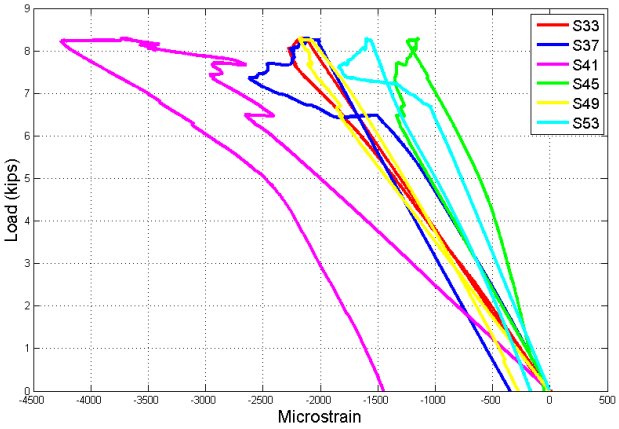

(b) FD-5 Test 2 load-FRP compressive strain data

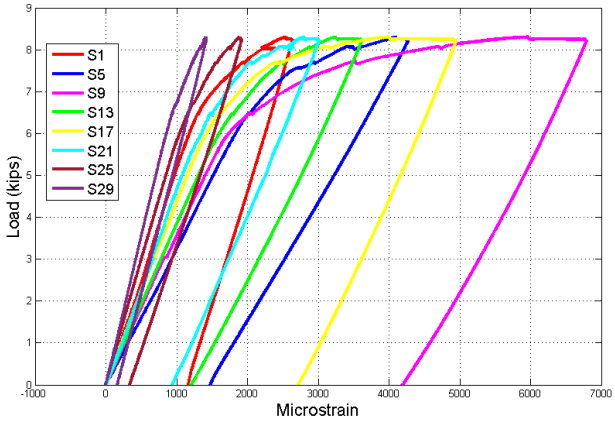

(c) FD-5 Test 2 load-steel tensile strain data

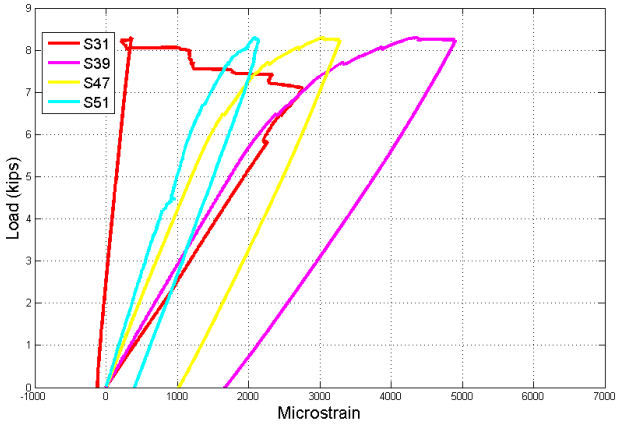

(d) FD-5 Test 2 load-FRP tensile strain data

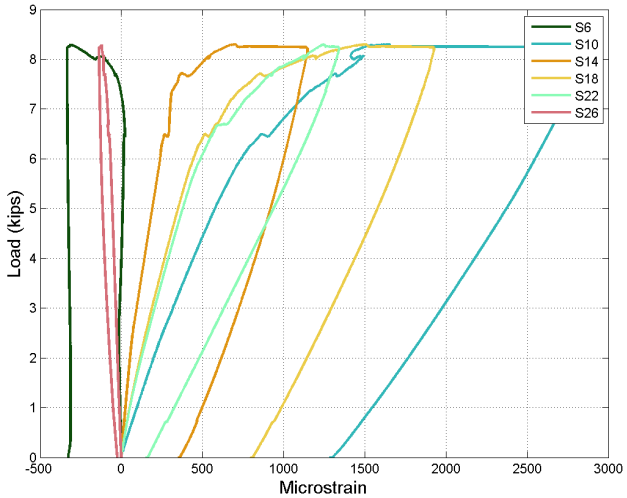

(e) FD-5 Test 2 load-steel transverse strain data

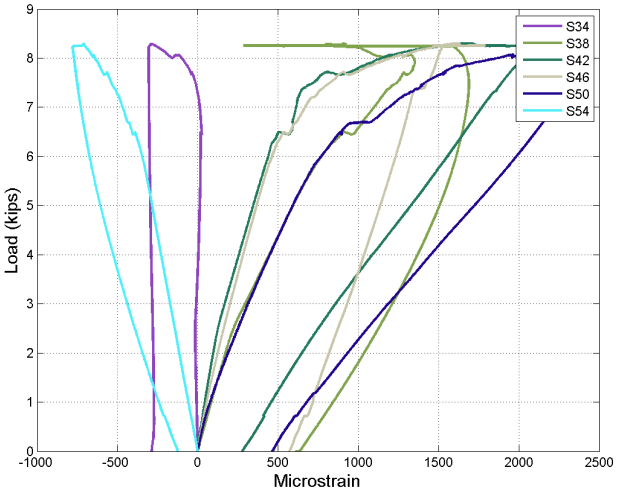

(f) FD-5 Test 2 load-FRP transverse strain data

Figure 163. FD-5 Test 2 load-strain data

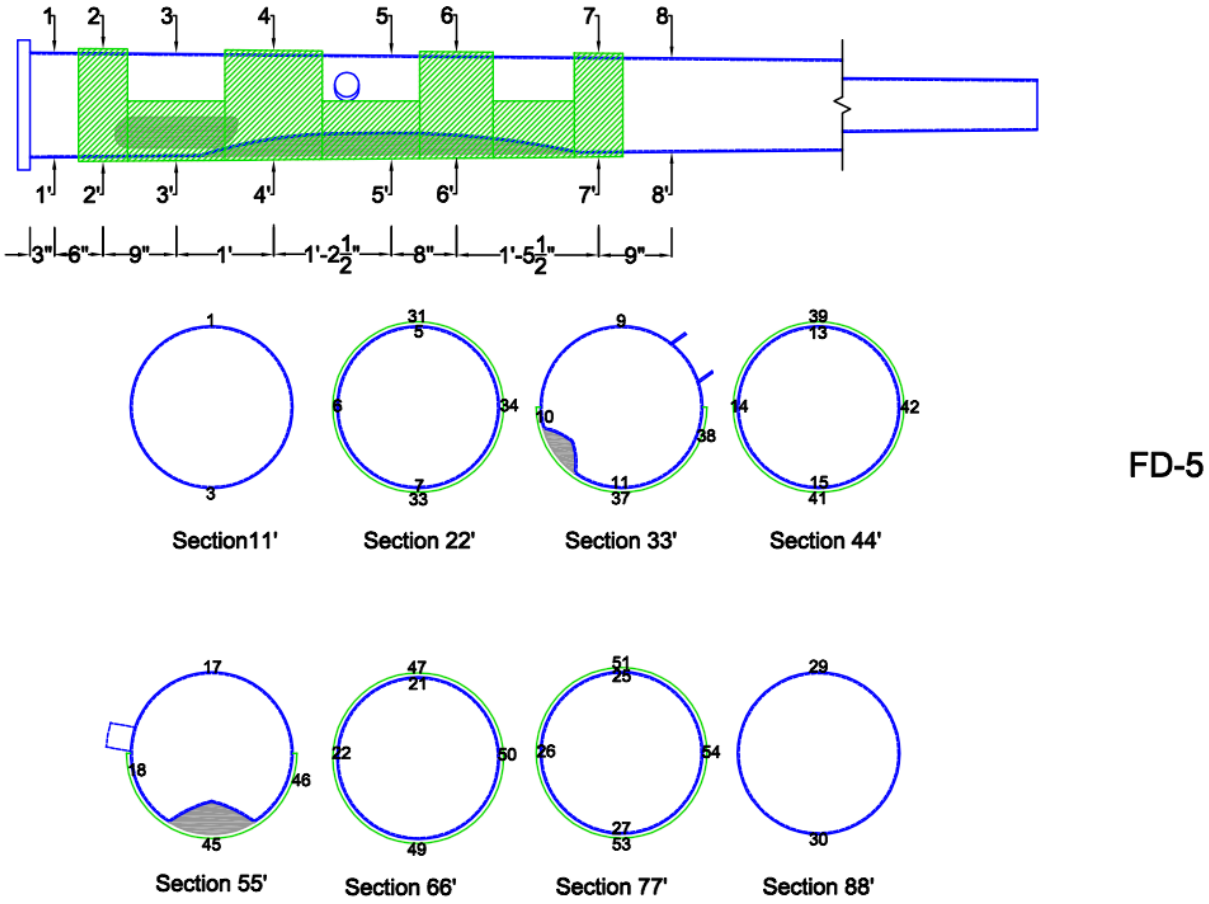

Figure 164. FD-5 strain gauges

The compressive steel hinged between S3 and the base flange, as visible in Figure 165 (b). Buckling in the FRP occurred on the bottom side of the pole about 20 to 23 in from the top of the base flange and wrapped its way up toward the top of the side of the pole where there was no FRP, as shown in Figure 165 (c). This is consistent with the FRP compressive strain measurements recorded in S41. Steel yielding in tension was evident for all gauges between sections 2 and 5, indicating a distributed plastic hinge forming because of the tapering of the moment demand and the capacity in the presence of the dent. A corresponding increase in the transverse strains was recorded in a similar range of sections, and the transverse steel readings showed yielding at sections 3 and 5.

The strain stiffnesses between Tests 1 and 2 were very similar, except for S3, S41, S45, and S38. As mention, the steel was already yielding during Test 1, as the compression FRP had potentially debonded, which was the reason for the different stiffnesses. Debonding was evident in the strain recordings at section 2 on the tension face. The load at debonding was approximately 7 kip and corresponds to the load at which the compressive steel yielded rapidly (as mentioned above). The transverse strain became negative (compression) at sections 2 and 7 during Test 2; however, it is not clear if this is because of the hinge formation, or whether it was because of the residual stresses that developed due to the prying of the base plate in Test 1.

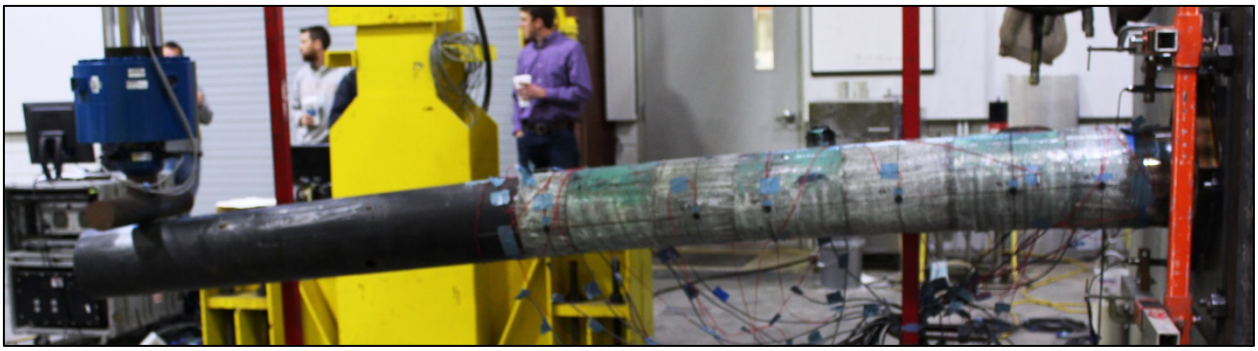

(a) Failed pole shape

(b) Buckled steel 2 in above base plate

(c) Buckled compression FRP fibers

Figure 165. FD-5 failure modes

5.2.2 Steel Induced-Damage Poles

An additional set of steel poles was dented in the laboratory to various depths. These poles were repaired with the FRP repair systems, and tested to failure in a cantilever-point load configuration. These 11-ft pole segments were taken undamaged from use in the field (and therefore had experienced an unknown amount of mechanical and environmental conditioning) and were dented using the method described in Chapter 4. The same test setup was used as with the field-damaged specimens. The poles have various diameters, and are dented to depths of 18 to 24% of their undented diameters. Each of the induced-damage steel poles is round, not multi-sided. Drawings of each pole, with is repair and instrumentation, can be seen in Appendix A.

5.2.2.1 ST-5

The base plate of pole ST-5 is a 1.5 in thick hexagon, and the diameter of the pole member at the joint with the base plate is 20.5 in. The pole has a 31 in high access port that is surrounded by a hexagonal plate. This plate begins approximately 8.75 in above the base plate and is 42.5 in in height. The pole was dented on the side opposite the access port, and the dent was centered 16 in above the base. The pole was dented to approximately 18% of its outer diameter, creating a 3.563 in deep dent. The repair system used consisted of glass fibers impregnated with an epoxy resin using traditional wet layup. As mentioned in the testing matrix, the repair for ST-5 was originally intended to be the pre-cured QB sheets. However, difficulties were encountered with

preventing voids underneath the pre-cured sheets, so the repair was performed using wet layup. The wraps were applied in the form of a main longitudinal wrap and two circumferential wraps, as shown in Figure 166 and Appendix A. The FRP reinforcing ratio at the base was approximately 36% (area of FRP was not adjusted for fiber volume fraction).

The pole was loaded to a maximum load of approximately 30.6 kips. The load-displacement and load-strain data are shown in Figure 167 and Figure 168. The locations of the various strain gauges are shown in Figure 169.

Figure 166. ST-5 test configuration

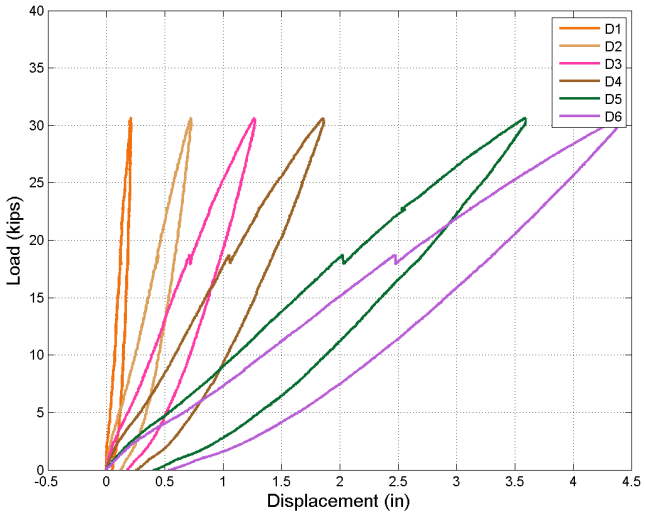

Figure 167. ST-5 load-displacement data

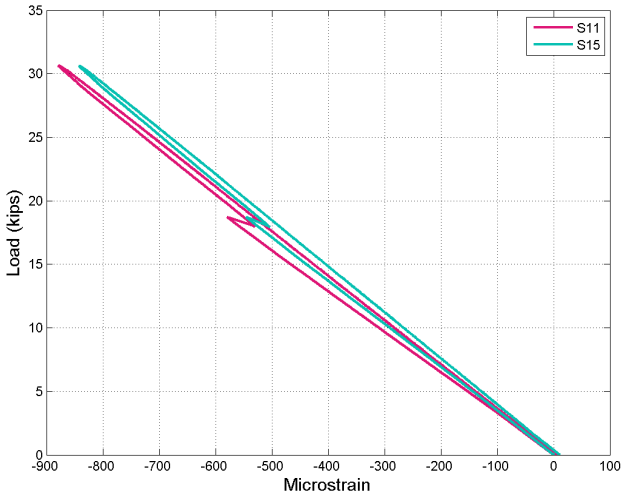

(a) ST-5 load-steel compressive strain data

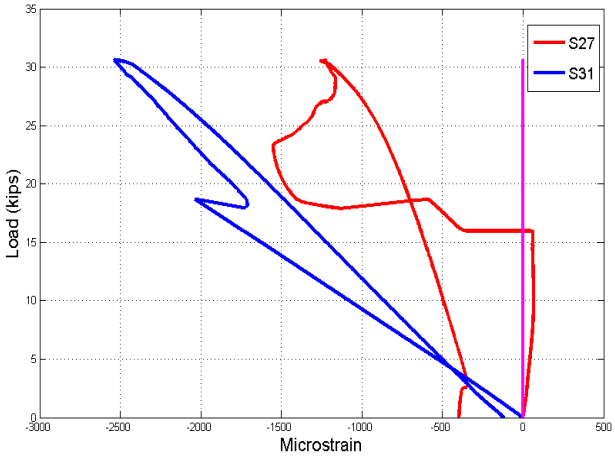

(b) ST-5 load-FRP compressive strain data

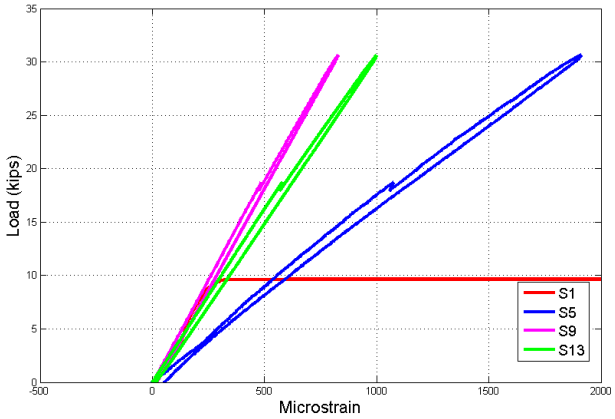

(c) ST-5 load-steel tensile strain data

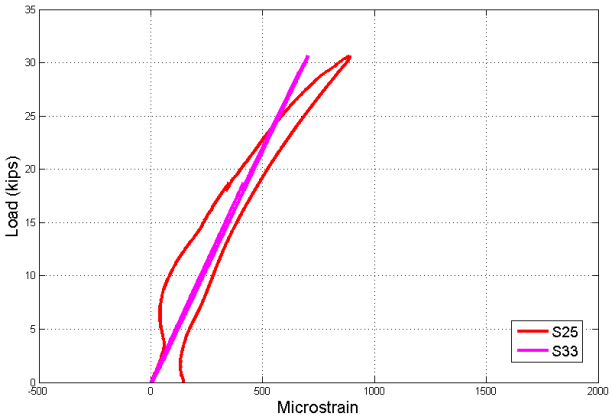

(d) ST-5 load-FRP tensile strain data

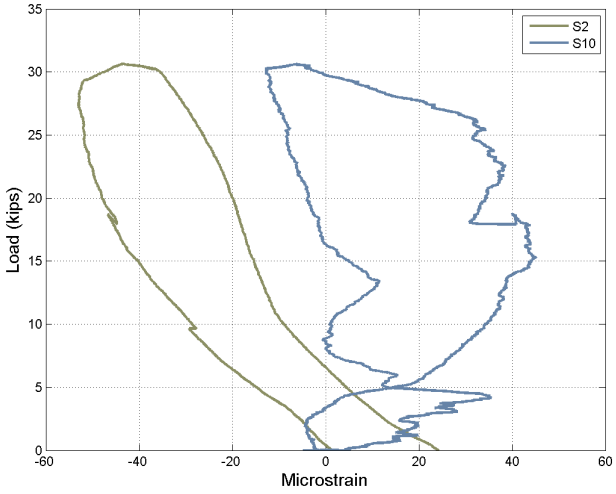

(e) ST-5 load-steel transverse strain data

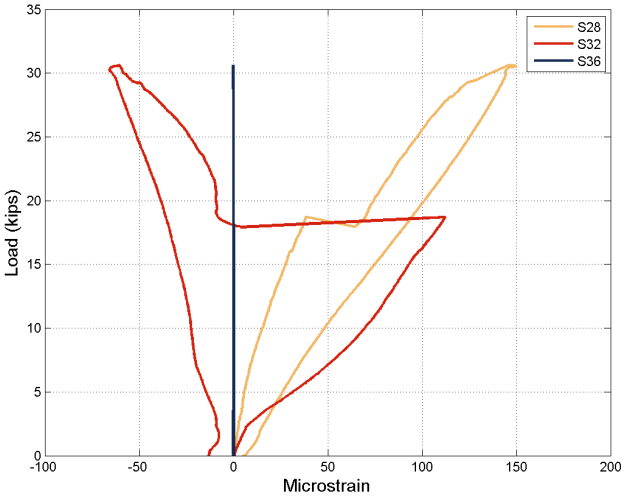

(f) ST-5 load-FRP transverse strain data

Figure 168. ST-5 load-strain data

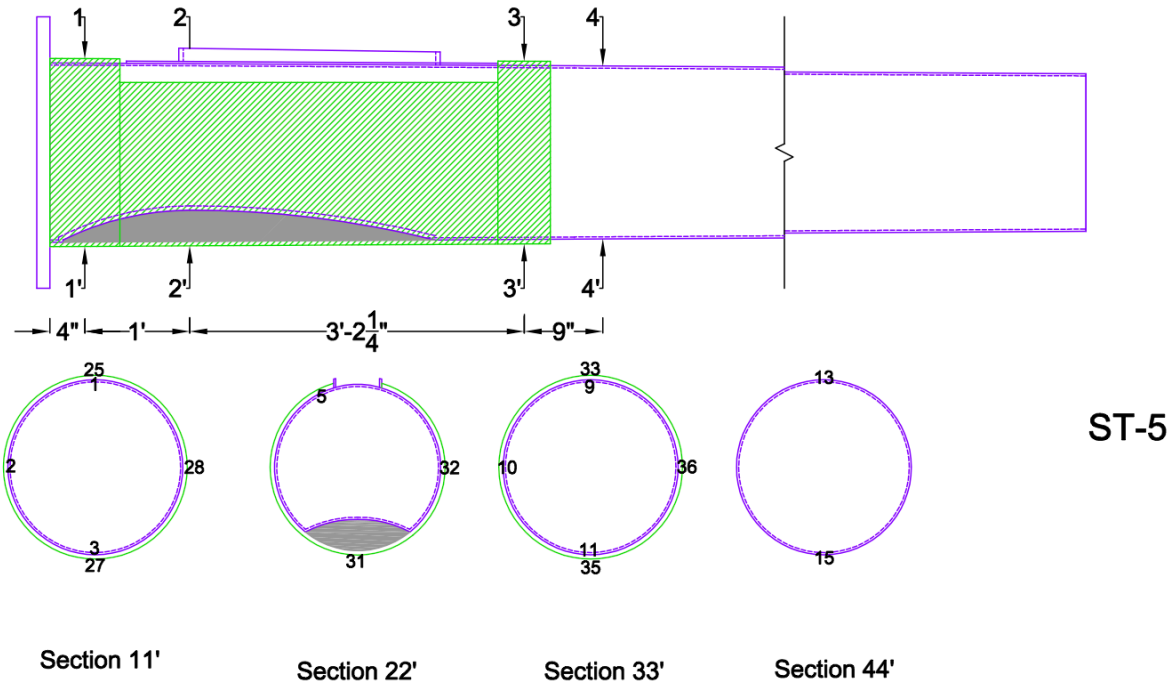

Figure 169. ST-5 strain gauges

The test was terminated prior to failure due to the capacity of the test setup being reached. A majority of the strain responses were still in the linear range; therefore, the pole may have carried a substantially higher load. In addition, a forensic investigation showed that the pole may have been strengthened on either side of the dent by inserting steel ribs, as shown in Figure 170 (a). Therefore, for this specimen it is difficult to ascertain the effectiveness of the FRP repair that was applied. The jump in the load that occurred around 18 kip appears to be from crushing of the fill material or local buckling of the FRP that was not visible on inspection, but may be indicated by the section dilation in Figure 170 (b). The compressive strain decreased at this load, but regained additional strain thereafter at all gauge locations.

The reinforced access port had an additional plate surrounding the side wall that prevented the transverse wraps from being placed close the center of the dented region. The transverse strains recorded during the test were correspondingly small. It is possible at the onset of hinging that S2, S28, and perhaps S10 and S36 would have recorded substantially higher strains. However, the presence of the base plate would have prevented substantial dilation of the cross-section at the location of the strain gauges at section 1. The only functioning transverse gauge near the center of the dent was S32, which indicates the cross-section began to unload at the jump in load.

(a) Dent viewed from inside the pole with additional steel ribs on either side of dent

(b) Slight dilation of cross-section in the region of the dent

Figure 170. ST-5 after testing

5.2.2.2 ST-6

ST-6 is an 18-sided pole with a rectangular, 31.38 in tall access port. The bottom of the access port is 14.31 in above the 1.5 in thick base plate. The diameter of the pole at the base is 20.25 in. A small, 1.25 in deep dent was found in the pole 13 in above the base plate and 90° from the access port when the pole was obtained from the field. An additional 3.75 in dent (19% of the outer diameter) was applied to the pole in the laboratory. This dent is centered 16 in above the base plate and 150° from the center of the access port and 120° from the existing dent. This pole was repaired with a glass/polyurethane composite wrap. The geometry of the pole and wrap are shown in Appendix A, and the test configuration is shown in Figure 171. The FRP reinforcing ratio at the base was approximately 40% (area of FRP was not adjusted for fiber volume fraction).

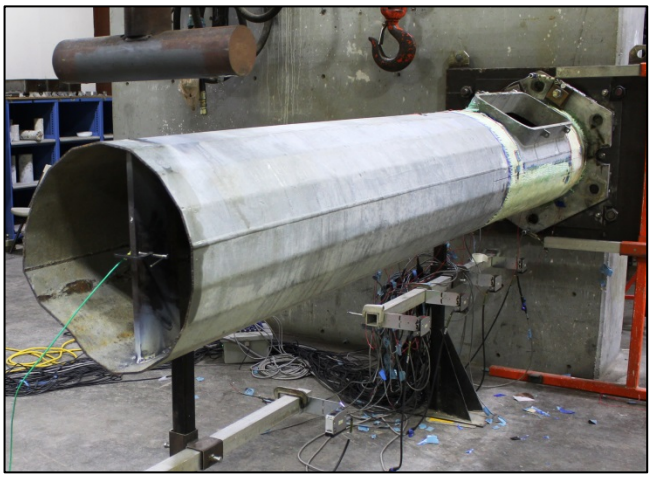

Figure 171. ST-6 test configuration

The pole was loaded to failure. The load-displacement and load-strain data are shown in Figure 172 and Figure 173, respectively. The locations of the various strain gauges are shown in Figure 174. This pole likely didn't have enough transverse FRP on it. Compared to the other monotonic large-scale specimens, this pole reached the lowest load with respect to the theoretical yield load. As with the component-level tests, the multi-sided steel specimens do not appear to exhibit the same beneficial strengthening. The displaced shape of the pole at the end of the test is shown in Figure 175.

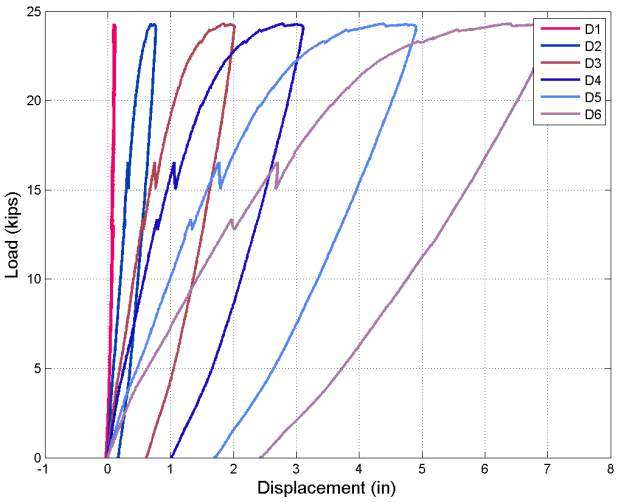

Figure 172. ST-6 load-displacement data

The FRP on the compression face at section 1 buckled at a relatively low load (approximately 14 kip). A small jump in the load-displacement is visible at this level. A substantial area of debonded and buckled FRP was evident after the test on the compressive face, as shown in Figure 176 (a), (b), and (d). A more substantial jump in the load occurred at 16.5 kip, at which point S3 was lost and the fill material crushed. The load continued to increase until the transverse strains in S4 (section 1), and the tension strains at the same section indicated yielding. Although no debonding on the tension face is evident in the strain data, several regions on the face of the pole opposite the access port showed debonding, as seen in Figure 176 (c).

Near the peak load, the laminate near S36 appears to have debonded or was forced into compression due to the rupture in the transverse FRP that developed on both sides of the pole, as shown in Figure 176 (e) and (f). This appears to have been the ultimate failure mode of the pole and initiated in the longitudinal wrap at the location where the transverse strip was terminated. Due to the lip surrounding the reinforced access port, the actual width of the transverse strip near the base was not optimal. The longitudinal wrap was similarly not extended sufficiently around the perimeter between sections 2 and 4, together with the lack of transverse FRP contributed to the failure. In addition, the strip at section 4 was perhaps too narrow, although the transverse strain data at that location confirm that this cross-section was too far removed from the center of the dent to substantially affect the repair capacity.

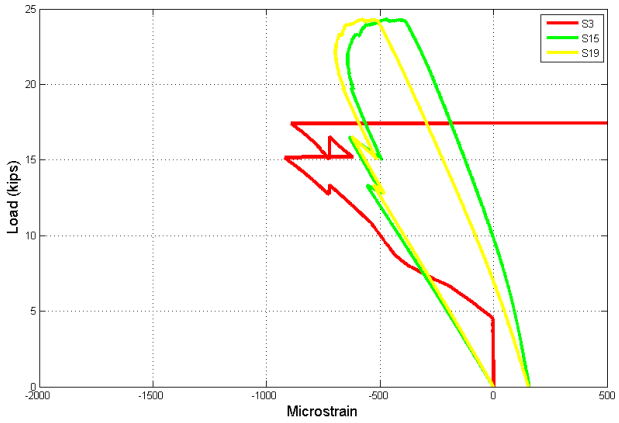

(a) ST-6 load-steel compressive strain data

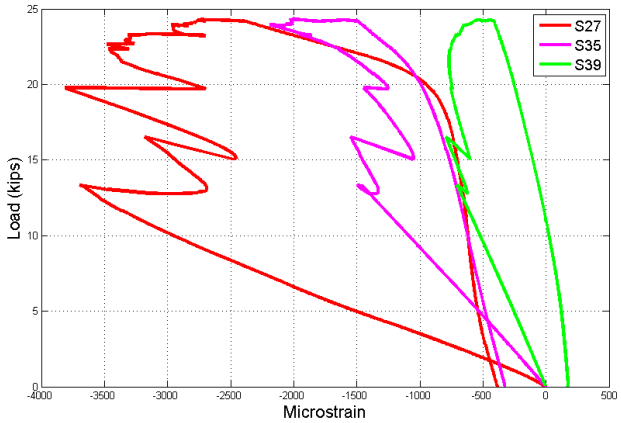

(b) ST-6 load-FRP compressive strain data

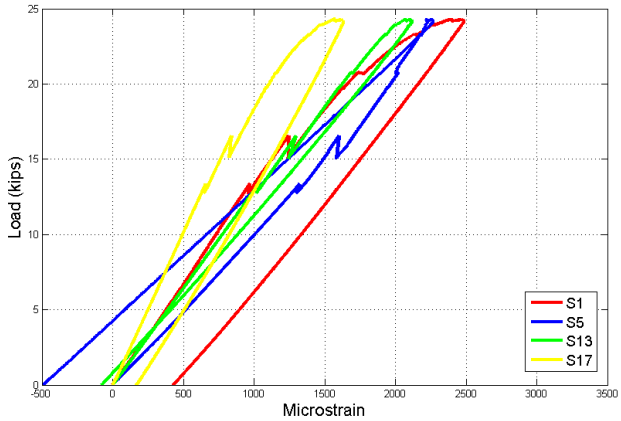

(c) ST-6 load-steel tensile strain data

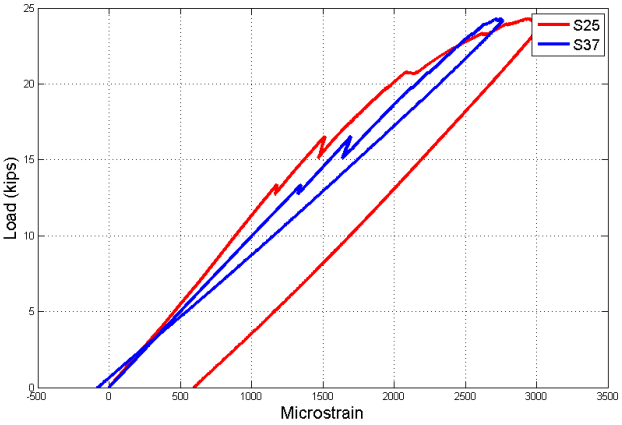

(d) ST-6 load-FRP tensile strain data

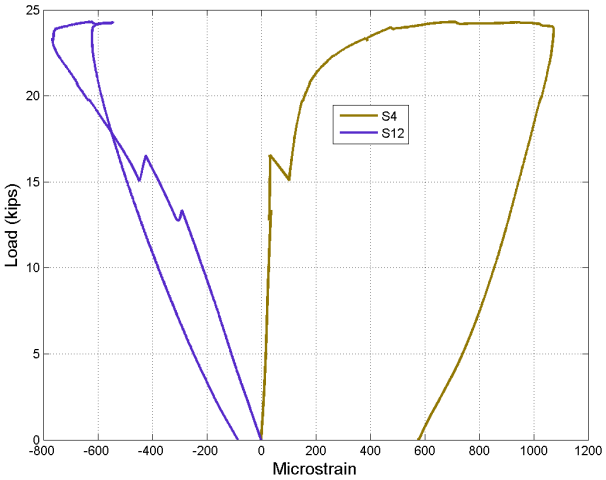

(e) ST-6 load-steel transverse strain data

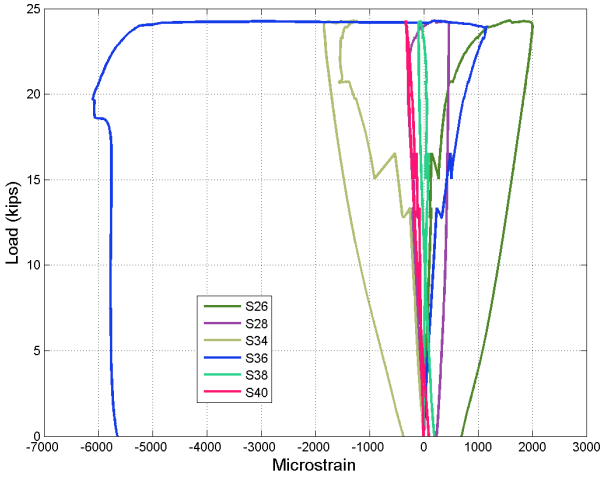

(f) ST-6 load-FRP transverse strain data

Figure 173. ST-6 load-strain data

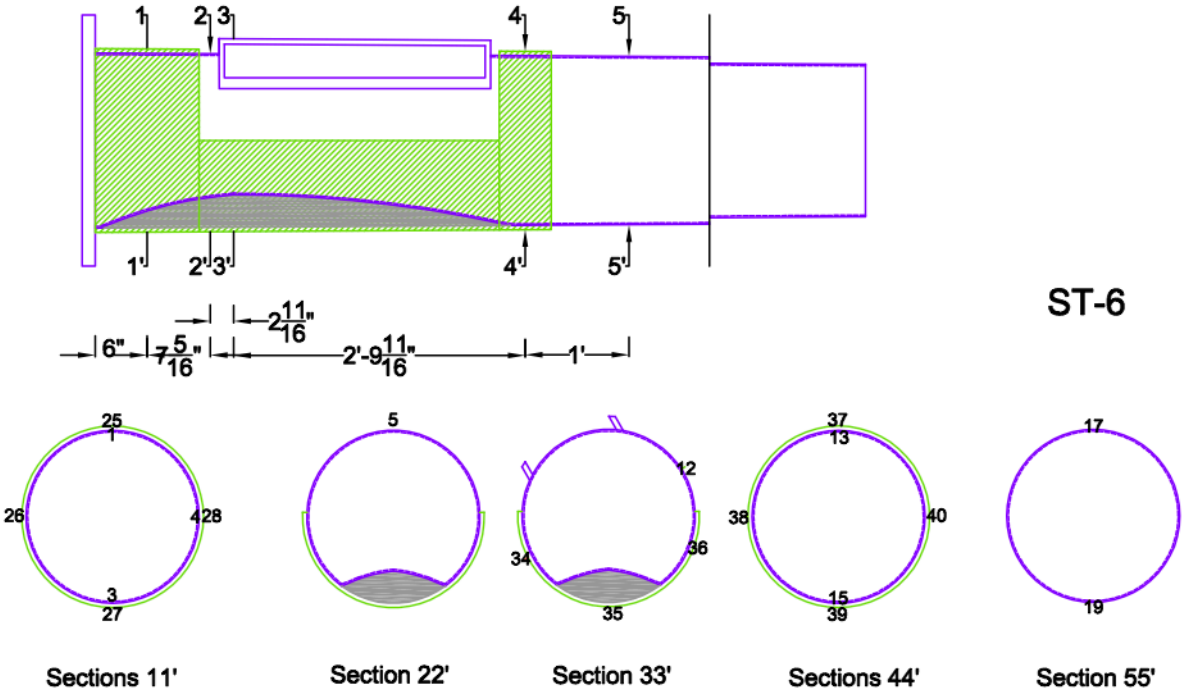

Figure 174. ST-6 strain gauges

The transverse strains measured in the proximity of the dent (S34 and S36) show compression behavior, as do the steel strain at S12 just adjacent to the access port. The distribution of the stresses in the cross-section were clearly being affected by the presence and orientation of the access port with a substantial reinforced side wall (relative to the principal axis of bending). However, it is also unknown based on the strains recorded what the role of the multi-sided pole was on stress concentrations and lack of uniform engagement of the wraps that may also have contributed to the premature failure.

Figure 175. ST-6 deflected shape at failure

(a) Compression face – debonded FRP

(b) Bottom of base – evidence of rotation

(c) Tension face – debonded FRP

(d) FRP buckling near base

(e) Lower east – FRP fracture

(f) Lower west – FRP fracture

Figure 176. ST-6 failure modes

5.2.2.3 ST-8

Pole ST-8 is a round pole with a base diameter of 17.63 in, and was dented in the laboratory to a depth of approximately 4.25 in, or 24% of its outer diameter. The dent is centered 22 in above the base plate, and 90° from the access port. The access port has a large perimeter that is reinforced with a side wall and an internal plate. The guidelines for selecting the number of FRP layers for a dented pole repair from the component-level studies suggested that a dent of 25% or more of the outer diameter should be repaired with two FRP layers. However, ST-8 was dented to just under 25% of its diameter, and therefore received a single-layer repair consisting of basalt

fibers and an epoxy matrix, which was installed using a wet layup process. Repair details and geometry are shown in Appendix A. The repaired pole is shown in its cantilever test configuration in Figure 177. The FRP reinforcing ratio at the base was approximately 36% (area of FRP was not adjusted for fiber volume fraction).

The pole was tested to failure. The load-displacement and load-strain data are shown in Figure 178 and Figure 179, respectively. The locations of the various strain gauges are shown in Figure 180.

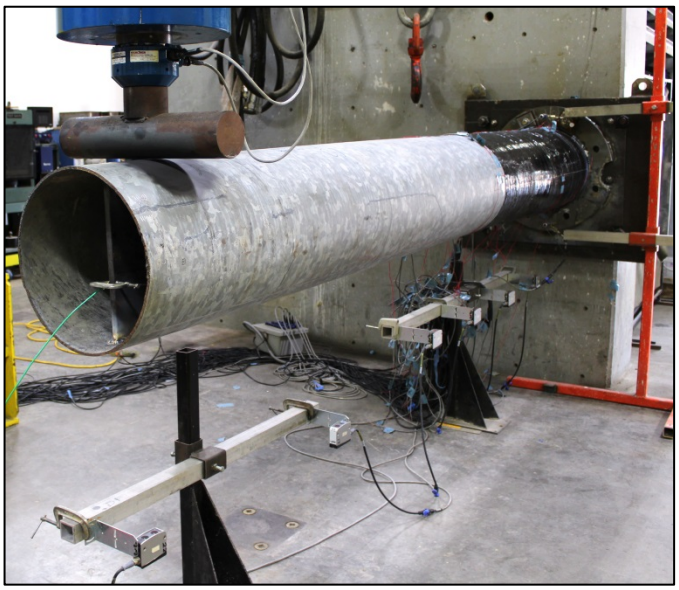

Figure 177. ST-8 test configuration

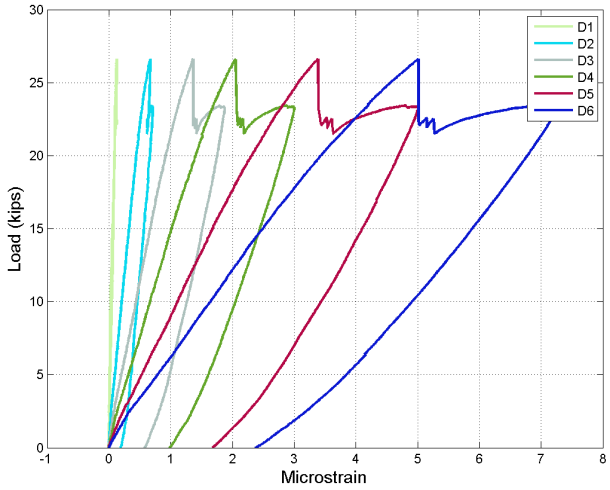

Figure 178. ST-8 load-displacement data

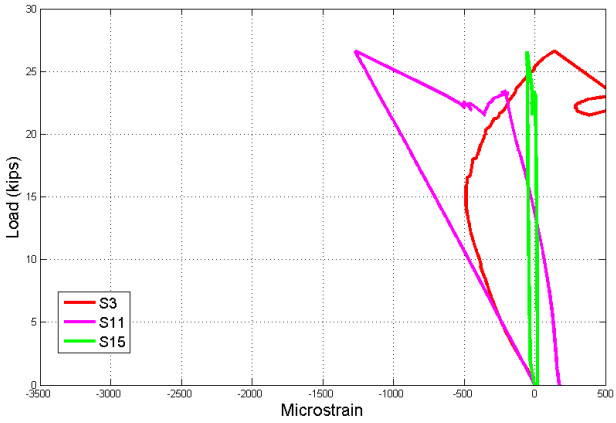

(a) ST-8 load-steel compressive strain data

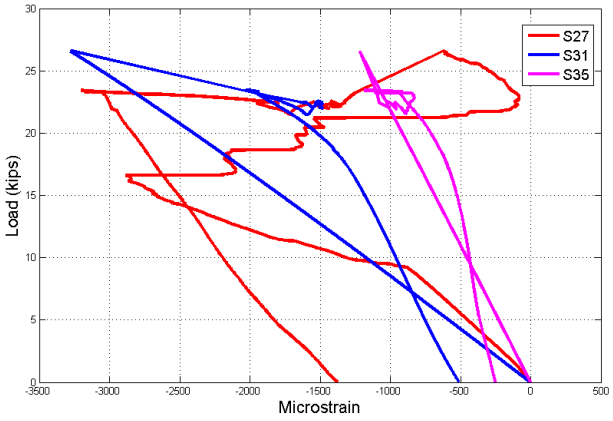

(b) ST-8 load-FRP compressive strain data

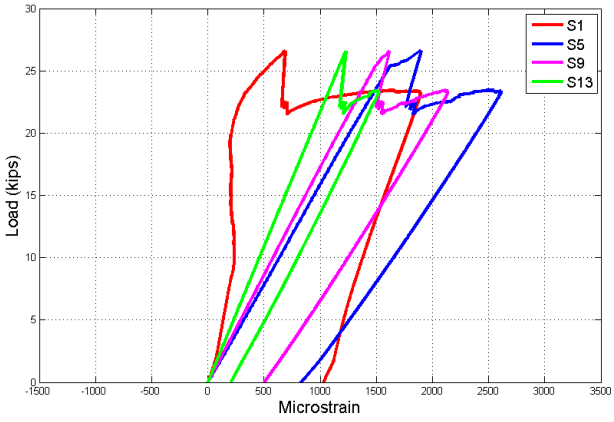

(c) ST-8 load-steel tensile strain data

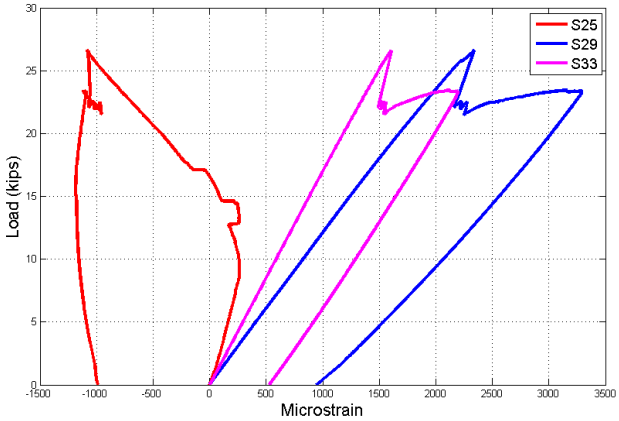

(d) ST-8 load-FRP tensile strain data

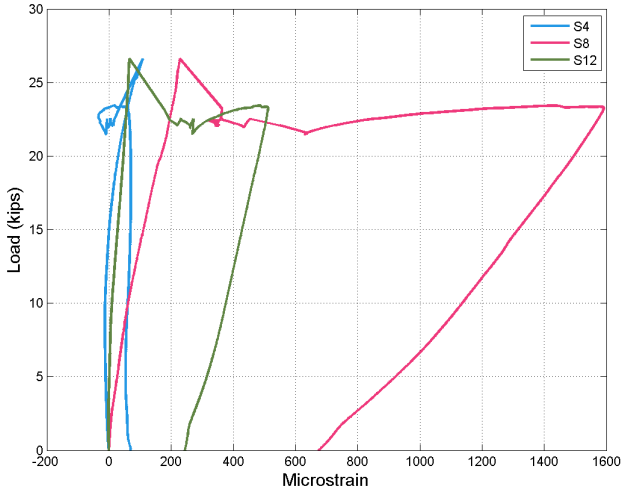

(e) ST-8 load-steel transverse strain data

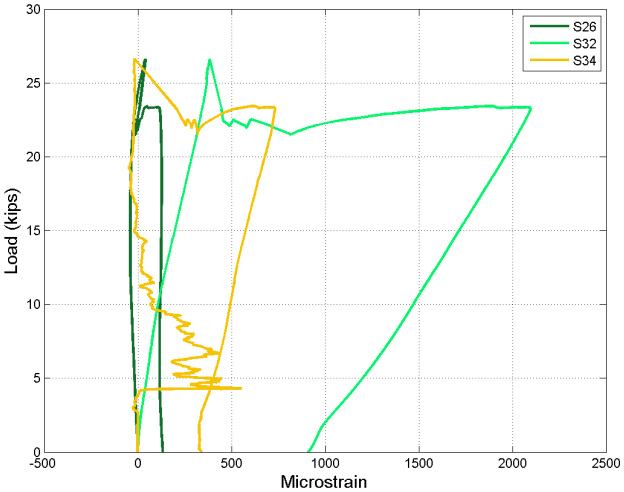

(f) ST-8 load-FRP transverse strain data

Figure 179. ST-8 load-strain data

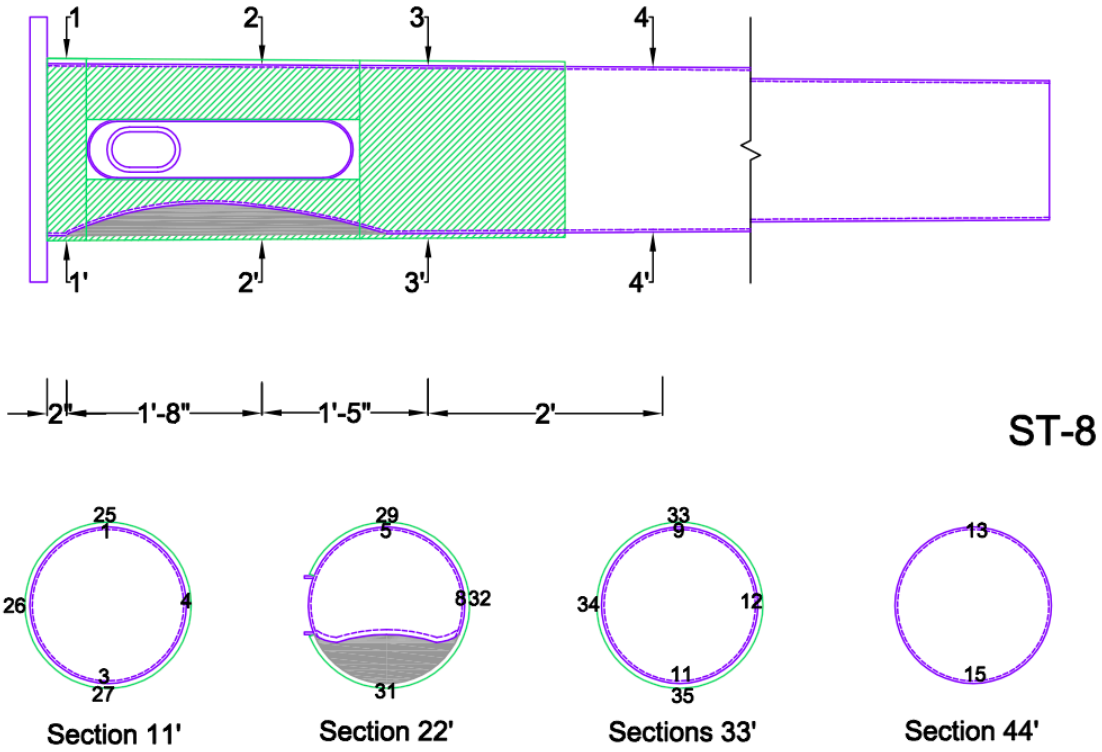

Figure 180. ST-8 strain gauges

The load reached a maximum value of 26.5 kip before a sudden brittle failure. The load did, however, stabilize and continue to increase again followed by a peak at 23.5 kip. Although the dent was large, the size of the access port and proximity to the dent allowed a substantial amount of FRP in both the longitudinal and transverse direction. The transverse strains mobilized in the wraps were very high, demonstrating efficacy of the repair, and no rupture occurred in the transverse wrap, so the selection of a single layer in each direction appears justified. However, a second layer would have enabled a higher load relative to the estimated theoretical capacity, because of the sudden increase in transverse strains observed after the load drop.

The final state of the pole after testing is shown in Figure 181 (a). The reinforced wall of the access port clearly contributed to the flexural response of the pole, as evidenced by the permanent flexural deformation of the side wall seen in Figure 181 (c). The cross-section has substantial visible dilation after the test, seen in Figure 181 (b). There is visible debonding near the access port in the longitudinal wrap (or partial transverse circumferential wrap), and some buckled fibers and debonding on the face of the pole opposite the access port, seen in Figure 181 (b) and (d).

The strain gauge on the compression steel near the support (S3) showed localized tension after the peak load was reached, similar to the FRP gauge at the same location. The tension FRP gauge at the support also exhibited unusual behavior (rapidly going into compression). However, the compression wrap was reengaged after the load drop, and may have ultimately shown signs of buckling near the support. The tension steel showed yielding between sections 2 and 3, and no debonding in the tension FRP was evident in the strain data. The drop in load at the peak may

have been due to crushing of the fill material and buckling of the FRP at section 2. There was a subsequent unloading of the compressive FRP and steel at several locations (e.g., S11, S31) as the load was transferred to section 1 (the load continued to increase again). The load increase is consistent with the rapid dilation of the cross-section at section 2 (and to a lesser extent at section 3). As with several of the other pole specimens the base flange appears to arrest the transverse strains near the base.

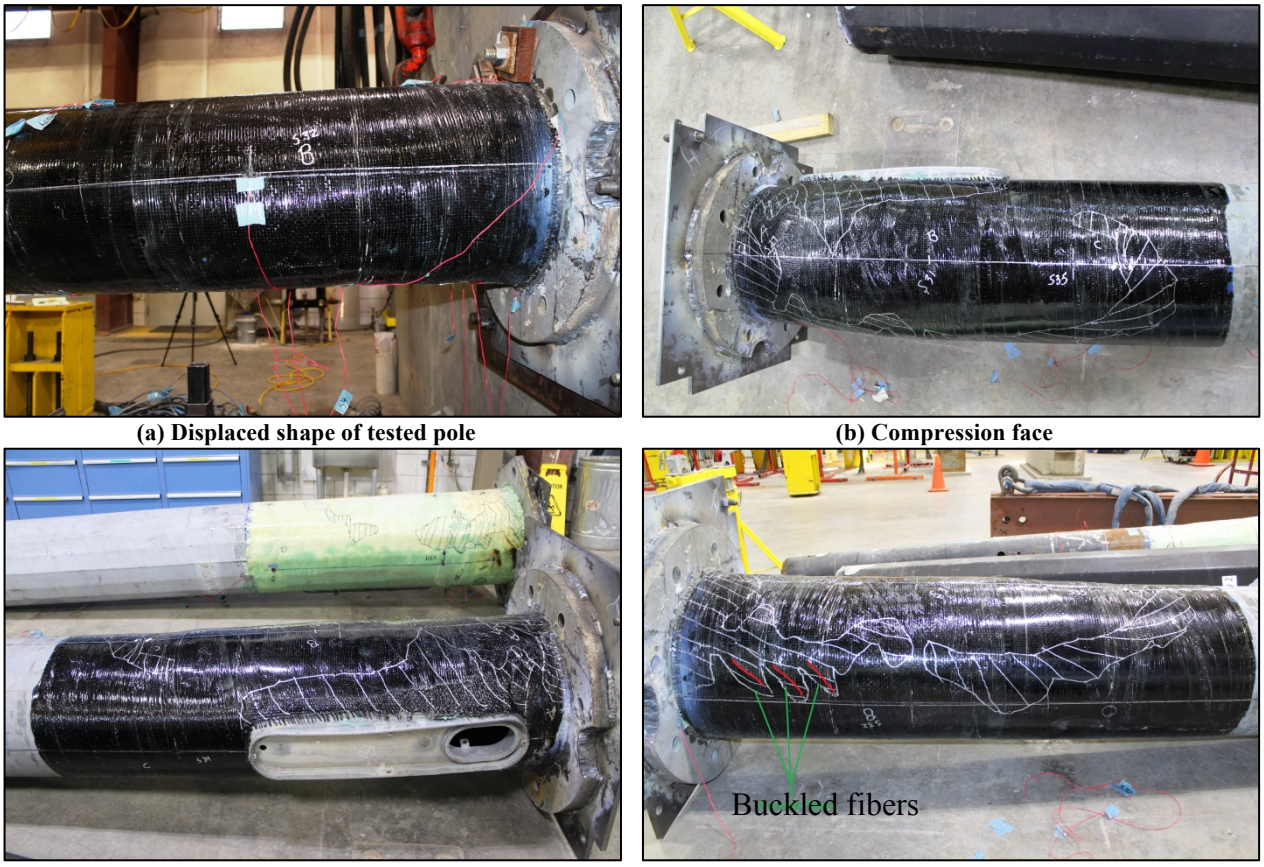

(a) Displaced shape of tested pole **(b) Compression face**

(c) East face **(d) West face**

Figure 181. ST-8 failure modes

5.2.2.4 ST-12

The final induced-damage steel pole to be tested, ST-12, was dented to 25% of its diameter at the dent location. The pole's diameter at the base plate is 16.56 in, and the applied dent is 4 in deep. The center of the dent is 22 in above the base plate, and the pole has no access port. This pole was repaired with a two-layer basalt/polyurethane composite wrap, which extended 5 ft above the base plate in order to cover the entire dent, as shown in Appendix A. The repaired pole is shown in Figure 182. The FRP reinforcing ratio at the base was approximately 40% (area of FRP was not adjusted for fiber volume fraction).

The pole was tested to a failure load of approximately 23.3 kips. The load-displacement and load-strain data are shown in Figure 183 and Figure 184, respectively. The locations of the various strain gauges are shown in Figure 185.

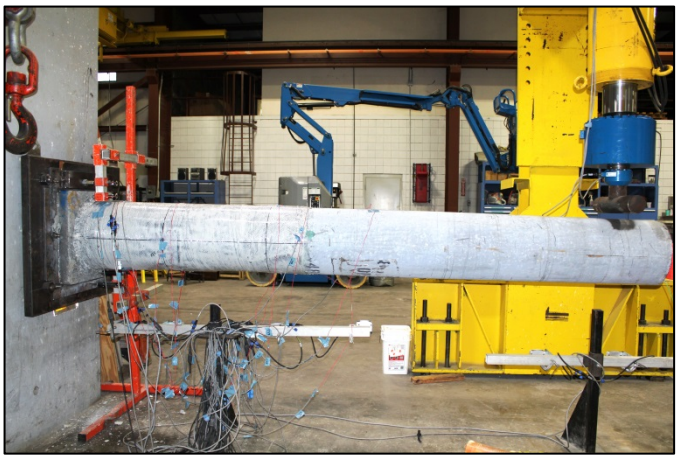

Figure 182. ST-12 test configuration

The pole reached a load of 23.5 kip before a sudden drop in the load occurred. The load continued to increase after this, attaining a maximum value slightly higher than the load at which the initial drop occurred. There may have been debonding at the base; however, it may also be due to the way the initial lay-up was performed with a considerable amount of adhesive collecting at the intersection of the base flange, as shown in Figure 186 (b). There is visible deformation at the base cross-section (expansion) seen in Figure 186 (c), and therefore, the pole should have developed substantial transverse strains. The failure mechanism of this specimen is somewhat similar to ST-8, although obviously ST-12 has no access port, and the two-layer wraps are continuous. For this test, no steel compressive strain gauges were placed on the pole due to the extents of the dent.

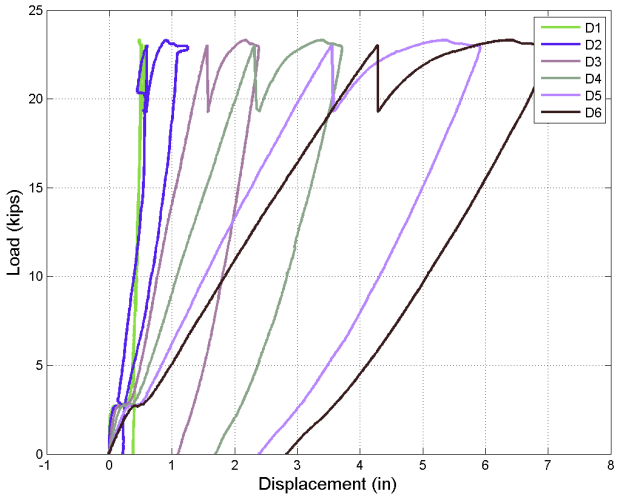

Figure 183. ST-12 load-displacement data

[no compressive gauges placed due to the extents of the dent and fill]

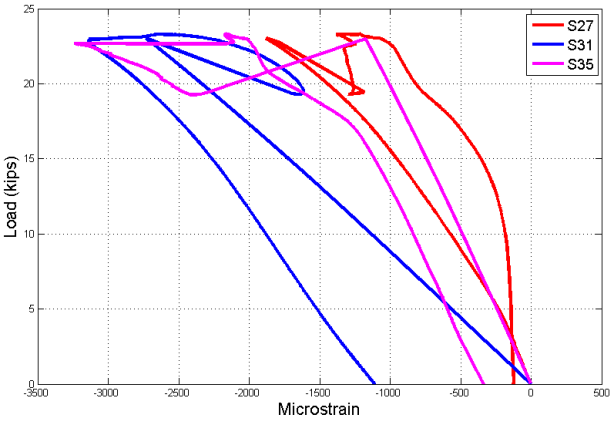

(a) ST-12 load-steel compressive strain data

(b) ST-12 load-FRP compressive strain data

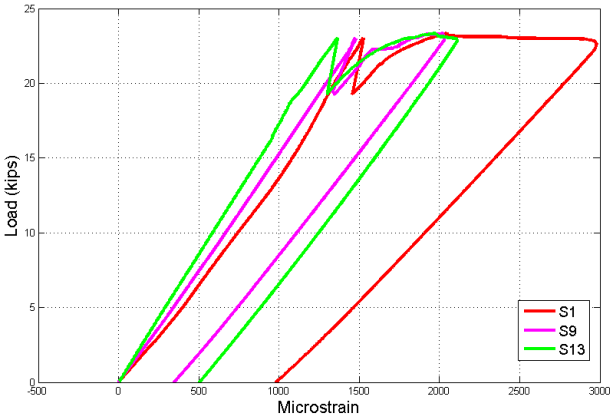

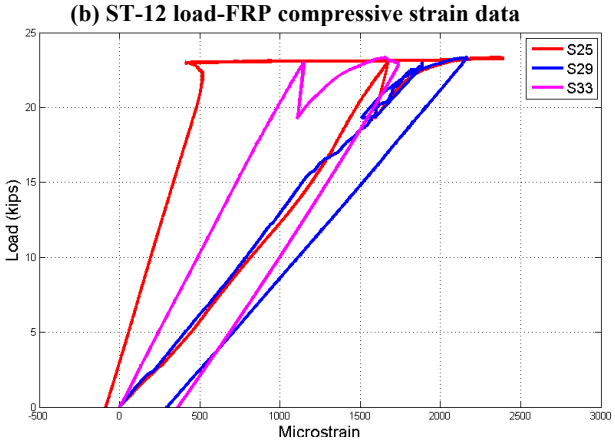

(c) ST-12 load-steel tensile strain data

(d) ST-12 load-FRP tensile strain data

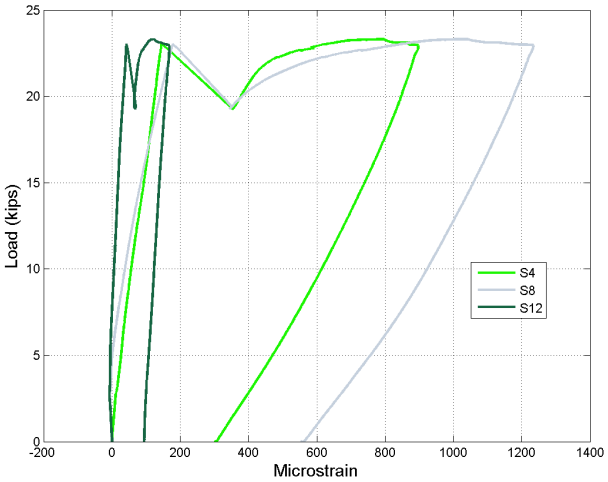

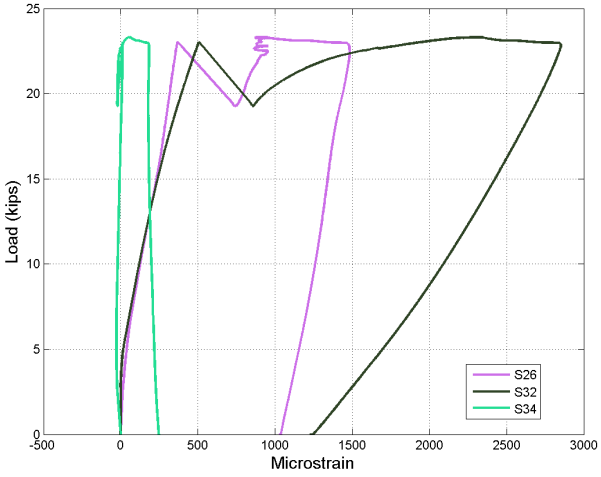

(e) ST-12 load-steel transverse strain data

(f) ST-12 load-FRP transverse strain data

Figure 184. ST-12 load-strain data

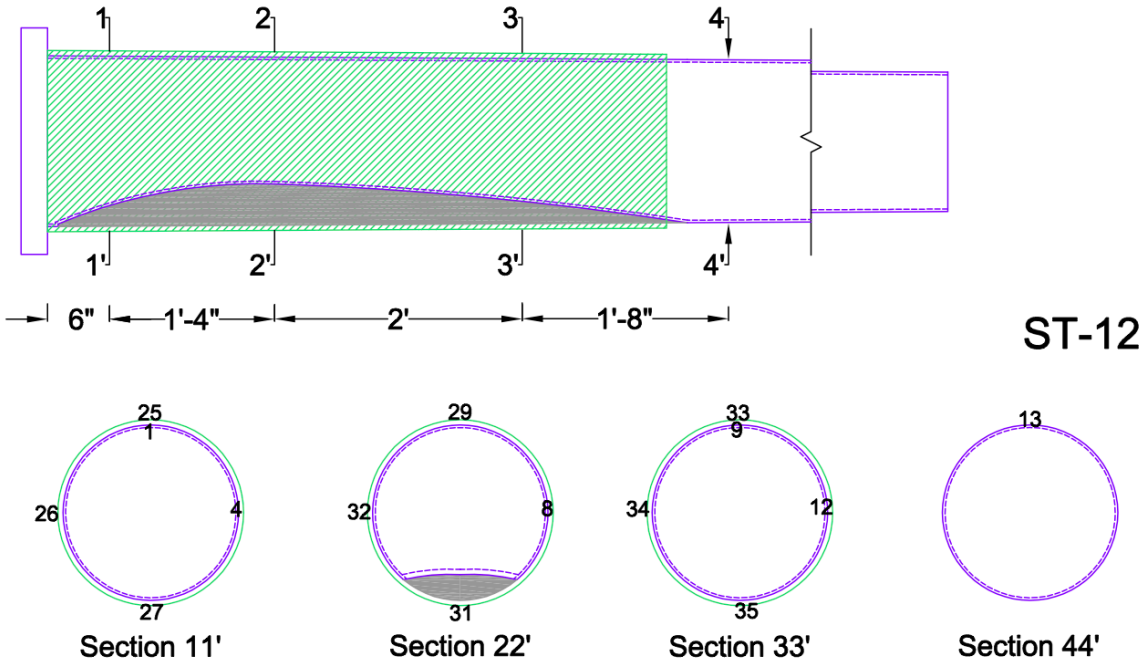

Figure 185. ST-12 strain gauges

(a) Displaced shape of pole

(b) FRP potentially debonded near the base and accumulation of resin near base flange

(c) Dilation of the base section and possible debonding

Figure 186. ST-12 failure mode

The displacement gauges show there may have been some rotation and slipping of the buttress connection before 3-kip load; however, the behavior stabilizes thereafter. The tension steel yielded between at section 1 after the specimen regained load. Debonding occurred in the tension FRP near section 1 and may have contributed to the sudden drop in load. However, more likely the buckling of the compressive FRP between sections 2 and 3 that resulted in the sudden unloading of these gauges is the major cause and may have a correspondence with the dent fill material failure. The increase in load after the first drop was manifested by increased compressive strains at section 2; however, no additional resistance was mobilized at sections 1 or 3. As with ST-8, the recovery of the load after the initial drop was accompanied by dilation of the cross-section and significant tensile strains in the transverse steel and FRP gauges. The transverse FRP was not near tensile rupture; however, and it appears that the capacity of the repaired system is in fact limited by the behavior of the fill and compressive FRP, counter to the limiting behaviors observed in the wrap configuration tests.

5.2.3 Aluminum Induced-Damage Poles

The three aluminum full-scale poles were dented, instrumented, and tested in the same way as the steel induced-damage test poles. The only difference in the aluminum test setup was the ability to bolt the pole bases directly to the 2 in steel plate due to the existing bolt pattern in the plate (and the consistent base geometry between all the aluminum poles). Each of the poles had a wall thickness of 3/16 in. These poles were loaded until failure by a point load 9 ft from their bases. This load configuration is designed to simulate wind loading that would be experienced by the poles in use.

5.2.3.1 AL-1.c

The first full-scale aluminum pole tested is shown in Figure 187 in its cantilever test configuration. The pole has a 4.5 in high sleeve extending up from the 1.5 in thick base plate, visible in Figure 191 (a). This sleeve surrounds the main pole member, which has a diameter of 8.3 in at the top of the sleeve. The pole does not have an access port. The dent was repaired with a single-layer of glass fibers saturated with an epoxy matrix. The geometry and instrumentation details of the pole are shown in Appendix A, as well as the FRP repair system. Pole AL-1.c is dented to a depth of 1.5 in, or 18% its undented diameter. The center of the dent is located 16 in above the base plate. The FRP reinforcing ratio at the base was approximately 40% (area of FRP was not adjusted for fiber volume fraction).

The load-displacement and load-strain data are shown in Figure 188 and Figure 189, respectively. The locations of the various strain gauges are shown in Figure 190. For clarity, the strain data are divided into six different plots. The first two plots show the compression strain measurements taken from longitudinal gauges located on the top side of the aluminum pole and the FRP wrap, respectively, in its test configuration. The third and fourth plots show the tensile strain measured from longitudinal gauges on the lower side of the pole on the aluminum and FRP surfaces. Finally, the last two plots show the measurements taken from the transverse gauges, which were placed transversely along the pole's neutral axis.

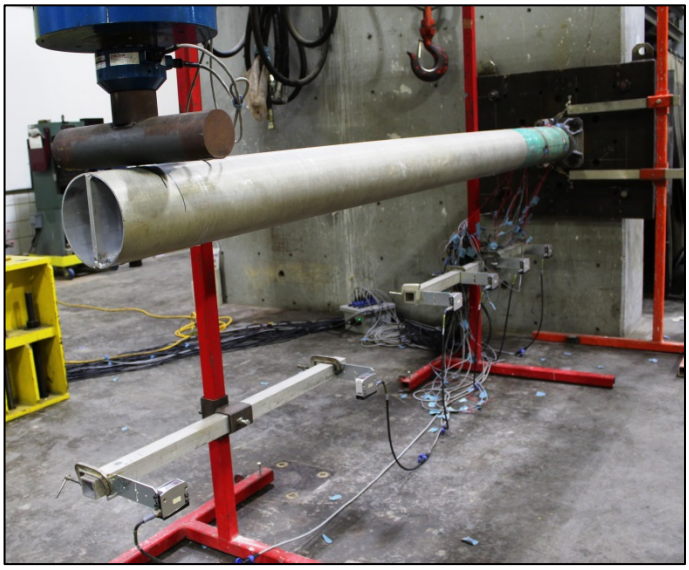

(a) AL-1.c monotonic loading configuration

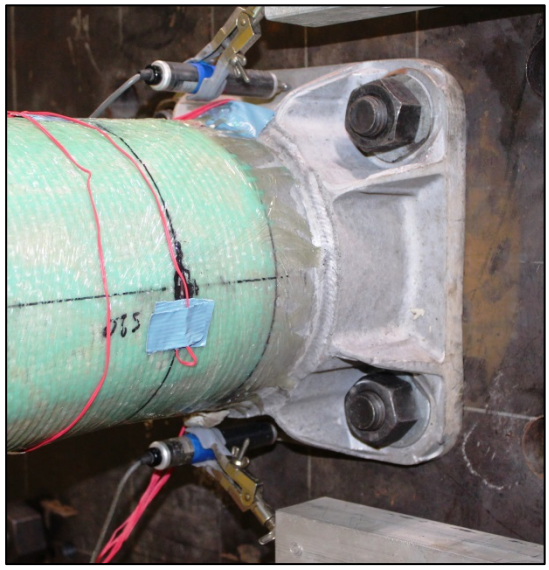

(b) AL-1.c sleeve and base connection

Figure 187. AL-1.c test configuration

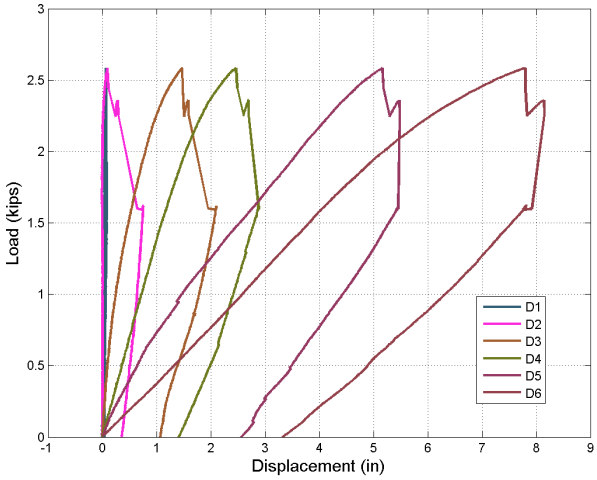

Figure 188. AL-1.c load-displacement data

The pole was loaded to approximately 2.58 kips at which point the base plate and aluminum sleeve at the pole's base fractured, as shown in Figure 191 (a). As the failure occurred outside of the extents of the repair system (and the pole base metal itself), the test result does not fully demonstrate the success of the repair system; however, the failure load was already higher than the predicted yield load. Some small, 1 in diameter areas of the FRP wrap delaminated from the aluminum substrate during testing, and an area of the wrap extending up to 3 in from the base of the wrap delaminated from the tension face, as seen in Figure 191 (b). However, the repair system was generally intact and undamaged at the time of the pole's failure as seen in Figure 191 (c), and the delamination was mostly due to the overlapping of the laminate with the 4.5 in sleeve.

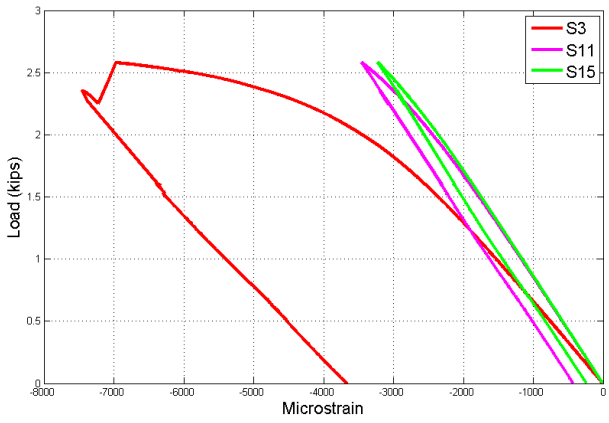

(a) AL-1.c load-aluminum compressive strain data

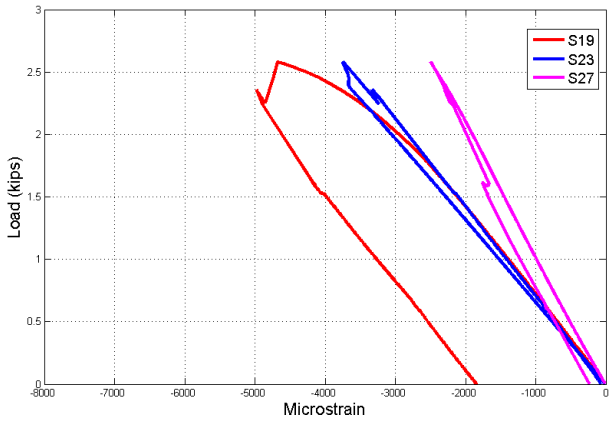

(b) AL-1.c load-FRP compressive strain data

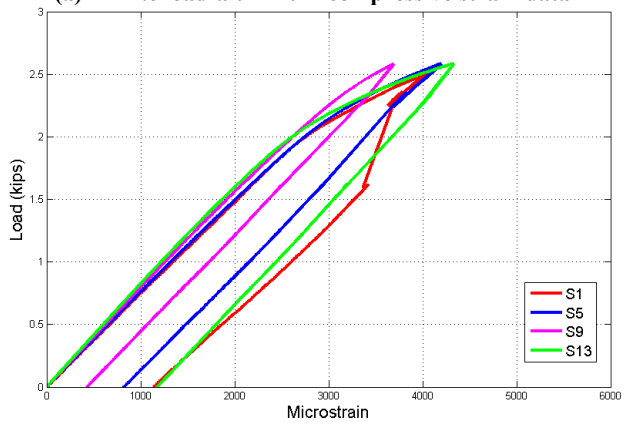

(c) AL-1.c load-aluminum tensile strain data

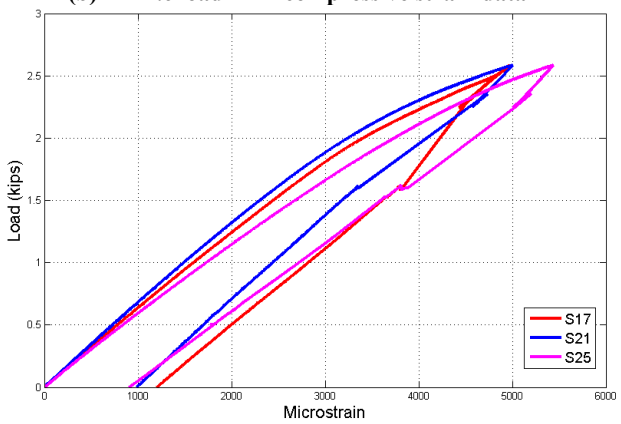

(d) AL-1.c load-FRP tensile strain data

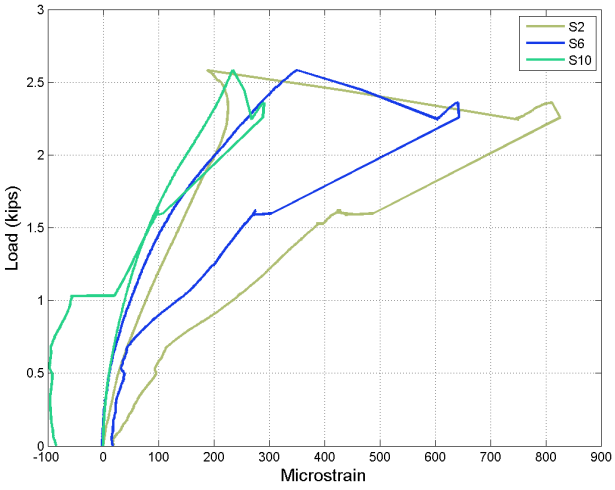

(e) AL-1.c load-aluminum transverse strain data

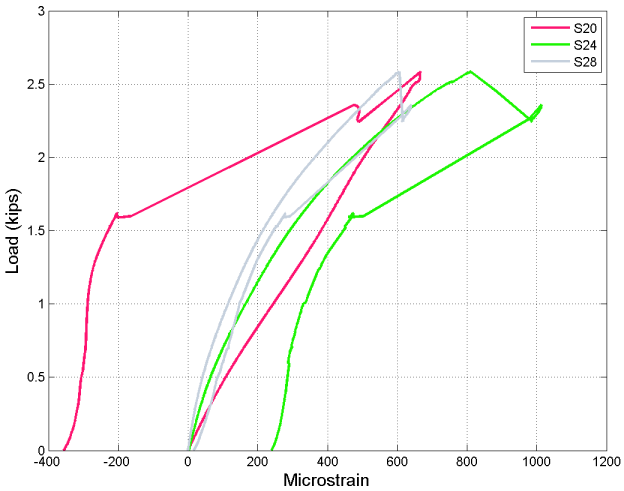

(f) AL-1.c load-FRP transverse strain data

Figure 189. AL-1.c load-strain data

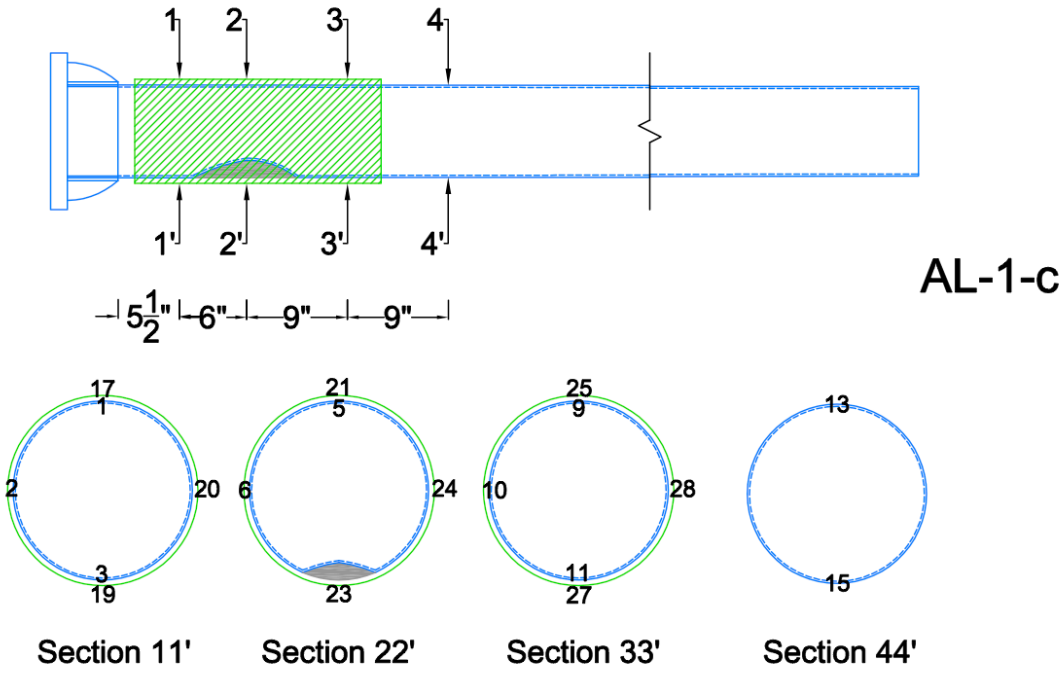

Figure 190. AL-1.c strain gauges

The strain data show that the aluminum had undergone yielding prior to failure, both in tension and compression at the base (section 1). The rapid increase in compression strain (-7000 με) may have contributed to the fracture at the top of the sleeve. Debonding occurred on the compressive face, evident in Figure 189 (b); however, the tension strain does not show any evidence of this to confirm the visual observations. Tension yielding in the aluminum may have occurred at several locations along the height of the pole, with readings at section 4 also showing 4000 με or larger. The transverse wrap was only moderately effective at the time of failure, with the transverse FRP gauge showing an increase in tension strain close to the failure load. As observed with several of the steel specimens, the additional rigidity of the pole base plate (and additional 4.5 in sleeve) effectively arrests the expansion of the cross-sections close to the base.

5.2.3.2 AL-2.c

Pole AL-2.c has the same geometry as AL-1.c, but was dented to a depth of 1.875 in or 23% of the pole's undented diameter. The repair consists of a one-layer wrap of glass fiber weave with a polyurethane matrix. As with AL-1.c, there was no access port. The pole details are shown in the drawing in Appendix A. The AL-2.c test setup is shown in Figure 192. The load-displacement and load-strain data are shown in Figure 193 and Figure 194, respectively. The locations of the various strain gauges are shown in Figure 195. The FRP reinforcing ratio at the base was approximately 40% (area of FRP was not adjusted for fiber volume fraction).

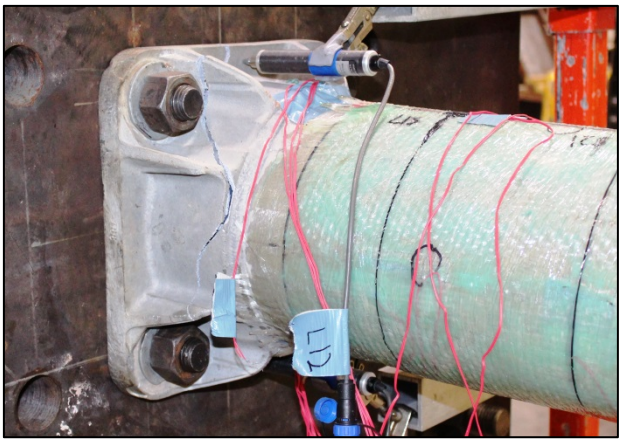

(a) Fractured base plate and sleeve

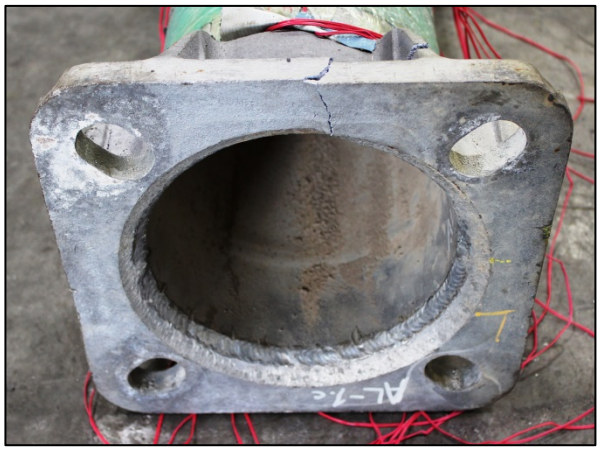

(b) Fractured base plate and sleeve

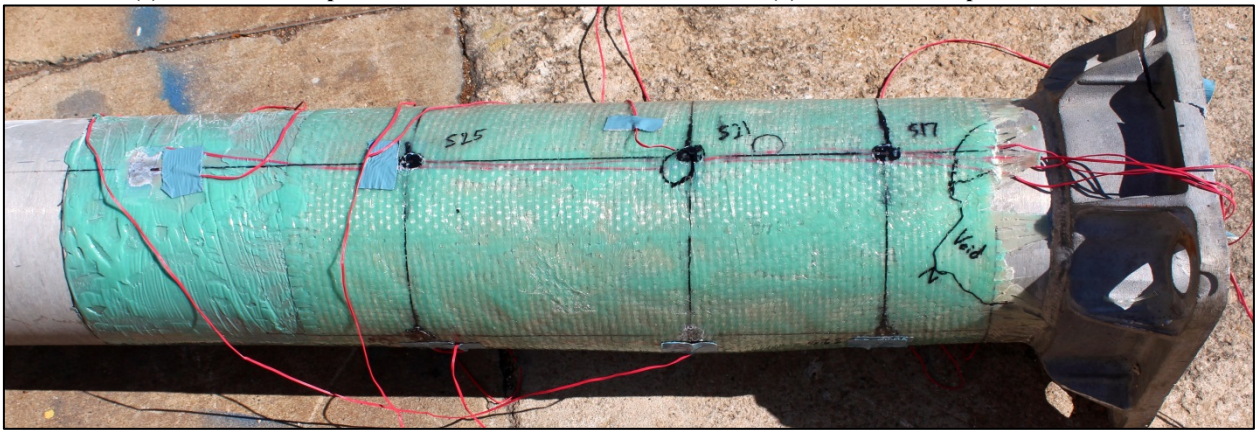

(c) FRP repair after testing with typical delaminated areas

Figure 191. AL-1.c failure modes

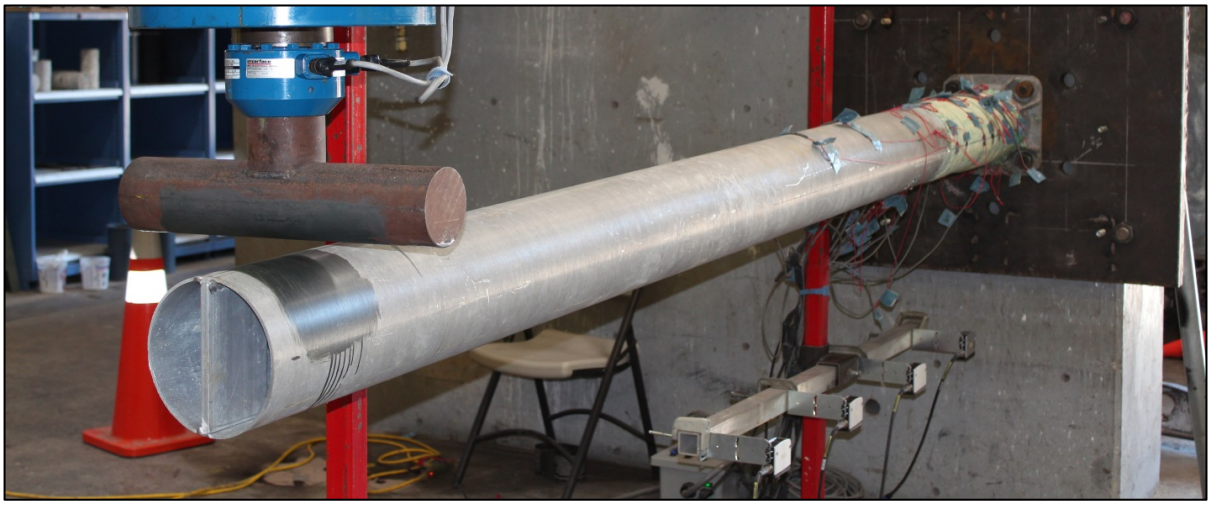

Figure 192. AL-2.c test configuration

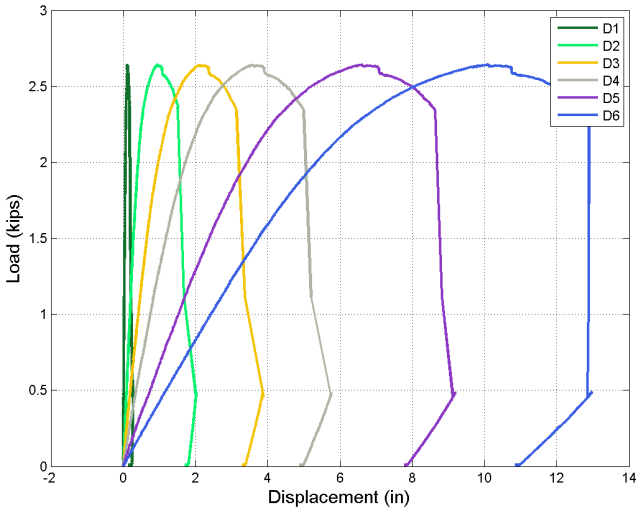

Figure 193. AL-2.c load-displacement data

The pole failed at 2.6 kip load when a hinge formed near the pole base and the base metal fractured 5 in from the base on the tension face. The substantial residual displacement at the end of the test is visible in Figure 196 (a). The fracture is shown in Figure 196 (b) and Figure 197 (a). The failure occurred at the termination of the sleeve, which is clear from the rotation in Figure 196 (c). Interestingly, the failure load was almost identical to AL-1.c although the failure did not occur in the base plate and the dent depth was larger. As with AL-1.c, the repair itself was therefore not tested to failure; however, the failure load was substantially larger than the theoretical yield capacity.

Substantial substrate and FRP strains were recorded near the base section and dented cross section, as shown in Figure 194. The aluminum compression strains reached -7500 με at section 1 and -4000 με at section 3. Substrate yielding likely occurred in a majority of the sections instrumented, with strains higher than 4000 με recorded in all the tension metal gauges across the top four sections. The FRP may have debonded on the compression face near the base (near S19) at the peak load, or it may be related to the rupture seen in Figure 196 (d) and Figure 197 (b). The rupture in the FRP at the base does not appear related to the dilation of the cross section, as the transverse strains remained small at all load levels, except for the engagement of the circumferential wrap at the dented section as would be expected (S24 recorded approximately 1300 με at the peak load). Therefore, it is likely the failure was due to splitting from the initial overlap of the wrap with the sleeve, as seen in Figure 196 (c and d) and Figure 197 (b), when the rotation of the cross section increased.

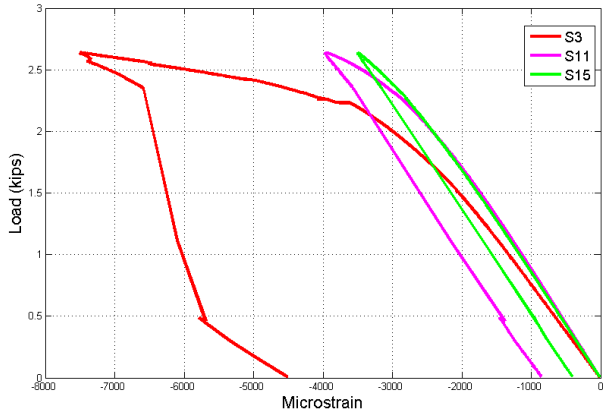

(a) AL-2.c load-aluminum compressive strain data

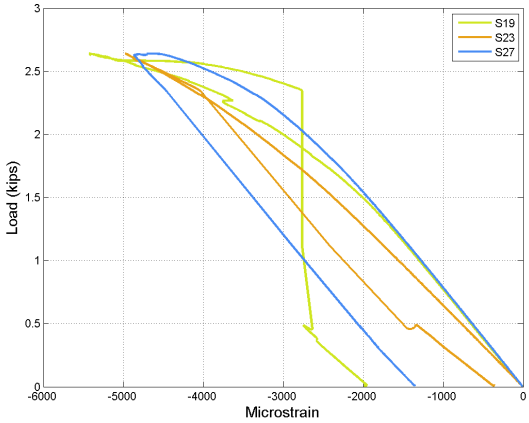

(b) AL-2.c load-FRP compressive strain data

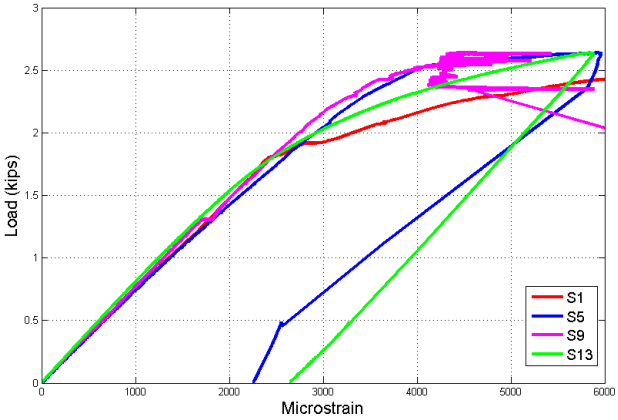

(c) AL-2.c load-aluminum tensile strain data

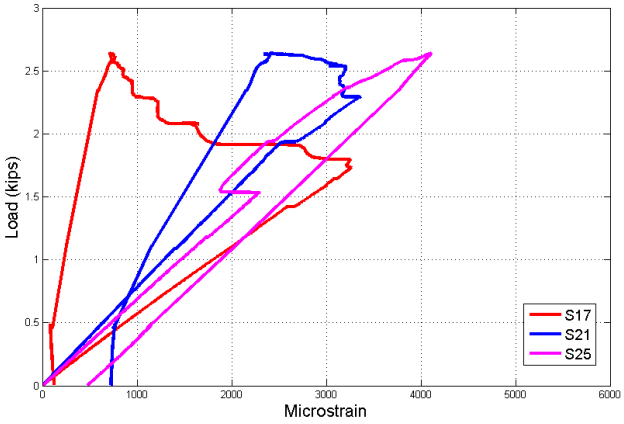

(d) AL-2.c load-FRP tensile strain data

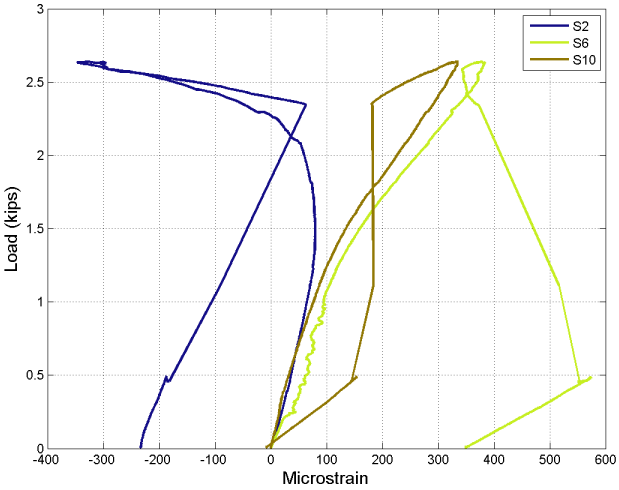

(e) AL-2.c load-aluminum transverse strain data

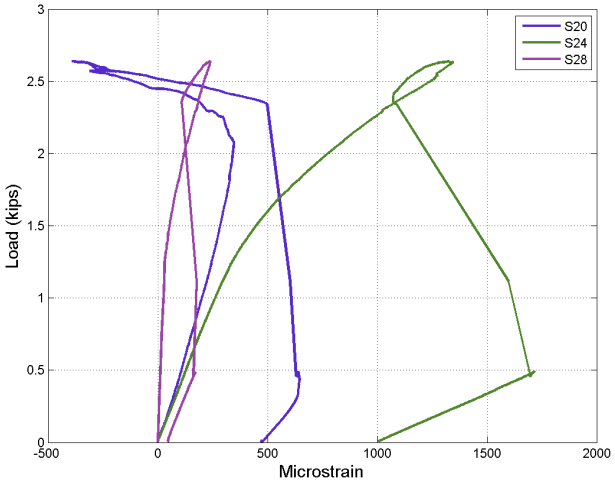

(f) AL-2.c load-FRP transverse strain data

Figure 194. AL-2.c load-strain data

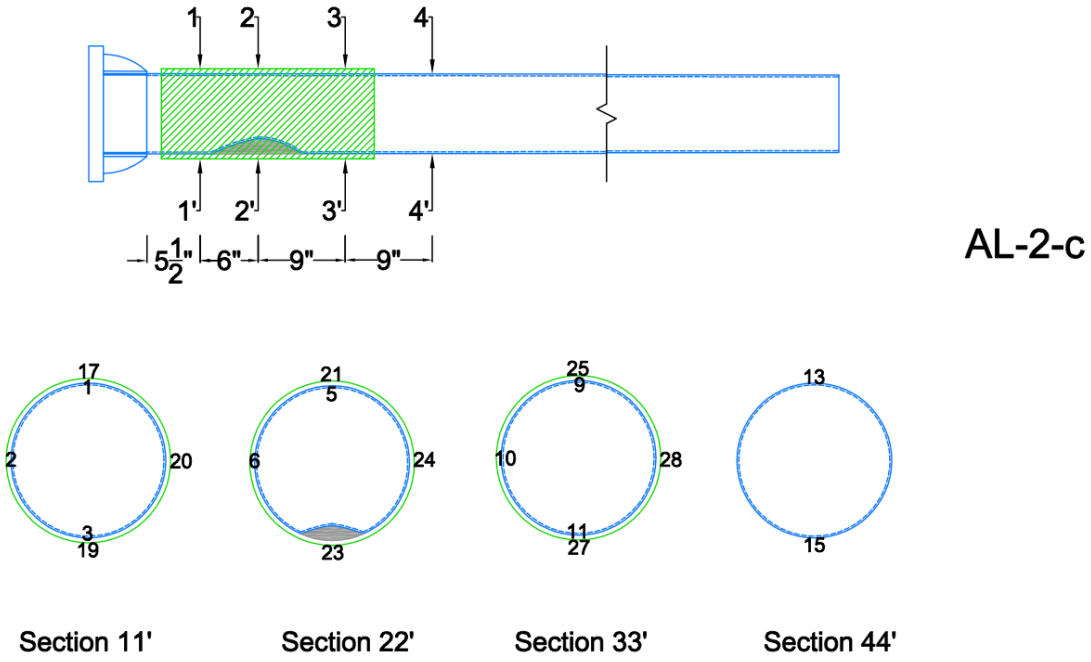

Figure 195. AL-2.c strain gauges

(a) Final displaced pole shape

(b) Failed base plate connection

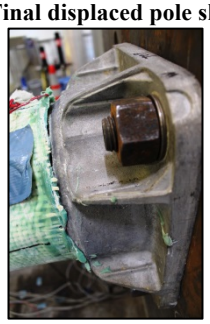

(c) Ruptured fibers and failed base plate connection

(d) Ruptured FRP fibers on compression side base plate

Figure 196. AL-2.c failure modes

(a) Rupture of the aluminum base metal

(b) Delamination of wrap at the base and rupture that initiated after delamination

Figure 197. AL-2.c after testing

The tension FRP gauge near the base (S17) shows there was no initial continuity between the substrate and laminate. The laminate debonded near section 2 (dented region) at a load of 2.3 kip, but the debonding does not appear to have propagated further along the pole. The achieved stress ratios for both AL-1.c and AL-2.c were 1.2, and may have approached the full plastic capacity if failure of the base plate or base metal had not occurred. Consistent with the component-level results, the use of a single layer of FRP appears to be highly effective in restoring dented aluminum poles to their original capacity.

5.2.3.3 AL-3.c

Pole AL-3.c is shown in Figure 198 in its cantilever test configuration. This pole also has an aluminum sleeve extending up from base plate as well as an access port (see Appendix A). The access port had a cover that was screwed into the reinforced walls (and the cover was left during the testing). The 30% (2.375 in) dent was applied to the pole 22 in above the base plate opposite the access port. The dent was repaired with a single-layer of glass fibers saturated with a polyurethane matrix. The wrap geometry consists of a main 21 in wide laminate that extends 2'-2" from the base of the pole and two circumferential wraps 5 in and 8 in wide below and above the access port, respectively. These circumferential wraps protect against premature delamination of the main wrap, and this is the only large-scale aluminum specimen that employed such a wrap design.

It should be noted that although the wrap was not continuous like AL-1.c and AL-2.c, this pole also behaved extremely well after being repaired. In comparison to the steel large-scale specimens, the access port is located considerably closer to the base and is smaller in size (and therefore the transverse wraps can be placed more efficiently across the dented region). In addition to this repair system, two small existing dents obtained in the field, located approximately 6 ft above the base of the pole, were repaired with a single layer of the FRP system. This wrap was applied to ensure that these dents would not interfere with the results of the test. The load-displacement and load-strain data are shown in Figure 199 and Figure 200, respectively. The locations of the various strain gauges are shown in Figure 201. The FRP

reinforcing ratio at the base was approximately 80% (area of FRP was not adjusted for fiber volume fraction).

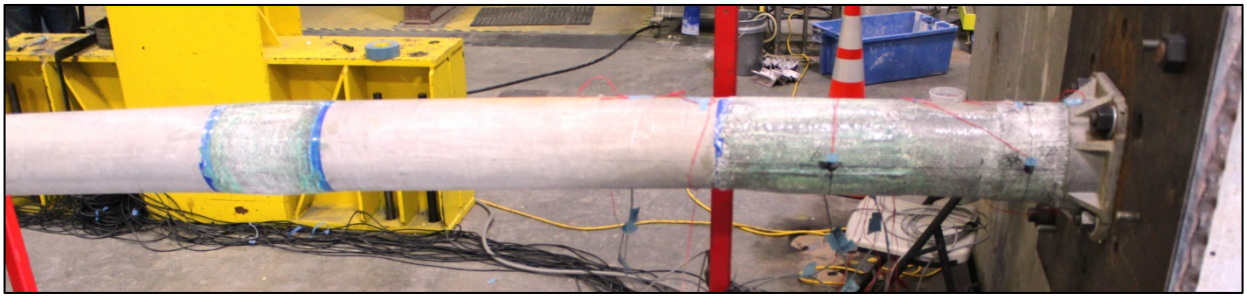

Figure 198. AL-3.c test configuration

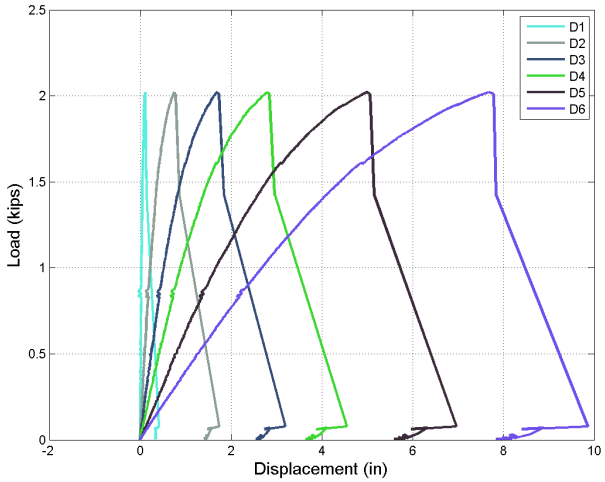

Figure 199. AL-3.c load-displacement data

The pole reached a load of 2 kip when it failed prematurely due to a sudden brittle fracture of the aluminum base plate around the two top bolt holes, as shown in Figure 202 (b). There was also a fracture seen through the outside corner of one of the bolt holes on the compression side of the connection, as shown in Figure 202 (a). Little to no debonding was present in the wrap and a majority of the strain responses were still in the linear region. Therefore, the repair system would likely have performed similar to AL-1.c and AL-2.c (in yielding a repair capacity substantially higher than the original undented capacity of the poles).

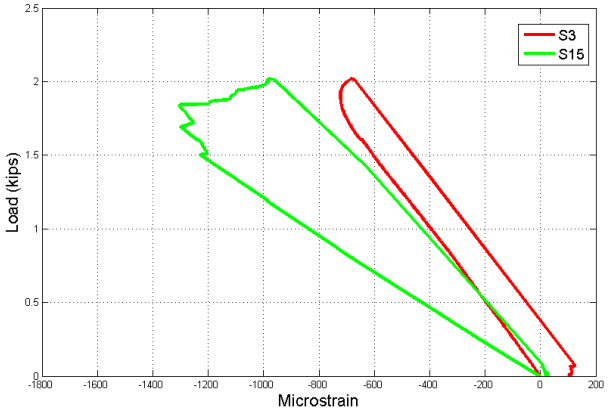

(a) AL-3.c load-aluminum compressive strain data

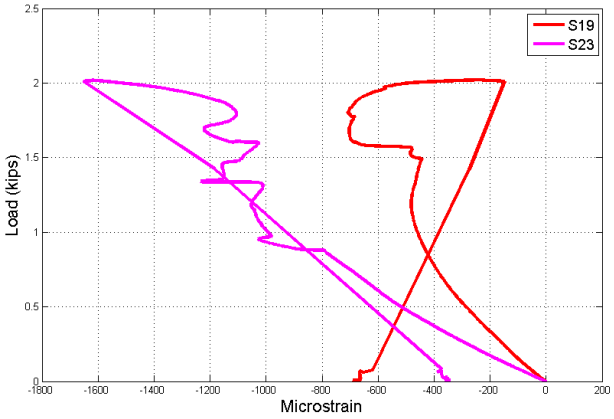

(b) AL-3.c load-FRP compressive strain data

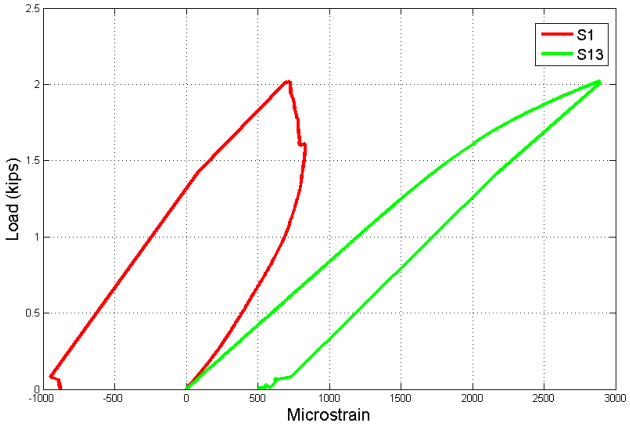

(c) AL-3.c load-aluminum tensile strain data

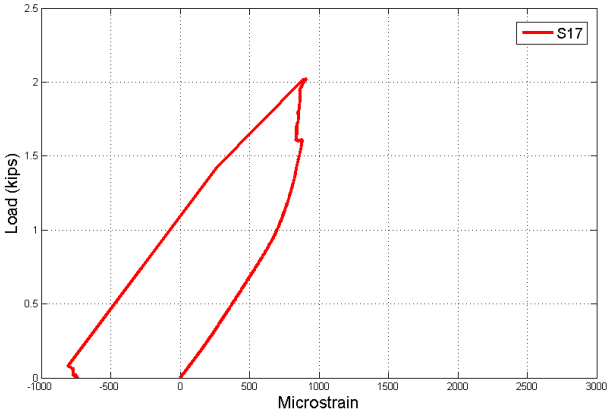

(d) AL-3.c load-FRP tensile strain data

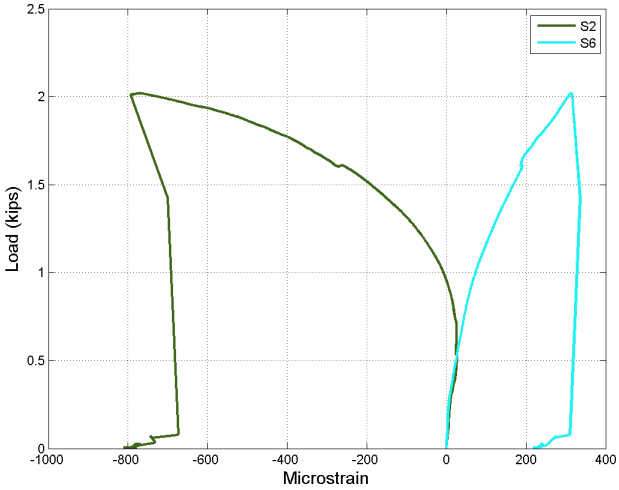

(e) AL-3.c load-aluminum transverse strain data

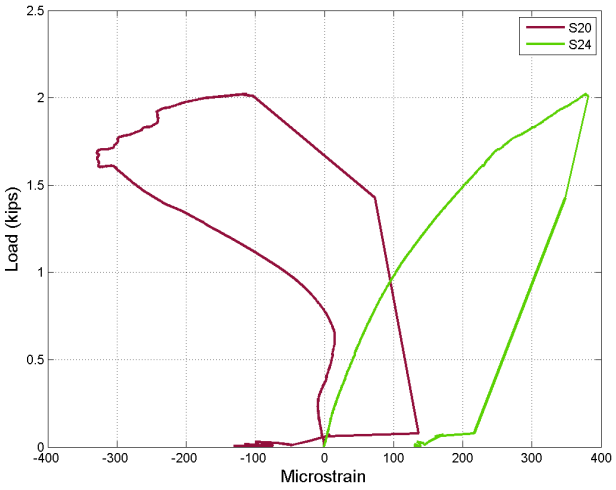

(f) AL-3.c load-FRP transverse strain data

Figure 200. AL-3.c test data

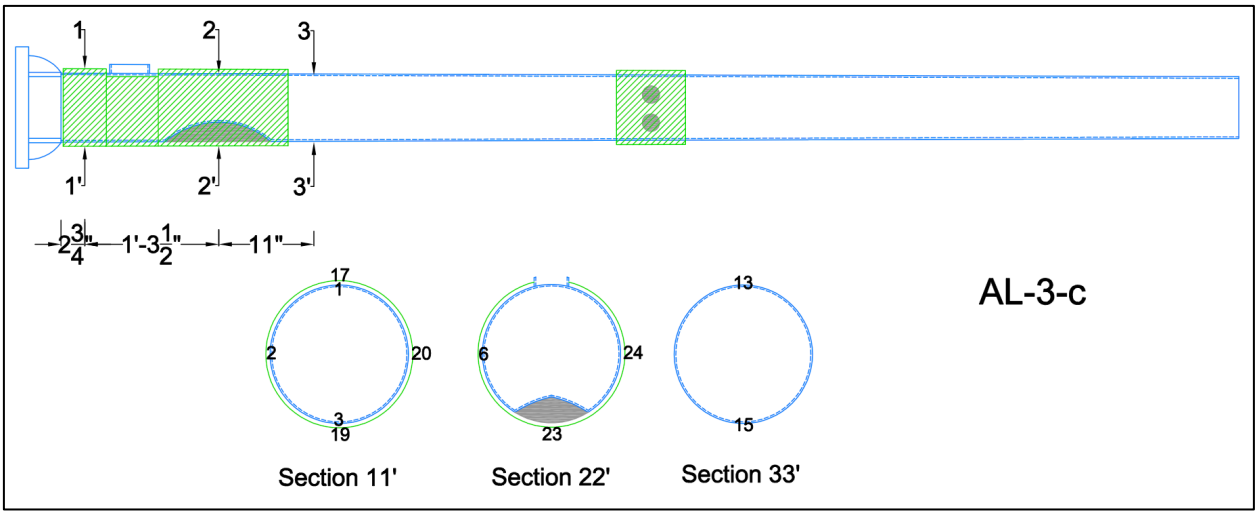

Figure 201. AL-3.c strain gauges

(a) Fractured base plate **(b) Fractured and ruptured base plate**

Figure 202. AL-3.c base plate failure

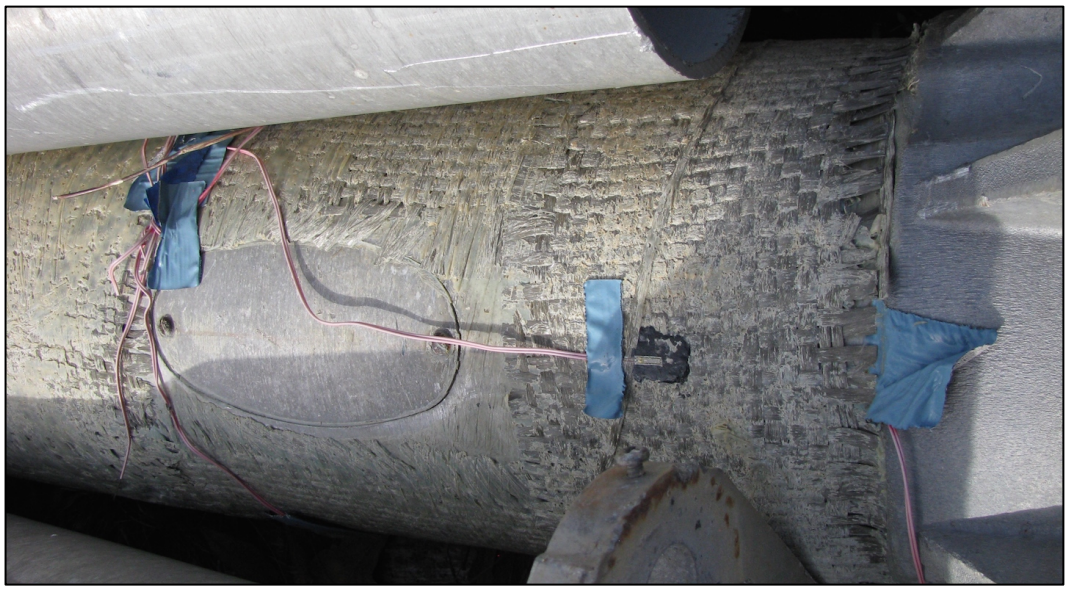

Figure 203. AL-3.c laminate surrounding access port cover

5.3 Summary of Large-Scale Monotonic Test Results

Similar to the summary provided in the component-level chapter, the results for all the monotonic large-scale tests are compiled in Table 30 in the form of a stress factor. The stress factor is computed as the ratio of the experimental load to the estimated load based on the theoretical yield moment. The theoretical value contains the best estimate of the cross section thickness and yield stress; however, it is not known the true variation of these within the cross-sectional areas close to the pole base or in the dented regions. In addition, the theoretical values do not contain an adjustment for the presence of access ports, buttons, stress concentrations near the pole base, stress concentrations in multi-sided pole cross sections, etc.

Table 30. Large-scale monotonic result summary

Pole ID	Section Geometry	Dent Depth (%)	Repair System	Stress Factor	Failure Mode
AL-1.c	Round	18	Glass/QB	1.2	Base plate fracture
AL-2.c	Round	23	Glass/PU	1.2	Base metal fracture
AL-3.c	Round	31	Basalt/PU	1.0	Base plate fracture
ST-5	Round	18	Glass/QB	0.74*	Did not fail
ST-6	18-sided	19	Glass/PU	0.64	FRP debonding/buckling
ST-8	Round	24	Basalt/QB	0.81	FRP debonding/buckling
ST-12	Round	25	Basalt/PU	0.91	FRP buckling, Hinge formation
FD-1	Multi-sided	?	Glass/PU	0.72*	Did not fail
FD-2	12-sided	7	Basalt/QB	0.92	FRP debonding/buckling, Hinge formation
FD-3	Round	21	Glass/PU	1.13	Likely metal yielding
FD-5	Round	24	Basalt/PU	1.04	Hinge formation, FRP debonding/buckling

There do not appear to be any consistent trends in the monotonic tests differentiating the behavior of the different matrix and fibers employed in the repair systems.

Chapter 6: Large-Scale Fatigue and Impact Testing

Sign and signal structures are widely used on main arterials and highways to control the traffic and pedestrian movement and giving the road information and directions. These structures are exposed to wind-induced and traffic-induced vibration and fatigue because of their flexibility, which depends on the length, height, thickness, mast arm and signal mass, etc. As a result of the cumulative vibrations over the service life, the welded connections are prone to fatigue cracking. Two cantilever sign structures collapsing were recorded in Michigan at the beginning of 1990 resulting in damages and injuries because of the strength reduction due to the cracks (Ness & Till, 1992). Since that time, many projects in different states have been performed to investigate the suitable ways to reduce damage or retrofit those structures. For the purposes of this project, it is of interest whether the proposed FRP repair system would be fatigue prone, or whether the original metal and welded connections would remain the fatigue critical details.

Similarly, due to the proximity of the poles to intersections and heavy traffic areas, they are often subjected to impact loading, as is discussed as the primary motivation for developing the in situ repair method for this study. Within the last 3 decades, fatalities and injuries have been increasing because of the utility pole crashes. Many states have started looking for different ways to reduce the casualties. FDOT with Utilities Coordinating Committee (FUCC) (Ivey & Scott, 2004) have investigated the possibilities to reduce the number of conflict points (crash hotspots) depending on statistics. For pole locations, it is required to relocate if other reasons like pavement rutting are excluded (Gabler et al., 2007). However, it is entirely possible that a pole that was restored to service using the proposed FRP repair system would be impacted again. Therefore, it is of interest in this study to determine whether such an impact would be detrimental to the repair as well as the overall stability of the pole.

This chapter examines the experimental behavior of the proposed FRP repair systems when the repair (full-scale) pole is subjected either to repeated cyclic loading or dynamic impact. The first section of the chapter is dedicated to the fatigue/cyclic tests and the second section to the impact tests.

6.1 Fatigue/Cyclic Testing

Over the last few decades, loss of serviceability for highway sign structures such as cantilevered steel sign structures has been increasing because of the wind-induced fatigue cracking (NCHRP-176, 2011). As a result, the cost of repairing and/or replacing the damaged parts has been increasing. Hence, the urgent need for the reliable assessment of fatigue performance of these structures is valuable, and the ability to verify whether repair techniques such as the proposed FRP systems are susceptible to fatigue themselves.

Usually, highway sign structures are built from one vertical lightweight rounded or multi-sided column that is connected to the base plate by welding (Figure 204). In this case, the dynamic characteristics for them are commonly 1 Hz for the natural frequency and damping less than 1% of critical. Wind-induced aero-elastic effects such as galloping and vortex shedding will cause large amplitude and long duration vibrations. Fatigue cracking that results from the vibration will

commonly initiate at the weld toe location at the pole-to-base-plate connection, as seen in Figure 205.

Figure 204. Typical light pole base

Figure 205. Fatigue cracking at the connection pole-base plate fillet weld toe (NCHRP-176, 2011)

Several past studies have been focused on cantilevered sign structures used around the world that are susceptible to failure because of wind-induced fatigue. One research study by the Illinois DOT (South, 1997) was concerned with the actual fatigue strength of tube-to-plate connections by testing 24 poles with 3 in outside diameter, 0.125 in thick AISI DOM (drawn over mandrel) steel tubes. Those poles were tested at 6 different stress ranges at 3 Hz to develop the relationship between the nominal stress and number of cycles until the failure. In this test, crack detector gauges and strain gauges were used. The position of the strain gauges were 0.03125 in from the weld toe at a point of maximum bending stress and the center of the gauge was 0.0467 in from the weld toe (tube-to-plate fillet weld). The stress concentration factor was measured to have an average of 1.78. Recommendations were made to improve the fatigue behavior of the connection area, such as grinding, weld-toe dressing, and peening, but none of them was performed.

(Frymoyer et al., 2009) evaluated the remaining life for in-service luminaire support structures. The selected structures were previously in service for nearly 25 years, and the testing was focused on fatigue resistance of complete penetration groove weld (CJP) connected pole- to-base plate and stiffened hand hole connection in addition to anchor bolts. Those poles were tapered with outer diameter 9.43 in at the base and thickness 0.1280 in galvanized steel with lengths of 89.375 in and 87.375 in, respectively. The reason behind the short length was to keep the ratio of bending moment to shear force high. Before starting the fatigue test, 5 cycles quasi-static loading were applied to test the instrumentation and to select a starting point for the stress distribution, stiffness, and stress concentration factors. According to AASHTO, the poles were classified to be in category E for both connected locations. Although the predicted numbers of cycles to failure were 653,500 and 662,100 for the two poles, no initial cracking was recorded during the first 1,362,627 and 2,429,211 cycles for each specimen, respectively. The first pole test was stopped when the number of cycles reached 1,499,587 due to change in stiffness and

cracks propagated at the upper right corner of the hand hole. The second pole test was terminated at 2,570,302 cycles when cracks occurred in the area of the hand hole. At the pole-to-base plate connection, no cracks were recorded for both poles. It was concluded that the remaining fatigue lives for those poles were higher than AASHTO specification for new constructions and those pieces did not have high accumulated stresses in the field within the past 25 years.

Another study was performed on reinforcing a pole, which had previously been tested for fatigue until the initiation of the cracks at welding area (Sim & Uang, 2011). The procedure of repairing the pole was applying 8 layers in two different directions (i.e., longitudinal and transverse) with two different types of epoxy resin (Tyfo MB-3 and Tyfo S) to generate the adhesion and saturating the fibers. After the test, they found that applying FRP increased the strength of the pole because the number of the cycles increased from 40,000 to 120,000 cycles. After removing the fibers, they found that there was no development in cracks after applying FRP.

6.1.1 Fatigue/Cyclic Sample Poles

Table 31 shows the testing matrix for the fatigue test, repair type and dimensions, and damage level of each pole. This is a subset of the large-scale specimen matrix presented in Table 28. As with the large-scale monotonic tests in Chapter 5, the fatigue/cyclic test setup was the same horizontal cantilever configuration shown in Figure 133. The pole length was 11 ft, and the center of load applicator was 9 ft from the pole base. The laser displacement gauges were changed from Balluff to MTI Instruments LTS 300-200. Slight modifications were made to the pole base connection to accommodate positive and negative displacement excursions and to minimize the displacement of the pole tip due to deformations and rotations associated with the plates mounted to the buttress. A 55 kip MTS actuator was used to replace the 800 kip Enerpac used during the monotonic tests.

A set of four plates were welded to the pole tip and then bolted to the actuator to allow continuous push/pull force without slip. To prevent localized deformations of the cross-section at the tip, an additional stiffener plate was welded vertically to the interior of the pole section, as shown in Figure 206. A 1 in plate (instead of ½ in) was welded to the base of each fatigue pole specimen. This plate was then bolted to the 2 in plate using six (6) 1 in diameter bolts as with the monotonic tests. However, the fillet weld of the pole base plate to the 1 in plate was made continuous all around to resist load in both directions, and an additional plate washer was placed on top of the pole base plate before bolting with the 1 in bolts to stiffen the connection. The cantilever configuration connection to the buttress is shown in Figure 207. Details of the plate weld and bolt patterns for the fatigue specimens are shown in Appendix B.

Table 31. Full –scale testing matrix for fatigue test

Pole ID	Fiber Type	Matrix Type	Dent Height Above Base	Angle Between Port and Dent	Wrap Dimensions (in)				No. of Layers
ST-7	B	PU	22″	-	45×54				1
ST-10	G	PU	16″	90°	4×58	12×58	44×49		1
ST-11	G	QB Wet	16″	90°	9×58	12×58	6×58	48×26	1

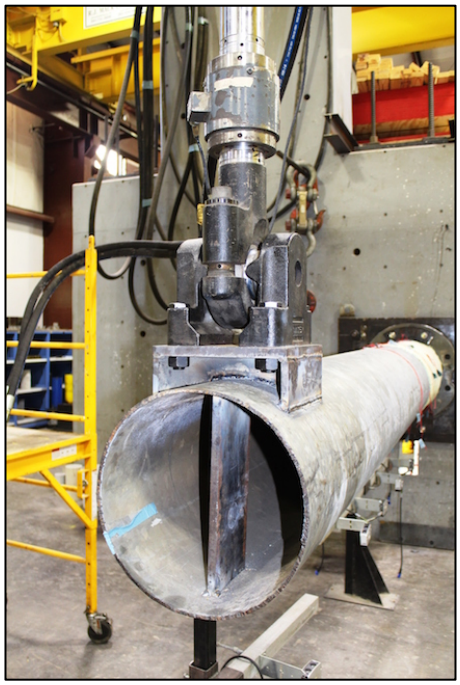

Figure 206. Fatigue test actuator connection with stiffener at end section

Figure 207. Fatigue test connection to buttress with plate washers on top and bottom

The loading protocol for the fatigue/cyclic tests was separated into two parts. The first part of the loading protocol involved the application of a fully-reversed (zero mean), constant load amplitude with a specified target of two million cycles. The stress range corresponding to the load amplitude in this phase was selected to be proportional to one of the AASHTO (AASHTO, 2012) fatigue categories (A = 24 ksi, B = 16 ksi, B' or C' = 12 ksi, C = 10 ksi, D = 7 ksi, E = 4.5 ksi, E' = 2.6 ksi). The details of the loading and load amplitudes are presented specific to each specimen tested in the following sections. The loading rate was dependent on the stroke necessary for each individual pole but typically was in the range of 1.5 to 2.5 Hz. Data was recorded based on discrete triggering times to minimize the total number of cycles of data recorded.

In the event that no failure occurred during the first two million cycles, the second part of the loading protocol commenced. The second part of the loading protocol involved the application of a fully-reversed, constant load amplitude for 1000 cycles, where the load amplitude was increased proportional to the subsequent AASHTO fatigue category after each successive 1000 cycles were completed. For example, a specimen tested for two million cycles at a stress range proportional to category E would undergo 1000 cycles at each of category D, C, etc. until failure occurred. Data was collected continuously during these successive 1000 cycle tests in the second part of the loading protocol. Due to the increasing displacements at larger stress ranges, the loading rate diminished below 1 Hz.

Specimens ST-7 and ST-11 followed the abovementioned two parts of the loading protocol. However, specimen ST-10 experienced fracture after only approximately 1500 cycles during the first part of the loading protocol. Therefore, the anticipated fatigue life, based on the local-stress

approach presented in AASHTO (2013), was computed to determine whether such a failure would be expected for a new specimen. It should be reiterated that it is unknown the number of cycles of mechanical loading the specimens already received in the field prior to be used in this study. It is also unknown what environmental conditioning the specimens received or the initial weld quality.

6.1.2 Fatigue Stresses by Using AASHTO Design Criteria

To resist the stresses due to wind-induced and gust-induced load, freestanding support structures have to be designed for fatigue. In general, the wind load-induced stress range should be less than the fatigue resistance (i.e., below the constant fatigue threshold providing infinite life, because the finite life approach may be unreliable and cannot be used in the design). Different approaches have been developed depending on the models for fatigue life that are listed below (Stephens et al., 2000):

- The nominal stress-life *(S-N)* model.
- The local strain-life *(ε-N)* model.
- The fatigue crack growth *(da/dN-ΔK)* model.
- The two-stage model. It is the combination of the first two models to merge macroscopic fatigue crack formation and fatigue crack growth together.

Depending on the model selected, the fatigue life and resistance vary. In general, the nominal stress-life (*S-N*) model is the most widely used.

6.1.2.1 Nominal Stress-Based Design

As is typical with design based on capacity and demand, the following relation has to be followed:

$$(\Delta f)_n \leq (\Delta F)_n \tag{6-1}$$

where $(\Delta f)_n$ and $(\Delta F)_n$ are the nominal wind-load induced stress and fatigue resistance. At the location of potential fatigue cracking, the nominal stress is calculated. For example, the nominal stress for socket connection (fillet-welded tube-to-transverse-plate connection) is calculated on the gross section of the tube at the fillet-weld toe on the tube. Based on AASHTO (2013) Table (11.9.3.1-1) and Table (11.9.3.1-2), the geometric parameters in Table 32 for each of the pole specimens tested are listed. For the tube-to-transverse-plate connection type sign structure, the corresponding schematic that illustrates the geometry is shown in Figure 208. The constant C_{BC} is the ratio of D_{BC} to D_T.

Table 32. Additional pole geometric parameters necessary for AASHTO equations

Pole #	External diameter D_T (in)	Diameter of circle through the fasteners in plate D_{BC} (in)	Thickness of tube t_T (in)	Thickness of transverse plate t_{TP} (in)	C_{BC}
ST-7	16.5625	26.075	0.25	2.5625	1.574
ST-10	17.625	22.25	0.25	1.75	1.262
ST-11	17	23	0.25	2.25	1.353

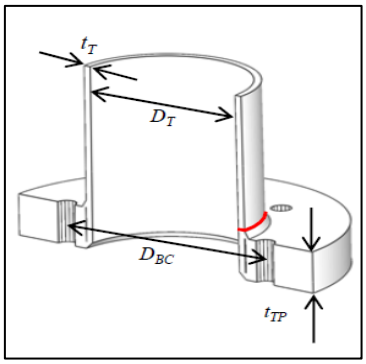

Figure 208. Tube-to-transverse-plate connection, location of anticipated fatigue crack at the weld toe on the tube is shown in red (AASHTO, 2013)

Table 33. Fatigue calculations for nominal stress

Pole	K_F	K_I	$(\Delta F)_{TH}$ (ksi)	$Ax10^8$ (ksi^3)
ST-7	2.86	6.15	4.5	3.9
ST-10	3.17	6.92	4.5	3.9
ST-11	2.83	6.10	4.5	3.9

The fatigue stress concentration factors for finite and infinite life, respectively, are denoted as K_F and K_I. The equations for each are shown below and can be computed based on the quantities in Table 32:

$$K_F = 2.2 + 4.6(15t_T + 2)(D_T^{1.2} - 10)(C_{BC}^{0.03} - 1)t_{TP}^{-2.5} \quad (6\text{-}2)$$

$$K_I = [(1.76 + 1.83t_T) - 4.76{\times}0.22^{K_F}]K_F \quad (6\text{-}3)$$

The resulting finite life constant A and the constant amplitude fatigue threshold (CAFT) ΔF_{TH} are shown together with the stress concentration factors in Table 33. The CAFT values correspond to the AASHTO category E.

For failure to occur at the target number of two million cycles selected for testing, the corresponding finite life stress range (according to the values in Table 33) is approximately 6 ksi for the three specimens. In the loading protocol for the three specimens, it was assumed that the tip load amplitude was determined directly from the AASHTO stress category. Because the load cycles were fully reversed (zero mean), the stress range necessary when computing fatigue life estimates using the AASHTO equations was therefore doubled (and is accounted for in the predicted cycles to failure for the specimens presented below). For specimens ST-7 and ST-11, stress category E was selected. Therefore, the stress range was 9 ksi (2 times 4.5 ksi). The stress range for ST-10 was selected to be substantially higher at 28 ksi (2 times 14 ksi), between categories B and C.

6.1.2.2 Local Stress-Based Design

Given the observed fracture near the weld toe, it was of interest what the predicted fatigue life of ST-10 would be using the local stress based design methods in AASHTO. Both the finite life and infinite life methods are summarized in this subsection, as presented in AASHTO (2013) and the background NCHRP document (NCHRP-176, 2011). To use the local stress method for fatigue design, the welded connections are designed by using finite element analyses (FEA) and the following relation should be achieved:

$$(\Delta f)_l \leq (\Delta F)_l \tag{6-4}$$

where $(\Delta f)_l$ is wind induced local stress at the weld toe and $(\Delta F)_l$ is the local fatigue resistance. For some welded connections, like the tube-to-transverse plate and tube-tube connections, the fatigue performance for the connection will be affected by geometric stress concentration at the location of the weld transitions. With finite life, this method is balanced against fatigue cracking at the weld toe. In the case of design for infinite life, fatigue crack initiation and crack propagation have to be prevented. Because of that, the procedure recommended for one method is not appropriate for the other method.

A linear FEA of a (3D) model of the connection was used to determine the local stresses in welded connections. In thin tubular structures, the geometric stress concentration will be influenced because the weld is going to act like a tiny stiffener. The suggested finite element model for determining stresses based on the finite life approach is shown for ST-10 in Figure 209.

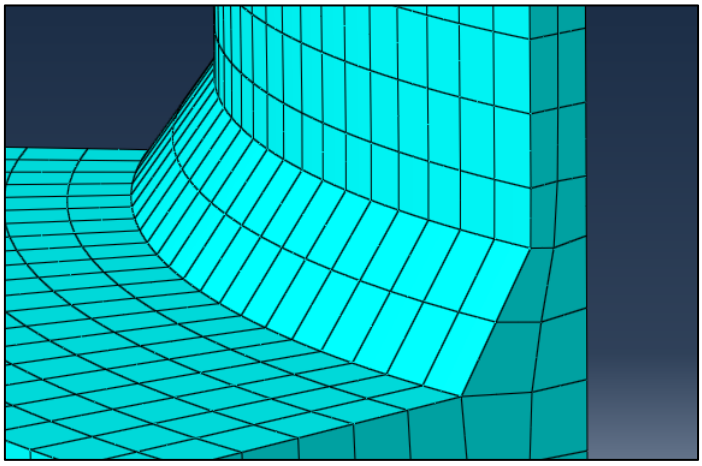

Figure 209. Finite element model for finite life (ST-10)

The finite element model shown in Figure 209 has met special requirements according to (AASHTO, 2013) including:

- The model has to be large enough to neglect the effect of load and boundary conditions assumptions on calculated results.
- Reduced integration 20-node solid isoparametric elements are preferred for modeling the connection.
- Twenty-node solid hexahedron elements of isoparametric formulation are standard elements used for stress analysis.

- In tubes, a mesh size of ($t \times t$) (t is the thickness of the tube) has to be used at least three rows of elements in front of the weld toe.
- Two elements have to be used in the thickness direction.

To use this model for fatigue design as the local stress, the maximum (tensile) principal stress on the tube surface at a location $0.1(r \times t)^{0.5}$ ahead of weld toe will be used, where r is the outer radius of the tube and t is the tube thickness. In this model, fixed boundary conditions at the base of the model were used and a uniform stress (in the axial direction) was applied to the top of the tube. While the AASHTO guidelines were intended for use on purely metallic sign and pole structures, the presence of the FRP wrap will clearly have an impact on the local stresses. Therefore, to account for the stress concentration arising from the termination of the wrap near the weld, an additional layer of elements was added to the finite element model. The thickness of the additional elements was assumed to be 0.1 in, based on having two layers of FRP at that pole base and treating them using the same material properties as the base metal using an equivalent modulus approach. The resulting finite element model is shown in Figure 210.

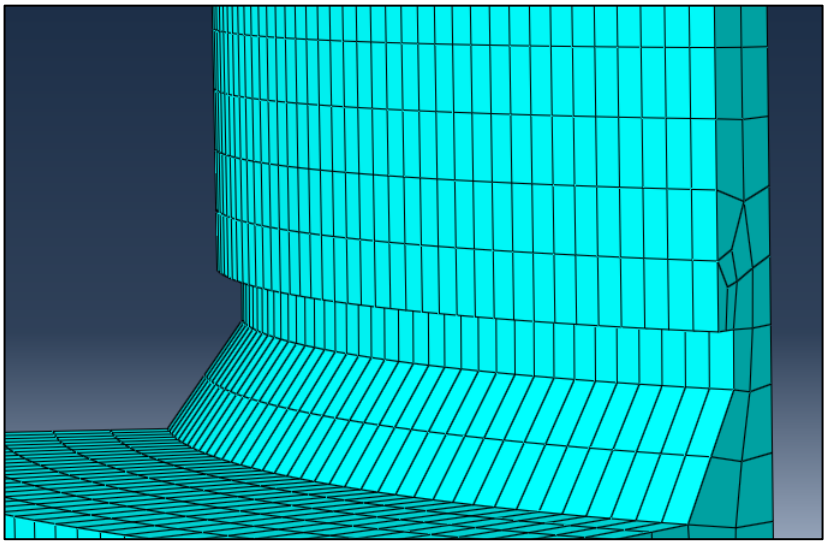

Figure 210. Finite element model for finite life with supplemental FRP layer (ST-10)

In the finite life case, the local fatigue resistance can be determined:

$$(\Delta F)_l = \left(\frac{A}{N}\right)^{\frac{1}{3}} \tag{6-5}$$

where N is the number of wind-load induced stress cycles expected during the lifetime of the structure.

The design for infinite fatigue life was intended to prevent cracks regardless of the service life. Accordingly, it was suggested that the weld toe notch should have imperceptible damage, and the notch stresses are completely elastic. In some cases, some cracks will be initiated at the weld toe notch but not spread; that is, dormant cracks, which might cause local damage with increasing cyclic loads. Consequently, the local stress at the weld toe notch should be determined for

infinite life design (NCHRP-176, 2011). Figure 211 and Figure 212 show the infinite life finite element model mesh and a detail view of the notch area.

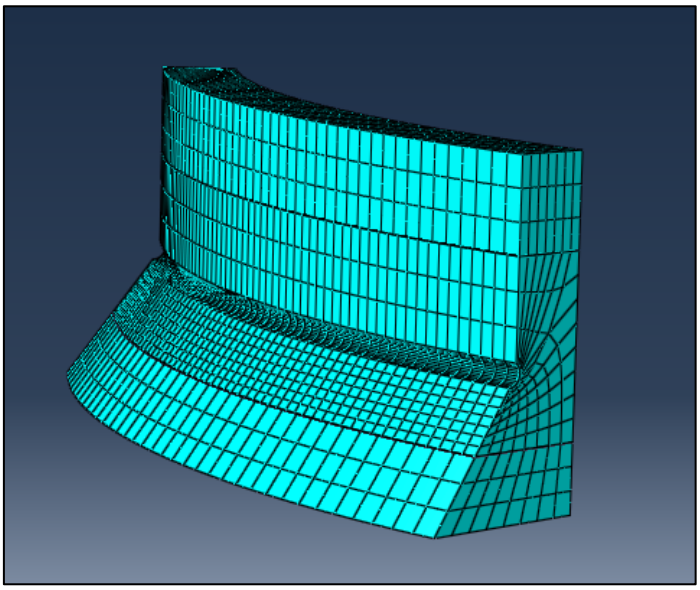

Figure 211. FEM for infinite life

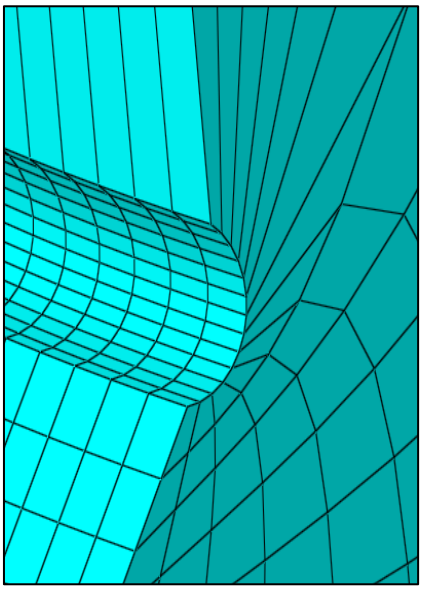

Figure 212. Enlarged mesh detail for notched area

The above model has some features following the requirements that are summarized below (AASHTO, 2013):

- The model has to be large enough to neglect the effect of load and boundary conditions assumptions on calculated results.
- Reduced integration 20-node solid isoparametric elements have to be used to model the connection and the weld toe region.
- At least eight elements have to be used along the rounded notch edge.
- A radius of 0.04 in has to be located at the center of the notch to obtain a fatigue effective stress at the weld toe notch.

By using the material properties, the local stress resistance for the infinite life case can be calculated using the following formula:

$$(\Delta F)_l = \frac{1}{3.2}[-F_y + \sqrt{F_y^2 + 4F_u^2}] \quad (6\text{-}6)$$

where F_y is the yield strength of the material and equal to 54.8 ksi for the poles in Table 31 and F_u is the tensile strength of the material and equal to 67.6 ksi. From the finite element model analysis, the maximum tensile stress in the wall of the tube that corresponds to $(\Delta F)_l$ can be back calculated (because the model is linear). The following figures show the finite element analysis results for the finite (Figure 213) and infinite (Figure 214) life fatigue models specific to the geometry and properties of ST-10.

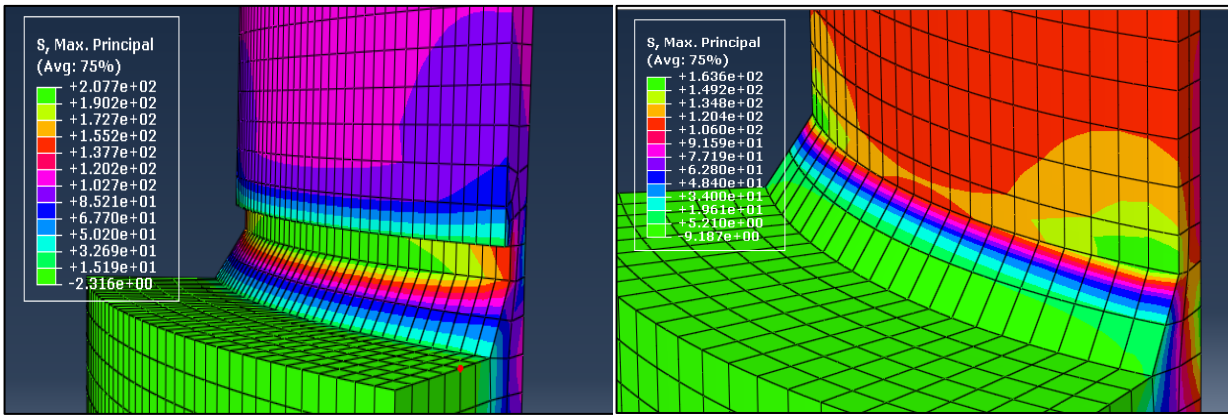

(a) Pole with FRP attached **(b) Original pole geometry**

Figure 213. FEM for finite fatigue life (ST-10)

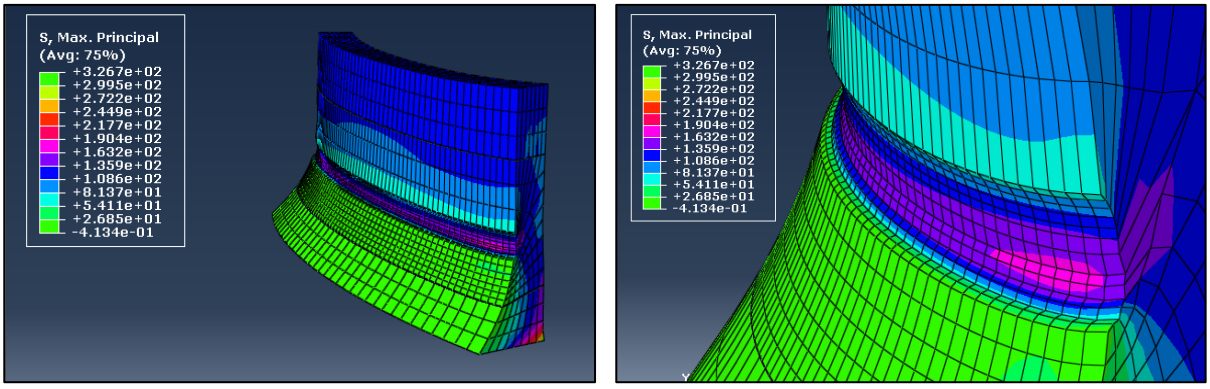

(a) Contours of stress for original pole geometry **(b) Contours of stress in the notched region**

Figure 214. FEM for infinite fatigue life (ST-10)

The results shown in Figure 213 and Figure 214 are in metric stress units (N/mm^2). To more easily interpret the results relative to the prescribed limits for each AASHTO category, the values delineating the contour boundaries are shown in Table 34 below in both unit systems.

Table 34. Stress contour magnitudes in both U.S. and SI units from Figure 213 and Figure 214 (ST-10)

Finite Life				Infinite Life	
Without FRP		With FRP			
N/mm^2	ksi	N/mm^2	ksi	N/mm^2	ksi
163.6	23.7	207.7	30.1	326.7	47.4
149.2	21.6	190.2	27.6	299.5	43.4
134.8	19.6	172.7	25.0	272.2	39.5
120.4	17.5	155.2	22.5	244.9	35.5
106	15.4	137.7	20.0	217.7	31.6
91.59	13.3	120.2	17.4	190.4	27.6
77.19	11.2	102.7	14.9	163.2	23.7
62.8	9.11	85.21	12.4	135.9	19.7
48.4	7.02	67.7	9.82	108.6	15.8
34	4.93	50.2	7.28	81.37	11.8
19.61	2.84	32.69	4.74	54.11	7.85
5.21	0.756	15.19	2.20	26.85	3.89

For the finite life design, the fatigue resistance can be estimated, as well as the number of cycles. The maximum principle stress located at $0.1(r \times t)^{0.5}$ or 0.21 in ahead of weld toe was used. To calculate the number of cycles for finite life, the stress range ahead of the weld toe of 15.4-17.5 ksi was determined from the model. With A = 3.9e8 ksi and the mentioned values, the number of cycles to failure predicted are 72,770-104,045. This is far in excess of the stress range imposed and number of cycles observed in ST-10.

Based on the infinite life fatigue resistance of 28.5 ksi for ST-10, the converged maximum (tensile) surface stress at the center of the rounded notch of 19.7-23.7 ksi can be compared to the stress in the tube. The tube stress that corresponds to this resistance was 9.5 ksi. As expected, the infinite life stress range is lower than the experimental value imposed on the specimen.

6.1.3 Fatigue Test For Poles in The Laboratory

Details from the three pole specimens tested under cyclic loading at Florida Department of Transportation (FDOT) Structural Research Center (SRC) are presented in the following subsections. Similar to the full-scale monotonic tests, the displacement gauges D1 through D6 were located at distances of 9, 27, 45, 63, 95, and 129.625 in from the face of the buttress. The strain gauge plans were also unique to each specimen and shown below with each individual specimen's results.

6.1.3.1 ST-7

This round pole had been dented to around 16% of the undented diameter and retrofitted with one layer of basalt/polyurethane composite wrap that was extended 45 in up the pole to cover the whole dent. It has 0.25 in wall thickness and 16.5625 in diameter at the base with no access port. This pole had one large dent and the center of the dent was located at 22 in from the base plate. The pole was prepared for the test like the previously discussed monotonic pole specimens, with repair details and geometry shown in Appendix A. The repaired pole is shown in its cantilever test configuration in Figure 215.

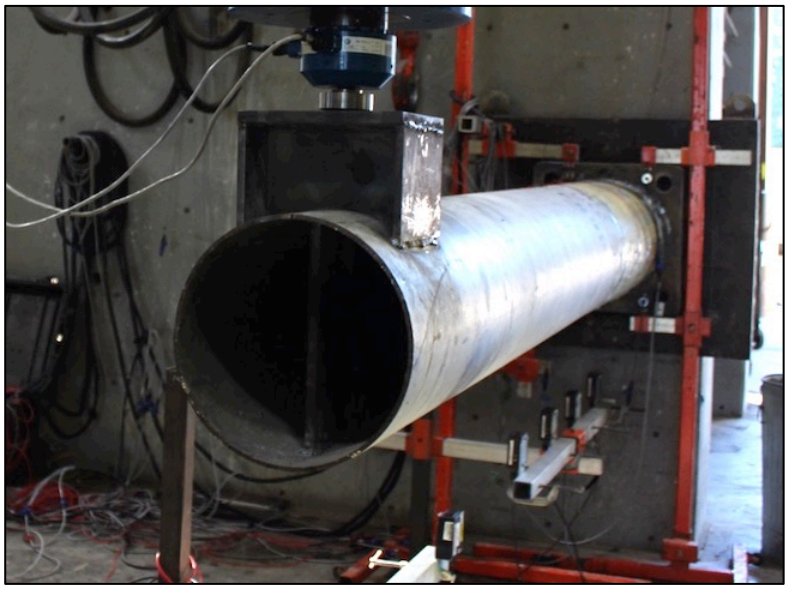

Figure 215. ST-7 test configuration

The pole was tested to 2 million cycles of constant amplitude (load control) at a stress amplitude of -4.5 to 4.5 ksi, or load amplitude of -2.14 to 2.14 kip. The stress range therefore corresponds to twice AASHTO category E and is consistent with the CAFT presented in Table 33. The cycles were fully reversed (same positive and negative load achieved at each cycle). The predicted number of cycles to failure based on Equation 6-5 is 535,000. The displacement compliance and strain data with respect to the cycle number are shown in Figure 216. The locations of the various strain gauges are shown in Figure 217.

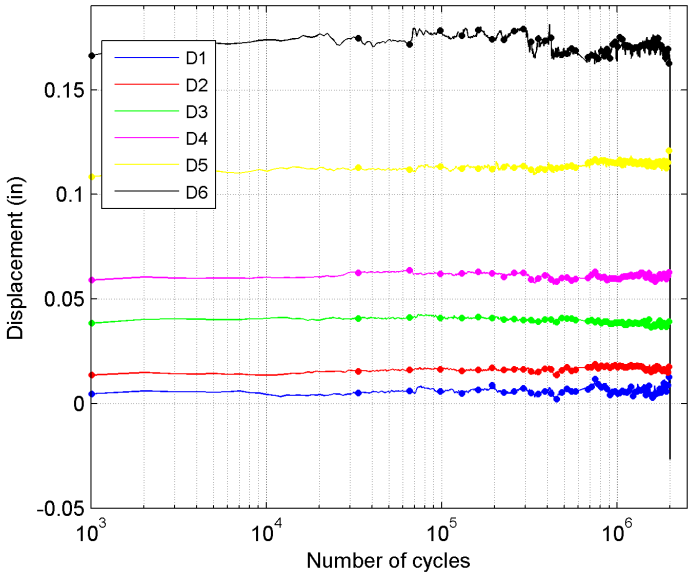

(a) ST-7 displacement compliance data

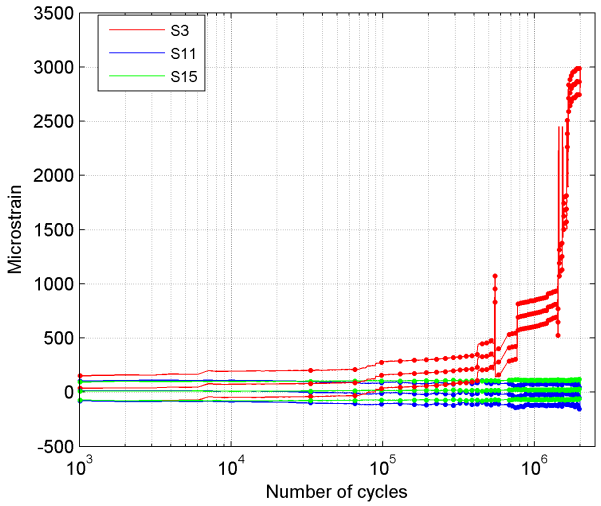

(b) ST-7 steel bottom strain history

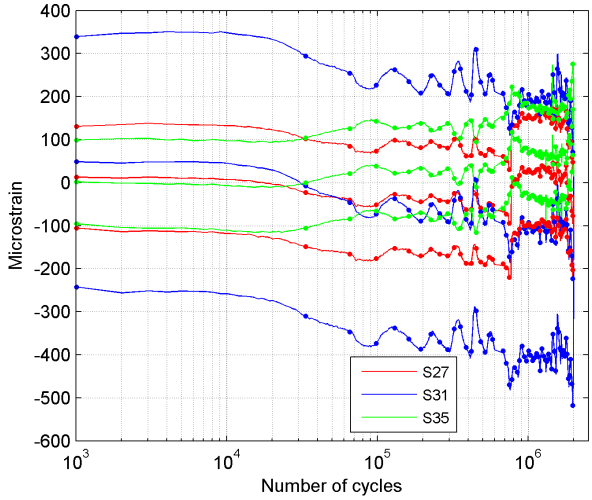

(c) ST-7 FRP bottom strain history

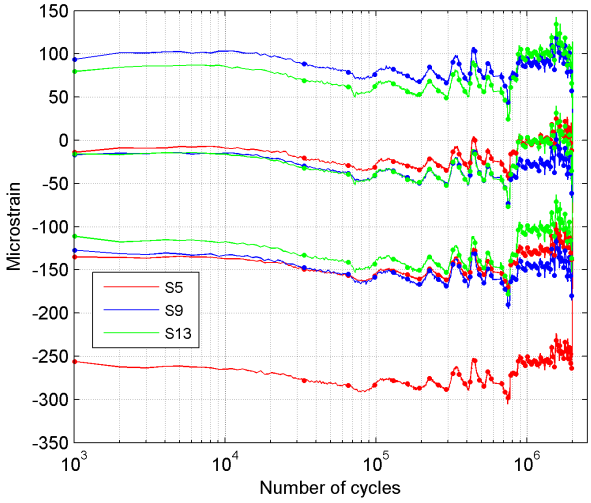

(d) ST-7 steel top strain history

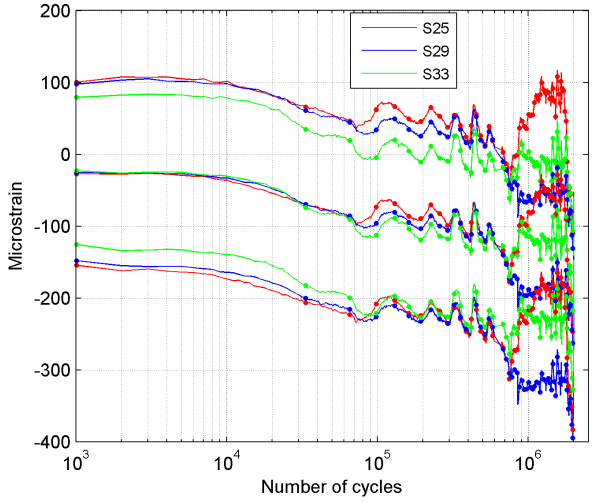

(e) ST-7 FRP top strain history

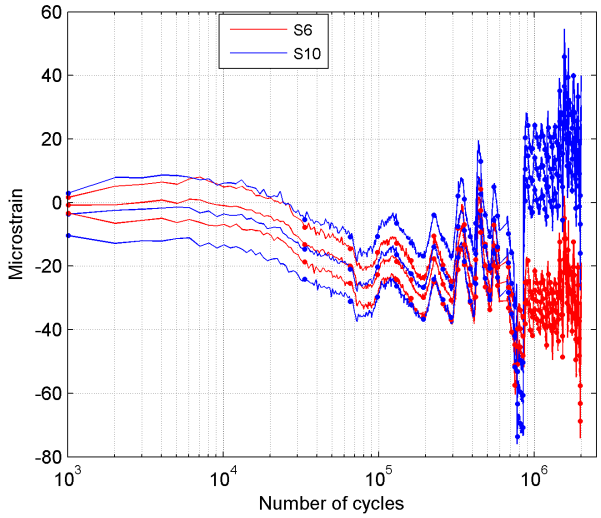

(f) ST-7 steel transverse strain history

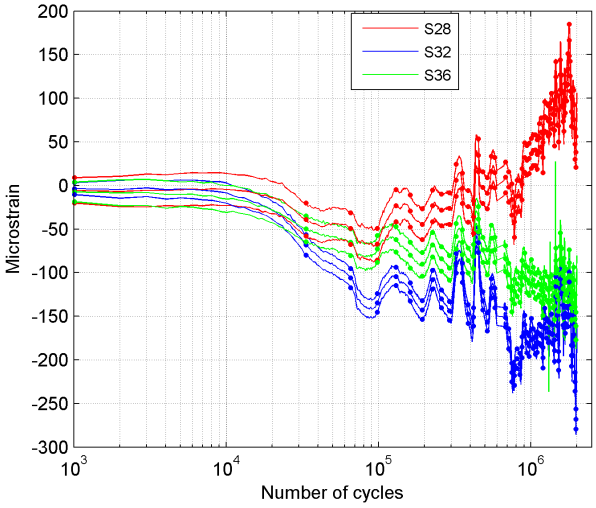

(g) ST-7 FRP transverse strain history

Figure 216. ST-7 test data during first 2 million cycles

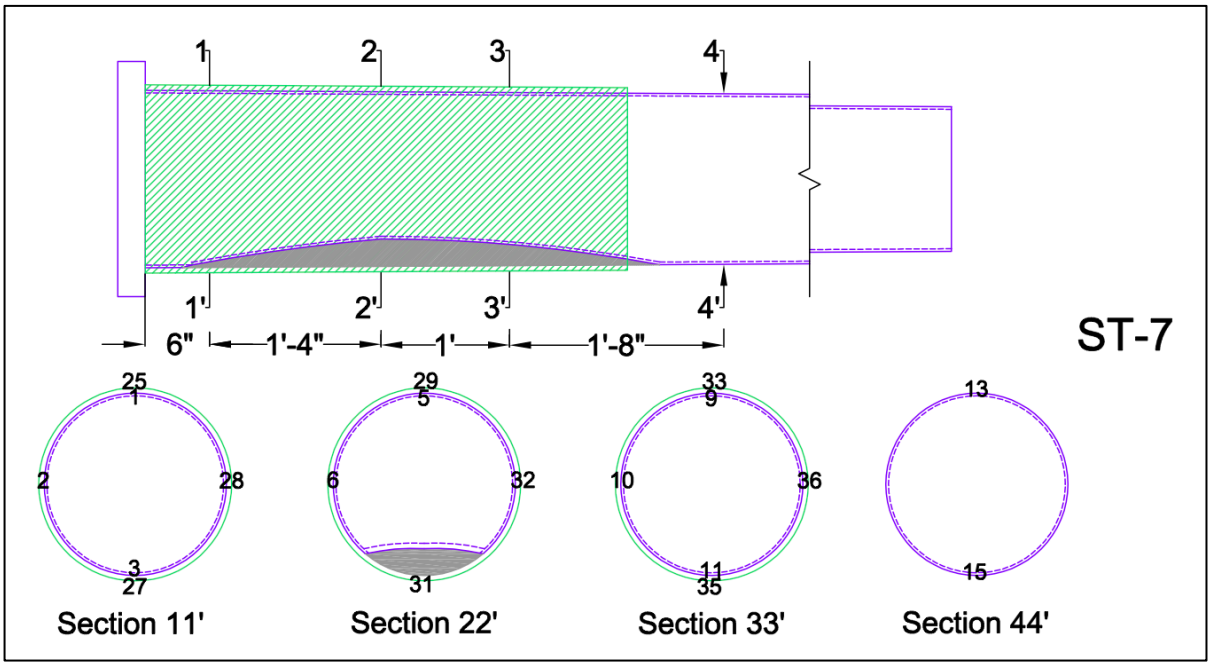

Figure 217. ST-7 strain gauges

The displacement compliance in Figure 216 (a) demonstrates that neither the base metal, nor the FRP repair, experienced any degradation of stiffness throughout the first 2 million cycles. The strain data shown in Figure 216 (b-g) are shown in triplicate for each gauge, showing the maximum, mean, and minimum strain at each cycle number. The phasing of the load and the strain were assumed to be the same (the peak strains correspond to the load peaks and the mean strain corresponds to the zero load). Top steel strain ranges during all cycles were stable at around +/- 100 με, although the gauge nearest to the base (S1) did not record any data.

Bottom steel strain ranges were also stable, except for S3 that showed rapidly increasing strains (in tension) that are due to the location of the gauge at the edge of the dented region. Tensile strains indicate the tension (upward) stroke caused the dent to actually straighten (note that S5 at the same section becomes compressive). The strains shown in Figure 216 (b) are likely not beyond yield; however, due to the jumps in the strain channel that are not physical (and do not correspond to similar jumps in the bottom FRP or adjacent section). The largest strain ranges recorded were for S31, which is the gauge mounted to the laminate (bottom of pole). A mild increase in the strain range was recorded in the transverse strain gauges, although the magnitudes were very small. No debonding is evident in the strain data at any of the sections.

After the 2 million cycles, the pole was subjected to 1000 cycles each at successively higher load amplitudes corresponding to each of the AASHTO categories until failure (D, C, B', B, and A). However, at the end of the stress category A, the pole was still intact, and therefore was monotonically loaded to failure (the only one of the three fatigue specimens for which this occurred). The load-displacement response of the pole after 2 million cycles is shown in Figure 218. The loops are essentially linear and stable for all cycles and load levels. The load amplitudes corresponding to each of the sequentially increasing stress categories are 3.34, 4.77, 5.72, 7.63, and 11.4 kip, respectively.

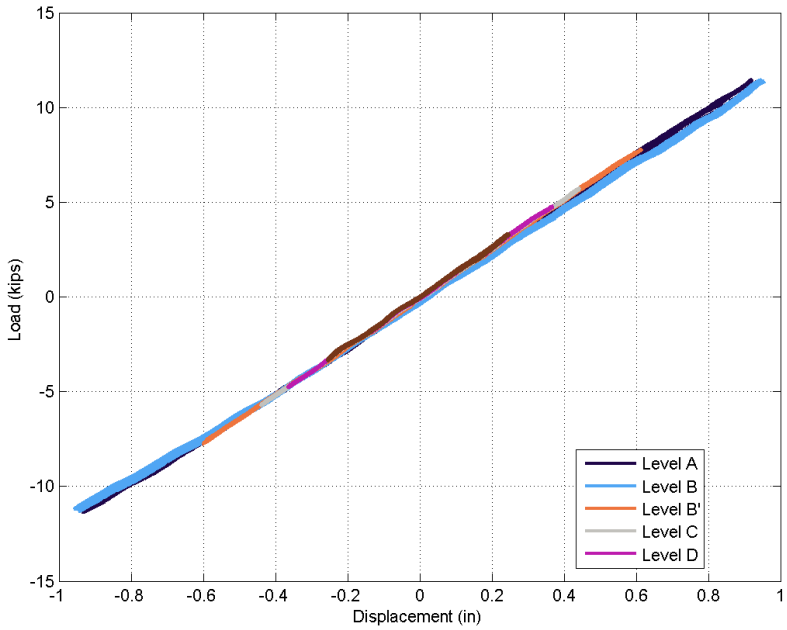

Figure 218. ST-7 load-displacement hysteresis during increasing fatigue category level

During the increased stress level increments of 1000 cycles each, the strain was monitored and the maximum strains during each cycle extracted. For each strain gauge, the strains are plotted in Figure 219 for steel and Figure 220 for FRP. Each point on the curve corresponds to the maximum strain during a single full cycle. Any instrument drift or residual strain from the previous two million cycles was removed (hence S3 shows strain magnitudes similar to S27, for example). The growth of the maximum strain is approximately linear with load in a majority of the gauges, except the transverse gauges (where the strain magnitudes are small). The largest steel strain maxima occur at stress level A and correspond to a less than half the yield stress of the base metal (approximately 20 ksi). This would indicate that the thickness of the pole at the base was nominally larger than the expected value of 0.25 in. Dogbone coupons removed from the pole for tensile testing indicated thicknesses of 0.3 in, which confirm this observation.

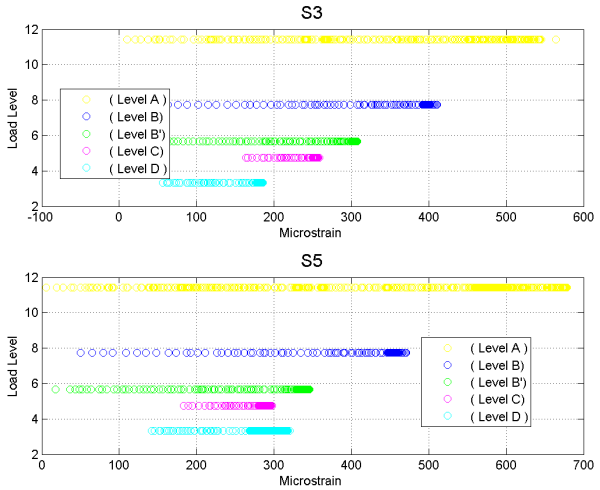

(a) ST-7 strain gauges S3 and S5 maxima

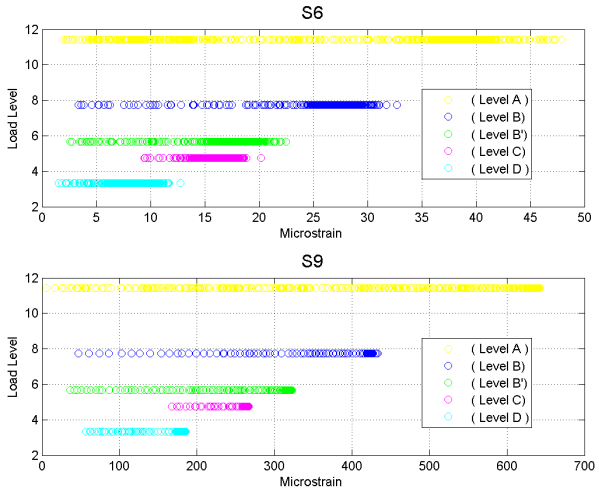

(b) ST-7 strain gauges S6 and S9 maxima

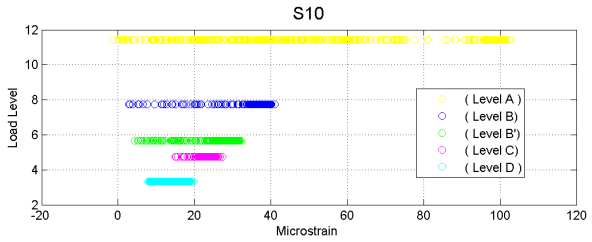

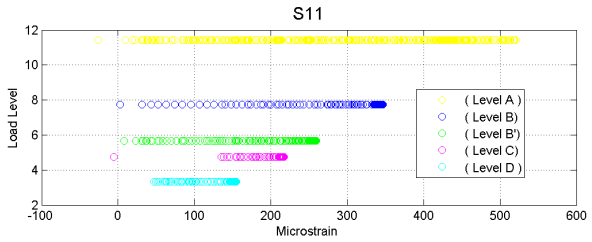

(c) ST-7 strain gauges S10 and S11 maxima

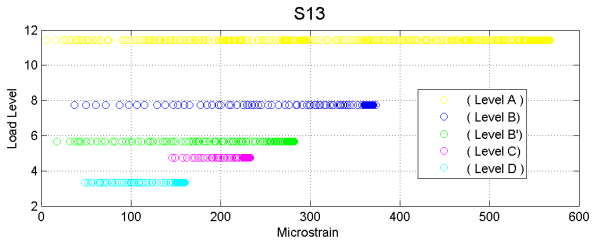

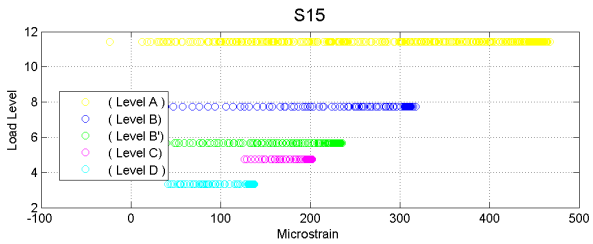

(d) ST-7 strain gauges S13 and S15 maxima

Figure 219. ST-7 steel strain data during higher stress level cycles

As with the initial two million cycles, the largest strain recorded was the FRP gauge mounted on the dented region (pole bottom). The maximum strain was 1600 με, which is lower than any critical strains measured during the compression tests in Chapter 3. During stress level A, it appears that there was some debonding near section 3. There is some evidence of this in the post-failure photos in Figure 222 (c) and (d); however, the extents likely correspond to the failure test and not the 1000 cycles under stress level A. No other debonding was evident based on the strain data during any of the increased stress amplitude cycles.

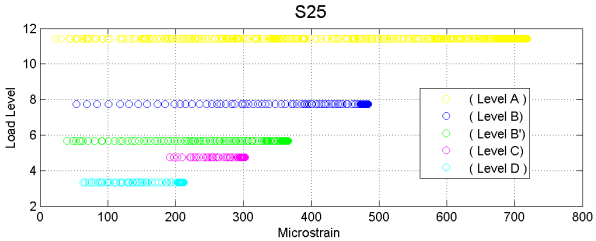

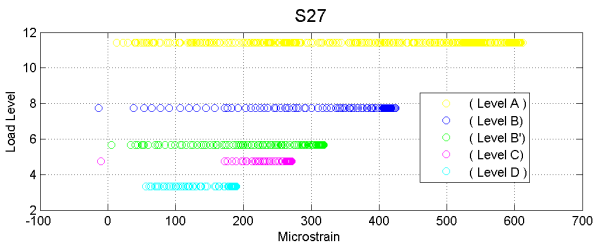

(a) ST-7 strain gauges S25 and S27 maxima

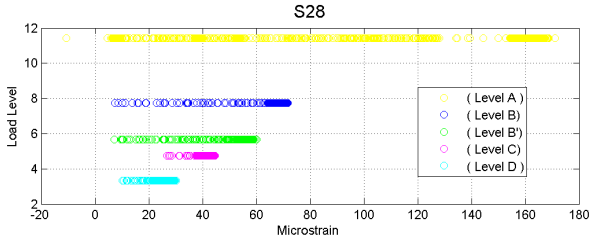

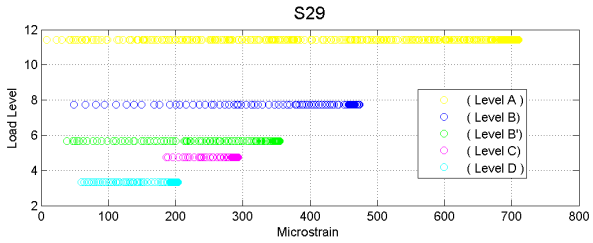

(b) ST-7 strain gauges S28 and S29 maxima

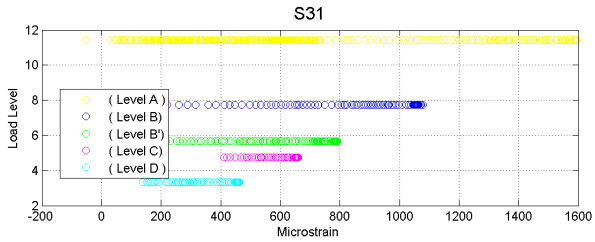

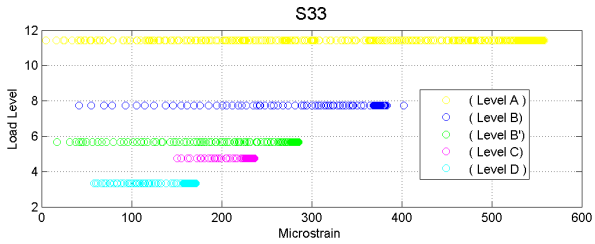

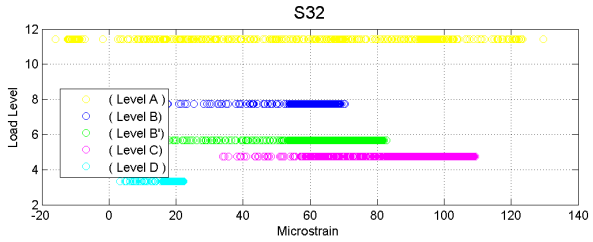

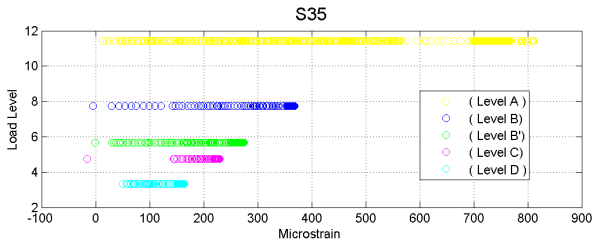

(c) ST-7 strain gauges S31 and S32 maxima **(d) ST-7 strain gauges S33 and S35 maxima**

Figure 220. ST-7 FRP strain data during higher stress level cycles

Following the cycles at stress level A, the pole was monotonically loaded to failure. The test was stopped at the initiation of a crack at the weld toe on the tension face of the pole, as seen in Figure 221 (a) and (b). Such a crack at the weld toe is expected in fatigue prone details, and may have initiated during the 1000 cycles at stress level A. The post-fatigue monotonic test also resulted in substantial damage to the repair system. The circumferential laminate near the damaged section ruptured, as shown in Figure 222 (a), and compressive buckling occurred on the bottom of the pole surrounding the debonded region, as shown in Figure 222 (b). The debonding at the dented region likely began during the cycles at stress level A, but propagated in the monotonic test. Debonding at the pole base on the top side of the pole is shown in Figure 222 (c), and debonding on the bottom side of the pole is shown in Figure 222 (d).

(a) Cracking at weld toe

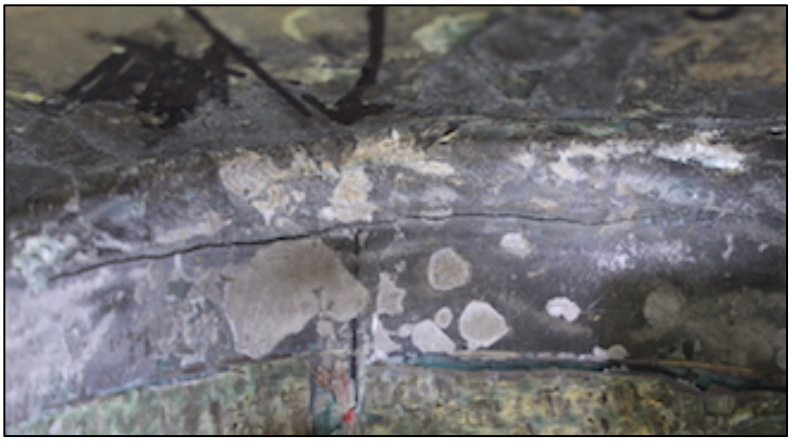

(b) Crack detail

Figure 221. ST-7 cracks after post-fatigue monotonic test

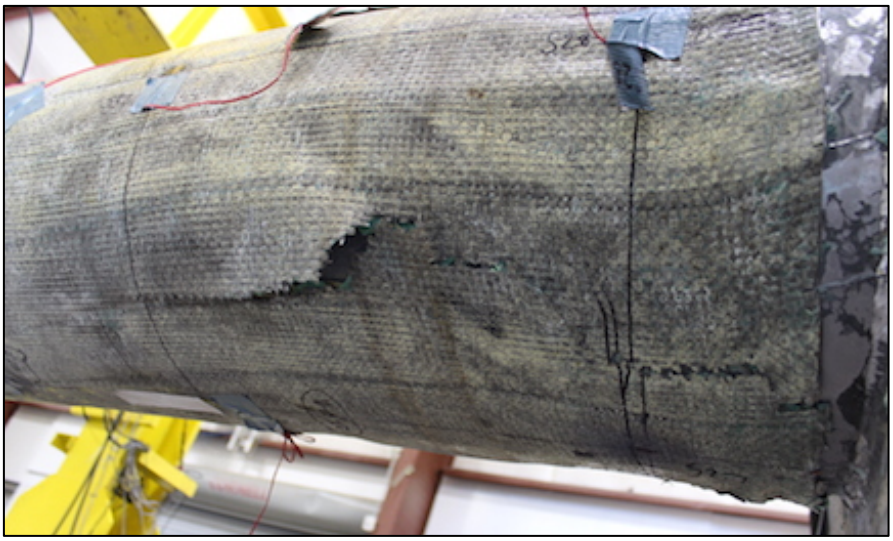

(a) Delamination and rupture of wrap initiating near base and propagating to midsection

(b) Compression wrap failure

(c) Debonded areas (top)

(d) Debonded areas (bottom)

Figure 222. ST-7 failure modes after post-fatigue monotonic test

6.1.3.2 ST-10

The second pole that was tested for fatigue is ST-10. This pole is round with dent length 44 in from the base plate and 21% of its outer diameter in depth. The dent is centered 16 in above the base plate and 90° from the access port. The access port dimensions are sizeable, as shown in the drawings of Appendix A, and contains a 1 to 2 in external lip plus reinforcement inside the access port. The pole was repaired by using a single-layer repair consisting of glass/polyurethane composite wrap. The pole was wrapped with three transverse pieces to cover the dent because of the existence of the access port, as seen in Appendix A. The repaired pole is shown in its cantilever test configuration in Figure 223.

The applied load level was -7.56 to 7.56 kip, which was selected to be above the threshold for infinite fatigue life based on the nominal stress approach. The load level corresponds to a stress range of 28 ksi (2x14 ksi, which is between AASHTO categories B and C). The computations for finite and infinite fatigue life based on finite element models were presented in the previous

section. The predicted number of cycles to failure based on the nominal stress method and finite life models were 17,800 and 104,000, respectively. The cycles were fully reversed (same positive and negative load achieved at each cycle). In the event no failure occurred (unlikely), the intent was to also complete 2 million cycles as was done for ST-7 and ST-11.

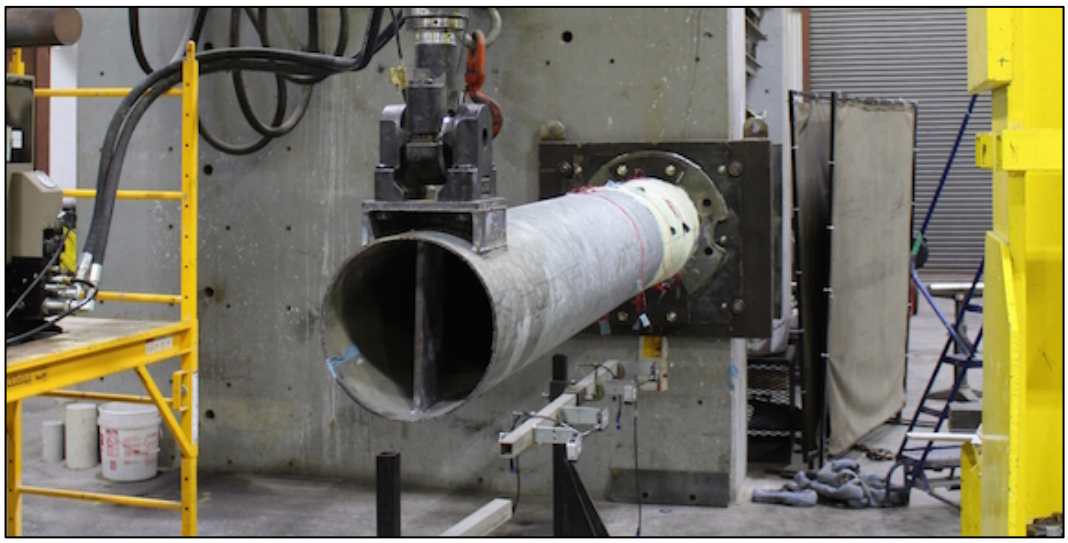

Figure 223. ST-10 test configuration

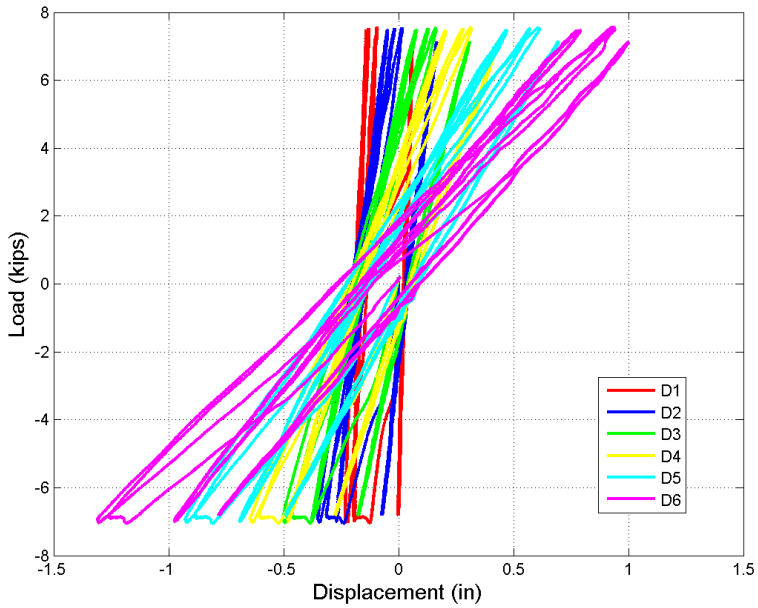

Figure 224. ST-10 load-displacement data during load ramps and all recorded cycles for the test

After only approximately 1500 cycles, the pole failed suddenly due to a rupture of the weld between the tube and base flange. The displacement compliance and strain data with respect to load are shown in Figure 224 and Figure 225, respectively, shown only for the cycles in which the data acquisition was acquiring data. The recording was not continuous; therefore, not all the test data for this pole is available due to the short number of cycles before failure. The locations of the various strain gauges are shown in Figure 226.

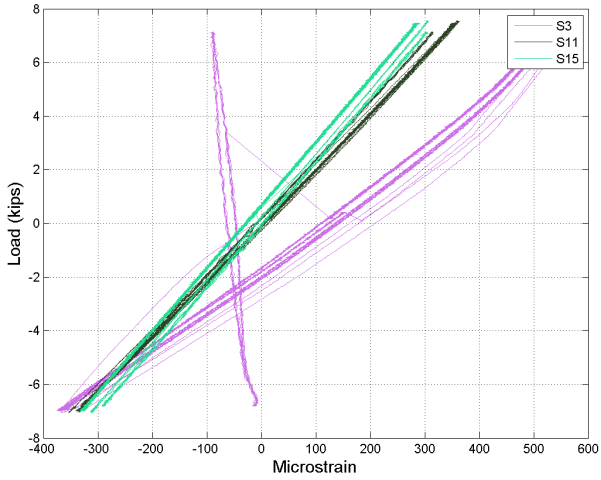

(a) ST-10 load-steel bottom strain

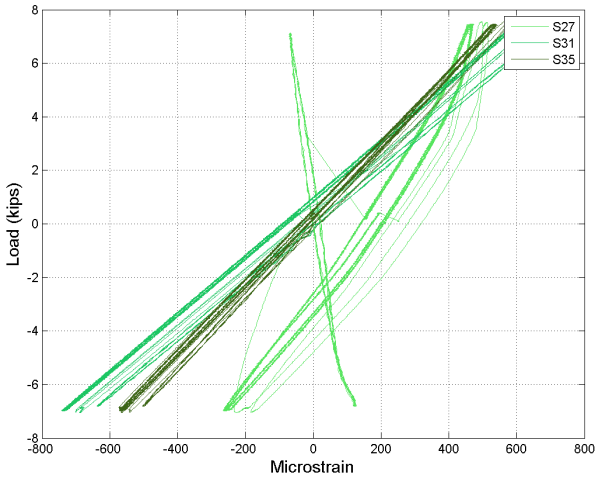

(b) ST-10 load-FRP bottom strain

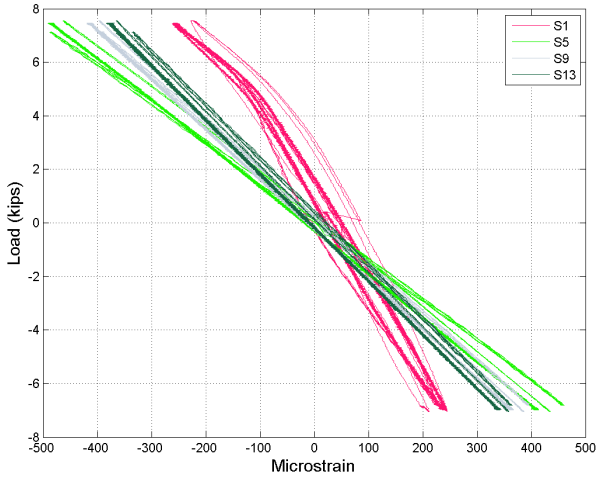

(c) ST-10 load-steel top strain

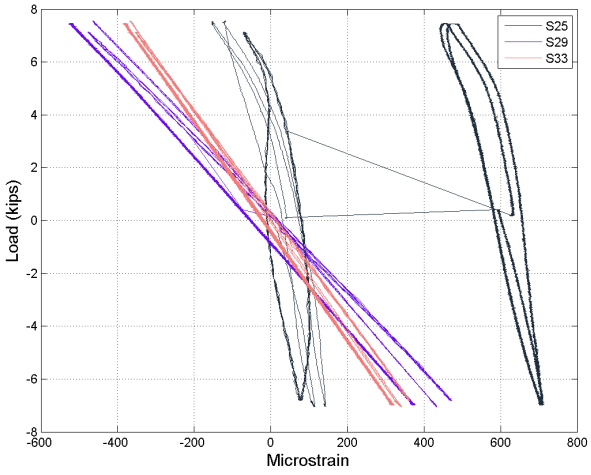

(d) ST-10 load-FRP top strain

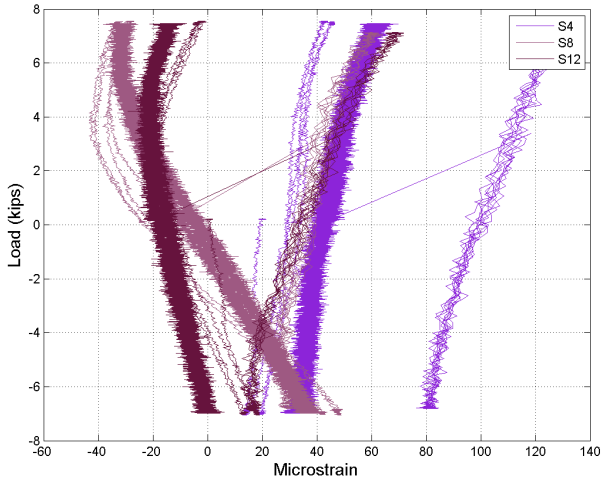

(e) ST-10 load-steel transverse strain

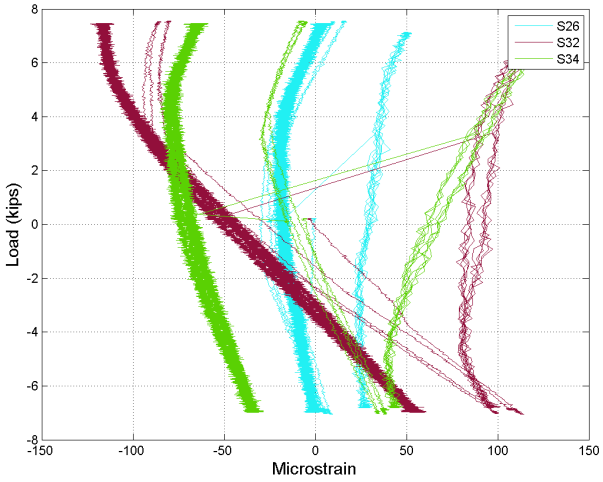

(e) ST-10 load-FRP transverse strain

Figure 225. ST-10 load-strain data during load ramps and all recorded cycles for the test

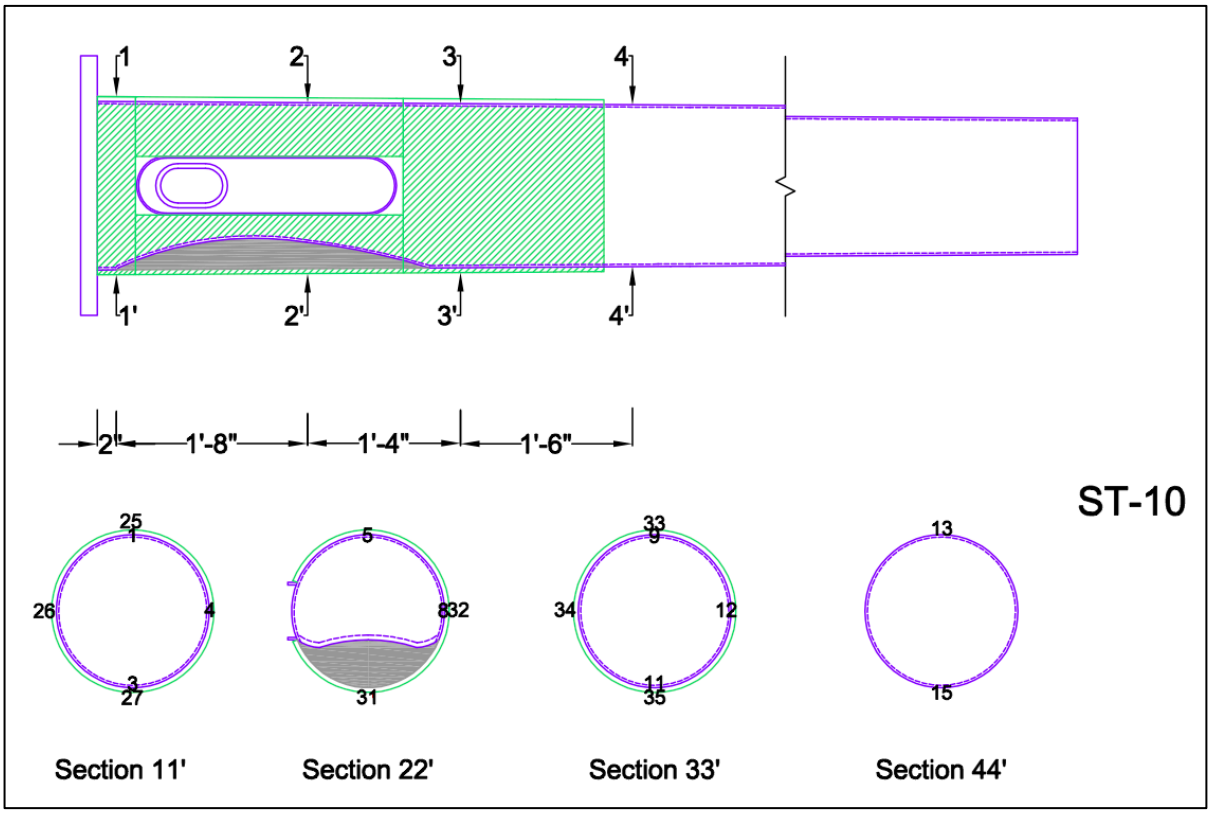

Figure 226. ST-10 strain gauges

The pole cracked at the weld toe and no further testing was completed. The crack and propagation of the crack around the circumference of the pole base is shown in Figure 227. As indicated by the predicted number of cycles to failure using the methods above, the fracture occurred significantly earlier than expected. No damage or delamination was evident in the repair system. A small portion of the wrap near the base was removed to better show the crack, as shown in Figure 227 (b) and (c), and was not a byproduct of testing.

6.1.3.3 ST-11

The last pole in this test is ST-11. The pole is also round with dent length 48 in and dent center 16 in from the base plate and 90° from the access port. In addition, the dent was 19% of 17 in (the pole diameter) in depth. Like the other poles, this pole was repaired by using one layer consisting of glass fibers and an epoxy matrix, which was installed using a wet layup process. Because of the existence of the access port, the transverse wrap was proportioned into three pieces, the full details of the repair are shown in Appendix A. The repaired pole is shown in its cantilever test configuration in Figure 228. There was some minor damage to the wrap near the neutral axis at the base east side from torching out the edge of the base plate for the through bolt, but this had no impact on the wrap performance.

(a) Wrap not damaged

(b) Crack propagated nearly full depth

(c) Crack detail

Figure 227. ST-10 wrap and crack at base weld

Figure 228. ST-11 test configuration

The pole was tested to 2 million cycles of constant amplitude (load control) at a stress amplitude of -4.5 to 4.5 ksi, or load amplitude of -2.26 to 2.26 kip. The stress range therefore corresponds to twice AASHTO category E and is consistent with the CAFT presented in Table 33. The cycles

were fully reversed (same positive and negative load achieved at each cycle). The predicted number of cycles to failure based on Equation 6-5 is 535,000. The displacement compliance and strain data with respect to the cycle number are shown in Figure 229 and Figure 230, respectively. The locations of the various strain gauges are shown in Figure 231.

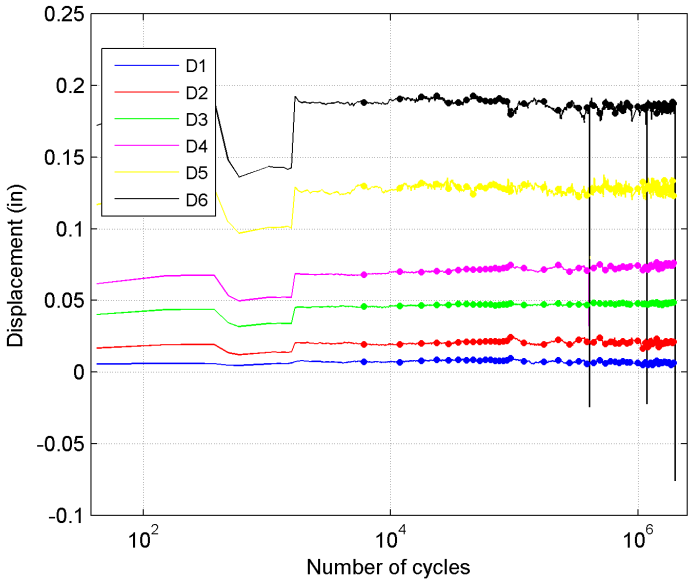

Figure 229. ST-11 displacement compliance during first 2 million cycles

The displacement compliance in Figure 229 demonstrates that neither the base metal, nor the FRP repair, experienced any degradation of stiffness throughout the first two million cycles. The strain data shown in Figure 230 (a-f) are shown in triplicate for each gauge, showing the maximum, mean, and minimum strain at each cycle number (same format as presented for ST-7). The only bottom steel strain gauge was S19 due to the location and extents of the dent. It recorded stable amplitudes of around +/- 100 με for all cycles.

The top gauges illustrated more interesting behaviors due to the locations near the base and center of the dented region. The top steel strain gauges exhibited stable behavior until approximately 250,000 cycles when S5, S9, and S17 increased in tension. The jumps; however, are likely not physical and do not correspond to similar jumps in the FRP gauges at the same cross sections. The steel gauge at section 2 drifts by approximately 300 με in tension, accelerating just after one million cycles. This is seen to a lesser extent in S9. However, only the change in S9 appears to correspond to decreasing behavior on the bottom side (S35). It is possible that localized debonding occurred on the top of the pole near section 3, although no evidence of this was found after completion of the higher stress level tests.

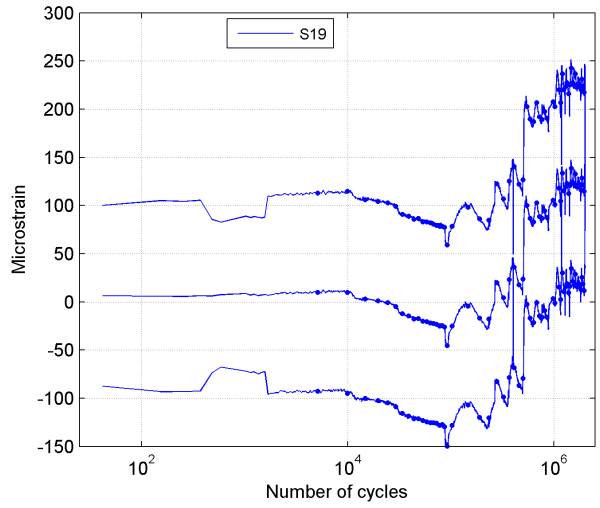

(a) ST-11 steel bottom strain history

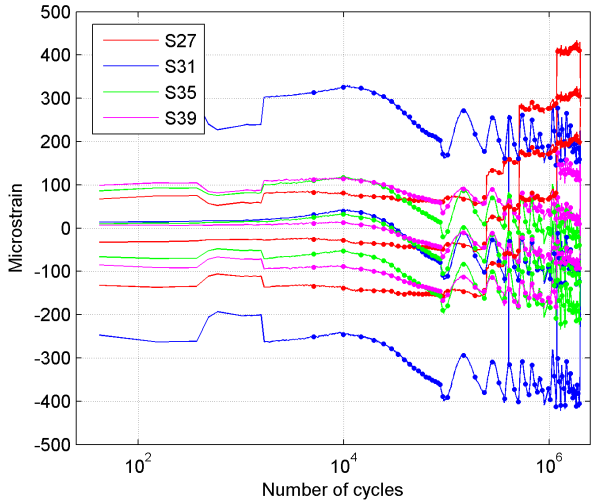

(b) ST-11 FRP bottom strain history

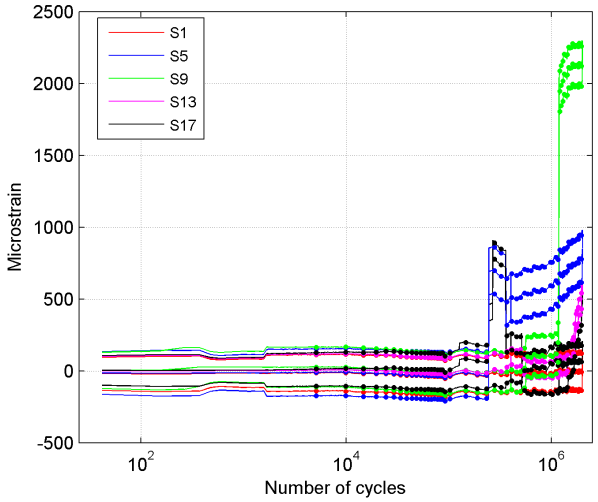

(c) ST-11 steel top strain history

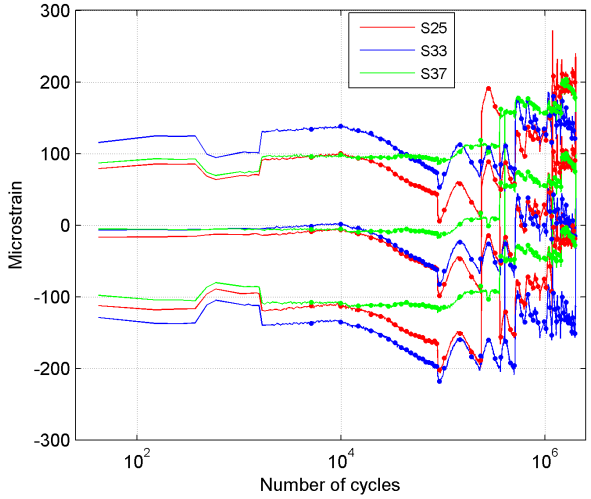

(d) ST-11 FRP top strain history

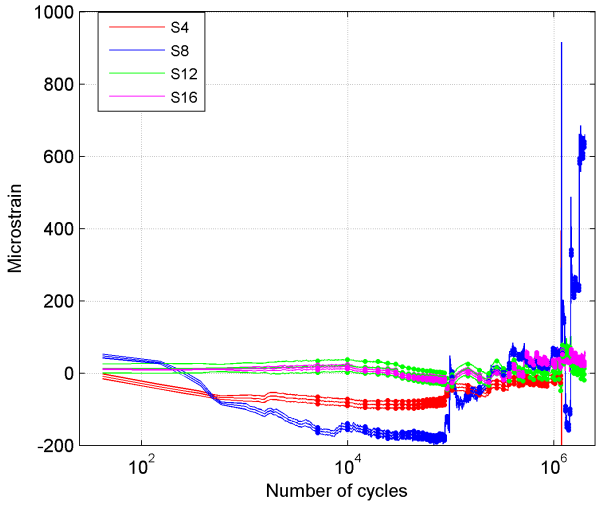

(e) ST-11 steel transverse strain history

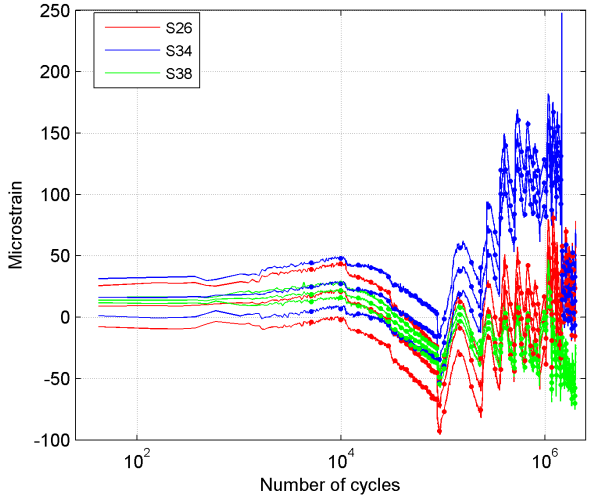

(f) ST-11 FRP transverse strain history

Figure 230. ST-11 strain data during first 2 million cycles

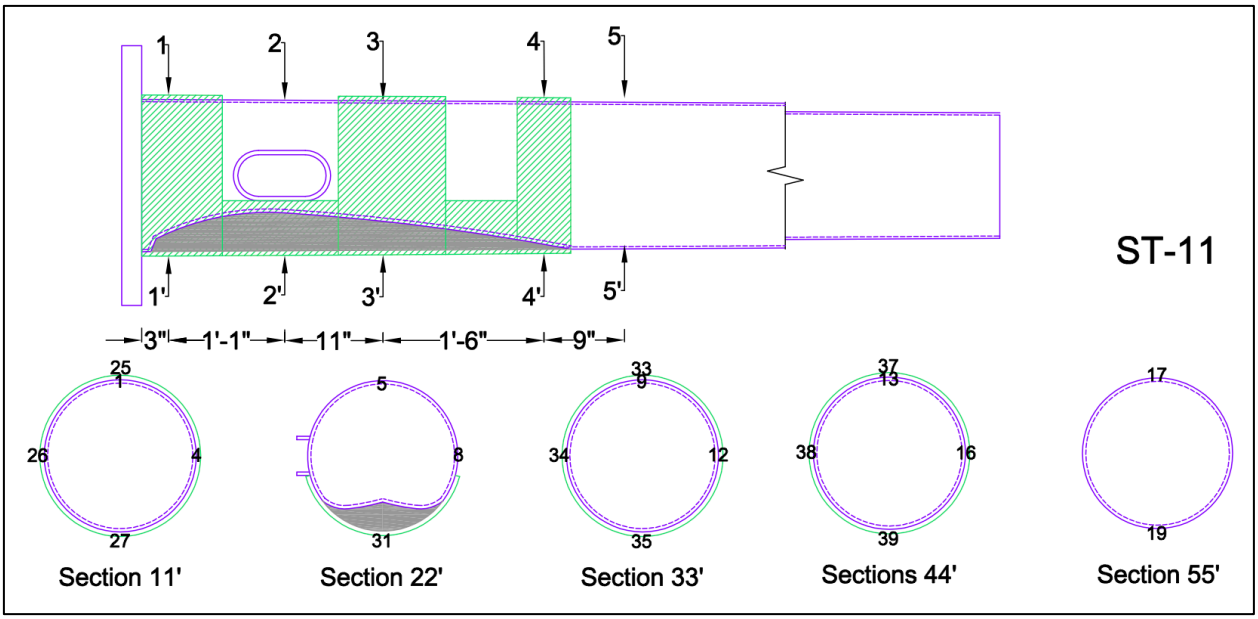

Figure 231. ST-11 strain gauges

As with ST-7, the largest strain ranges measured where in the FRP gauge at the center of the dented region. However, no gauges recorded amplitudes or strain ranges near yield, as would be expected at such a low stress level. All of the measured transverse strains were extremely small, except for some small fluctuations recorded in the transverse gauge on the opposite side of the pole from the access port.

After the 2 million cycles, the pole was subjected to 1000 cycles each at successively higher load amplitudes corresponding to each of the AASHTO categories until failure (D, C, B', B, and A). The load-displacement response of the pole after 2 million cycles is shown in Figure 232. The load amplitudes corresponding to each of the sequentially increasing stress categories are 3.52, 5.03, 6.03, 8.04, and 12.1 kip, respectively. The test was interrupted during the cycles at the load amplitude corresponding to B'; therefore, a second B' data set appears in the figures (labeled as B''). The load amplitude in the first few B'' cycles was slightly larger.

The pole developed substantial hysteresis during the 1000 cycles of increased load/stress levels, as shown in Figure 232. However, not all of the hysteretic behavior is due to yielding or degradation in the pole. Movement and slip at the steel plate to buttress and pole base to 1 in steel plate were noticed throughout the fatigue tests, and become pronounced under the higher load level cycles for ST-11.

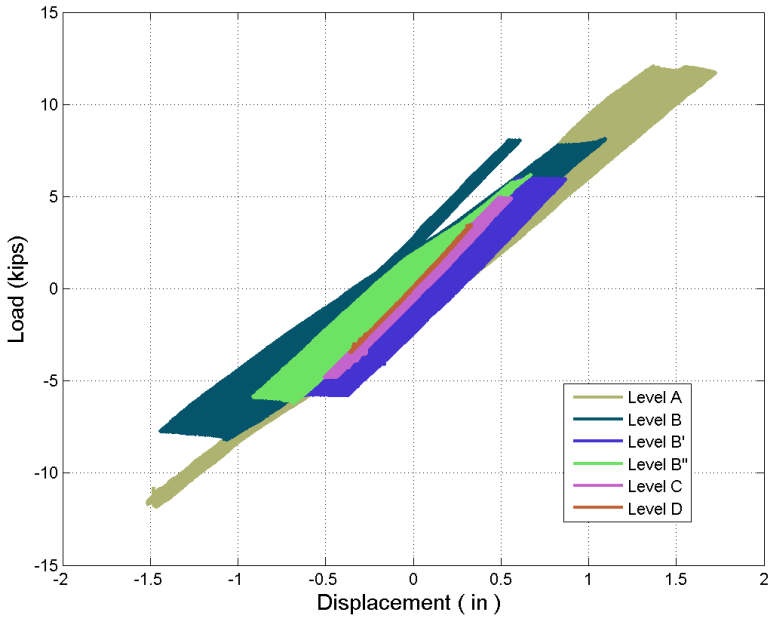

Figure 232. Load vs. displacement for ST-11 during increasing amplitude cycles

During the increased stress level increments of 1000 cycles each, the strain was monitored and the maximum strains during each cycle extracted. For each strain gauge, the strains are plotted in Figure 233 for steel and Figure 234 for FRP. Each point on the curve corresponds to the maximum strain during a single full cycle. Any instrument drift or residual strain from the previous two million cycles was removed (hence S9 shows strain magnitudes similar to S33, for example). The growth in maximum strain is approximately linear with load in a majority of the gauges, except the transverse gauges (where the strain amplitudes are small). The strain maxima begin to deviate rapidly during cycles corresponding to stress level A.

Unlike ST-7, the peak strains measured were more consistent with the load amplitudes applied, i.e., the stress estimated from strain readings at sections 1 and 2 correspond closely to the stress used to compute the load amplitude. Prior to failure of the pole, the largest steel strains were recorded on the top of the pole in the region between transverse wraps (section 2). The transverse strain recorded on the opposite face to the access port (and close to the location where the longitudinal wrap was terminated around the circumference of the pole) started to show substantial strain concentrations, which is consistent with the fluctuations seen during the first two million cycles.

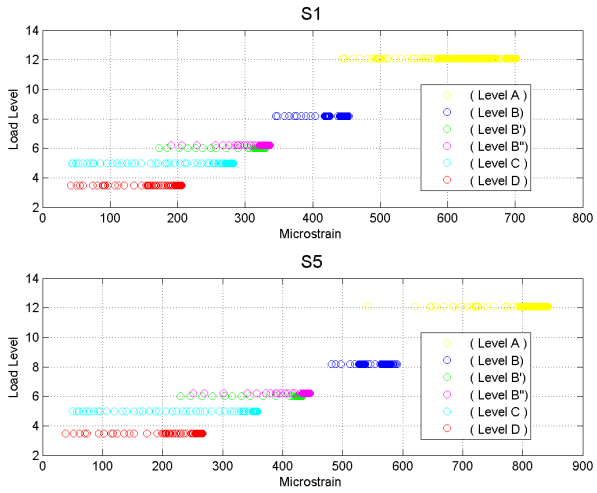

(a) ST-11 strain gauges S1 and S5 maxima

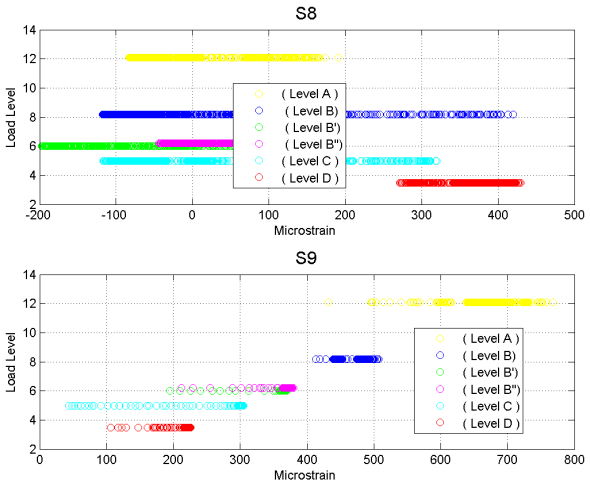

(b) ST-11 strain gauges S8 and S9 maxima

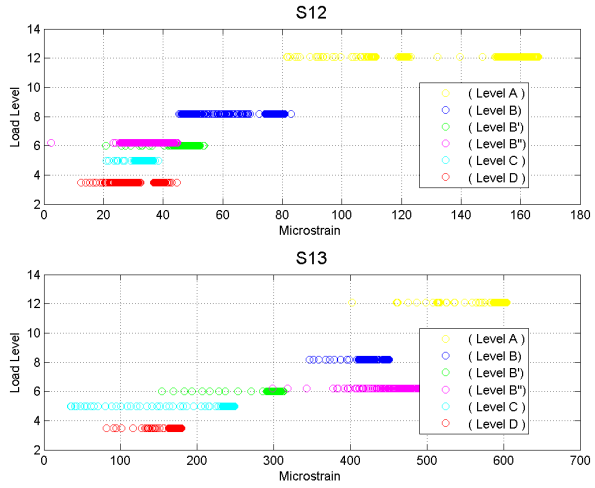

(c) ST-11 strain gauges S12 and S13 maxima

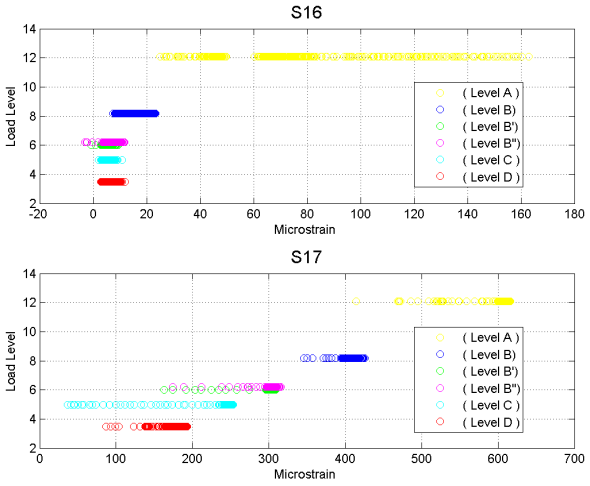

(d) ST-11 strain gauges S16 and S17 maxima

Figure 233. ST-11 steel strain data during higher stress level cycles

As with the first two million cycles, the largest strains were recorded in the FRP in the center of the dented region. However, it is not known what the FRP strain was during the cycling at level A, gauge S31 was lost after level B. Debonding may have initiated at the base section at the top of the pole during level B, as the continuity of the steel and FRP gauges are lost during level A. This may correspond to the large maximum strain range for the FRP gauge at the bottom of the pole at the same section and ultimately the initiation of the crack in the base metal at that location. The maximum FRP strain recorded at that location was -1600 με, which confirms the stress concentration on the bottom face. No debonding or buckling of the FRP was visible after the test at the base cross section, or elsewhere on the repaired portion of the pole.

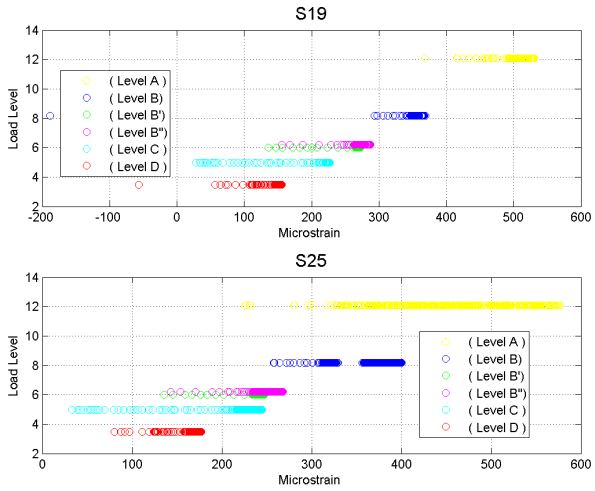

(a) ST-11 strain gauges S19 and S25 maxima

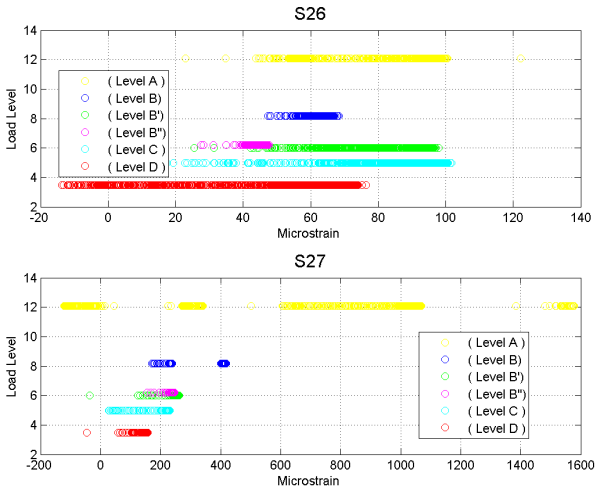

(b) ST-11 strain gauges S26 and S27 maxima

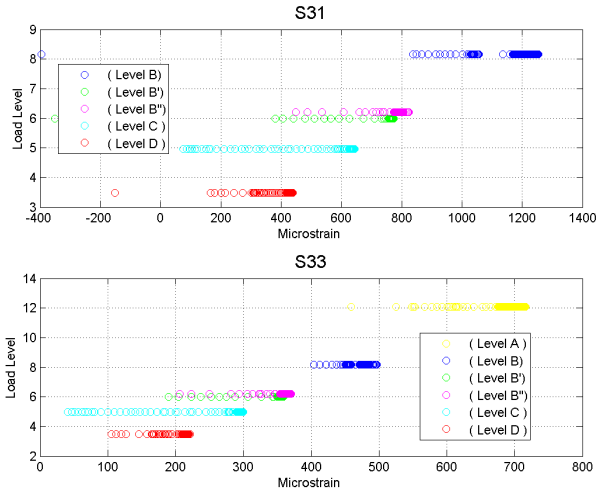

(c) ST-11 strain gauges S31 and S33 maxima

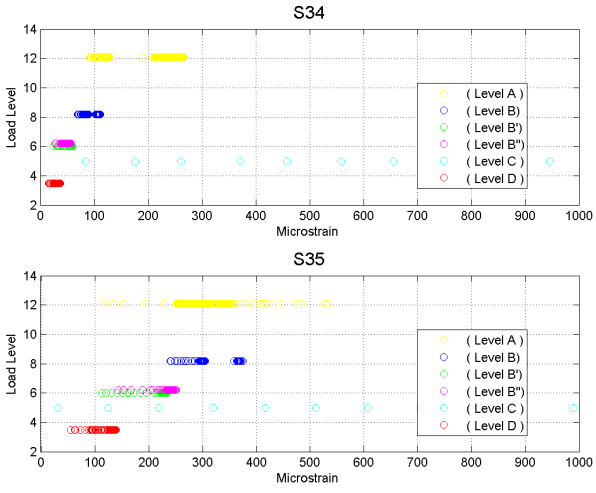

(d) ST-11 strain gauges S34 and S35 maxima

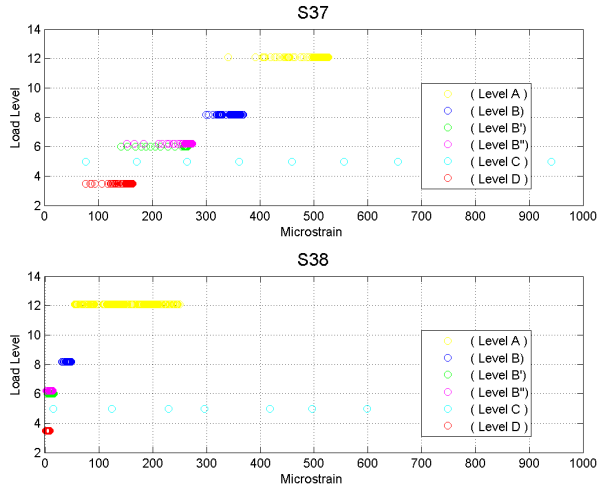

(e) ST-11 strain gauges S37 and S38 maxima

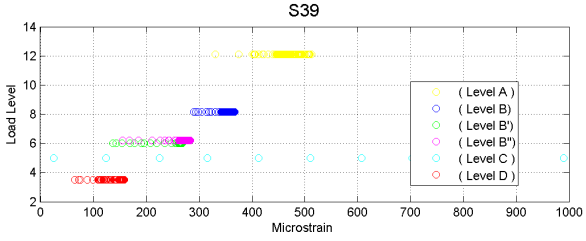

(f) ST-11 strain gauge S39 maxima

Figure 234. ST-11 FRP strain data during higher stress level cycles

During cycling at stress level A, the pole experienced a fracture in the weld toe at the base connection. The following figures show the state of the pole after the fatigue crack stopped the test. After the increased stress amplitude cycles, no debonding or delamination was apparent in the repair, as shown in Figure 235 (a). The crack encircled a majority of the circumference at the bottom side of the pole, Figure 235 (b) and (c). The laminate was cut and removed to show the crack. Prior to removal of the pole from the buttress, the crack can be seen propagating through the grout surrounding the plate washer in Figure 235 (d).

(a) No debonding or delamination in wrap

(b) Crack near weld toe, wrap removed to show crack

(c) Crack with dye

(d) Crack propagated through grout at plate washer near bottom of pole

Figure 235. ST-11 failure modes

6.2 Impact Testing

The final set of validation tests on the repaired full-scale specimens was a simulated vehicular impact. Due to the proximity of the structures to intersections and roadways, it is possible for an already damaged and repaired pole to be impacted a second time during its service life. Therefore, the performance of the FRP repaired poles under impact loads were assessed experimentally using an impact pendulum and poles mounted in a vertical cantilever configuration.

According to the NCHRP report (NCHRP-350, 1993), there are two recommended tests for utility poles, which are low speed test (35 km/h) and high-speed test (100 km/h). An alternative is using the recommended vehicle designated 820C (820 kg) or another type of vehicle (optional) designated 700C, and in both tests, passenger risk is of concern. Particularly, the low speed test is used to assess the separatism (breakaway), rupture, or yielding mechanism of the support. The high-speed test is utilized for assessing vehicle and test article route (trajectory). Depending on the main purpose of the test, the type of the vehicle might be replaced or another type added. The selection should be based on the front profile for the two vehicles and the geometry of the impacted objects that could potentially penetrate the impact assembly. For example, if the main purpose of the test is to penetrate the impacted object totally or partially instead of impact velocity and ridedown acceleration and/or vehicular stability, vehicle 2000P with or without vehicle 820C is preferable.

A study was performed to assess the safety performance for octagonal fiberglass reinforced composite (FRC) utility poles and was done at the Southwest Research Institute (SwRI) test facility located at Brooks Air Force Base in San Antonio, Texas (Foedinger et al., 2002). Two full-scale poles were tested according to NCHRP-350 criteria, so an 820 kg Geo Metro was used to impact the two poles with two different velocities (50 km/h and 70 km/h) at 15 degrees from the normal direction of traffic. Accordingly, the low speed test led to obvious fracture initiation of the composite material along the corners, while the high-speed test led to fracture propagation until the vehicle stopped. Moreover, there was no stability loss for the poles and the vehicle safety was acceptable because there was no damage for both the windshield and the occupant compartment intrusion. However, the front bumper and hood experienced extensive damage before starting the pole crushing and fracture propagation along the corners. In this way, the test results were acceptable according to NCHRP-350.

One study in New York City was performed on an aluminum pedestrian pole of length 10 ft (Rosenbaugh et al., 2009). The impact assembly was a pendulum whose weight was 1898 lb that consisted of crushable nose and aluminum honeycomb material. That pole was attached to a rigid foundation consisting of a steel W18x119 and two adapter plates. The pendulum was centered to impact the pole at a height 17.5 in from the base plate. After performing the test, the pedestrian signal pole was fractured into four pieces and some cracks propagated, but the pole remained attached to the rigid foundation. The pole was disconnected from the base plate and broken into two pieces that were rested at different distances from the original location. As it was concluded that this test did not meet all the requirements for this test because the pole fell down and neither pendulum deformation nor the pole's potential for penetrating.

Recent work has been ongoing by FDOT to develop an impact pendulum and employ it for a variety of studies ranging from breakaway details for poles to barge impact on bridges. The recent study performed at the University of Florida (Consolazio et al., 2012) was to characterize connection performance for multi-post ground signs subjected to vehicular impact or hurricane winds. The impact test was done using the pendulum at the Structures Research Center in Tallahassee with weight 2425.08 lb and drop height of 12 ft. Previous research was also performed on calibration of the performance of the impact assembly and honeycomb aluminum material for the impact head. The impact tests performed during this study utilized the resulting configuration of the impact head and aluminum honeycomb material directly.

6.2.1 Impact Sample Poles

This test was performed at structural research center for FDOT. To reduce the cost of the test, a pendulum with weight 1080 lb was used instead of a small car with low speed. By using this surrogate system, the pole will be hit by dropping the weight from 12 ft in height. Figure 236 shows the pendulum support structure that was designed and prepared to meet the requirement for the test. The system was designed according to the load combinations of dead plus wind load and dead plus pendulum live load. The pendulum mass is connected to a crushable nose to simulate energy dissipation at impact. The crushable nose is fabricated from a series of energy-absorbing aluminum honeycomb segments. The aluminum honeycomb segments have a cellular structure with a prescribed crushing strength. The materials were obtained from the Plascore line of products with prescribed nominal crushing strengths of 550 psi and 275 psi. Each aluminum honeycomb segment was separated by a ¾ in FRP plate made of Garolite G-10.

Figure 236. Impact pendulum at Structures Research Center in Tallahassee (IM-2 on pedestal)

Figure 237 shows the National Crash Analysis Center (NCAC) pendulum impact block assembly and is a similar design to the one used in FDOT tests. The sequence of aluminum honeycomb cartridges and Garolite spacer plates used in the test were based on 7 sequential sets of increasing size (increasing in size moving toward the mass block). All cartridges were 3 in thick. The cartridges were tapered (3 in thickness at the centerline), unlike those shown in the figure, to better mimic the energy dissipation and mass of the intended vehicular impact. The first 5 cartridges utilized the lower crushing strength aluminum, while the last 2 cartridges used the higher crushing strength aluminum. The final crushable nose when assembled for one of the tests is shown in Figure 238.

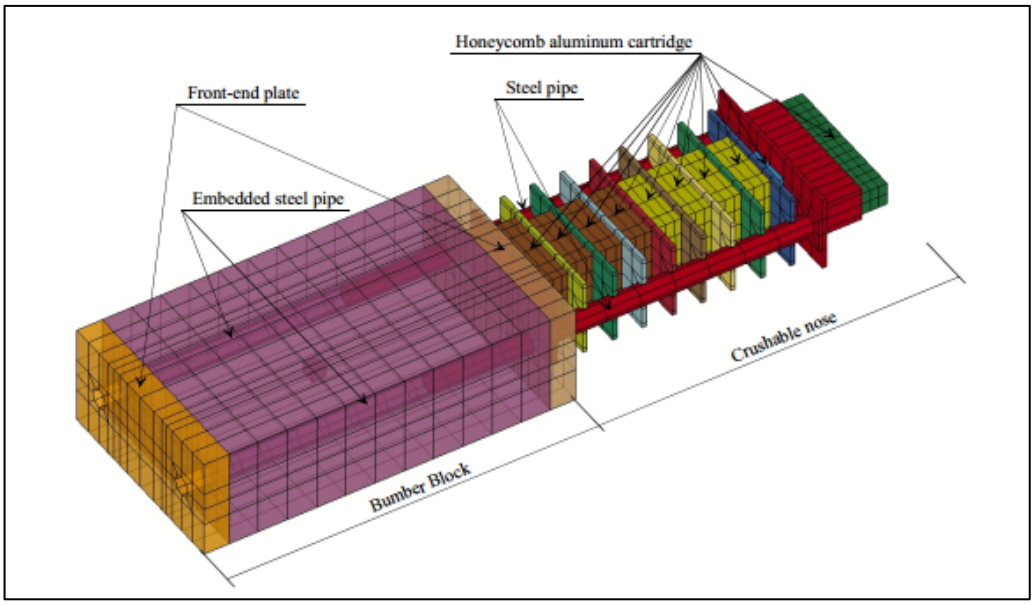

Figure 237. FEM for pendulum impact assembly (Consolazio et al., 2012)

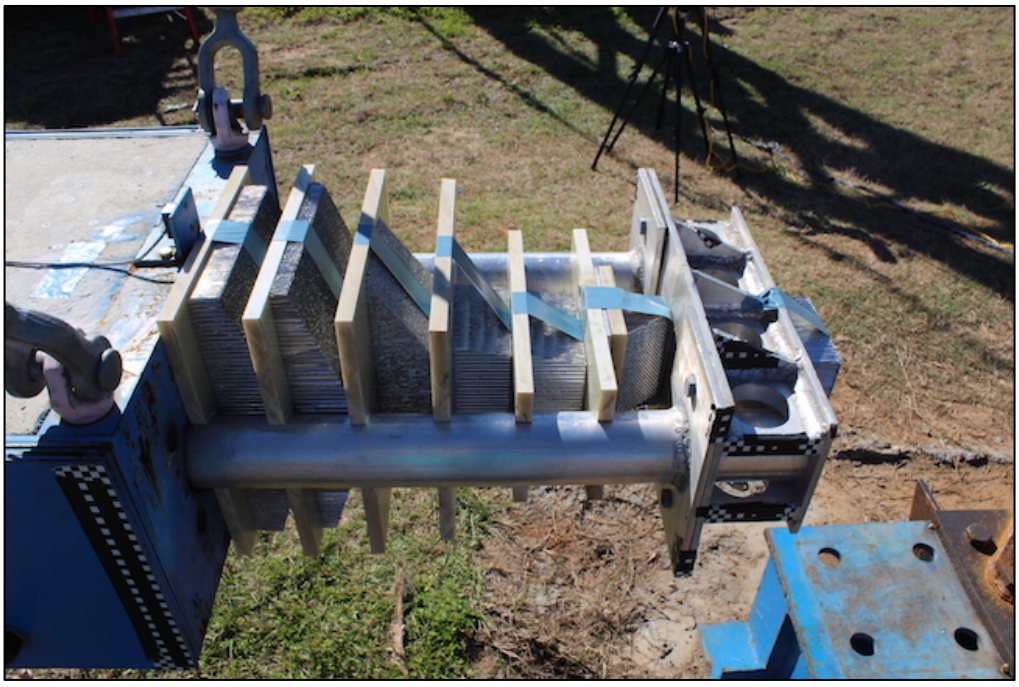

Figure 238. Crushable nose for IM-1 after connecting to mass block

To measure the acceleration during the test, accelerometers were attached to both the impact block and the pole. The first four accelerometers were attached to the impact block and the second four to the pole specimen. In addition, several strain gauges were used, mounted directly on the pole specimen in a fashion similar to the monotonic and fatigue full-scale test specimens. Instrumentation details are described specific to each specimen in the following subsections.

The poles were fixed to the pedestal foundation bay in the FDOT pendulum setup. A blue W14x99 steel wide flange section was anchored at the bottom flange using eight 1.125 in

diameter threaded rods coming up from the pedestal foundation. The connection detail to the large steel section is specimen dependent. The connections are shown in Figure 239 and Figure 240 for IM-1 and IM-2, respectively. The connection detail for IM-1 included a 1 in plate bolted to the large steel section using the four 1 in diameter bolts shown in the figure. In addition, a set of two through bolts (through the top flange, 1 in plate, and the pole base plate) were added with a plate washer on the impact side of the pole. The pole itself was welded to the 1 in plate using the partial joint penetration weld lengths shown in the figure. The existing anchor bolt holes in the pole base plate were not used.

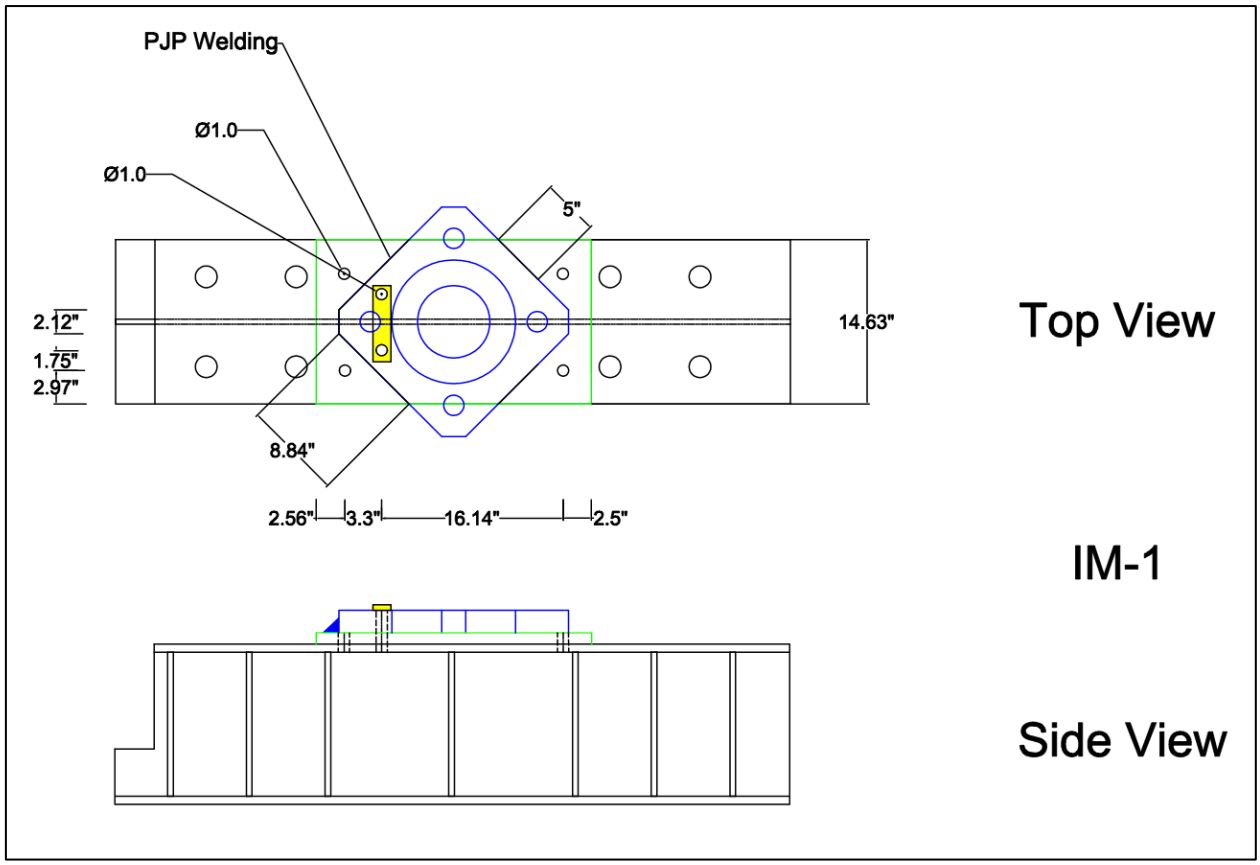

Figure 239. IM-1 connection to the pedestal foundation

The blue pedestal beam was modified slightly to accommodate the connection for IM-2 due to the large diameter of the pole. The closest set of existing holes in the pedestal beam top flange was utilized with 1.75 in high strength threaded rods. Matching holes were torched in the pole base flange to accommodate the through rods, and plate washers were placed on top of the pole base flange. The existing stiffeners were extended laterally away from the pedestal beam, tapering to the original width at the bottom flange of the beam. This was to provide out of plane resistance to the extents of the outer tube diameter. As with IM-1, a 1 in plate was welded to the pole base plate using partial joint penetration welds. In addition, the 1 in plate was fillet welded to the top flange of the pedestal beam and stiffeners as well as to the underside of the pole base plate at the lateral extents of the stiffeners.

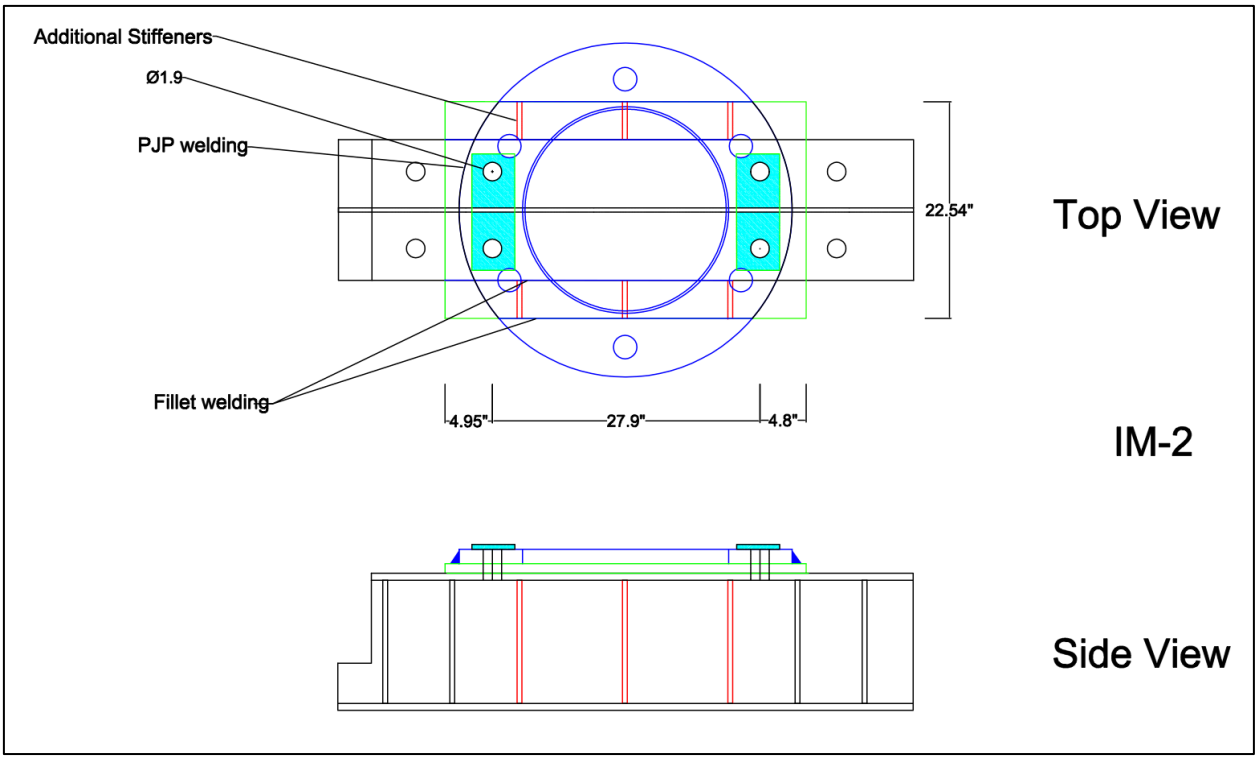

Figure 240. IM-2 connection to the pedestal foundation

The following table (Table 35) lists the pole specimens prepared for this test and their corresponding repair systems. It is a subset of the information presented previously for all large-scale specimens in Table 28.

Table 35. Large-scale test matrix for impact test

Pole ID	Fiber Type	Matrix Type	Loading Type	Dent Height Above Base	Angle Between Port and Dent	Wrap Dimensions (in)			No. of Layers
IM-1	B	PU	Impact	32″	135°	6×44	9×44	26×31	1
IM-2	G	QB Wet	Impact	33″	130°	9×78 (x3)	70×45		1

The center of the impact head with respect to the top of the base plate was set at 22 in for IM-1. Due to the increased thickness of the pole base for IM-2, the relative distance between the top of the base flange and the center of impact was slightly less for IM-2 (the pendulum height remained fixed). Accelerometers A1 through A4 were on the mass block or impact nose and common to all specimens. Accelerometers A1 and A2 were on the top of the center of mass with 30 g and 50 g maximum range, respectively. Accelerometer A3 had a 250 g range and was located on the impact nose in the direction of motion, and A4 was mounted transverse to the direction of motion at the front (impact side) of the mass block (with a range of 10 g).

In addition to the strain and acceleration channels of data recorded using the portable data acquisition system, high speed video was recorded using two different digital cameras triggered to capture video of the impact event by laser break beams or tape switches.

6.2.2 Specimens Tested Using Impact Pendulum

Based on the 12 ft drop height for the two impact specimens, the theoretical horizontal velocity of the impact assembly at the time of impact was 27.8 ft/s. The peak horizontal acceleration at the time of release of the mass block was 0.775 g and the predicted time to impact was 1.79 s. It should be noted that the poles were tested without any additional mass from the mast arm.

6.2.2.1 IM-1

One of the poles dented in the field is IM-1 (whose original designation in the testing matrix was FD-4), with a circular cross-section. Its outside diameter at the base is 13 in and thickness 0.1875 in. This pole is somewhat different from the other poles because it has two different dent depths (0.375 in and 1.375 in) and the centers of the two dents are 18 in and 32 in from the base plate. The pole is prepared for the test by using the repair system that is mentioned in Table 35.

Because of the existence of the access port, the transverse wrap was proportioned into two pieces. A longitudinal wrap was placed on the dent side of the pole extending around the perimeter to the lip of the access port on each side. The transverse and longitudinal wraps were terminated at a height just below the pedestrian button. The full details of the repair are shown in Appendix A. The repaired pole is shown in its vertical cantilever test configuration in Figure 241.

Figure 241. IM-1 test configuration

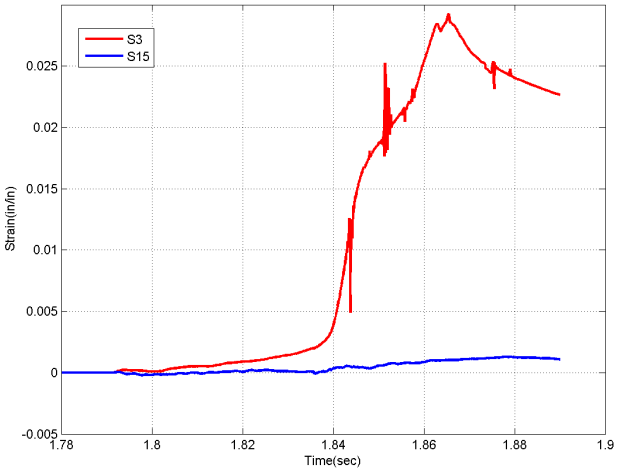

(a) IM-1 steel impact side strain history

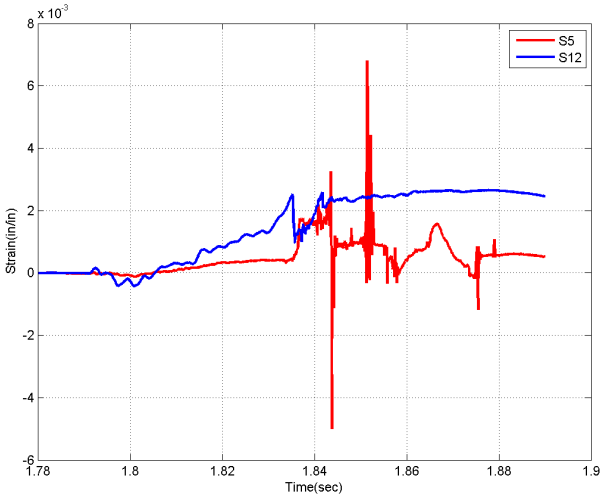

(b) IM-1 FRP impact side strain history

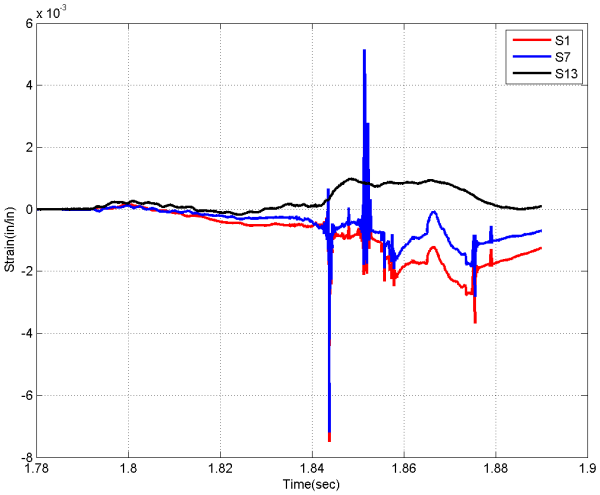

(c) IM-1 steel free side strain history

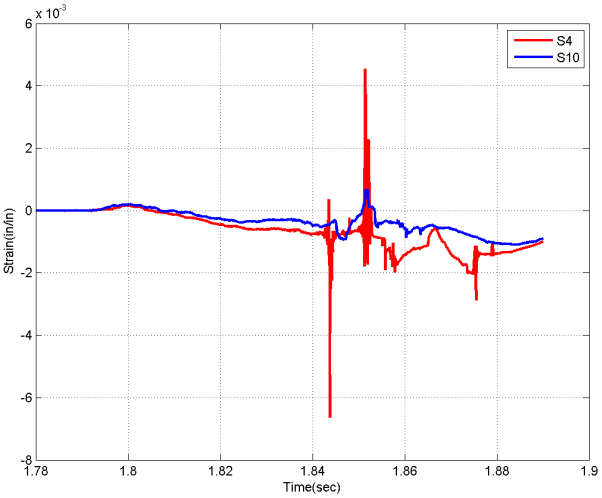

(d) IM-1 FRP free side strain history

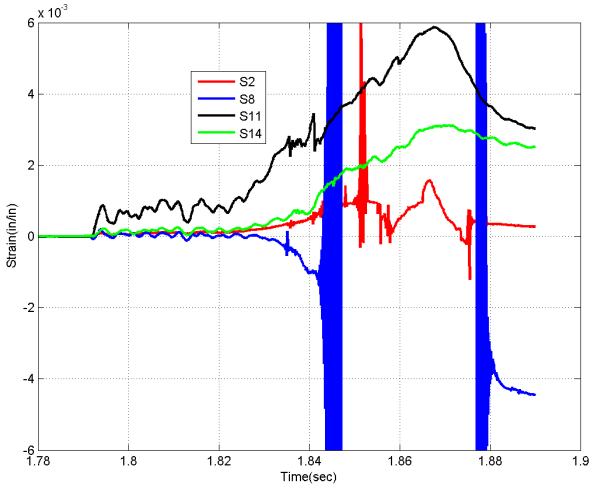

(e) IM-1 steel transverse strain history

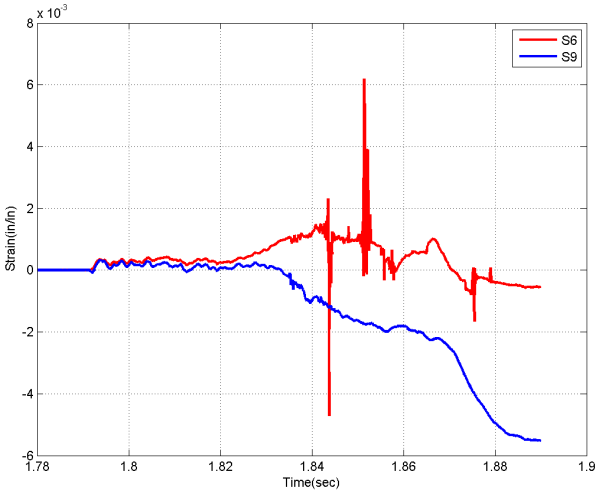

(f) IM-1 FRP transverse strain history

Figure 242. IM-1 test strain data

The pole was impacted using the pendulum and a 12 ft drop height. During the impact sequence of IM-1, the first three aluminum honeycomb cartridges behind the steel impact piece crushed sequentially. The first cartridge (behind the steel impact piece) began to crush at the instant of impact together with the single cartridge attached on the impact side of the steel impact piece. The deformation of the impacted section of the pole during these sequential secondary impacts was minimal, and potentially had a rigid body component from the rotation of the pedestal foundation. At the end of the crushing of the fourth cartridge, substantial plastic deformations occurred in the pole. Some minor compression of the second to last cartridge may also have caused some additional plastic deformation in the pole before rebound occurred.

The strain time histories are shown in Figure 242. The locations of the various strain gauges are shown in Figure 243. The acceleration time histories for the accelerometers on the mass block and the pole are shown in Figure 244 and Figure 245, respectively. The accelerometers A5 through A8 were located at distances of 1.125, 22.25, 40, 135.25 in from the top of the base plate and the axis of the accelerometers oriented in the direction of impact. The accelerometer locations are shown in Figure 246. Accelerometers A5 through A8 had ranges of 20 g, 30 g, 20 g, and 10 g, respectively.

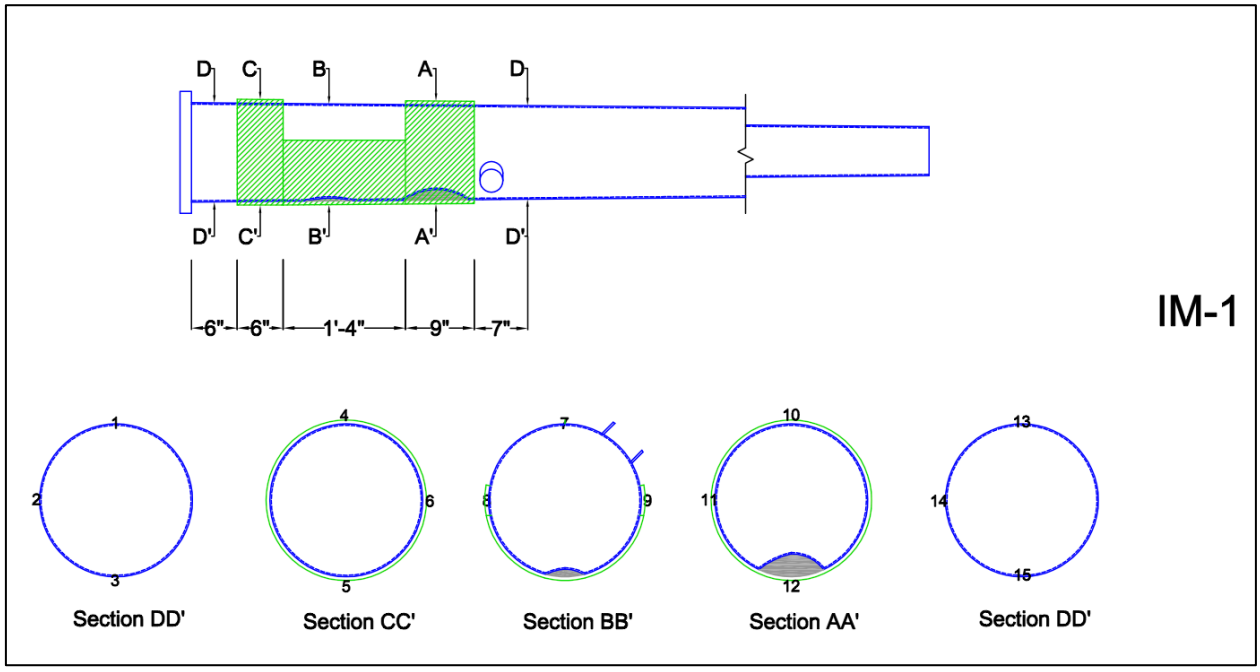

Figure 243. IM-1 strain gauges

The strain amplitudes on the pole show three discrete secondary impact events (at times of 1.844, 1.851, and 1.874 sec), corresponding to the crushing of the aluminum honeycomb cartridges. The clearest representation is from the impact side gauge at the base cross section. The first two cartridges (on either side of the steel impact piece) lead to a gradual increase in strain, followed by the strain jumps due to transfer of energy to the subsequent cartridges. The second and third cartridges behind the steel impact piece appear to have crushed together, hence the drop in strain on the impact side by the time of the crushing of the fourth cartridge.

The steel strains are in excess of yield at several locations below section AA'. This includes both tension and compression yielding near the base cross section (tension strains reaching a maximum of 0.029 in/in, substantially larger than the free-side compression strain), and yielding in the transverse gauges at all locations within the dented region. The transverse gauges at the location of impact show accumulation of compressive strain due to the crushing of the cross section, while the sections above the impact all show substantial tension yielding (and effectiveness of the wrap in confining this expansion).

The acceleration time histories show consistent behavior with the strain time histories. As the plastic strain accumulates as the fourth cartridge crushes (and the impact-face unloads at the base cross section), the acceleration plateaus and then begins to decrease (actually the mass block is decelerating and the deceleration returns rapidly to zero after this point). The accelerations in A3 are substantially higher than the mass block itself (accelerations of 150 g or more). The accelerometers saturated for A7 and A8, so it is difficult to determine the peak accelerations in these gauges. There is one excursion in A5 and several in A6 that also did not record the peak, but these are easily recovered using the velocity signal.

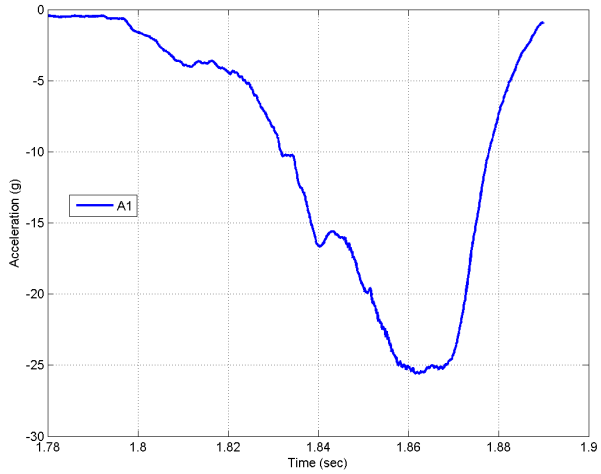

(a) IM-1 A1 acceleration history

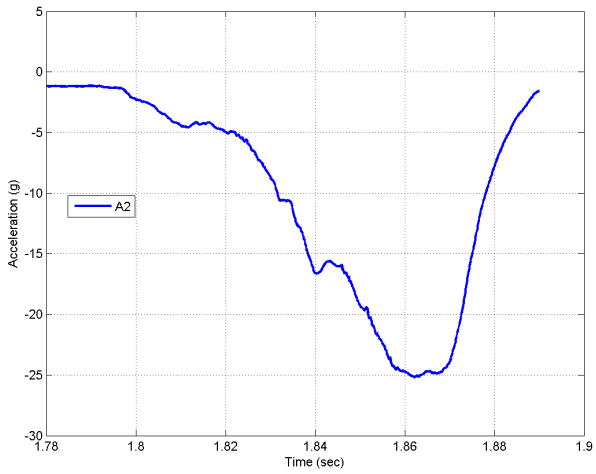

(b) IM-1 A2 acceleration history

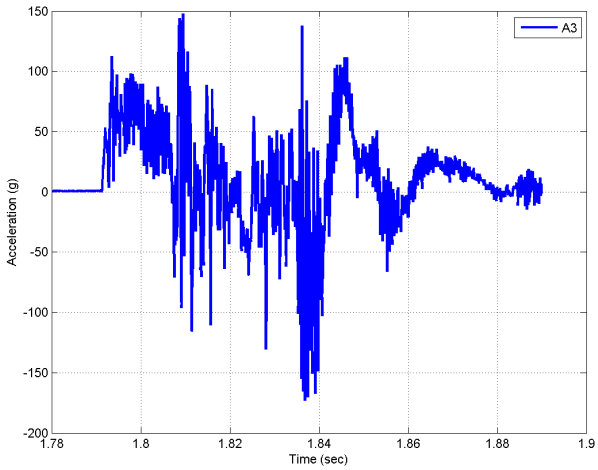

(c) IM-1 A3 acceleration history

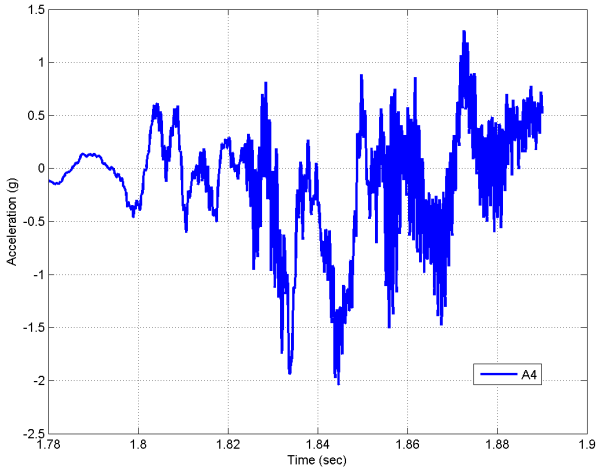

(d) IM-1 A4 acceleration history

Figure 244. IM-1 mass block acceleration data

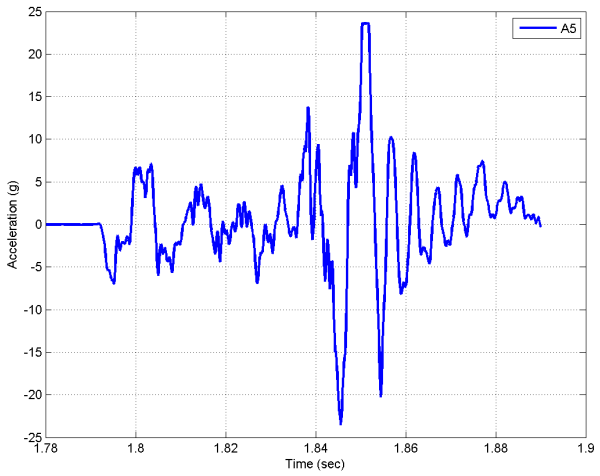

(a) IM-1 A5 acceleration history

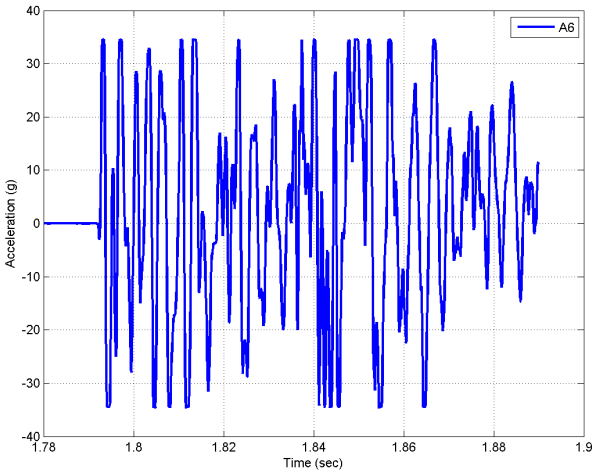

(b) IM-1 A6 acceleration history

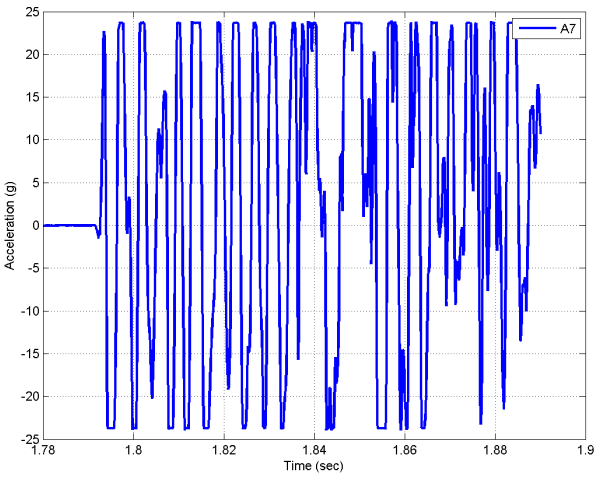

(c) IM-1 A7 acceleration history

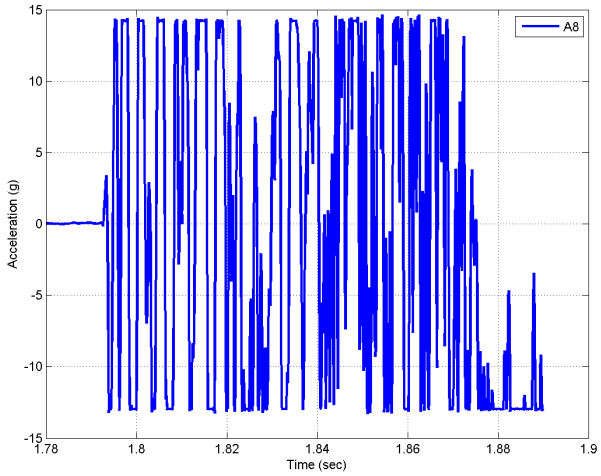

(d) IM-1 A8 acceleration history

Figure 245. IM-1 pole acceleration data

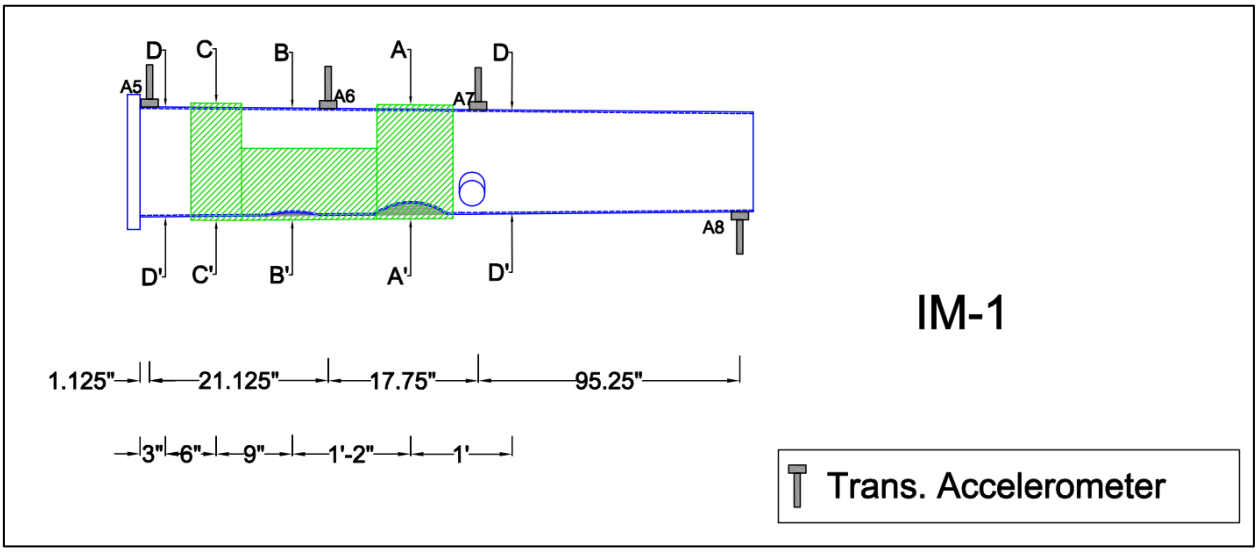

Figure 246. IM-1 accelerometers

The aluminum honeycomb cartridges after the test are shown in Figure 247 (b). As mentioned previously, the final two cartridges did not crush during the test. The final deformed shape of the pole, indicating substantial plastic deformations, is shown in Figure 247 (a). The strain gauge that recorded compression values is in the foreground at the lower side of the dent profile. The FRP repair itself did not suffer any visible delamination, buckling, fracture of fibers, or other permanent damage, except for the location where the steel impact piece bore directly on the laminate. The damage in the impact region can be seen in Figure 248 (c) and (d) where both hinging occurred as well as some longitudinal splitting. The access port itself also has visible plastic deformation. However, the global stability of the pole was not affected and the residual displacement at the tip of the pole was negligible.

(a) Profile of dent created by impact head

(b) Deformation of aluminum honeycomb cartridges

Figure 247. IM-1 post-test state of the pole and crushable nose

(a) Deformation of the access port and rupture in FRP

(b) Local deformation and rupture of FRP in impact head region

Figure 248. IM-1 post-test state of repair material at impact location

6.2.2.2 IM-2

The second pole for impact testing was also retrieved from the field and had a substantial dent and damage to the pole. In addition, the pole itself was significantly larger than IM-1 with a base diameter of 21 in and a multi-sided cross-section. A small access port was present, oriented approximately 130° from the dented face. This pole had one large dent centered 33 in from the base plate, but with extents of the dent almost 5 ft from the base flange up the pole. The dent depth was 5 ¾ in, or approximately 28% of the outer diameter at the center of the dent location. This pole was prepared for the test by filling the dent, which was performed initially with the fill material used for the other poles. However, due to the volume of the fill, some additional Bondo material was used to restore the pole to its initial geometry prior to wet layup. The extents of the dent and the volume of fill material required are evident in Figure 249. The fill material was applied in several batches, and noticeable shrinkage cracks developed after the first batch cured.

Figure 249. IM-2 dent cavity volume requiring fill material

The repair system consisted of glass fibers and epoxy saturating resin. Because of the existence of the access port, the transverse wrap was proportioned into three pieces, the full details of the repair are shown in Appendix A. The repaired pole is shown in its vertical cantilever test configuration in Figure 250. As with IM-1, IM-2 was tested without any additional mass at the top of the pole, i.e., from a mast arm. The pole was impacted using the pendulum and a 12 ft drop height. The strain time histories are shown in Figure 251. The locations of the various strain gauges are shown in Figure 252.

Figure 250. IM-2 test configuration

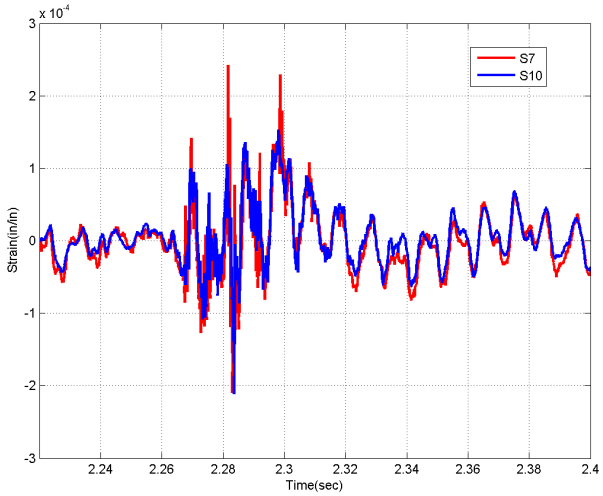

(a) IM-2 steel impact side strain history

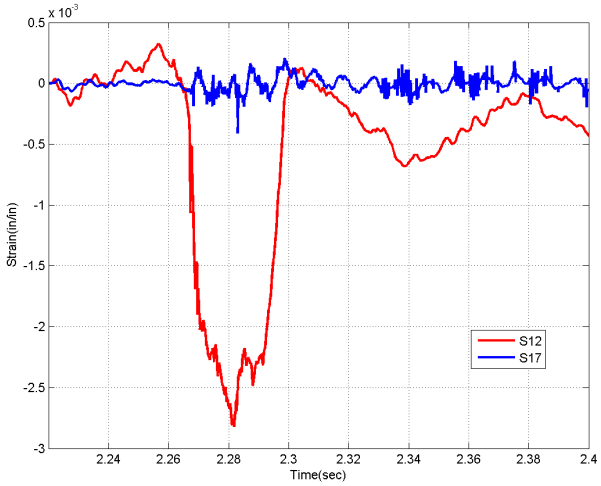

(b) IM-2 FRP impact side strain history

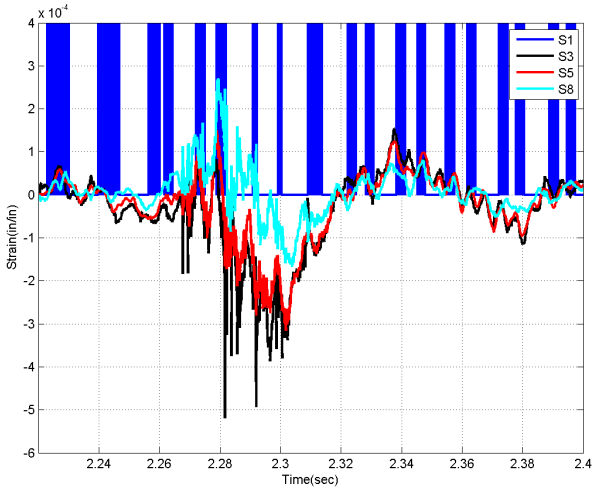

(c) IM-2 steel free side strain history

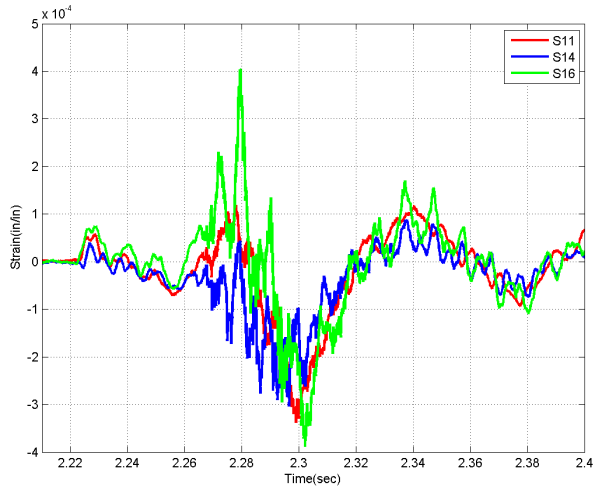

(d) IM-2 FRP free side strain history

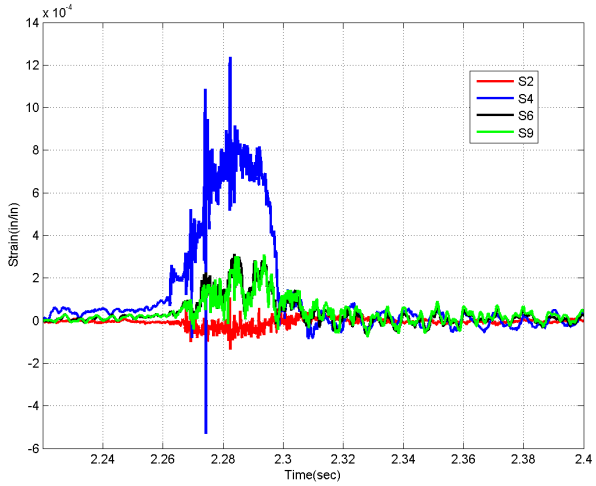

(e) IM-2 steel transverse strain history

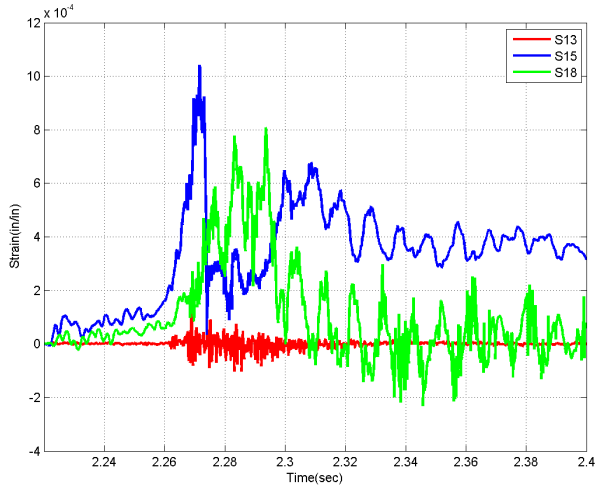

(f) IM-2 FRP transverse strain history

Figure 251. IM-2 strain data

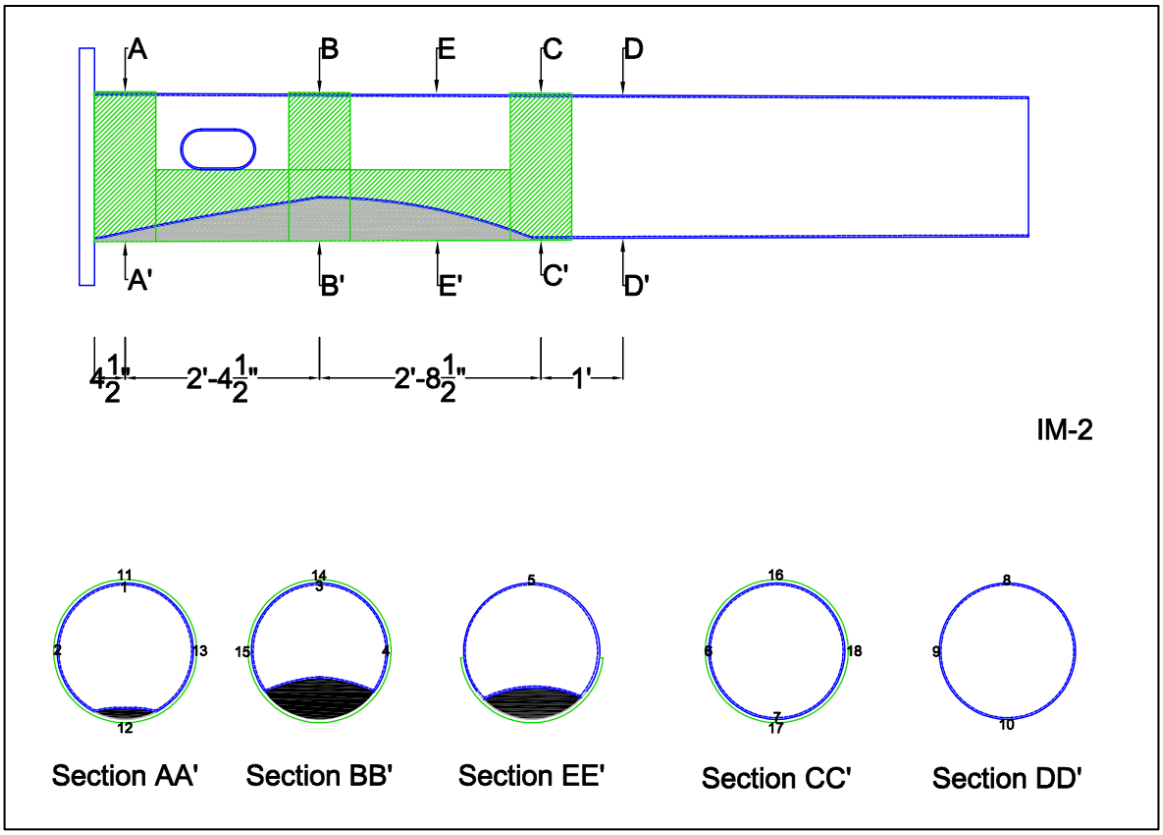

Figure 252. IM-2 strain gauges

The sequence of aluminum honeycomb cartridge crushing was similar to IM-1. Due to the minimal deformations in the pole and repair material, the corresponding difference in energy was dissipated through some plastic deformation in the last two cartridges closest to the mass block. The impact test on IM-2 yielded almost no visible damage or deformation to either the pole or the FRP wrap. Unlike IM-1, almost all the impact strains were recovered after rebound and the strain amplitudes were smaller. The only gauge where possible plastic deformations were observed was in the transverse gauge at the center of the dented region. The peak strain (-2800 με) recorded was in the FRP on the impact side, although in compression due to the large extents of filler material. The free-side steel gauge did not record reliable data and there was no impact-side steel gauge to indicate whether yielding may have occurred in the base metal near the base.

The acceleration time histories for the accelerometers located on the mass block and pole are shown in Figure 253 and Figure 254, respectively. The accelerometers A5 through A8 were located at distances of 1.0625, 21.25, 46.125, and 134.5 in from the top of the base plate and the axis of the accelerometers oriented in the direction of impact. Accelerometers A5 through A8 had ranges of 20 g, 50 g, 30 g, and 20 g, respectively. The accelerometer locations are shown in Figure 255 and on the schematic in Appendix A.

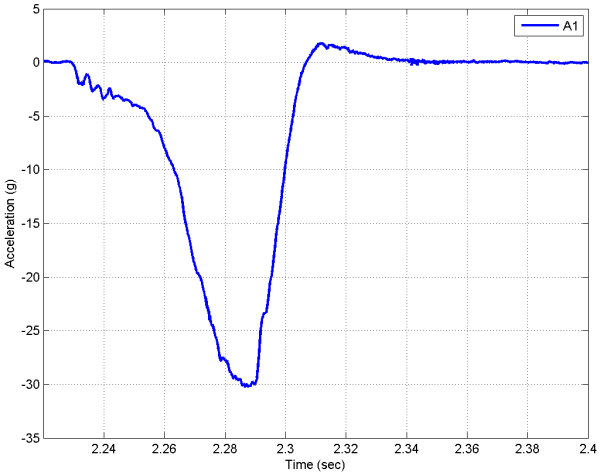

(a) IM-2 A-1 acceleration history

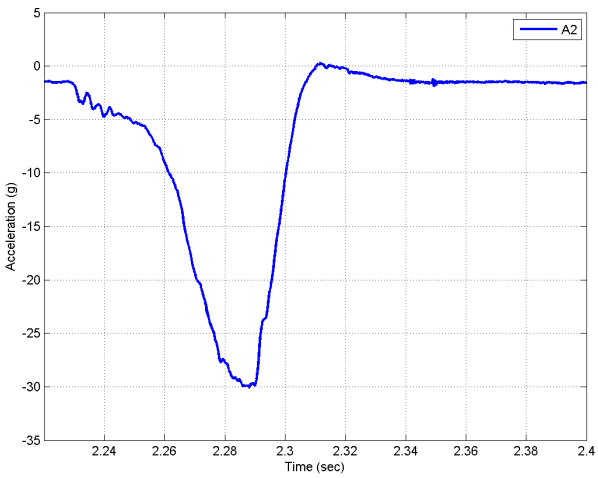

(b) IM-2 A-2 acceleration history

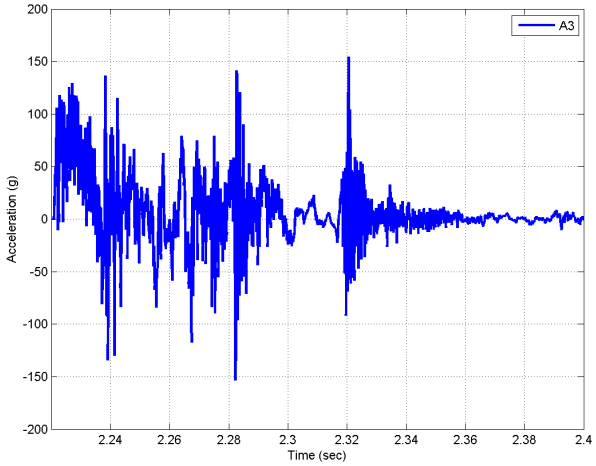

(c) IM-2 A-3 acceleration history

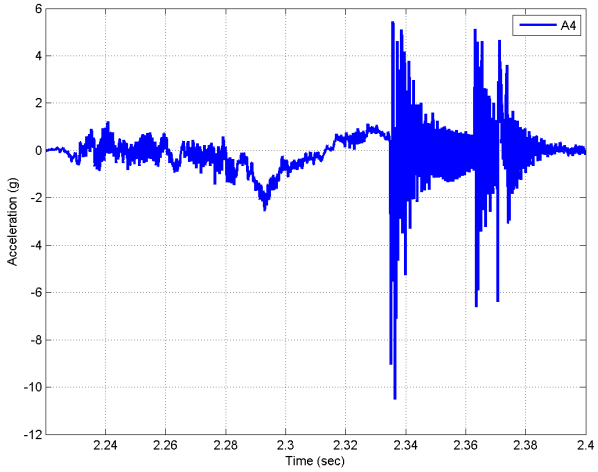

(d) IM-2 A-4 acceleration history

Figure 253. IM-2 mass block acceleration data

The acceleration time histories from the mass block show similar trends and magnitudes to IM-1. More than 150 g (positive and negative) were recorded by A3 on the steel impact piece. Saturation of the acceleration recordings only occurred in A7 due to the change in the range of the accelerometers employed in the test. Also, there was an issue acquiring data from accelerometer A8, as evident in the magnitudes of the accelerations recorded.

Analysis of the strain shows substantial longitudinal and transverse strains developing, both in the FRP and steel, that effectively arrested any deformation of the pole in the repaired region. The pole had an initial vertical offset due to the initial damage sustained that was not affected by the impact, as seen in the post-impact state of the pole in Figure 256 (a). The minor dilation of the cross section in the center of the original dent is visible in Figure 256 (b), as confirmed by the strain data. The minor crushing of the tapered portions of the last two aluminum cartridges (closes to the mass block) are shown in Figure 256 (c).

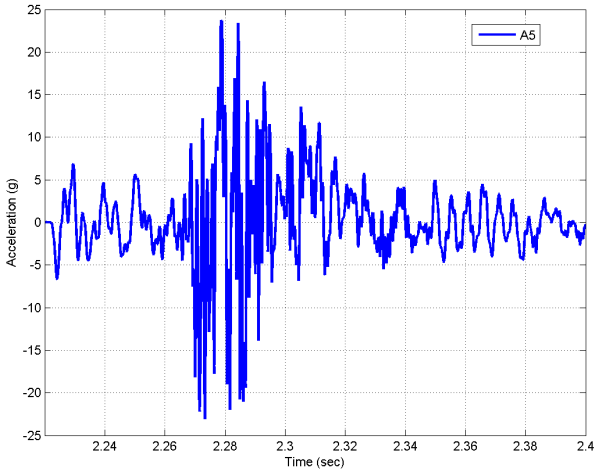

(e) IM-2 A-5 acceleration history

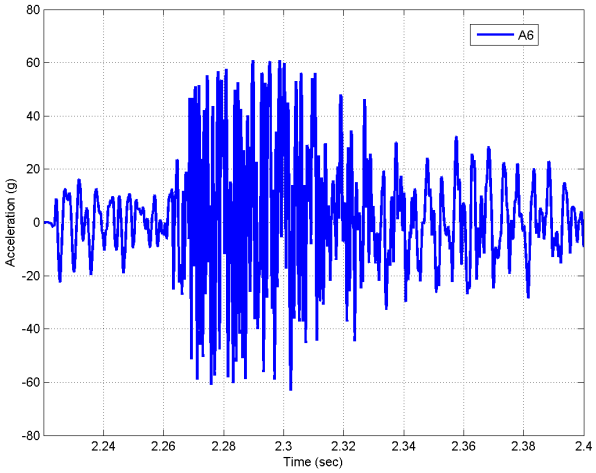

(f) IM-2 A-6 acceleration history

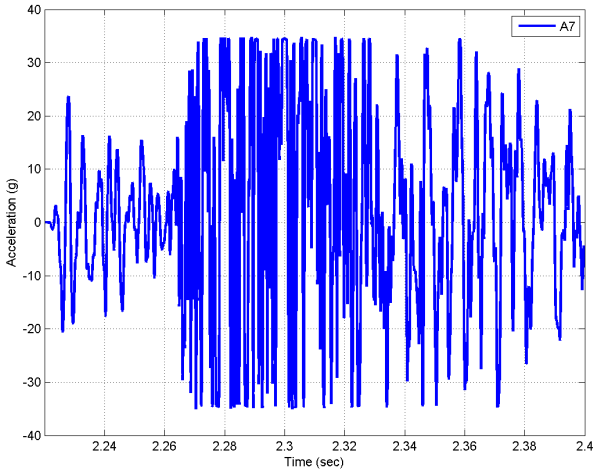

(g) IM-2 A-7 acceleration history

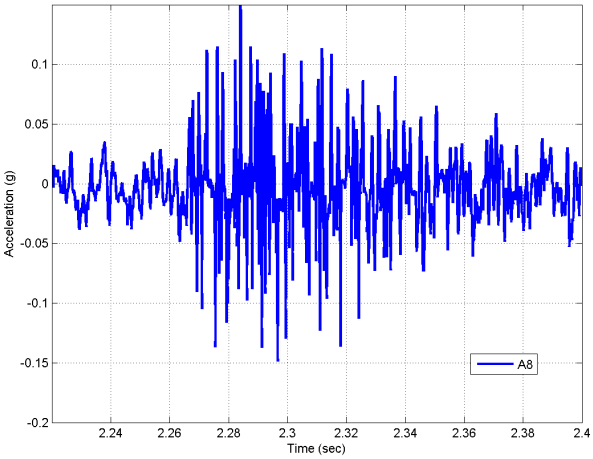

(h) IM-2 A-8 acceleration history

Figure 254. IM-2 pole acceleration data

To investigate whether the repair had sustained damage that was not visible, the exterior laminate was cut off the pole after testing. The fill material remained bonded to the pole with the only damage a longitudinal crack near the impact location, as shown in Figure 257 (a). The adhesive bond between the laminate and the fill material appears to have been highly uniform sufficient to cause failure in a thin layer in the fill material. The fill material on the other side of the longitudinal crack remained bonded to the laminate when removed, as shown in Figure 257 (b).

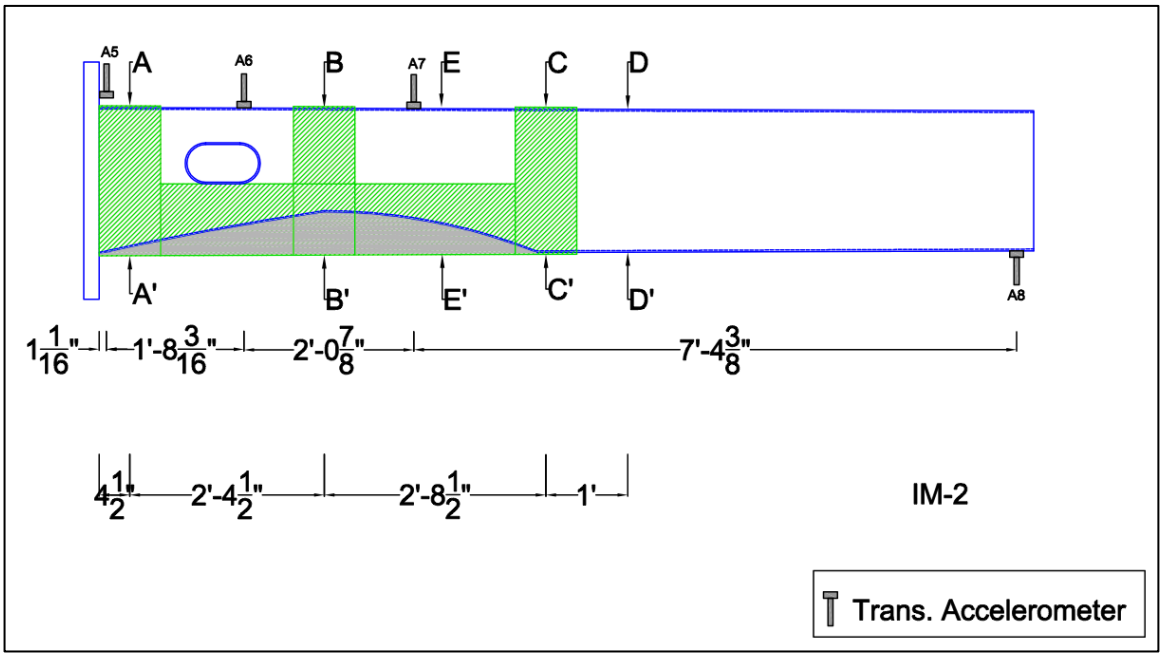

Figure 255. IM-2 accelerometers

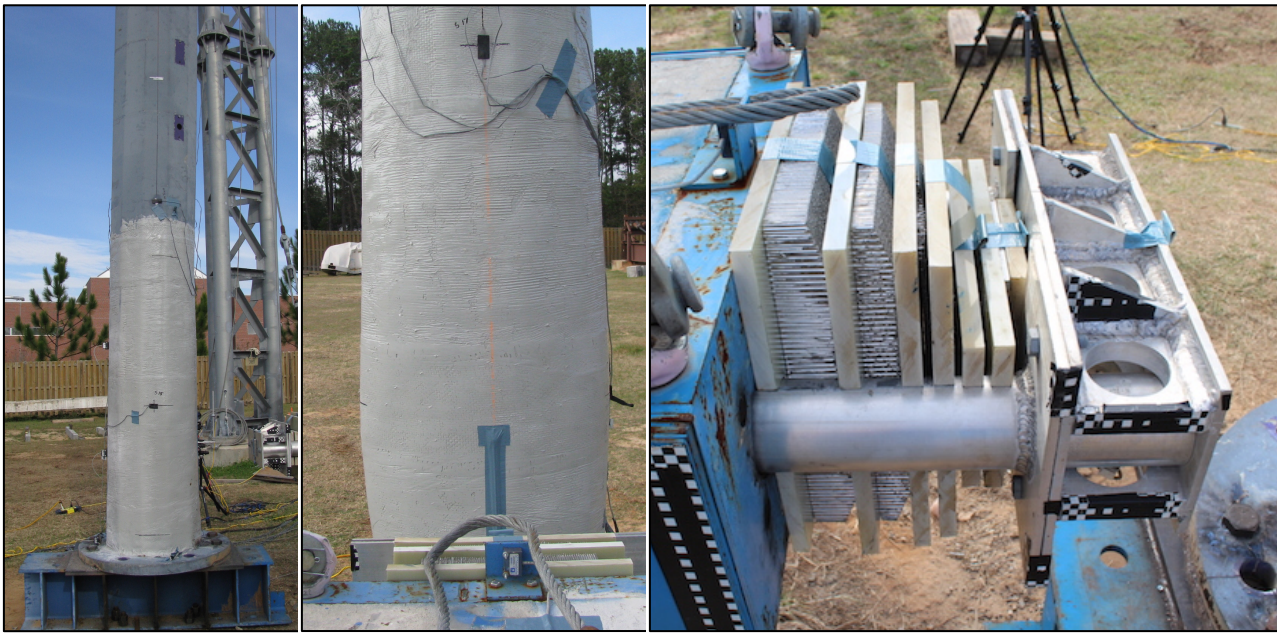

(a) After impact **(b) Transverse dilation of specimen at impact location** **(c) Aluminum material deformation in nose**

Figure 256. IM-2 post-test state of the pole and crushable nose

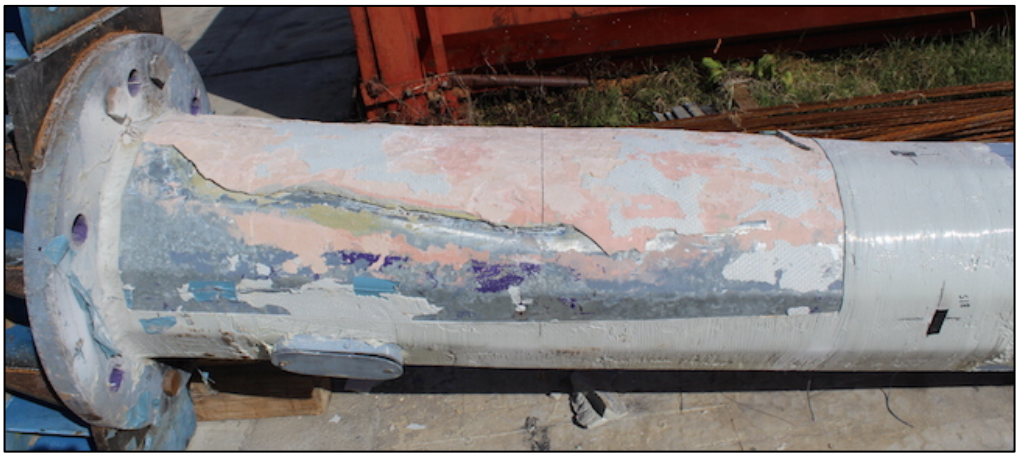

(a) Fill material after impact with wrap removed

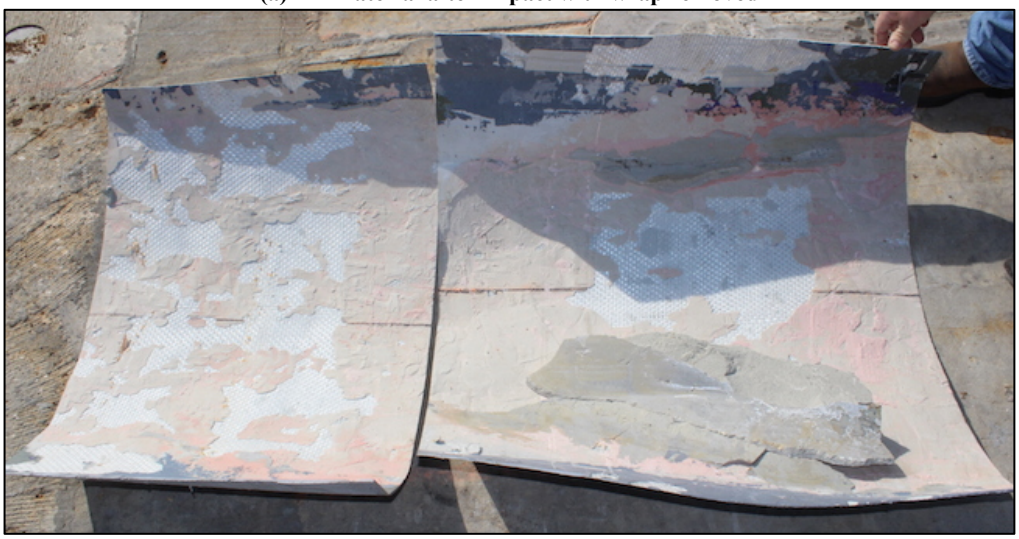

(b) Adhesive and wrap on adhered impact side of pole

Figure 257. IM-2 forensic view of the repair material

Chapter 7: Recommendations

Based on the results of the data gathered, the following recommendations are presented for the design and application of FRP composite repairs to dented metallic utility and mast arm poles. In addition to the experimental data, the recommendations are also based on the experience working with FRP materials and installation of repairs gained during the course of this investigation. It is recommended that FRP repair systems should consist of an epoxy dent filler, a viscous epoxy adhesive, a fiber-reinforced polymer composite, and protective coating. Important considerations for material selections are discussed, followed by recommendations for wrap geometry design and field installation.

7.1 Material Recommendations

The fill material should be extremely viscous so that large amounts of it to be placed in the dented region without slumping, and to allow for it to be shaped to the curvature of the pole in the vertical position. Two options for this application are the Sikadur 31 Hi Mod Gel used in this project and Pilgrim EM 5-2 Gel, each combined with half the maximum allowable amount of dry sand aggregate. A final candidate used for IM-2 and in the previous pole study (Mackie et al., 2011) was Bondo body filler, which has desirable workability. However, it was not evaluated for mechanical performance or bond in this study.

The adhesive epoxy is required to be viscous enough to be applied to a vertical pole surface without significant slump. A no-sag epoxy is sufficient. The strength of the epoxy must also be sufficient to withstand the required loading. Additionally, the pot life of the mixed epoxy must be considered. A good candidate for this type of application is QuakeWrap's QuakeBond™ J201TC Tack Coat.

The FRP system used for a pole repair should consist of either a glass or basalt fiber weave impregnated with polyurethane or epoxy resins. The fiber weave should be bi-directional and have a density of 24 oz/yd^2 to prevent the need for application of multiple layers. When a polyurethane resin is used, it should be prepared as a pre-impregnated composite. An example of such a composite is NRi's Syntho-Glass® XT system. Epoxy resin composites can be installed as pre-cured sheets or in a wet layup procedure. The epoxy material used in this project, QuakeWrap's QuakeBond™ J300SR Saturating Resin, is a good product for this application. Other alternatives used with success are Sikadur 301 impregnating resin.

An approved environmental coating or paint should be used to protect FRP repairs. The products used in this investigation are Carbozinc 859 and Carbothane 133 LH by Carboline.

7.2 Wrap Geometry Recommendations

Several guidelines should be taken into consideration when determining the geometry of an FRP wrap repair. These include features of the pole that may interfere with the wrap. Access ports and crosswalk signal buttons in repaired poles should remain accessible whenever possible. If one of these features exists within the same height as the proposed repair area, the wrap should be cut so that it does not interfere with them. In this case, transverse strips should be secured around the repair at convenient locations in order to provide circumferential confinement. In

general, the repair should extend at least 6 in beyond the edges of the dent, and should encompass the circumference of the pole whenever possible. Based on the lap shear testing performed, it is likely that the laminates considered in this study can be fully developed with an extension less than 6 in in the event the dent occurs closer to the base or have larger extent of dent damage.

Based on the Damage Determination and Single-Ply tests performed in this investigation, recommendations for the minimum number of layers to be used in an FRP repair have been developed. The number of layers is used here to mean a layer of bidirectional FRP that extends completely around the circumference of the pole and is sufficiently long to develop the laminate on either side of the dent. For aluminum poles, one layer can be used for dent depths up to 25% of the pole's outer diameter. For dents between 25% and 35%, two layers of FRP should be used. With steel poles, dent depths up of 20% of the diameter can be repaired with a single layer FRP repair, while dents between 20% and 35% should be repaired with two-layer repairs. For larger dents, replacement of the pole is likely necessary. These designations are summarized in Table 36, below.

Table 36. Guide for determining repair action

Action	Dent Depth (% of Pole Diameter)	
	Aluminum	Steel
No Repair	≤5%	≤5%
Single-Layer Repair	5% to 25%	5% to 20%
Two-Layer Repair	25% to 35%	20% to 35%
Replace Pole	≥35%	≥35%

Based on the monotonic full-scale tests, it appears the presence of the access port and the structural stiffness of reinforced rim of the access port have a major impact on the efficacy of the transverse wraps. Therefore, for access ports with little or no reinforcement around the perimeter, additional transverse layers of FRP should be provided, or additional width of the transverse layer should be provided above or below the access port. It also appears based on both the component-level and large-scale monotonic results that 12-, 18-, and multi-sided steel poles may be more susceptible to loss of capacity from dent damage, and therefore, the number of layers provided should be increased for these cases.

7.3 Repair Installation Recommendations

In this section, recommendations for the installation of FRP repairs are presented in the form of a repair procedure. Important considerations are mentioned, and several of the techniques outlined are specific to the materials used in this investigation. If other materials are used, manufacturer instructions should be observed. In addition, prior to commencing the repair procedure outlined below, the pole should undergo an investigation for cracking due to the impact, or cracks that may have initiated or propagated due to service loads or environmental degradation. Particular attention should be paid to the presence of dents in aluminum structures and a careful investigation of cracks performed prior to determining the repair action, because of the high probability that the impact generated a brittle crack that will lead to premature failure even with the composite repair. Such brittle cracks were observed in a majority of aluminum specimens considered during the project.

I. Surface Preparation: The pole surface should be prepared by sand blasting, sand papering, or other method for removing rust, scale and paint. For galvanized steel poles, the top galvanizing layer should also be removed. The surface should then be cleaned to remove any grease, oil, or debris. The location of the laminates on the pole should be marked.

II. Dent Fill:
   a. Mix enough of the epoxy fill material to fill the dented region and restore the round shape of the pole, including sand aggregate.
   b. Apply the fill material to the dent. Apply in multiple layers if necessary to avoid slumping of the epoxy.
   c. Wrap the filled section with wax paper to create a smooth surface, and allow time for curing (about 1 hour).
   d. Remove the wax paper and rough-sand the surface, if necessary.

III. Composite Wrap Repair
   a. Pre-impregnated polyurethane FRP:
      i. Remove the glass/polyurethane pre-impregnated composite material from its packaging. If necessary, cut the wrap to the sizes to be applied to the pole.
      ii. Lay the cut laminate pieces out on a flat surface and mist with water. Roll the material with FRP rollers for about 5 minutes, or until the resin is worked throughout the fibers and no bubbling is apparent.
      iii. While the FRP is being cut and rolled, the adhesive epoxy should be mixed and applied to the entire repair extent, about 30 mils thick.
      iv. Apply the first layer of the wrap to the pole and roll with FRP rollers. Ensure that there is good contact between the wrap and the pole.
      v. Apply additional layers or transverse strips to the pole in the same manner.
      vi. Smooth the composite surface with additional adhesive epoxy.
      vii. Wrap the repair with plastic wrap in two stages. Wrap tightly around the circumference of the pole, except where an access port is present, to prevent movement of the wrap. In the section where an access port is present, wrap to the edges of the port, and then apply additional plastic wrap around the edges of the access port (vertically) in order to secure that the wrap is tight near the port. Apply magnets over the plastic wrap near the access port edges. Puncture the plastic wrap to allow the laminates to release CO_2.
      viii. Continue to roll the laminates through the plastic wrap for 15-20 minutes, or until no air pockets/voids are apparent from the curing process.
      ix. Allow the composite to harden (about 4 hours) and remove the magnets and plastic wrap.
   b. Wet lay-up epoxy FRP:

i. Cut the dry fiber weave to the sizes to be applied to the pole.
ii. Mix the epoxy saturating resin.
iii. Lay the dry fibers on a flat surface and add the saturating resin. Enough resin should be added to completely saturate the fibers.
iv. Mix the adhesive epoxy and apply it to the entire repair extent, about 30 mils thick.
v. Apply the first layer of the wrap to the pole and secure with ties or hose clamps. Ensure that there is good contact between the wrap and the pole.
vi. Apply additional layers or transverse strips to the pole in the same manner with a layer of adhesive epoxy between each FRP layer.
vii. Smooth the composite surface by with additional adhesive epoxy, if necessary.
viii. Wrap the repair with plastic wrap in two stages. Wrap tightly around the circumference of the pole, except where an access port is present, to prevent movement of the wrap. In the section where an access port is present, wrap to the edges of the port, and then apply additional plastic wrap around the edges of the access port (vertically) in order to secure that the wrap is tight near the port. Apply magnets over the plastic wrap near the access port edges.
ix. Allow the composite to harden (about 4 hours) and remove the magnets and plastic wrap.

IV. Protective Coating:
a. To give the repair a smooth appearance, additional epoxy saturating resin can be brushed onto the laminate to fill voids, create resin fillets where wraps terminate, and the provide a surface for applying the coating.
b. Final sanding should be done to remove surface imperfections from resin fillets, resin-rich areas from punctured holes in the plastic wrap, etc.
c. Apply approved coating as needed to provide color and an environmental barrier to restrict deterioration of the laminate (particularly visible discoloration of the PU resin due to UV exposure).

7.4 In-situ Installation on Impact-damaged Pole in Tallahassee

During the course of the research project, numerous pole structures experienced vehicular impacts around the state of Florida. One such case was a pole on Caliark and Tennessee Streets in Tallahassee that had minor damage near the base of the pole, making it a good candidate for a trial field installation of the repair system. The pole was not removed from service due to the relatively minor dent (1 ¾ in or approximately 10% of the base diameter). The extents of the dented region were approximately 15 in wide and 16 in high at an angle 150º from the access port (not directly opposite). The repair system consisted of glass fibers and polyurethane resin

(pre-impregnated system). Because of the existence of the access port, the transverse wrap was proportioned into two pieces above and below the access port, the full details of the repair are shown in Appendix A. The damage to the pole prior to repair and the location of the pole at the site are shown in Figure 258. An immediate benefit of the repair is limited or no interruption to traffic, as evident from Figure 258 (b). The canvas and plastic enclosure was erected surrounding the work area to protect the workers and repair materials and to protect the public from airborne debris or direct exposure to the repair materials.

(a) Pole damage at base

(b) Protective plastic tent during installation

Figure 258. In-situ damaged pole and site preparation

To allow for potential problems or delays, a three-day maintenance of traffic window was used. The first day was used to prepare the site and the pole. As described in the recommended procedures in this chapter, the galvanizing layer in the area of repair was removed using a sandpaper flapper wheel and angle grinder, as shown in Figure 259 (a). In addition, the region with the dent was scored with a grinding wheel to promote bond between the metallic substrate and filler and adhesive materials. After surface cleaning, the filler material (Bondo in this case) was prepared and applied with a spatula to return the original geometry of the pole. The fill was sanded after curing, as shown in Figure 259 (b), in preparation for the FRP installation.

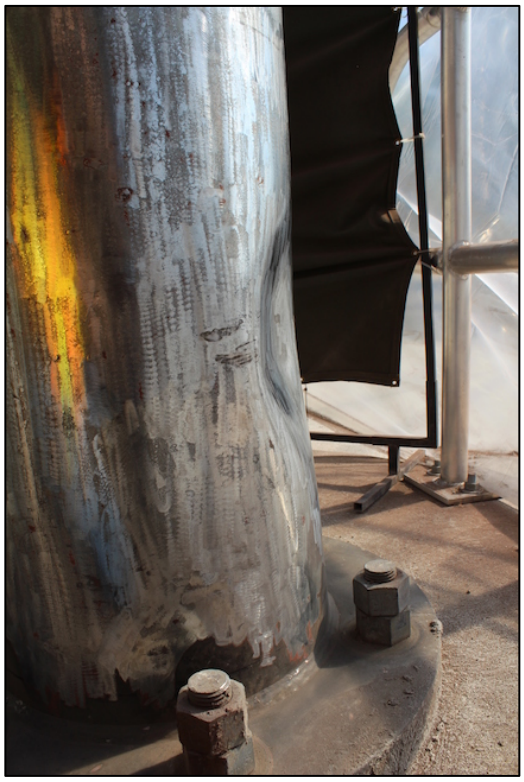

(a) After surface preparation in the repair region

(b) After dent filler application and sanding

Figure 259. Pole surface preparation

On the second day, an adhesive layer (Sika 32) was applied to the locations where FRP laminates were to be bonded. The FRP layers were installed directly to the primed pole after misting water onto each of the pre-preg wraps from the sealed bags (order of laminates: L = longitudinal, L, T = transverse, and T), as shown in Figure 260 (a). Each layer was rolled with a FRP roller for several minutes continuously to prevent build up of carbon dioxide bubbles from the curing process. After all layers were installed, a thick plastic wrap was installed and tensioned around the wrapped region. Punctured holes in the plastic wrap allowed continuous rolling (and exchange of gas) until fully cured, as shown in Figure 260 (b). In addition, the plastic wrap prevented the layers from sagging, resin rich areas could easily be identified and rolled more, and the irregular geometry of the pole, access port, laminates, etc. could be supported as the plastic is only temporary.

(a) Rolling transverse layer of GFRP

(b) Perforated plastic wrap for rolling

Figure 260. Pole wrapping

On the third day, the perforated plastic wrap was removed and the pole was painted. Prior to painting, any additional resin that was added during the wrapping phase was sanded off to provide a smoother finish for painting. The painting of the pole and the final product are shown in Figure 261.

(a) Wrapped pole before painting

(b) Painting in progress

(c) Close-up after painting

(d) Final state after removing protective enclosure

Figure 261. Painting and final product

Chapter 8: Conclusions

8.1 Report Conclusions

The results of an experimental investigation on the fiber-reinforced composite repair of vehicular-damaged utility poles was presented in this report. The results of this study indicate that the FRP composite repair systems considered in this study were effective in restoring both field-damaged and laboratory-damaged tapered utility poles to acceptable capacities. The single-ply component-level tests showed that dented poles tested in a four-point bending setup could be returned to the original plastic capacity (indicated by a normalized stress ratio of 1) many times using only a single layer continuous wrap for dents up to 30% of the diameter at the dented location. The large-scale monotonic tests showed that not all of the repairs were successful in achieving the same result, particularly those with complicated geometries, access ports, multi-sided cross sections, extensive damage extents, and wraps that were not sufficient in length to be properly developed. The number of layers of FRP installed in the large-scale validation tests was based on the results from the component-level tests, and therefore the increase in capacity of the large-scale poles was evaluated relative to the estimate yield capacity. All the damaged and repaired large-scale specimens achieved more than 90% of the estimated undamaged yield capacity, except two specimens (ST-5 and FD-1) where the testing was stopped prior to pole failure, and two specimens (ST-6 and ST-8) that experienced premature failure in the dented regions.

Unlike traditional applications of FRP strengthening for flexural members, walls, or columns, the impact-damaged regions in the utility poles considered in this study posed a significant challenge for both the design of the composite repair as well as actual installation of the repair. The design of the repair was complicated by the location and extents of the dent, potentially with the cross-sectional geometry of the pole being different than the original tapered geometry (at the center of the dent location usually). In addition, a majority of poles considered contained an integral access port (hand hole) or series of pedestrian buttons that prohibited a standard repair that may be employed for pipes, for example. The installation of the repair is challenging due to the need for a vertical layup of the laminates and application of the dent filler material. Materials were selected such that mechanical behavior was acceptable; however, emphasis was placed on ability with which the materials could be brought to the site and installed with good control over quality.

8.2 Future Research

The results of this study demonstrate that more work is necessary to fully understand the behavior of the FRP composite repair systems, particularly the behavior of the large-scale poles with geometric irregularities. The behavior of the component-level repairs relative to the control specimens showed ability to achieve the original undamaged plastic capacity of the pole. However, this was harder to demonstrate in the large-scale specimens that lacked a true control specimen, as all the poles were retrieved from the field and had different geometries, dents, access ports, existing levels of conditioning, etc. Therefore, the basis for interpreting the success of the repair system was limited to a theoretical stress ratio (relative to a theoretical yield moment for a specimen without irregularities) or whether plastic strains developed in the

substrate indicating formation of a plastic hinge in the metal (between the repair and base of the pole).

Several other topics of interest exist for further investigation of such a repair system. A potential issue of interest in deploying this system is the torsional demand on the pole base (and FRP repair system) due to the large loads generated by wind in combination with the flexural loads from gravity and bending. Such torsional loads would create different shear and normal stress combinations in the bonded systems that were not accounted for in the current research program. The current testing also did not specifically address degradation of the poles due to environmental factors and exposure to mechanical conditioning. There is room to establish whether an externally-bonded composite repair system could be used to provide capacity to poles that have suffered environmental degradation or exhibit fatigue cracking, particularly in the connection to the mast-arm. Bondo is hygroscopic, so some long-term studies on whether fill and laminate materials respond poorly to aqueous environments, as part of broader efforts on the environmental behavior of composite materials applied to metallic structures, are of interest.

References

AASHTO. (2009). *LRFD Bridge Design Guide Specifications for GFRP-Reinforced Concrete Bridge Decks and Traffic Railings.* Washington, D.C.: AASHTO.

AASHTO. (2012). *LRFD Bridge Design Specifications.* Washington, D.C.: AASHTO.

AASHTO. (2013). *Standard Specifications for Structural Supports for Highway Signs, Luminaires, and Traffic Signals.* Washington, D.C.: AASHTO.

ACI. (2008). *Guide for the Design and Construction of Externally Bonded FRP Systems for Strengthening Concrete Structures.* Farmington Hills, MI: American Concrete Institute.

Akbar, I., Oehlers, D., & Ali, M. (2010). Derivation of the bond-slip characteristics for FRP plated steel members. *Journal of Constructional Steel Research, 66*, 1047-1056.

Arya, C., Clarke, J. L., Kay, E. A., & O'Regan, P. D. (2002). TR 55: Design guidance for strengthening concrete structures using fibre composite materials: a review. *Engineering Structures, 24 (7)*, 889-900.

Bhattacharya, B., & Seifried, A. E. (2005). *Cracking of Overhead Sign Structures and Their Repair Using Composite Fabric as a Wrap.* Newark, Delaware: Delaware Center for Transportation, University of Delaware, .

Buyukozturk, O., Gunes, O., & Karaca, E. (2004). Progress review on understanding debonding problems in reinforced concrete and steel members strengthened using FRP composites. *Construction and Building Materials, 18*, 9-19.

CAN/CSA-S806-02. (2007). *Design and Construction of Building Components with Fibre-Reinforced Polymers.* Toronto, Ontario, Canada: Canadian Standards Association.

Chahrour, A. H., & Soudki, K. A. (2006). Structural retrofitting of deteriorated concrete lighting poles using FRP sheets in wet layup – field application. *Journal of Composites for Construction, 10 (3)*, 234-243.

Consolazio, G. R., Bui, L. H., & Walters, R. A. (2012). *Pendulum impact testing of an-impact-breakaway, wind resistant base connection for multi-post ground signs.* Gainesville, Florida.

Fam, A., Witt, S., & Rizkalla, S. (2006). Repair of damaged aluminum truss joints of highway overhead sign structures using FRP. *Construction and Building Materials, 20*, 948–956.

FIB Bulletin 14, T. G. (2001). *Externally bonded FRP reinforcement for RC structures.* Lausanne, Switzerland: FIB: Féderation International du Béton.

Foedinger, R., Boozer, J., Bronstand, M., & Davidson, J. (2002). Development of an energy absorbing composite utility pole. *Paper presented at the Proc., TRB Annual Meeting.*

Frymoyer, M. C., Berman, J. W., & Northwest, T. (2009). *Remaining life assessment of in-serviceluminaire support structures.* Washington State Department of Transportation.

Gabler, H. C., Gabauer, D., & Riddell, W. (2007). *Breakaway Utility Poles.* Trenton: New Jersey Department of Transportation.

Gunes, O., Buyukozturk, O., & Karaca, E. (2009). A fracture-based model for FRP debonding in strengthened beams. *Engineering Fracture Mechanics, 76*, 1897–1909.

Haber, Z. B., Mackie, K. R., Zhao, L., & Olka, M. (2009). *Thermo-mechanical durability of carbon fiber reinforced polymer strengthened reinforced concrete beams.* Tallahassee FL: Florida Department of Transportation.

Haedir, J., Bambach, M. R., Zhao, X. L., & Grzbieta, R. H. (2009). Strength of circular hollow sections (CHS) tubular beams externally reinforced by carbon FRP sheets in pure bending. *Thin-Walled Structures, 47*, 1136-1147.

Hauch, S., & Bai, Y. (1999). Bending Moment Capacity of Pipes. *18th International Conference on Offshore Mechanics and Arctic Engineering.* OMAE1999.

Hollaway, L. C., & Cadei, J. (2002). Progress in the technique of upgrading metallic structures with advanced polymer composites. *Prog. Struct. Engng Mater, 4*, 131–148 .

ISIS Canada Research Network. (2006). *isiscanada.com*. Retrieved from http://www.isiscanada.com/research_past/2002-06/02-06_T3_overview.html

Islam, S. M., Zahurul, & Young, B. (2011). FRP strengthened aluminum tubular sections subjected to web crippling. *Thin-Walled Structures, 49*, 1392–1403.

Ivey, D. L., & Scott, C. P. (2004). *State of the Art Report: Utilities and Roadside Safety.* Washington, D.C: Transportation Research Board, Committee on Utilities.

JSCE No.41, C. E. (2001). *Recommendations for upgrading of concrete structures with use of continuous fiber sheets.* Tokyo: JSCE Research Committee on Upgrading of Concrete Structures with Use of Continuous Fiber Sheet.

Karimi, K., Tait, M. J., & El-Dakjakhni, W. W. (2010). Experimental Investigation of Two Novel FRP Retrofit Schemes for Strengthening Steel Columns. *Proceedings of the 9th U.S. National and 10th Canadian Conference on Earthquake Engineering*, (p. (Paper No. 364)). Toronto, Ontario, Canada .

Kaw, A. K. (2006). *Mechanics of Composite Materials,* (2nd ed.). Boca Raton: CRC Press.

Lanier, B., Schnerch, D., & Rizkalla, S. (2009). Behavior of steel monopoles strengthened with high-modulus CFRP materials. *Thin-Walled Structures, 47*, 1037–1047 .

Lu, X., Teng, J., Ye, L., & Jiang, J. (2005). Bond–slip models for FRP sheets/plates bonded to concrete. *Engineering Structures, 27*, 920-937.

Mackie, K. R., Slade, R. A., & Haber, Z. B. (2011). *FRP Composite Repair of Vehicle Impact Damaged Highway Sign Structures.* Orlando, Florida: Florida Department of Transportation.

Miller, T. C., Chajes, M. J., Mertz, D. R., & Hastings, J. N. (2001). Strengthening of a Steel Bridge Girder Using CFRP Plates. *Journal of Bridge Engineering, November/December 6*, 6.

NCHRP-176. (2011). *Cost-Effective Connection Details for Highway Sign, Luminaire, and Traffic Signal Structure.* Bethlehem: NCHRP.

NCHRP-350. (1993). *Recommended procedures for the safety performance evaluation of highway features.* San Antonio, Texas.

Ness, B. W., & Till, R. D. (1992). *Cantilever sign structure inspection. Final report.*

Pantelides, C. P., Nadauld, J., & Cercone, L. (2003). Repair of Cracked Aluminum Overhead Sign Structures with Glass Fiber Reinforced Polymer Composites. *Journal of Composites for Construction (ASCE), 7*, 118.

Pellegrino, C., Tinazzi, D., & Modena, C. (2008). Experimental Study on Bond Behavior between Concrete and FRP Reinforcement. *Composites for Construction, 12*, 1090-0268.

Polyzois, D., & Kell, J. A. (2007). Repair and rehabilitation of wood utility poles with fibre-reinforced polymers. *Canadian Journal of Civil Engineering, 34(1)*, 116-119.

Rosenbaugh, S., Faller, R. K., Lechtennberg, K. A., Bielenberg, R. W., Sicking, D. L., & Reiad, J. D. (2009). *Dynamic evaluation of New York state's aluminum pedestrain signal pole system.* New York: New York state department of Transportation.

Schaumann, P., Keindorf, C., & Brüggemann, H. (2005). Elasto-Plastic Behavior and Buckling Analysis of Steel Pipelines Exposed To Internal Pressure and Additional Loads. *24th*

International Conference on Offshore Mechanics and Arctic Engineering. Halkidiki, Greece: OMAE2005.

Schnerch, D., & Rizkalla, S. (2004). Strengthening of Scaled Steel-Concrete Composite Girders and Steel Monopole Towers with CFRP. *The Second International Conference on FRP Composites in Civil Engineering.* Adelaide, Australia: CICE2004.

Schnerch, D., Dawood, M., Rizkalla, S., & Sumner, E. (2007). Proposed design guidelines for strengthening of steel bridges with FRP materials. *Construction and Building Materials, 21 (5)*, 1001-1010.

Sen, R., Mullins, G., & Shahawy, M. (2007). Fiber-reinforced polymer repair and strengthening of structurally deficient piles. *Transportation Research Record, 2028*, 221-230.

Sim, H. B., & Uang, C. M. (2011). *Fatigue tests of welded connections in cantilevered steel sign structures.* San Diego, California: ISA.

South, J. (1997). *Fatigue of tube to plate fillet welds and methods for their improvement.* Springfield: Illinios Department of Transportation.

Stephens, R., Fatemi, A., Stephens, R., & Fuchs, H. (2000). *Metal Fatigue In Engineering.* NY: Wiley.

Su, Y. (2008). *Numerical Simulation of Strengthening Unreinforced Masonry (URM) Walls by New Retrofitting Technologies for Blast Loading* . Adelaide, AU: University of Adelaide School of Civil, Environmental and Mining Engineering.

Utilities, C. o. (2004). *Utilities and Roadside Safety.* Washington, D.C.: Transportation Research Board.

Wu, Z., Wang, X., & Iwashita, K. (2007). State-of-the-Art of Advanced FRP Applications in Civil Infrastructure in Japan. *Composites & Polycon.* Tampa, Florida: American Composites Manufacturers Association.

Zhao, X. L., & Zhang, L. (2007). State-of-the-art review on FRP strengthened steel structures. *Engineering Structures, 29 (8)*, 1808-1823.

Appendix A

Design drawings for large-scale pole repairs
Including aluminum, steel, field damaged, impact, and fatigue tests

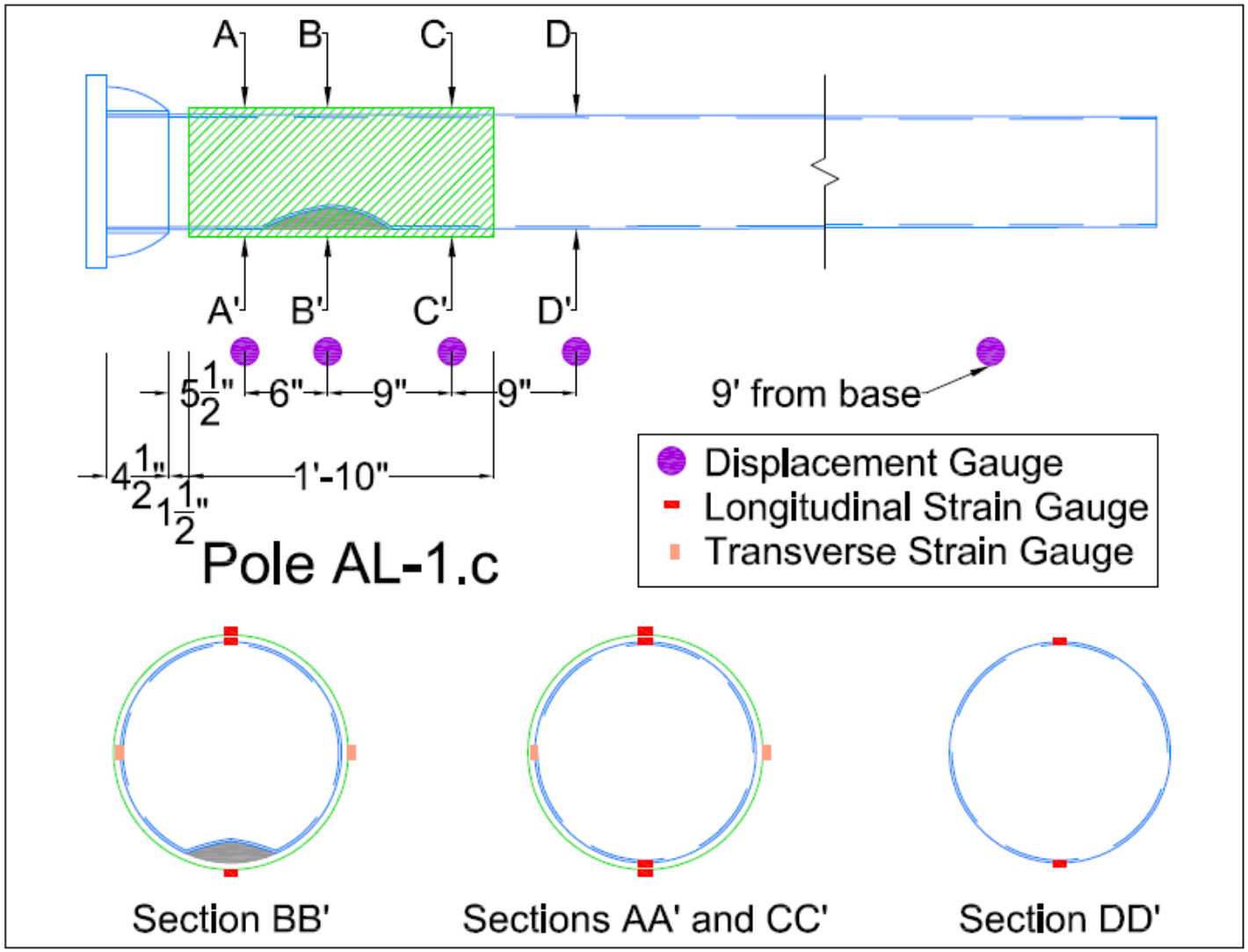

Figure 262. AL-1.c design drawing

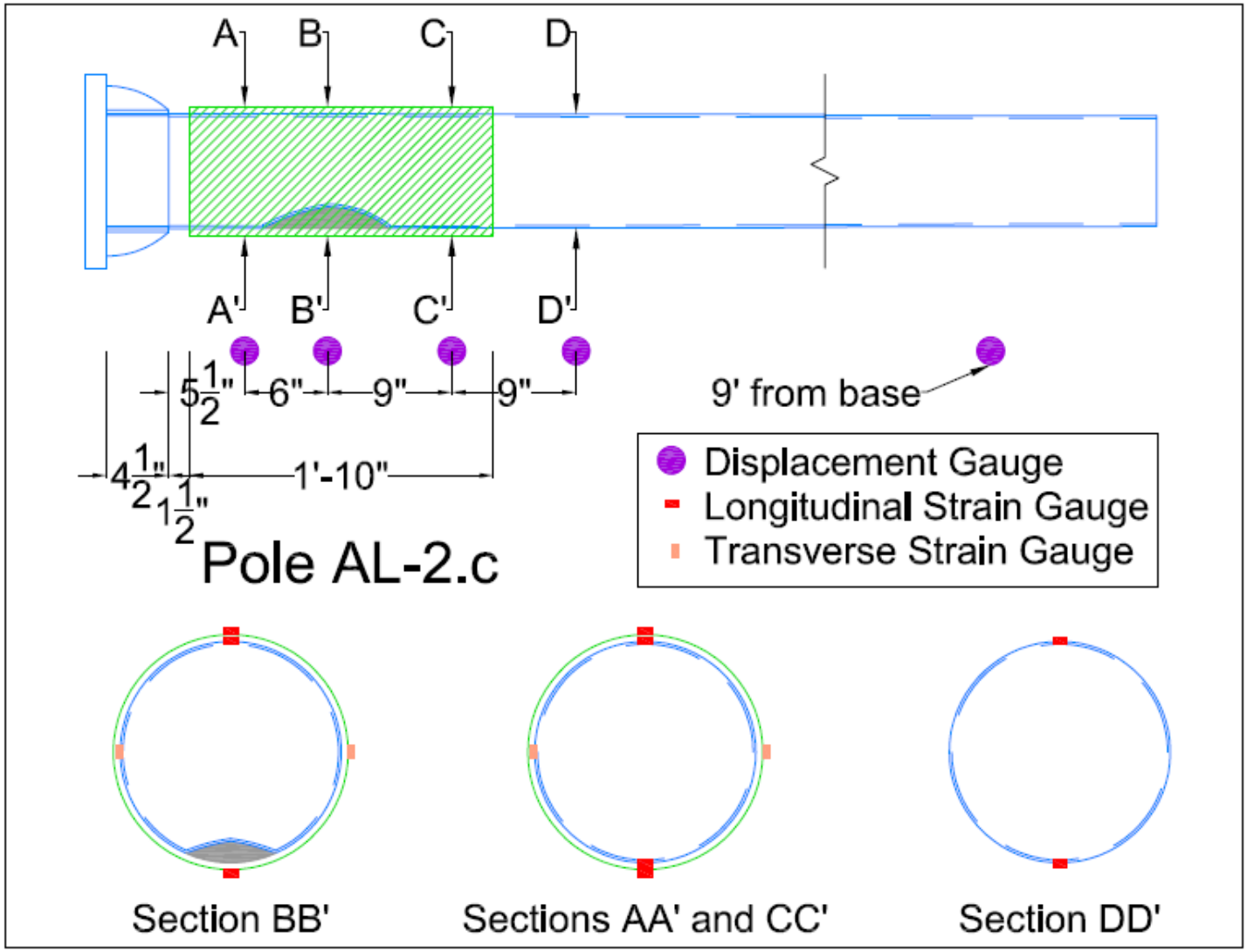

Figure 263. AL-2.c design drawing

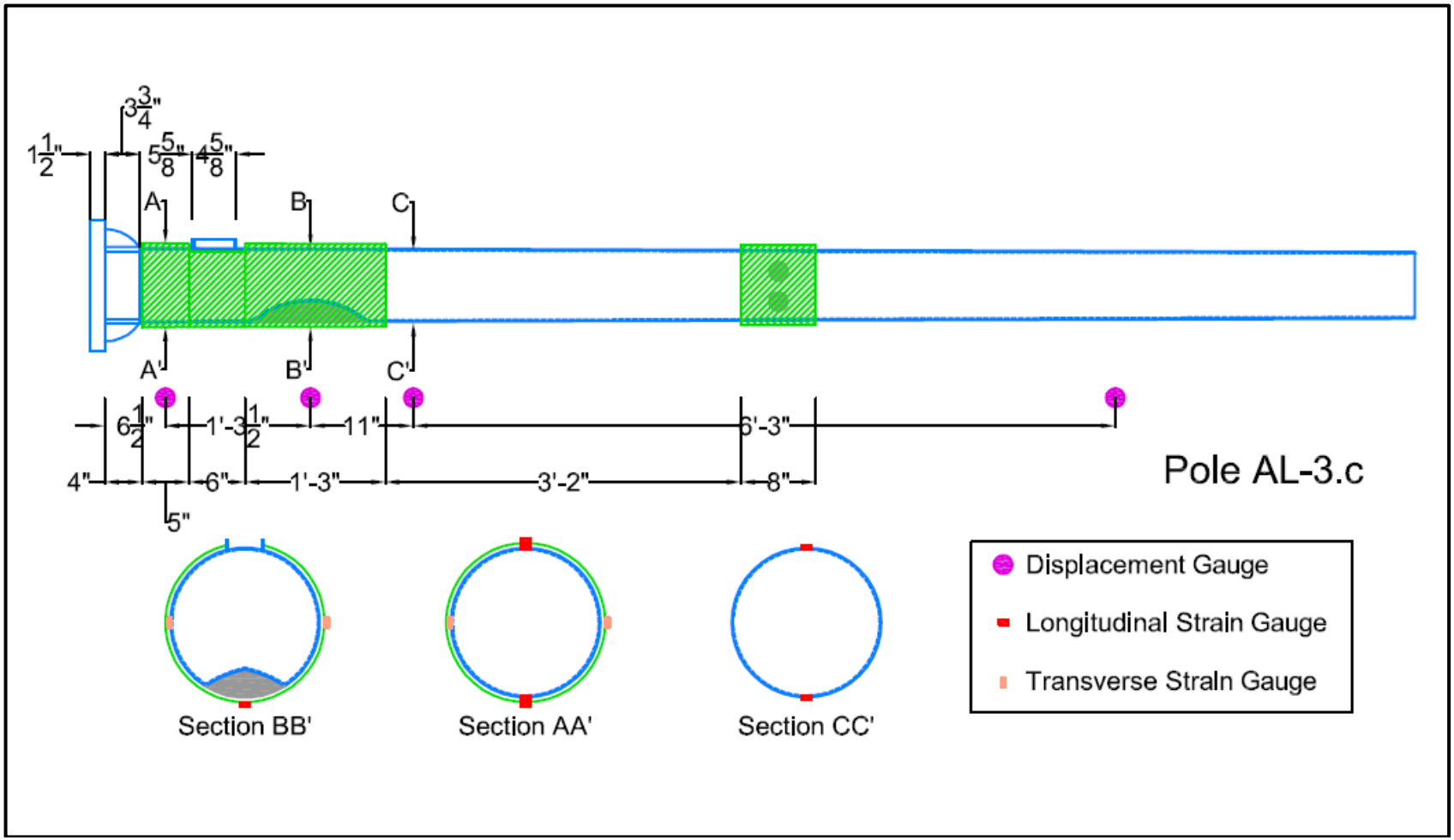

Figure 264. AL-3.c design drawing

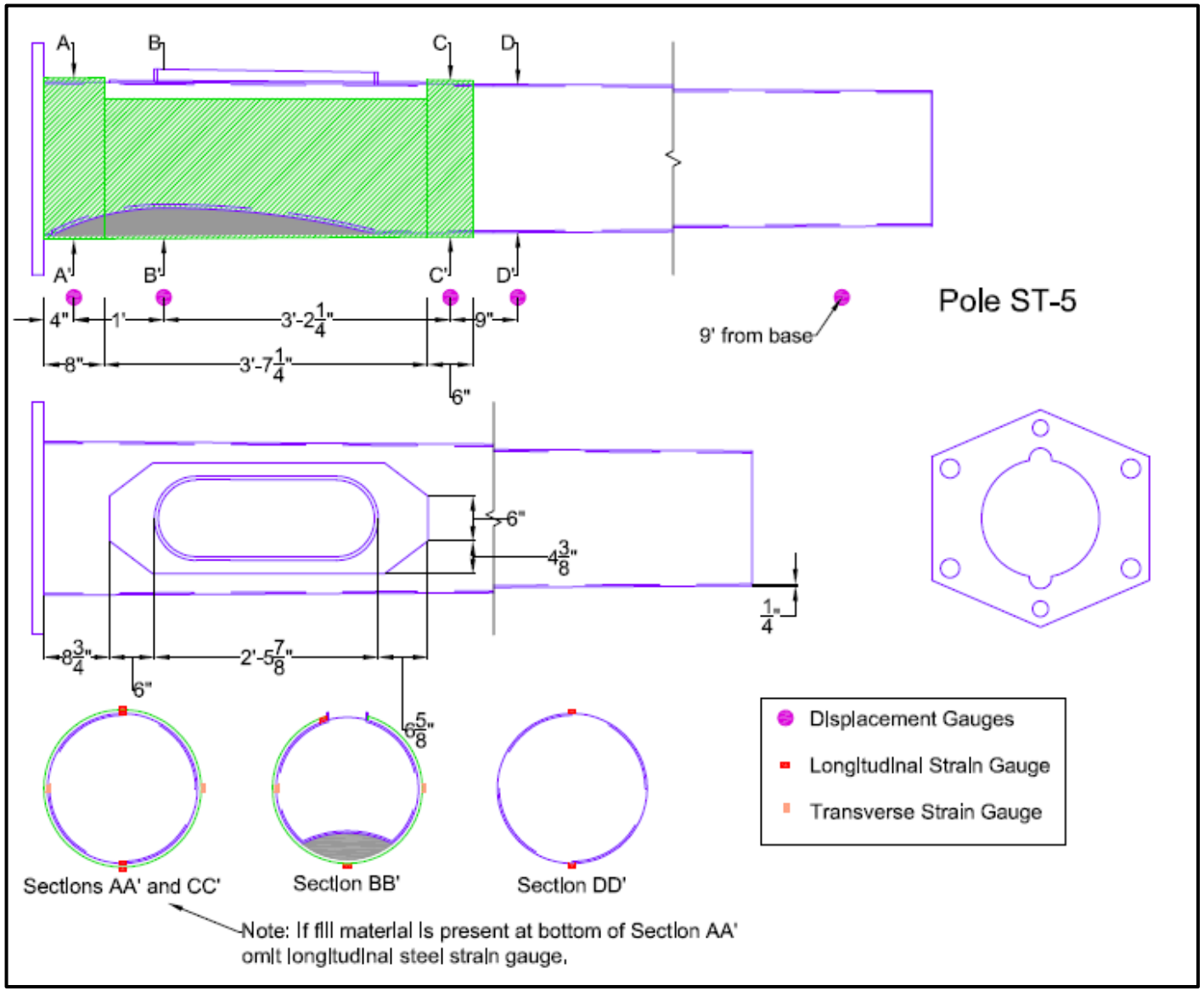

Figure 265. ST-5 design drawing

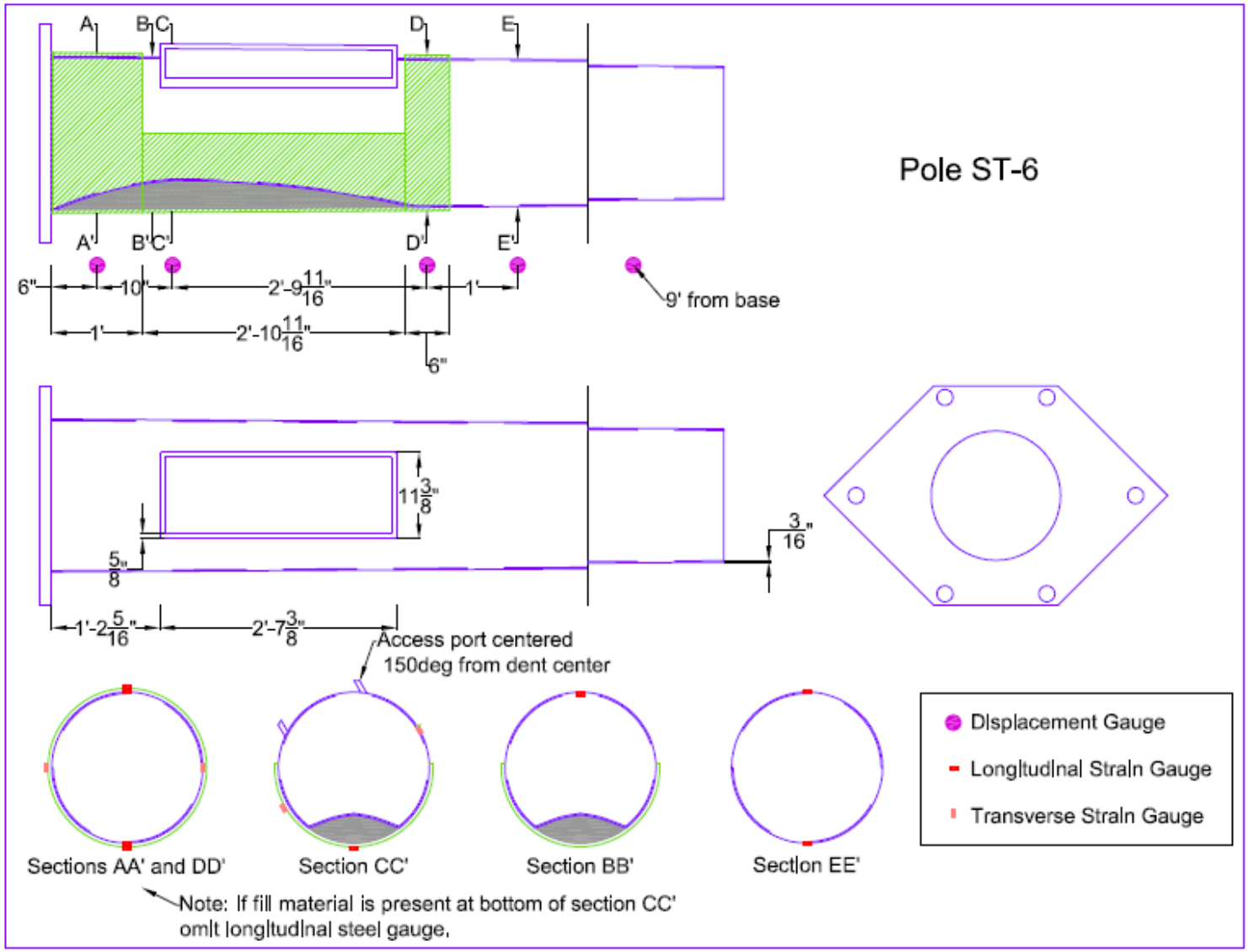

Figure 266. ST-6 design drawing

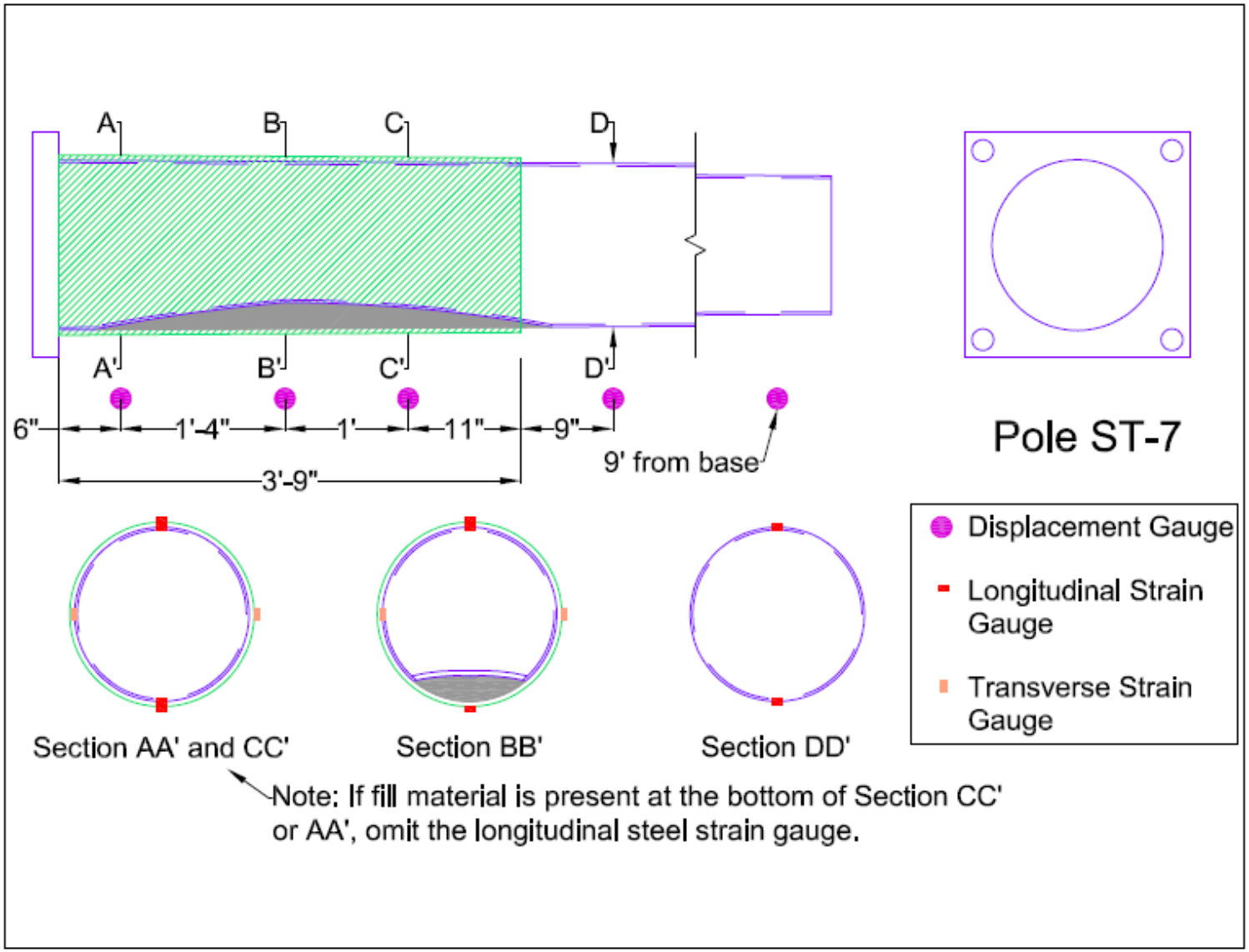

Figure 267. ST-7 design drawing

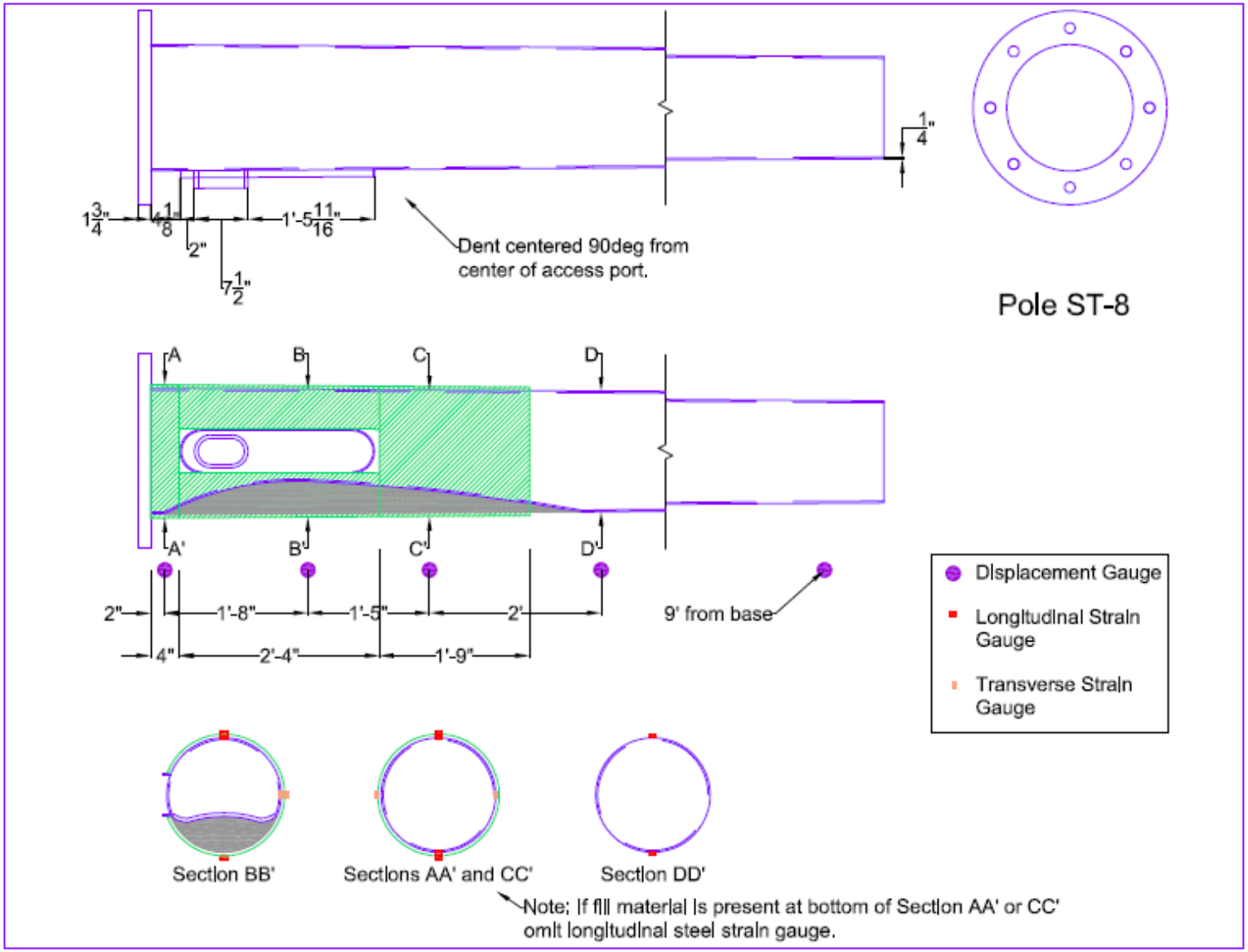

Figure 268. ST-8 design drawing

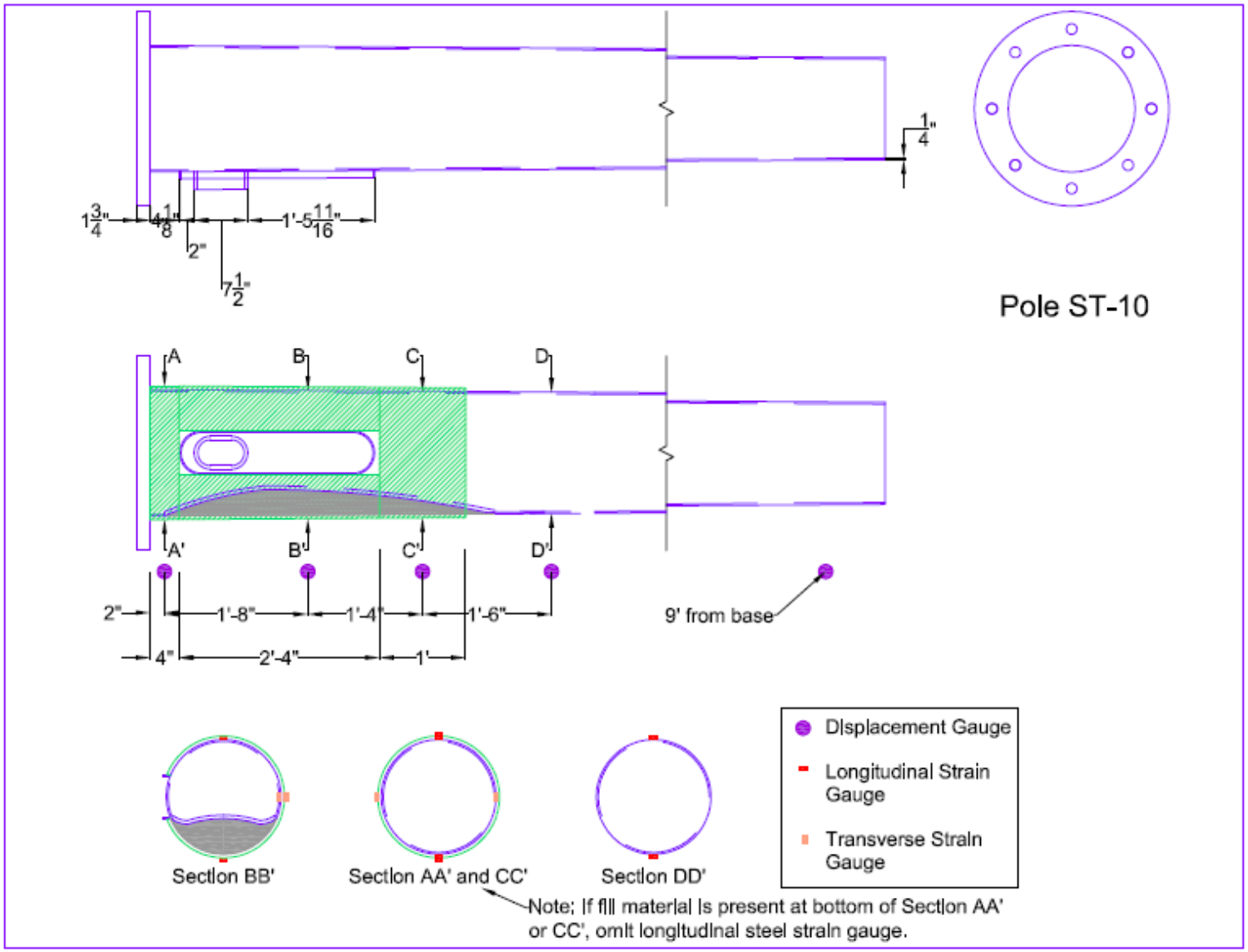

Figure 269. ST-10 design drawing

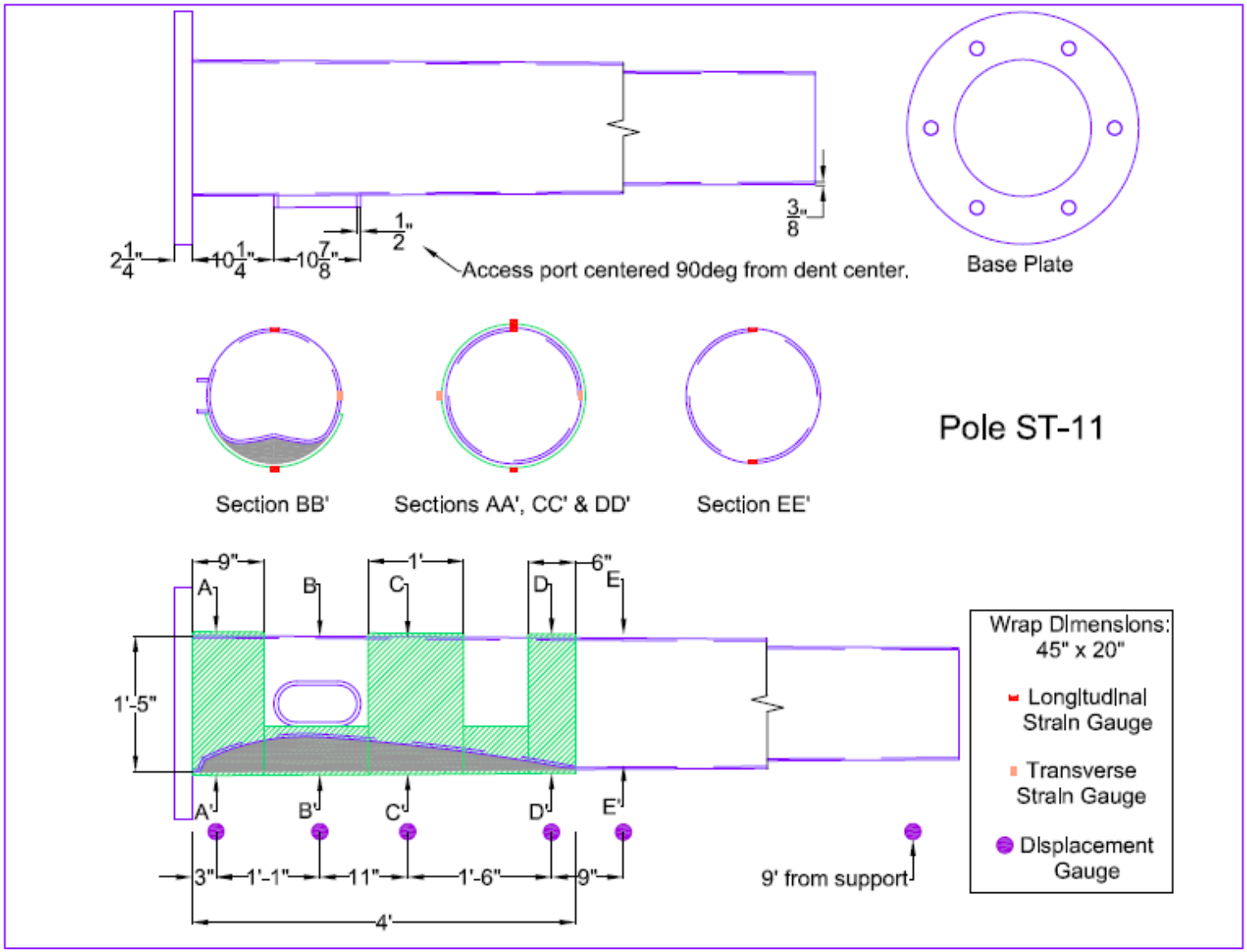

Figure 270. ST-11 design drawing

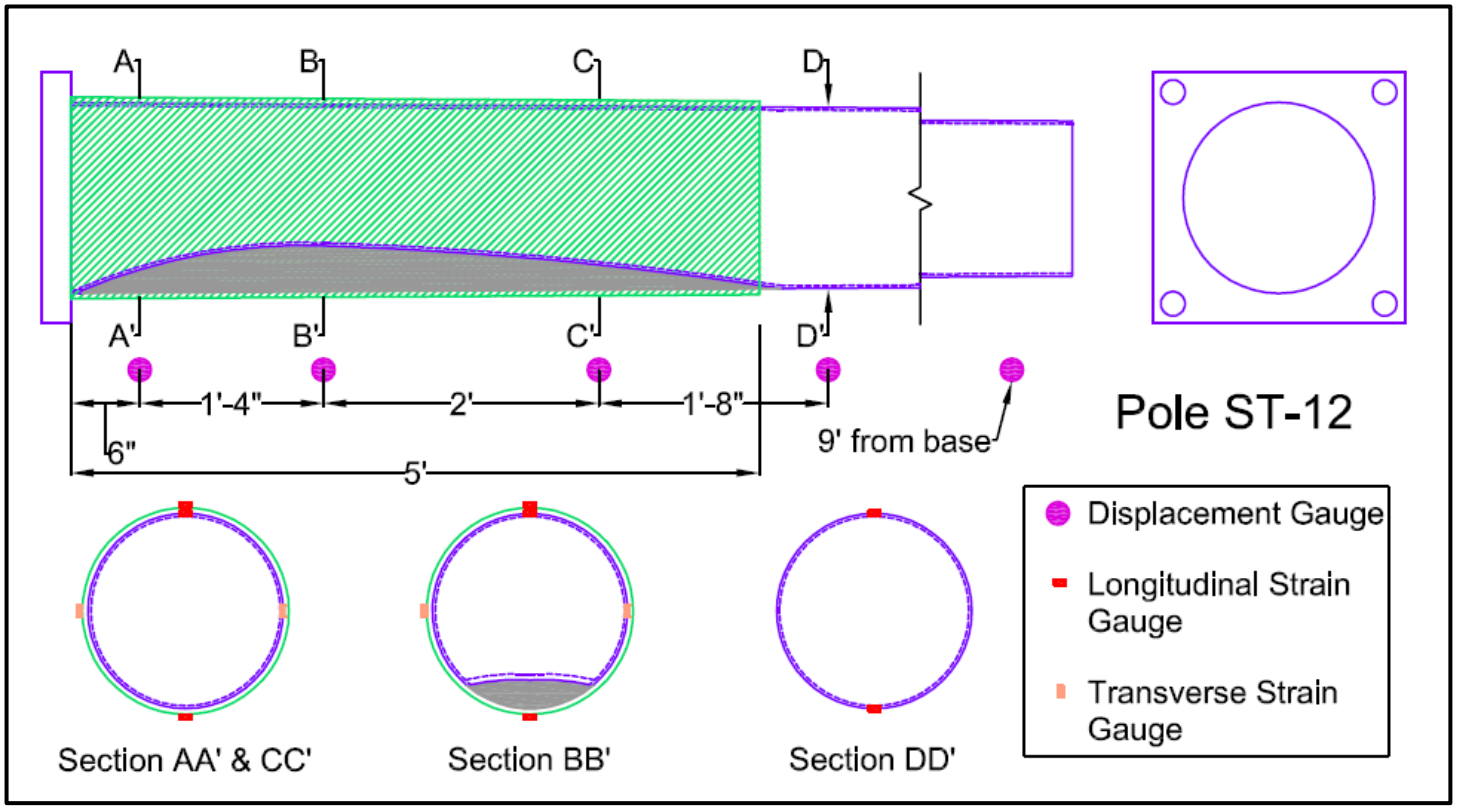

Figure 271. ST-12 design drawing

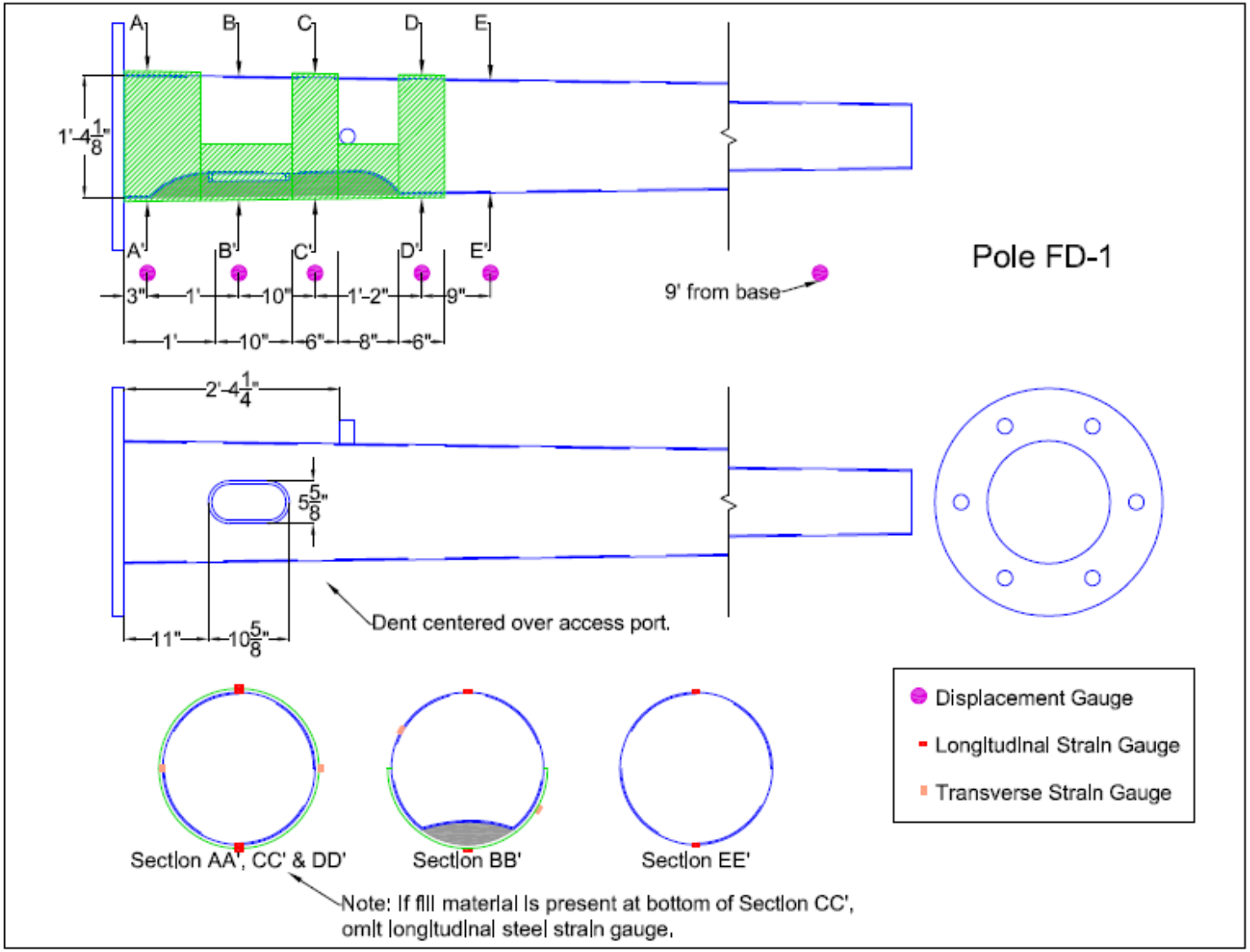

Figure 272. FD-1 design drawing

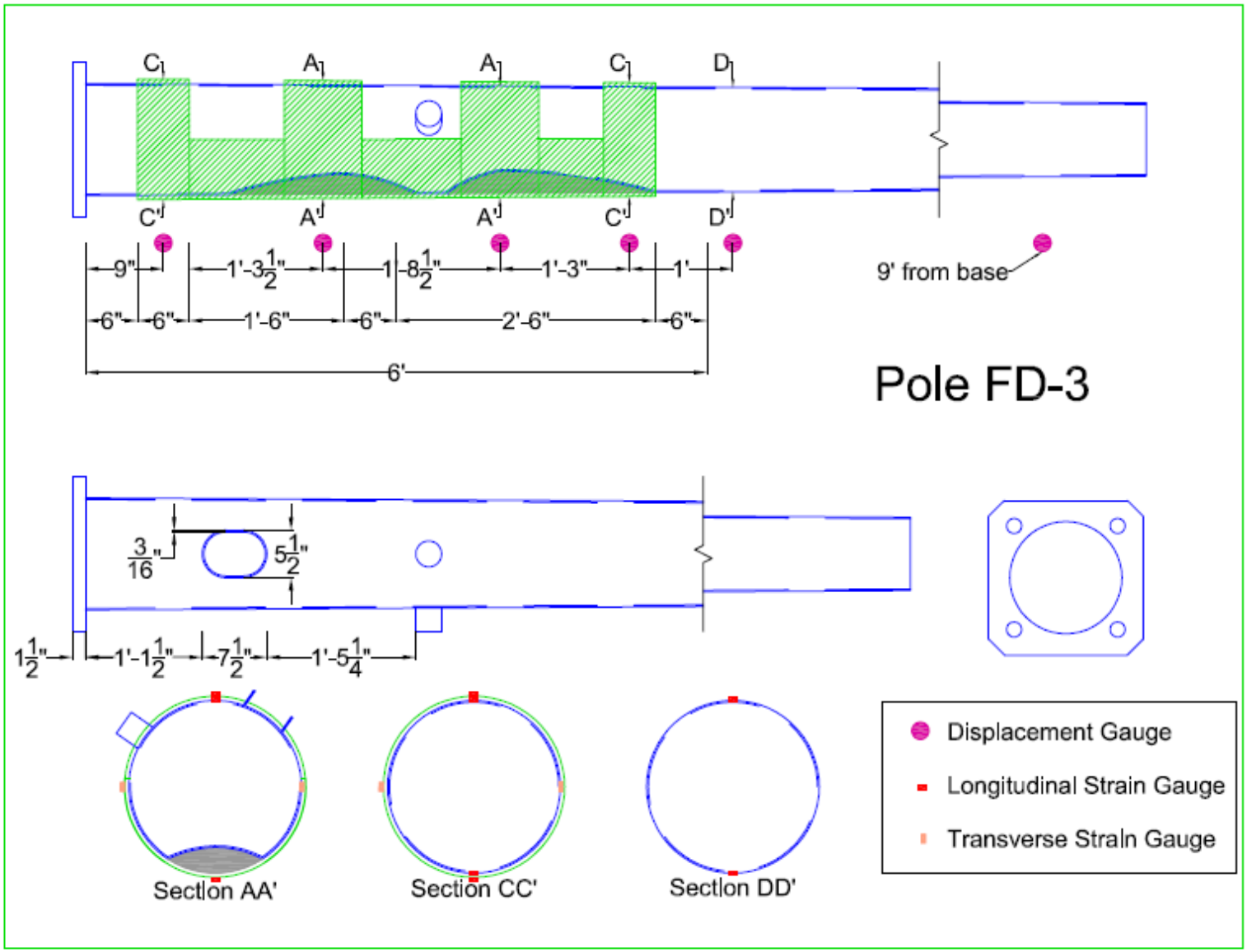

Figure 273. FD-3 design drawing

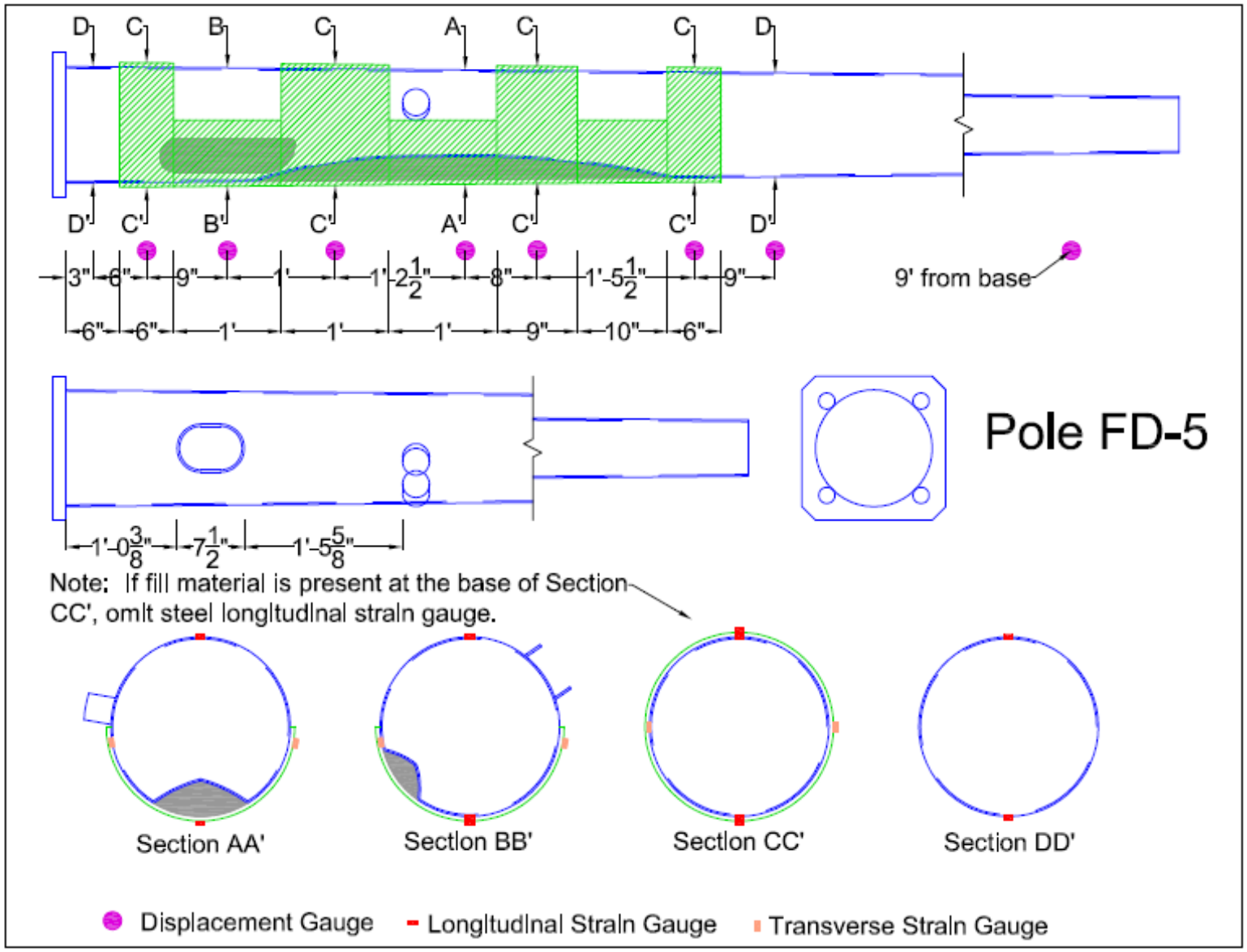

Figure 274. FD-5 design drawing

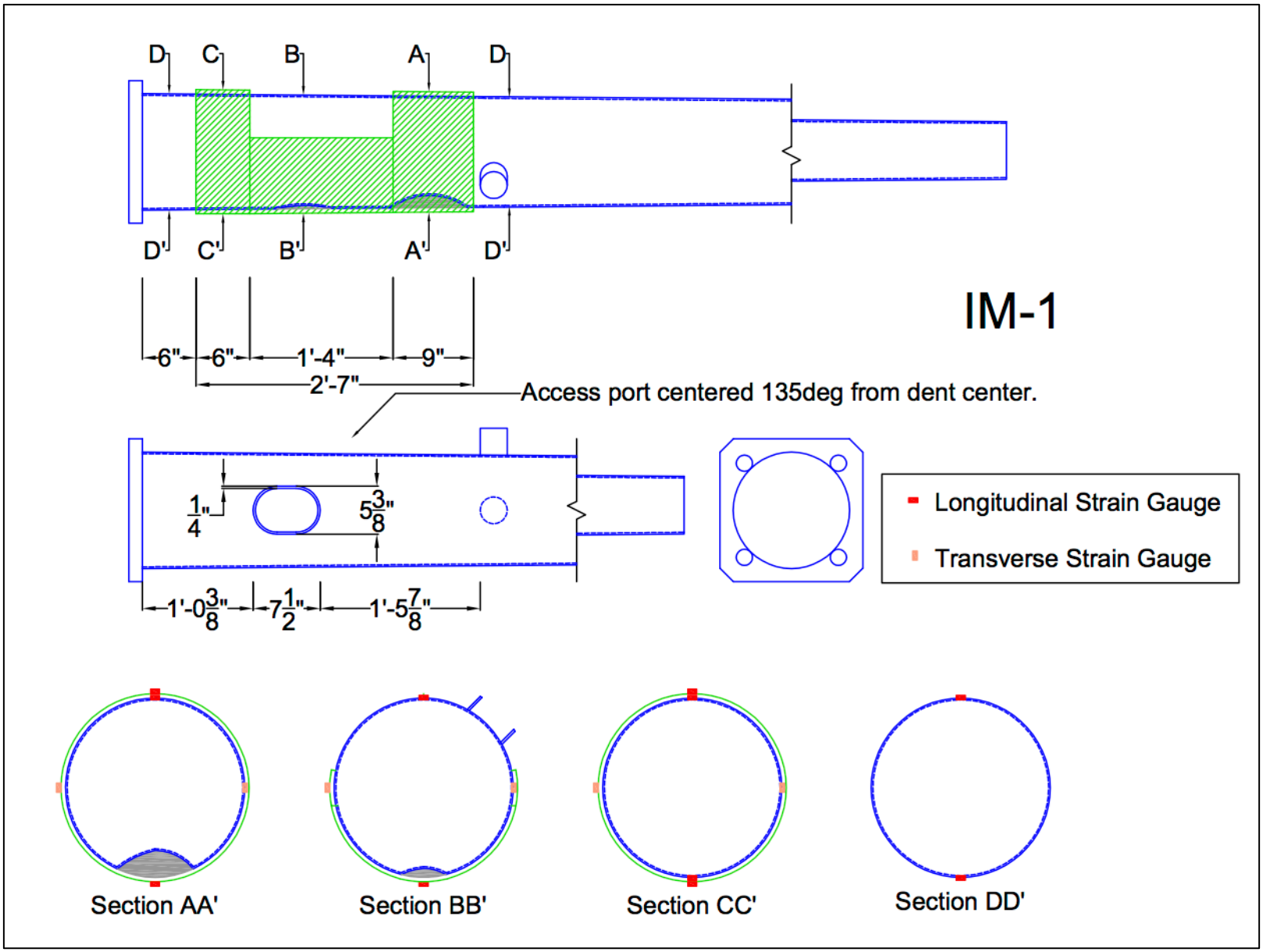

Figure 275. IM-1 design drawing

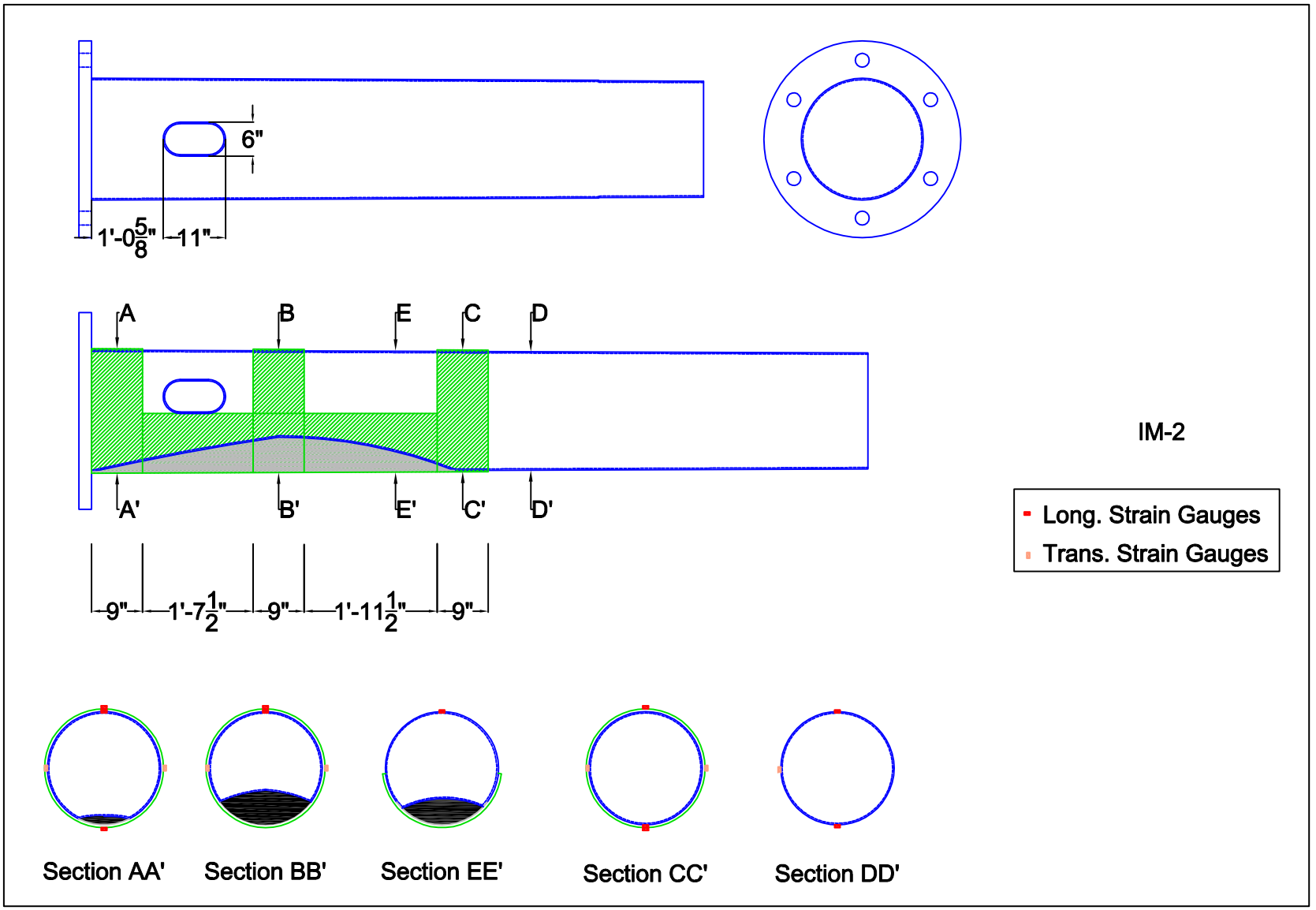

Figure 276. Pole IM-2 design drawing

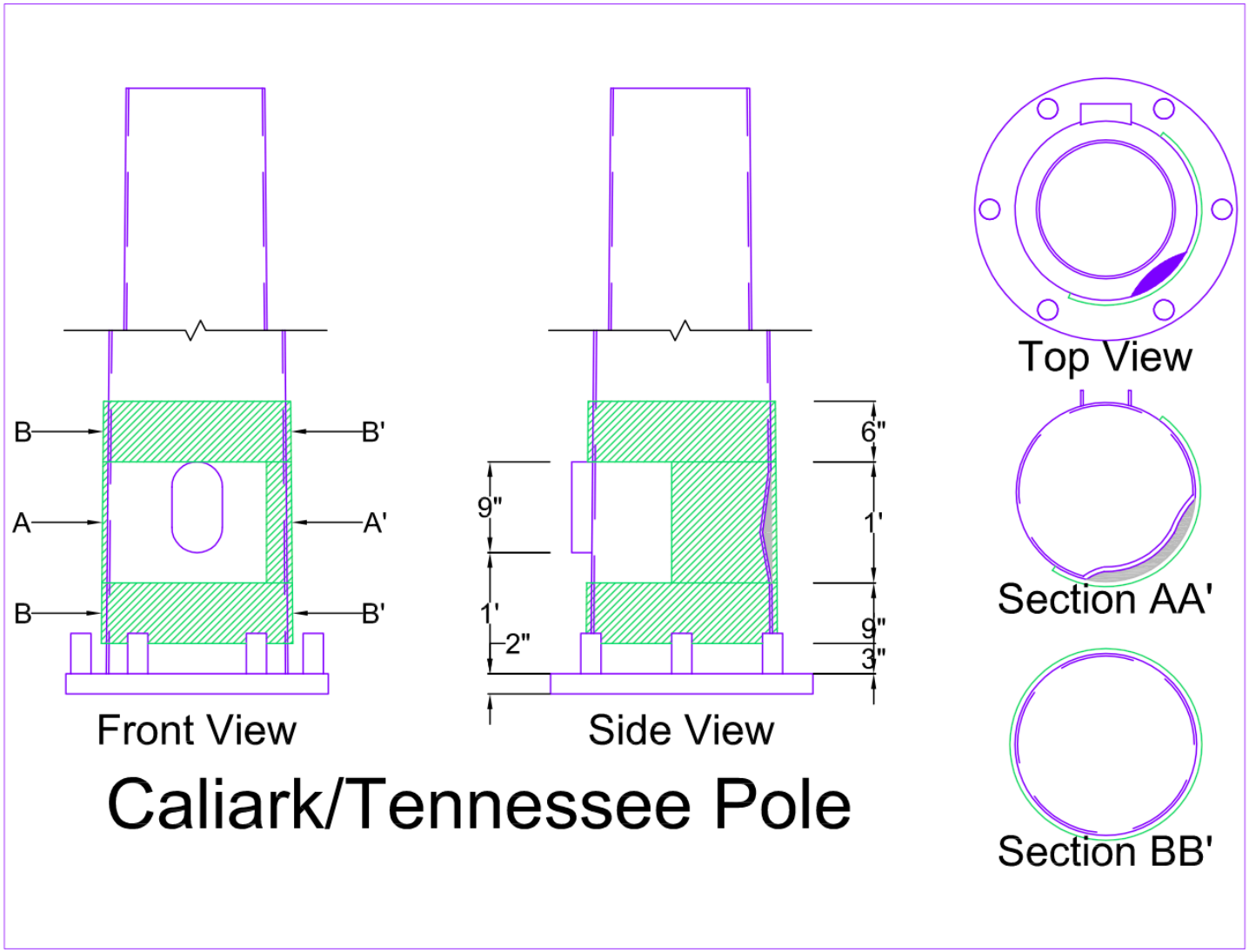

Figure 277. Caliark in-situ repair design drawing

Appendix B

Pole base connection (plate, weld, and bolt) details for all large-scale specimens (tested under monotonic or cyclic load)

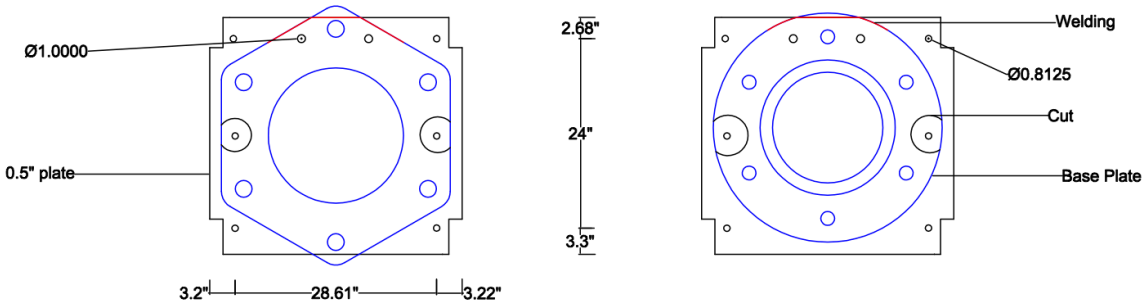

ST-6

ST-11

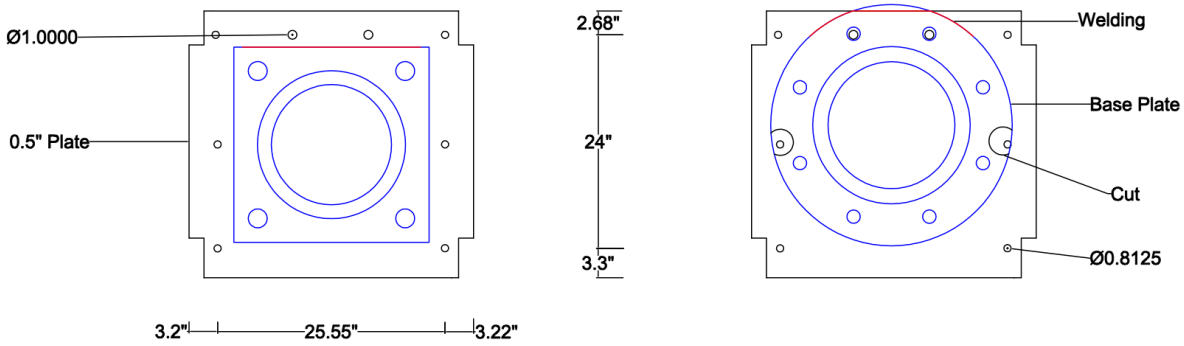

ST-7 & ST-12

ST-8 & ST-10

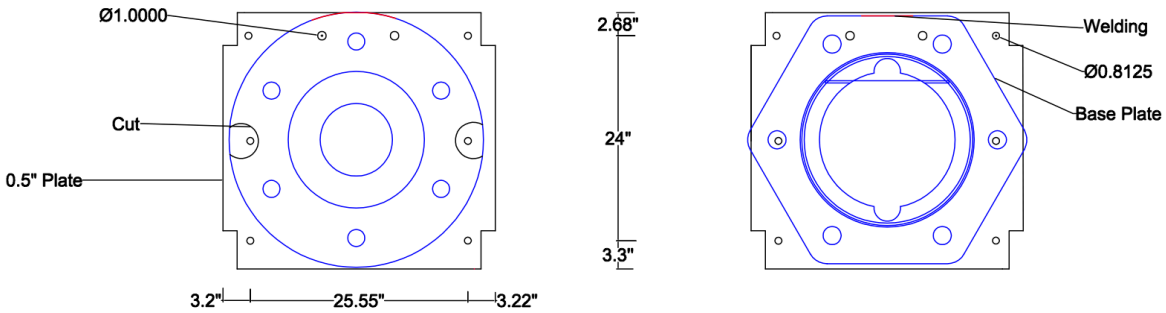

FD-1

ST-5

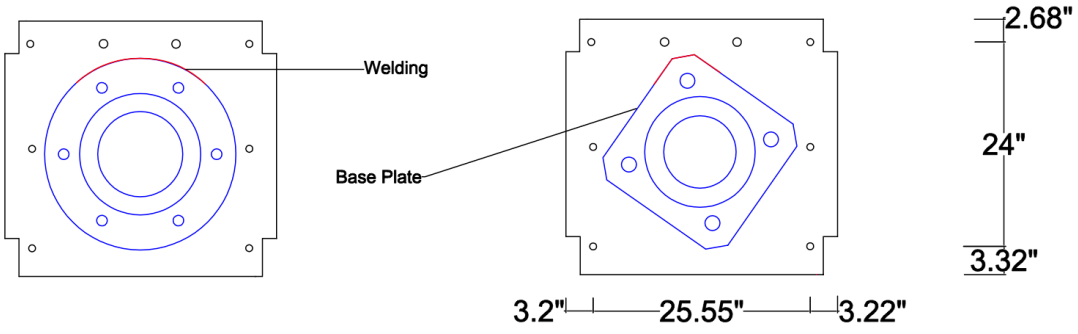
Welding
Base Plate
2.68"
24"
3.32"
3.2"
25.55"
3.22"

FD-2

FD-3

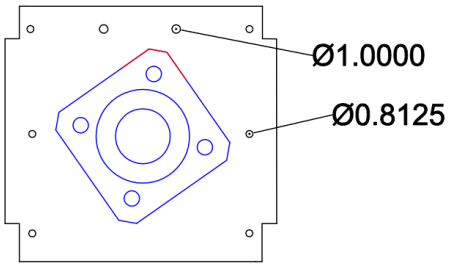
Ø1.0000
Ø0.8125

FD-5

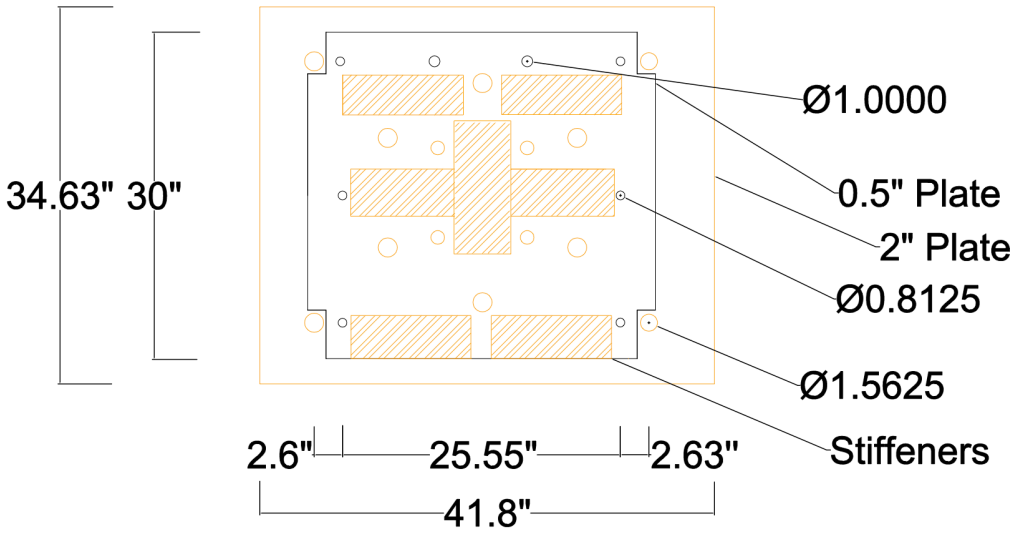
34.63"
30"
Ø1.0000
0.5" Plate
2" Plate
Ø0.8125
Ø1.5625
Stiffeners
2.6"
25.55"
2.63"
41.8"

Appendix C

Steel and aluminum dogbone coupon material stress-strain test data

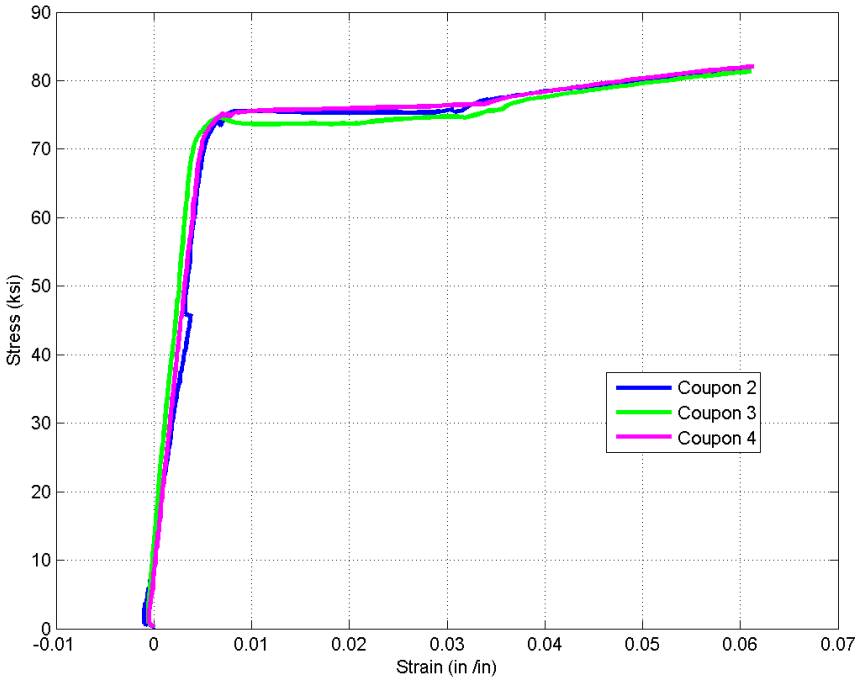

Figure 278. FD-1 coupon stress-strain data

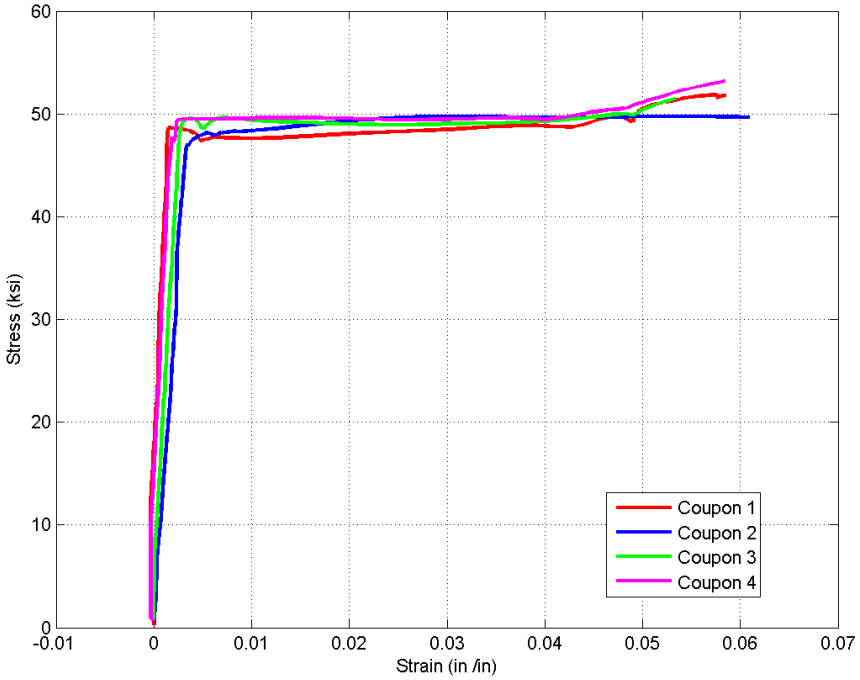

Figure 279. FD-2 coupon stress-strain data

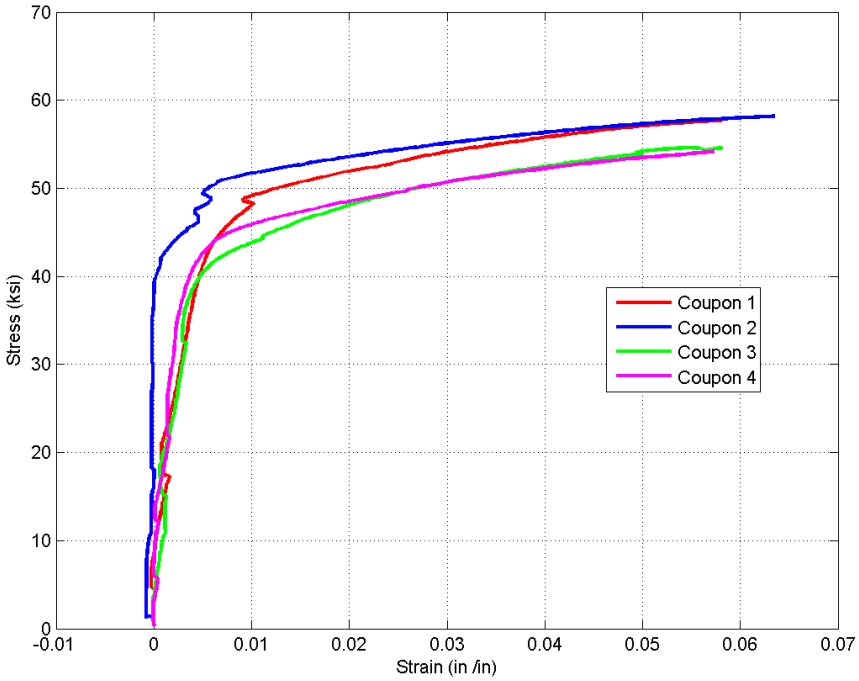

Figure 280. FD-3 coupon stress-strain data

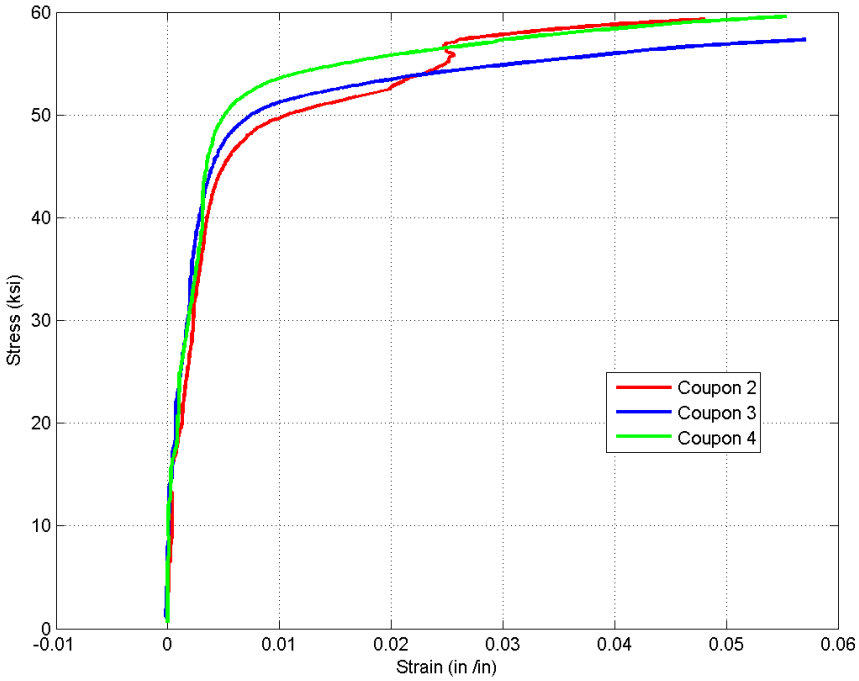

Figure 281. FD-5 coupon stress-strain data

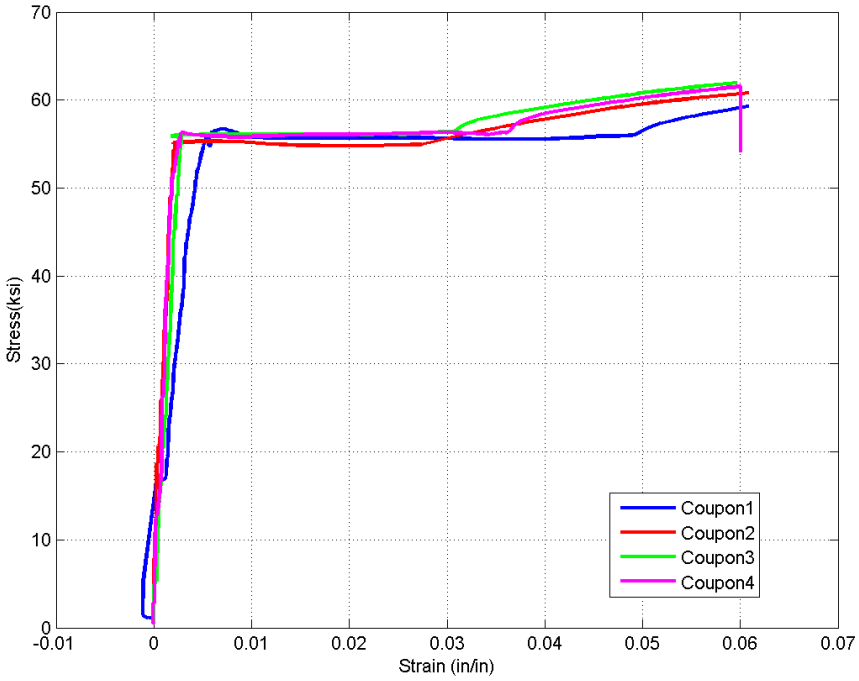

Figure 282. ST-5 coupon stress-strain data

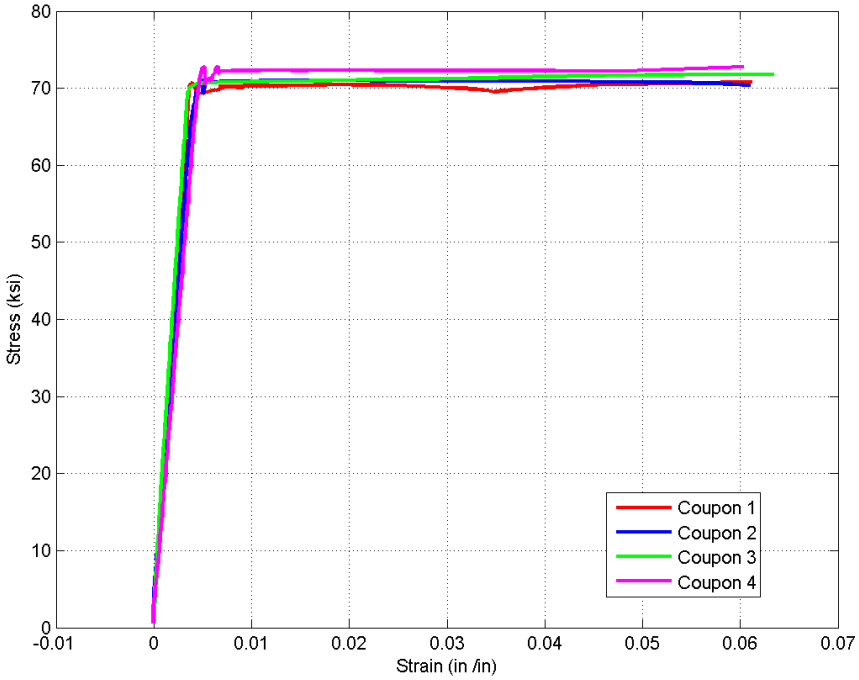

Figure 283. ST-6 coupon stress-strain data

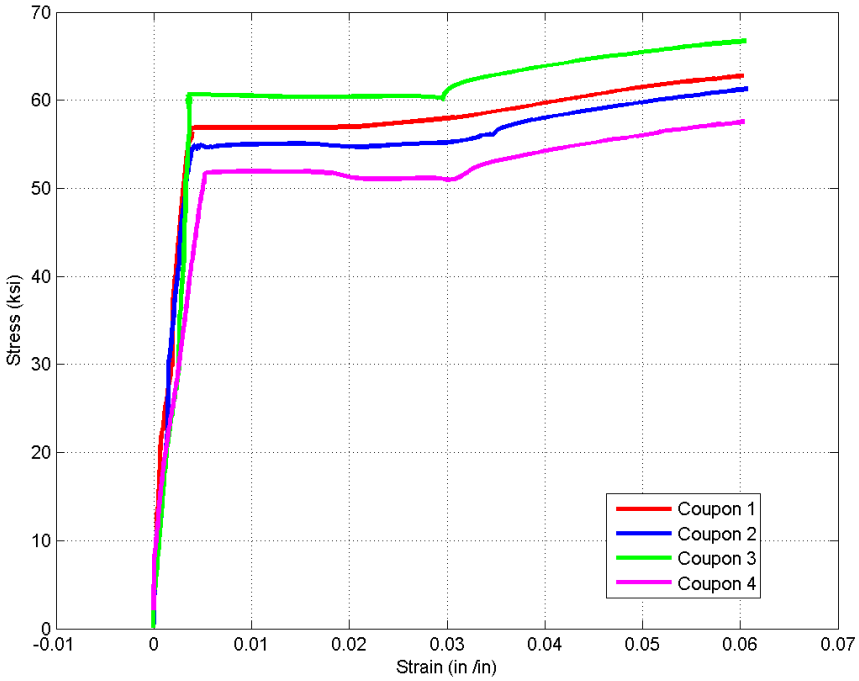

Figure 284. ST-7 coupon stress-strain data

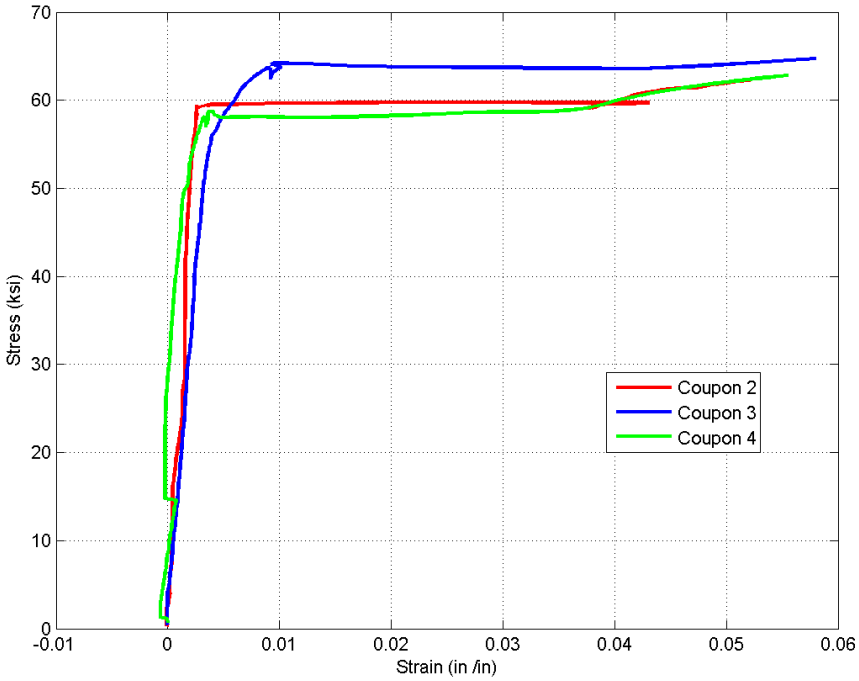

Figure 285. ST-8 coupon stress-strain data

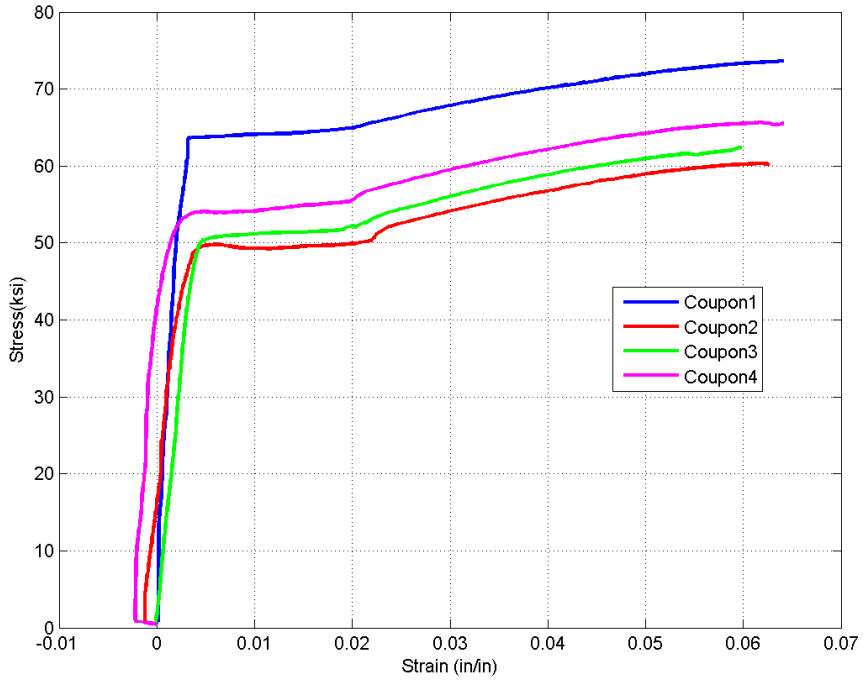

Figure 286. ST-10 coupon stress-strain data

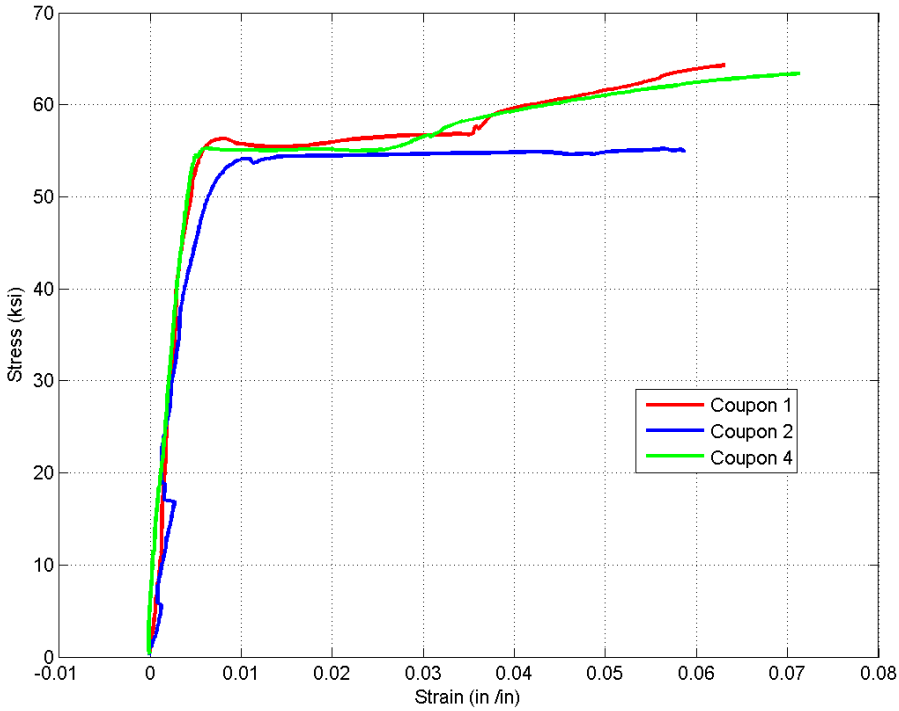

Figure 287. ST-11 coupon stress-strain data

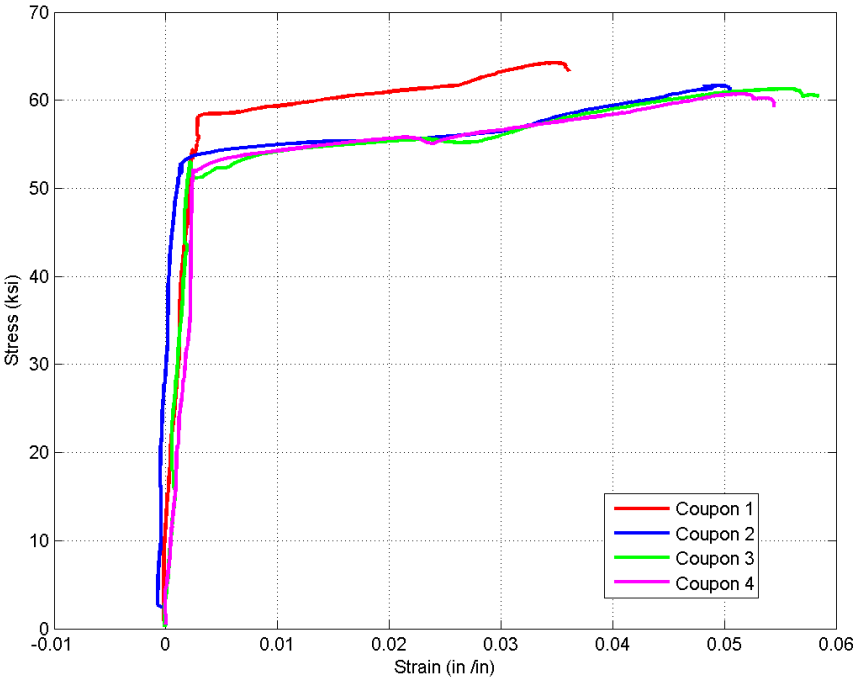

Figure 288. ST-12 coupon stress-strain data

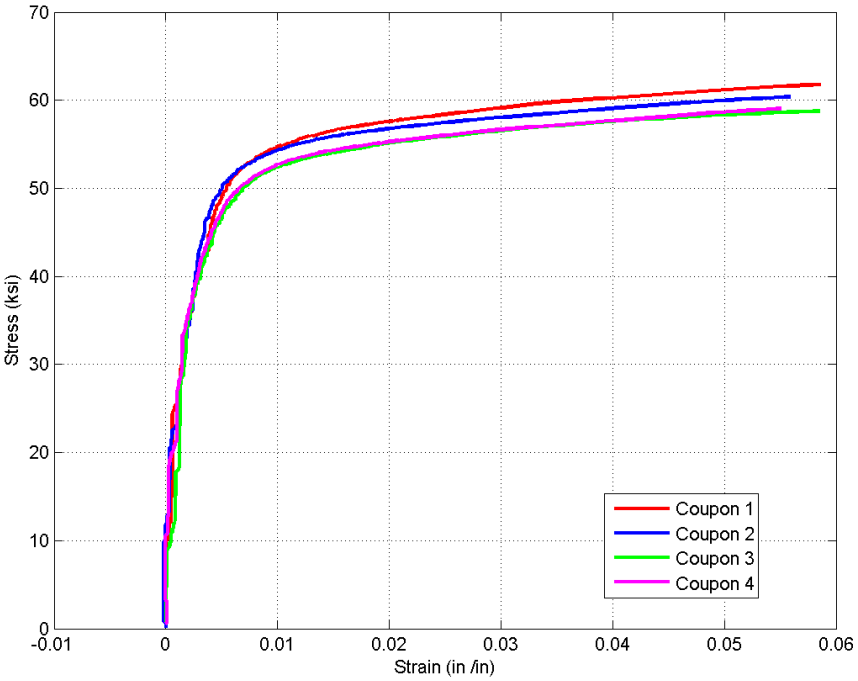

Figure 289. IM-1 coupon stress-strain data

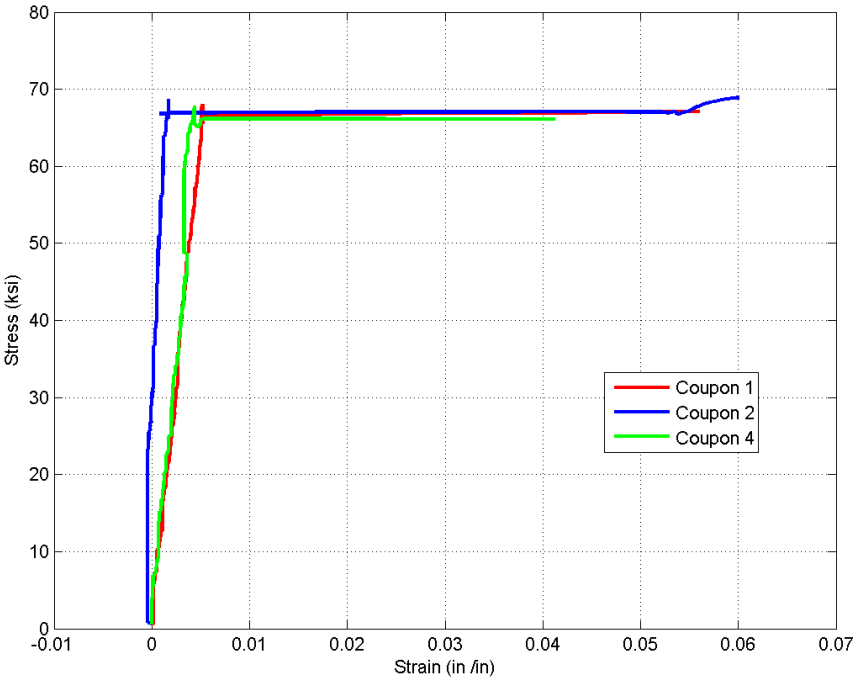

Figure 290. IM-2 coupon stress-strain data